Étude et caractérisation de coronographes stellaire pour la détection de planètes extra-solaires avec de très grands télescopes

Patrice Martinez

Observatoire de Paris - Meudon

École doctorale d'Astrophysique d'Ile-de-France

Coronagraphs characterization for high contrast imaging in the context of extremely large telescopes

THÈSE

présentée et soutenue publiquement le 12 Décembre 2008

pour l'obtention du

Doctorat de l'Université Paris VII - Denis Diderot

spécialité Astrophysique et instrumentation associée

par

Patrice Martinez

Composition du jury

Président :	Gérard Rousset
Rapporteurs :	Bruce Macintosh Claude Aime
Examinateurs :	Daniel Rouan Anthony Boccaletti Markus Kasper Jean-Luc Beuzit

ESO - European Southern Observatory
LESIA - Laboratoire d'Études Spatiales et d'Instrumentation en Astrophysique

Mis en page avec la classe thloria.

Acknowledgments

With these short lines, I would like to thanks all the people I met during my thesis. But before proceeding, I would like first to deeply thanks Benoit Mosser and Alain Abergel who are leading the Master degree "Astronomical and space-based systems engineering" at the Paris Observatory. This first one-year experience in the astronomical field before my PhD, was the best I had during my whole university background. Looking back, it was definitely a pretty good move. I met impressive teachers and engineers. Among them – and this will close this pre-PhD period – I am thankful to Guy Perrin, for the great teacher he is, following his curses has strongly influenced my choice of doing a PhD. Now let's start with the big part, that I will divided in the two places I shared during my PhD, LESIA and ESO:

The LESIA part:
Obviously, I am more than thankful to Daniel Rouan and Anthony Boccaletti for giving me the chance of working in the high-angular resolution field through this thesis. They trusted me for this present work, and gave me the necessary support among these three years.

I thanks Pierre Baudoz and Raphael Galicher (the SCC team) for support, and discussions. Many thanks to Céline Cavarroc for the 1.5 years coffee breaks (mornings and afternoons...), and for her support and for the many discussions we had. Also, even if I had many head-hatches because of his strange music, I am thankful to Pierre Riaud for discussions, advises and help.

Along this thesis, a part of my work was to develop prototypes of coronagraphs. For that I must deeply thanks Jacques Baudrand for his regular help in metrology, FQPM specifications and tests, and for the constant follow up of the FQPM manufacturing. His investment was a key advantage, and lead to a final good prototype owing his several iterations with the GEPI team.

The ESO part:
I would like to thanks to Norbert Hubin who accepted me in the Adaptive Optics department of ESO. A deep thanks to Markus Kasper for his help and support during my ESO time. I really appreciated the opened budget he gave me for prototyping coronagraphs, and for his idea of investigating the microdots technique for the manufacture of the apodizer of the APLC. That was a pretty good idea !

I thanks Sebastien Tordo for his regular help and support with the ITC and for several interesting serious and funny discussions. Also, a big thanks to Christophe Dupuy for his help with metrology inspection and with industrial designs. Thanks for giving me access to your lab several times.

I would like to deeply thanks Elise Vernet for her many helps at several occasions and on several different topics... She is definitely a key (staff 2009 ?) engineer in the AOD. Thanks to Natalia Yaitskova, for her help and suggestions on papers and for forthcoming work.

Thanks for Emmanuel Aller Carpentier, the HOT guy number 1, that makes possible HOT to work. Thank you for discussions, help and the forthcoming laboratory work we will share in 2009...

Also, thanks to Miska Le Louarn, Visa Korkiakoski, Richard Clare, a part of one of the AOD 10 am and 4 pm coffee groups, and for all the AOD people.

The Others:
The GEPI team, I am thankful to Christine Chaumond and Fanny Chemla. Thanks to their work, I am using several good Lyot coronagraphs and a four-quadrant phase mask.

I am also deeply thankful to Christophe Dorrer for the many discussions we had on the microdots technique, and for the work he did by producing these masks. Having so open discussions was a key advantage for the success of this experiment. Thanks also for the off-line discussions about your personal experience as a french expatriate.

The bonus track:
To close this acknowledgments part, I would like to thanks for a second round Anthony Boccaletti and Markus Kasper for their help and support during this PhD. I am deeply thankful for your help, advises and feedback on my work and papers. I am afraid that you both loss some hairs because of my english-writing (and english-speaking for Markus) that was really poor at the beginning... Thank you Anthony, for your feedbacks and corrections of this present manuscript.

By the way, I am also really thankful to the FP6 program that weekly full-filled my fridge and payed my bills during these 3 years of PhD... and thanks to Spooky, for his non-interest on human questions.

Far out in the uncharted backwaters of the unfashionable end of the Western Spiral arm of the Galaxy lies a small unregarded yellow sun.

Orbiting this at a distance of roughly ninety-eight million miles is an utterly insignificant little blue-green planet whose ape-descended life forms are so amazingly primitive that they still think digital watches are a pretty neat idea.

This planet has – or rather, had – a problem, which was this: most of the people living on it were unhappy for pretty much of the time.

Many solutions were suggested for this problem, but most of these were largely concerned with the movements of small green pieces of paper, which is odd because on the whole it wasn't the small green pieces of paper that were unhappy.

And so the problem remained; lots of the people were mean, and most of them were miserable, even the ones with digital watches.

Many were increasingly of the opinion that they'd all made a big mistake in coming down from the trees in the first place. And some said that even the trees had been a bad move and that no one should ever have left the oceans.

And then, on Thursday, nearly two thousand years after one man had been nailed to a tree for saying how great it would be to be nice to people for a change, a girl sitting on her own in a small café in Rickmansworth suddenly realized what it was that had been going wrong all this time, and she finally knew how the world could be made a good and happy place. This time it was right, it would work, and no one would have to get nailed to anything.

Sadly, however, before she could get to a phone to tell anyone about it, the Earth was unexpectedly demolished to make way for a new hyperspace bypass, and so the idea was lost, seemingly for ever.

D. Adams, from "The hitchhiker's guide to the Galaxy", 1979

Contents

II Optimizing coronagraph designs

III Preliminary system analysis

Bibliography*Bibliography*BIBLIOGRAPHYBIBLIOGRAPHY

Abstract

Direct detection and characterization of faint objects around bright astrophysical sources is highly challenging due to the large flux ratio and small angular separation. For instance, self-luminous giant planets are typically 10^6 times fainter than the parent star in the near-infrared. Even higher contrasts of up to 10^{-10} are needed to reach the realm of mature giant or telluric planets. To overcome this contrast issue, dedicated instruments for large ground-based telescopes such as SPHERE, GPI or EPICS for the future European-Extremely Large Telescope will use powerful Adaptive Optics systems coupled with coronagraphs.

A coronagraph used in conjonction with AO system can improve the sensitivity of an imaging system to faint structure surrounding a bright source. These devices block the core of the image of an on-axis source and suppress the bright diffraction rings and halo that would otherwise reduce the dynamic range of the imaging.

The state-of-the-art of coronagraphy has impressively envolved during the last ten years as the motivation of detecting and imaging exoplanets, ideally down to Earth-like planets. Coronagraphs are now able to provide a very large on-axis exctinction as demonstrated in laboratory conditions. But their capabilities during sky observations are damped by the large amount of residual phase aberrations that are left uncorrected by the AO system. Although coronagraphy is a mandatory technique to suppress on-axis starlight and understood as a critical subsystem, a coronagraph can only reduce the contribution of the coherent part of the light. Hence, their capabilities on sky are in strong relation with AO efficiencies.

The intent of our work is threefold: 1/ Compare a wide range of coronagraphs (the ones potentially proposed for planet finder projects) through their sensitivity to error sources that occur in a coronagraphic Extemely Large Telescope. Along this system analysis, we proposed for the Apodized Pupil Lyot Coronagraph (APLC) a way to optimize its parameter space with respect to ELT characteristics. 2/ Evaluate the effect of several aberrations on the performance of a coronagraphic eXtreme Adaptive Optics (XAO) and Differential imaging systems. The aim of this analysis is to derive relevant informations to choose/design coronagraphs for large ground-based telescopes. 3/ Develop several prototypes to be implemented on HOT, the High-Order Testbench developed at ESO, which includes star and turbulence generator to mimics realistic conditions at a telescope. This enables realistic comparison of coronagraphs coupled with AO system and will help to derive relevant informations for choosing or designing baseline concepts for ELTs. So far, we have developed several coronagraph prototypes: Lyots, APLC, FQPM and are currently working to enlarge this selection to others. Since manufacturing of critical component is often an issue, we successfully investigated new technology solution for the manufacturing of the APLC apodizer (using halftone dot process, the so-called microdots apodizer). Considering the satisfactory results of this approach, we are extending this technology to new coronagraph developments (Band-limited and conventional pupil apodization, for instance).

Notations and acronyms

Al	Aluminium
AO	Adaptive Optics
APLC	Apodized Pupil Lyot Coronagraph
APRC	Apodized Pupil Roddier Coronagraph
AGN	Active Galactic Nuclei
AGPM	Annular Groove Phase Mask
BK7	near-IR optical glass
BL	Band-Limited coronagraph
BL4	Band-Limited coronagraph 4^{th} order
BL8	Band-Limited coronagraph 8^{th} order
BM	Binary Mask
CCD	Charge-Coupled Device
CFHT	Canada France Hawaï Telescope
CONICA	COude Near-Infrared Camera
Cr	Chrome
CSL	Centre Spatial de Liège
DI	Differential Imaging
DM	Deformable Mirror
DPM	Disk Phase Mask
DZ	Dual Zone coronagraph
ELT	Extremely Large Telescope
EPICS	Exo-Planets Imaging Camera and Spectrograph
ESO	European Southern Observatory
E-ELT	European-Extremely Large Telescope
FFT	Fast Fourier Transform
FPM	Focal Plane Mask
FQPM	Four Quandrants Phase Mask
GEPI	Galaxies, Etoiles, Physique et Instrumentation
GMT	Giant Magellan Telescope
GPI	Gemini Planet Imager
HOT	High Order Testbench
HST	Hubble Space Telescope
IAC	Interferometric Achromatic Coronagraph
IR	Infra-Red
IWA	Inner Working Angle
JWST	James Webb Space Telescope

LAM	Laboratoire d'Astrophysique de Marseille
LESIA	Laboratoire d'Etudes et d'Instrumentation en Astrophysique
MACAO	Multi Application Curvature Adaptive Optics
MAS	milliarcsecond
MIRI	Middle Infra-Red Instrument
NACO	NAOS-CONICA acronym
NAOS	Nasmyth Adaptive Optics System
NM	nanometer
OD	Optical Density
ODC	Optical Differentiation Coronagraph
OHP	Observatoire de Haute Provence
ONERA	Office National d'Etudes et de Recherche Aérospatiale
OVC	Optical Vortex Coronagraph
OWA	Outer Working Angle
OWL	OverWhelmingly Large Telescope
PFI	Planet Finder Instrument
PIAA	Phase Induced Amplitude Apodization
PIAAC	Phase Induced Amplitude Apodization Coronagraph
PKC	Phase Knife Coronagraph
PO	Precision Optical imaging
PSF	Point Spread Function
PTV	Peak-To-Valley
PWS	Pyramid Wavefront Sensor
RCWA	Rigorous Coupled Wave Analysis
RIE	Reactive Ion Etching
RMS	Root Mean Square
RTC	Real Time Computer
SHWS	Shack-Hartmann Wavefront Sensor
SPHERE	Spectro-Polarimetric High Contrast Exoplanet Research
SR	Strehl Ratio
TMT	Thirty Meter Telescope
TPF	Terrestrial Planet Finder project
Vis	Visible
VLT	Very Large Telescope
VLTI	Very Large Telescope Interferometer
VNC	Visible Nuller Coronagraph
XAO	eXtreme Adaptive Optics
WFS	Wave-Front Sensor

Introduction

Overcoming the contrast issue between bright astrophysical sources and sub-stellar companions is mandatory for direct detection and spectroscopy of extra-solar planets. The typical contrast is 10^{-10} in the visible range of wavelengths and 10^{-6} in the near infrared. To improve performance of exoplanet searches towards lower masses, ideally down to Earth-like planets, deeper contrast are even required. Efficient detection and characterization of Earth-like planet would required a system capable of delivering 10^{-10} contrast at less than $0.1^{¨}$.

Any forthcoming planet finder instruments for large ground-based telescopes such as SPHERE or GPI [18, 61, for 8-10 meters class telescopes] or EPICS for the future 42 meters European-Extremely Large Telescope [E-ELT, 56] will use a combination of eXtreme Adaptive Optics (XAO) system and a coronagraph. A coronagraph used in conjonction with an XAO system can improve the sensitivity of an imaging system to faint structure surrounding a bright source. Efficient XAO systems are required to correct wavefront errors due to the atmospheric turbulence while coronagraphs are designed to suppress or at least attenuate the starlight diffracted by the telescope. Although their capabilities during sky observations are damped by the large amount of residual phase aberrations that are left uncorrected by the XAO system, motivation is strong to pursue coronagraphic R&D activities to demonstrate performance and properties in laboratory conditions.

The objective of this work is to assess the impact of system parameters on several coronagraph concepts and to start a first order comparison in the context of ELTs. We have selected a few coronagraphs (or families) and we evaluate the behavior of the delivered contrast with respect to the main sources of degradations that occur in a coronagraphic telescope at three levels of contrast: 1/ diffraction limited regime (i.e the limitation is set by the diffraction of the pupil), 2/ considering the residual from an XAO system and 3/ when a calibration of the halo is performed by the use of a differential imaging system (i.e the residuals are set by the static aberrations).

In the first part of this thesis, we briefly remind the context and the solution of the exoplanet research field. Families of coronagraph will be presented as well as their current state-of-the-art. Major error sources that occur in a coronagraphic telescope (more specifically extremely large telescopes) will be listed as well as the common metrics used in coronagraphy to quantify the capability of such devices.

Before starting any comparison in between coronagraphs, what may be possible to optimize for the application (i.e ELTs) must be optimized as a fair comparison. Therefore, in Part II, optimization work will be address for amplitude-type coronagraphs where we will demonstrate that some coronagraph can operate with optimal configuration for ELTs.

In Part III, a first order sensitivity analysis is performed where only the limitation imposed by telescope parameters are considered (i.e ideal case).

Part IV will then deal with more realistic conditions when coronagraphs are combined with XAO system and differential imaging system. This will lead to some conclusions that will allow to perform a preliminary classification of coronagraphs with respect to science requirements.

Since some coronagraphs can be implemented in cascade, we undergo a suitability analysis for one of them (APLC) in Part V.

Finally, Part VI is dedicated to laboratory developments. We developed several prototype of coronagraphs for the High-Order Testbench and investigated new technology approach for a critical component of the Apodized Pupil Lyot Coronagraph.

Therefore, the work presented hereafter had for philosophy to optimize, characterize, compare and indentify promising designs, as well as develop prototypes to verify in laboratory therory and simulation predictions.

Part I

The hitchhiker’s guide to the hidden worlds

1

The need for high contrast resolution

Contents

Abstract - *A large number of optical telescopes with apertures up to 10 meters, the Very Large Telescope for instance, have been commissioned and have provided highly exciting scientific results that demonstrate the power of combining new technologies with large telescope apertures. At the same time, new astrophysical challenges to our knowledge and understanding of many astronomycal topics have already been defined and pushed for the need of larger telescopes. Extremely Large Telescopes (ELTs) are ground-based answer in this new area of fainter objects, higher resolution. Since the discovery of the first extrasolar planet (Wolszczan & Frail 1992 [102], Mayor & Queloz 1995 [70]), the field of extrasolar planet research has exploded and is still growing up. It has largely contributed to the interest on the possible presence of life outside our solar system. In this Part, we will make a short overview of science background that drives the interest of these new telescope'generations. Extra-solar planet detection and characterization technics will be discussed, and finally we will describe status of ELTs projects that are in progress.*

1.1 Scientific drivers and requirements

1.1.1 Fundamental scientific motivation

ELTs will be fundamental tools for investigating a very wide range of astrophysical topics such as:

- The "dark ages" when the first sources of light and the first heavy elements in the universe formed. The nature of 1st lights objects and their effects on the young universe are among the outstanding open questions in astrophysics. In that sense, ELTs will work in synergy with the first science of the James Webb Space Telescope (JWST, providing targets for detailed study with spectrometers).

- Galaxies and large-scale structures of our universe from the 1st lights to present day, including the period in which most of the stars and heavy elements were formed and the galaxies in today's universe were assembled.

- Investigation into fundamental physics by studying massive black holes, for instance. Recent discoveries under-light that black-hole formation and growth is closely tied to the processes that form galaxies and suggests that super massive black holes are at the centers of most or all large galaxies. ELTs will extend our capability to detect and investigate central black holes to cosmological distances. ELTs will paved the road of a better understanding of fundamental constants variations, structure of space-time, dark matter, dark energy, direct measure of deceleration...

- Planet-formation processes and the characterization of extra-solar planets. Extra-solar planets are of the most exciting challenges to astrophysics for the next decades: to understand the physical processes that lead to star and planet formation and to characterize the properties of extra-solar planets. Planets on other stellar systems are among the more enthralling topics for our utterly insignificant little blue-green planet. Ideally, earth-like planet may become accessible.

Most of the science outlined hereabove assumes that technology development and implementation capabilities will proceed rapidly during the next decade.

1.1.2 Extrasolar planet detection

This is certainly the most popular astrophysical topics that has a large favorable support from scientific and non-scientific communty as well. Since the discovery of the first extrasolar planet (Wolszczan & Frail 1992 [102], Mayor & Queloz 1995 [70]), the field of extrasolar planet research has exploded and has grown up. This subject implies the characterization and understanding of the planetary formation in our Galaxy, the understanding of planetary systems formation and evolution, characterization of the planetary atmospheres, biologic markers search and study, and ultimately to the search for intelligent life.

1.2 Detection and characterization techniques

To tackle the difficulties of searching for planets, many methods have been proposed. However, to date only five methods have contributed to positive results. These are mainly indirect detections (Doppler shift of the parent star induced by the planet in its orbit, star occultation by the planet, pulsar timing and gravitational microlensing) and recently direct detections: coronagraphy.

1.2.1 Indirect detection methods

Most of the discovered planets have been evidenced using indirect methods. In other words, for almost all planets discovered so far, it has been done without any planet photons collected on detector. Indirect detection methods rely on the effect of the planet on its parent star. Most of the known exoplanets have been discovered, starting with the first in 1995, using precise measurements of radial velocity through spectroscopic observations. According to Fig. 1.1, detection methods for exoplanets can be classified into four categories:

- Dynamical effects (radial velocity, astrometry, timing and pulsar planets)

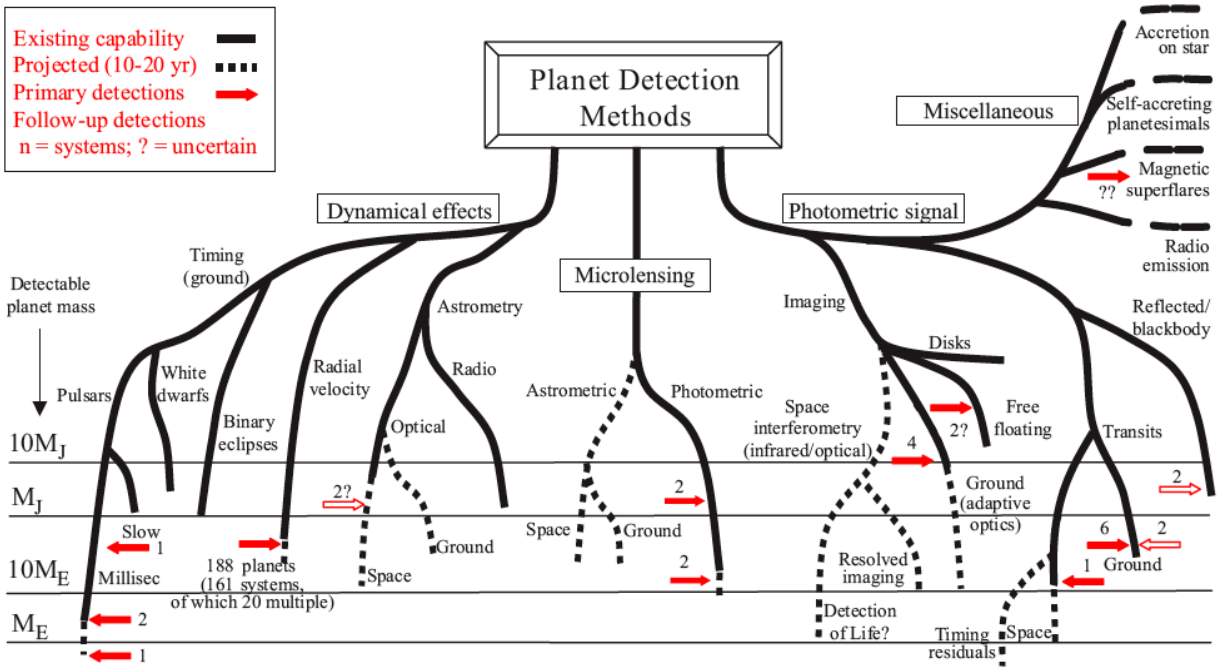

Figure 1.1: Detection methods for extrasolar planets from Perryman et al. 2000 [77] updated in 2006 by D. Mawet

- Microlensing effects (astrometric or photometric)
- Photometric signal (transits and direct imaging (see Fig. 1.3), radio emission)
- Miscellaneous effects (accretion on star...)

More details on indirect detection methods can be found in Perryman et al. 2000 [77], for instance.

1.2.2 Direct imaging methods: coronagraphy

Coronagraphy is a relatively young field in its first steps. It has only recently allowed imaging of exoplanets (Chauvin et al. 2005 [32]) in quite favorable case of young system for whom the companion is quite hot. Hence, the flux ratio between the parent star and the companion was only a few hundredths for a relatively large angular separation. Coronagraph can be defined as an instrument that strives to control the diffracted light from a bright astrophysical object to image faint off-axis companion in its close environment. A coronagraph is therefore a starlight suppression device designed to reduce the on-axis starlight as much as possible by preserving the off-axis companion signal. Its ability to do so in the close environment of the parent star is a major issue. All of the last ten years' coronagraph concepts strive to search for the ideal one. Nevertheless, at this time, none of them can simultaneously present all of the main high imaging contrast requirements. In Chapter 2, major coronagraph concepts are presented, and in Chapter 3 constraints that can restricted high contrast imaging capabilities of these devices are presented as well.

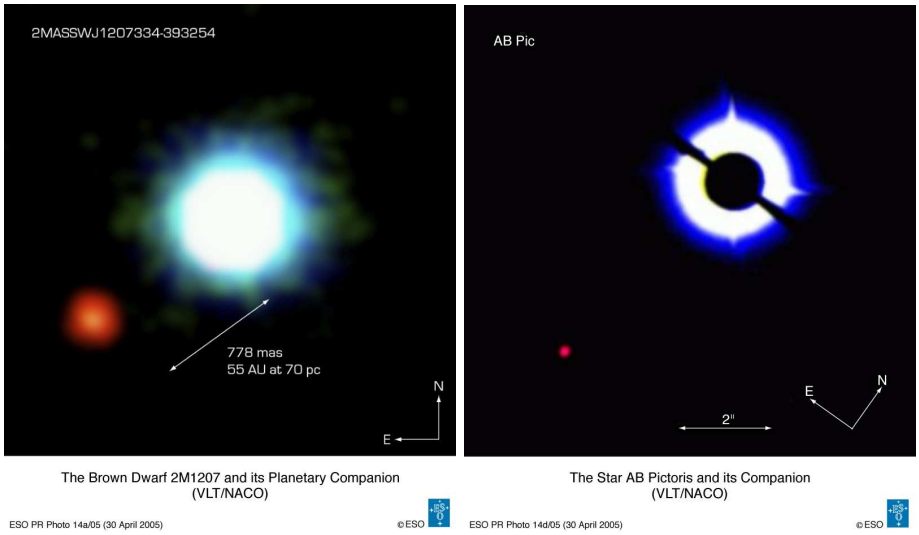

Figure 1.2: *Left*: The brown dwarf 2M12067 and its planetary companion (~ 5 M_J), image based on three near-infrared exposures with the NACO AO facility at the 8.2 m VLT telescope. *Right*: Coronagraphic image of AB Pictoris with its companion. Image obtained with VLT-NACO using a 1.4 arcsec occulting mask.

Extrasolar Planets Catalog

from the Extrasolar Planets Encyclopaedia

5 Planets	M[sini] (Mjup)	Period (days)	s-M Axis (AU)	Ecc.	Incl. (deg)	Ang. Dist. (arcsec)	st. Dist. (pc)	Spec. Type	st. Mass (Msun)	st. Metal.	st. Alpha	st. Delta
2M1207 b	4	-	46	-	-	0.877863	52.4	M8	0.025	-	12 07 33	-39 32 54
AB Pic b	13.5	-	275	-	-	6.030702	45.6	K2 V	-	-0.64	06 19 12	-58 03 15
GQ Lup b	21.5	-	103	-	-	0.735714	140	K7eV	0.7	-	15 49 12	-35 39 03
SCR 1845 b	8.5	-	4.5	-	-	1.168831	3.85	M8.5 V	-	-	18 45 07	-63 57 43
USco CTIO 108 b	14	-	670	-	-	4.62069	145	M7	0.057	-	16 05 54	-18 18 43

Figure 1.3: The 5 extrasolar planets discovered so far, by direct imaging technique. Image from the Extrasolar Planets Encyclopedia: http://exoplanet.eu/catalog.php.

1.3 Ground-based observations: the need of ELTs

1.3.1 ELTs opportunities

The discovery of 2M1207b and AB Pic b (Fig. 1.2), for instance, evidence that using the state-of-art instruments on the most advanced facilities can provide direct images of planetary companions and at the same time many promising ground-based projects were proposed and are currently under development like SPHERE at the VLT (Beuzit et al. 2007 [19]) or GPI (Macintosh et al. 2006 [61]). However, larger telescopes are desirable to improve performance of exoplanet searches towards lower masses and closer angular distances, ideally down to Earh-like planets. Several concepts of Extremely Large Telescopes (ELTs) are being studied worldwide (European-Extremely Large Telescope (E-ELT), Thirty Meter Telescope (TMT), Giant Magellan Telescope (GMT), for instance). Generally speaking, ELTs are wide field adaptive optics assisted telescopes with segmented large primary mirror, using active secondary mirror and built in a middle altitude site striving to reach diffraction limited performance by allowing fast instrument changes.

The first obvious but critical issue for telescopes is their capabilities to collect a large amount of light. As the amount of light collected goes up, the amount of information that can be extracted goes up as well. Obtaining light from very faint objects is one of the principal motivations for developing larger telescopes. For instance,

important informations can be extracted from spectra (chemical composition of objects...) while spreading light into a spectrum dilutes the intensity of light on the detector and as a result the amount of collected light is even more critical. Hence, through the large increase in the collecting area, ELTs will enable the spectroscopic study of objects that are beyond the accessibility of any current telescope.

The second major issue is the achievable angular resolution. For any telescope mirror the limit of the angular resolution is determined through the diameter (D) of the telescope and the wavelength (λ) of the light used. The angular image size is proportional to λ/D so in principle, large mirrors can produce smaller and sharper images. However, in the precise case of ground-based observations the atmospheric turbulence blurs the images and prevents this limit from being reached. In the same time, recent years have seen improvement of Adaptive Optics (AO) technology. AO is a powerful but complex technique that strives to provide real-time correction of atmospheric blurring, allowing high angular resolution to be obtained. This increase of angular resolution is crucial for many sciences interest areas in astronomy such as reflected-light jovian or terrestrial planets detection (Fig. 1.4).

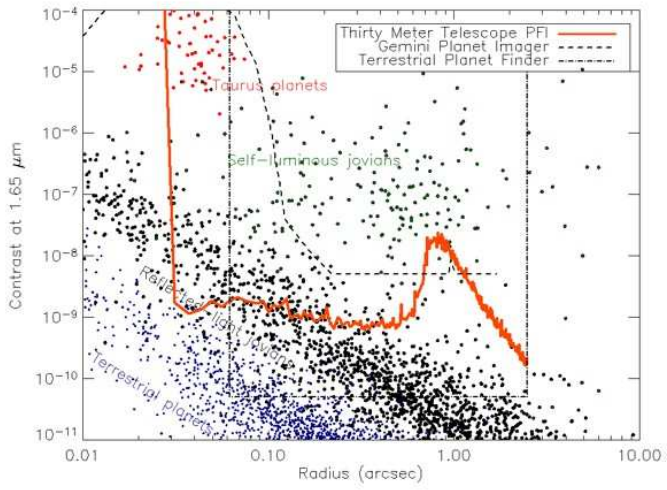

Figure 1.4: Contrast requested at 1.65μm (H band) as function of the angular separation for different planet types (From Macintosh slides 2006)

Observational science band

Ground-based observations are limited to visible and infrared bands owing to atmospheric transmission windows. In the precise case of planet detection, light from the planet can be divided from the starlight reflected by the planet (from visible to near-infrared) and the own planet thermal emission (medium-infrared). Both depends on the size, distance, phase and atmospheric composition of the planet. The near-IR commonly used bands (J, H, K) are set by the transmission of the atmosphere (and are somewhat water vapor dependent). In visible, the resolution is more appropriate to planet detection: a planet at 0.1 arcsecond with a 8 meter telescope is localized at $5\lambda/D$ while at 10μm planet is inside the first airy ring ($0.4\lambda/D$). However, AO systems are more efficient in near-infrared while phase defects are less critical ($1/\lambda$ law). Even if thermal background noise matters more, in thermal infrared planet contrast orbiting its parent star is more favorable than in visible (10^6 versus 10^9 for a Jupiter planet, Fig. 1.5).

1.3.2 Project planning & strategy

In this Section we will shortly describe the status of the three main concepts of future ELTs that are in progress worldwide: Giant Magellan Telescope (Johns et al. 2004 [GMT, 53]), Thirty Meter Telescope (Nelson et al. 2006 [TMT, 72]) and European-Extremely Large Telescope (Dierickx et al. 2004 [E-ELT, 35]).

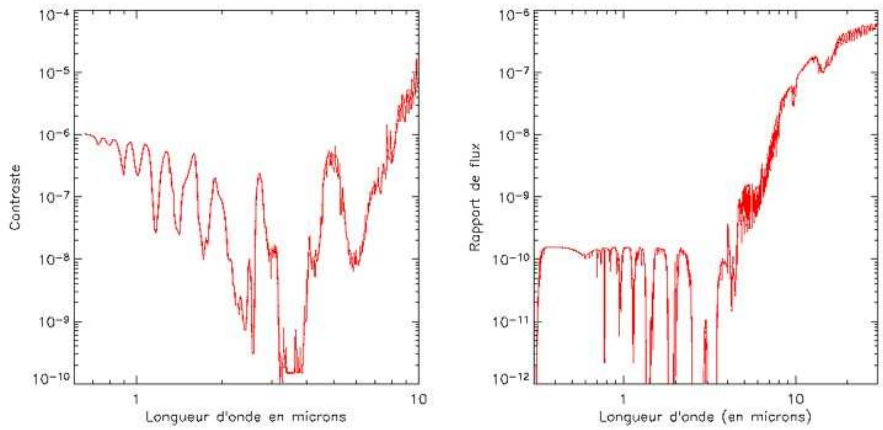

Figure 1.5: Contrast requirement as function of the wavelength for Jupiter-like detection (left) and Earth-like detection

GMT

GMT comes from a collaboration between Carnegie, Harvard, Smithsonian, University of Texas at Austin, Texas A&M, MIT, Michigan & Australian National University. It should be built at Las Campanas in Chile, and first light are planned for 2016-2017. The estimate budget is 550 M$. In Fig. 1.6, the GMT design is shown. GMT will have a segmented primary mirror consisting of six 8.4 meter off-axis circular mirrors arranged in a hexagon-like shape. A seventh 8.4 meter mirror in the center will be obstructed. The GMT optical design will use an aplanatic Gregorian configuration with a concave secondary mirror. The segments allows a very fast $f/0.7$ primary mirror focal ratio permitting an overall compactness of the GMT structure and reducing the size of the $f/8.0$ secondary mirror and instrumentation. For more informations, see GMT website: http://www.gmto.org. Six first generation instruments are planned, including:

- Visible multi-object spectrograph
- Visible high resolution spectrograph
- Near-IR multi-object spectrograph
- Near-IR imager combined with XAO
- Near-IR high-resolution spectrometer
- IR imager / spectrograph combined with AO system

TMT

TMT comes from a collaboration between Caltech, California University and Canada consortium. The proposal for construction is ready and will start in April 2009. First light is planned for 2016-2017. Possible sites are in Chile, USA and Mexico. The estimate budget is 750 M$. In its current design (see Fig. 1.7), the TMT will be a 30 meter alt-az Ritchey-Chretien telescope with 492 segments on the primary mirror and an active secondary mirror with a final focal ratio of $f/15$. For more details, see the TMT website: http://tmt.org. Six first generation instruments are planned, including:

- IR spectrometer imager
- Large scales optical spectrometer
- IR multi-objet spectrometer

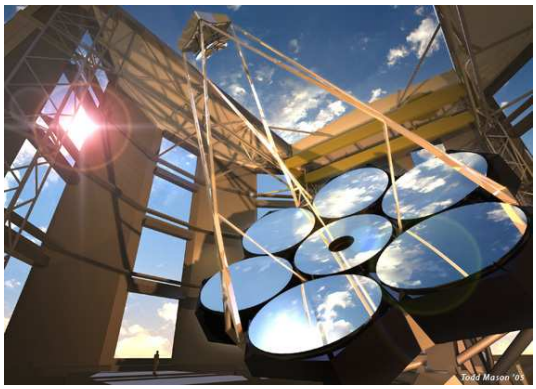

Figure 1.6: Artist view of the GMT

- IR high resolution spectrometer
- High resolution optical spectrometer
- High contrast planet imager

E-ELT

E-ELT is a European project leads by ESO and supported by community activities (FP6 and FP7). Earliest construction starts early 2010 and first light is planned in 2017. Possible sites are in Chile, Argentina, Morocco and Spain. The estimate budget is 900 M$. In its approved design (see Fig. 1.8, the E-ELT is a 42 meter segmented primary mirror telescope with 1148 segments. The secondary mirror is fully active of 6 meters and the whole design is a 5 mirrors configuration. For more details, see the E-ELT website: http://www.eso.org/projects/e-elt/. First generation instruments are planned, including:

- Near-IR multi-integral field unit spectrograph combined with AO
- High resolution and stability visual spectrograph
- Planet imager and spectrograph
- Single integral field unit wide spectral band spectrograph
- IR camera / spectrograph

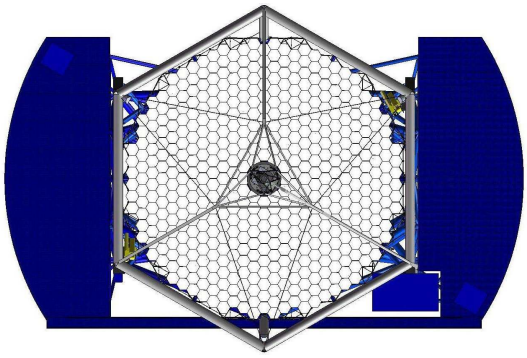

Figure 1.7: View of the TMT

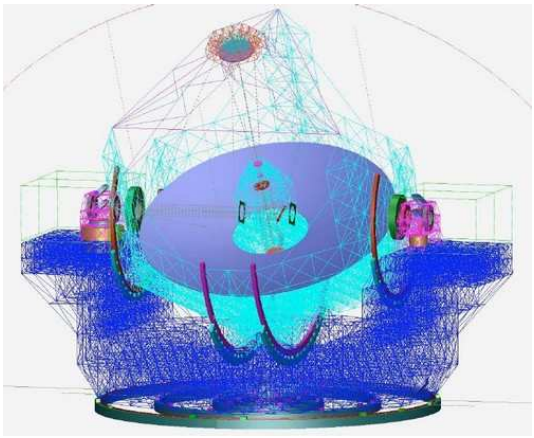

Figure 1.8: Mechanical view of the E-ELT

2

State-of-the art of Coronagraphy

Contents

Abstract - *Coronagraphy was introduced by B. Lyot in the 1930's for solar application. Since that time, the concept has evolved to stellar application. A coronagraph is an instrument that strives to control the diffracted light from a bright astrophysical object to image faint off-axis companions in its close environment. Recent years have seen intensive research and development of new high contrast imaging coronagraph concepts. Most of them have been studied from a theoretical point of view while some of them have been developed and tested in laboratory conditions. Only a few of them have been implemented on actual telescopes and provided scientific results. In this Chapter, principle, concepts and status of the coronagraphy field will be presented. Finally, concepts analyzed through this thesis will be listed.*

The term high contrast imaging (HCI) refers to a large number of optical techniques combined by one common aim. This aim is detection and imaging of faint objects (planets, planetary disks, companions etc.) against the background formed by scattered and diffracted light from the parent star. Generally speaking there are two characteristic inputs of this task: first is that the background is much brighter than the object (typically the difference is 4-5 orders of magnitude), and second, that the faint object is located relatively close to the star (as close as 20 mas angular separation). The purpose of HCI is to suppress the star light in the area of the expected planet location with minimal suppression of the planet light.

All high contrast imaging techniques are divided into two main groups according to the optical principle of light suppression. In nulling interferometry the light is collected in several pupils, the phase offset between which equals π for the on-axis beam (from the star). The efficiency of nulling is defined by number of pupils and the accuracy of the phase offset. The nulling interferometry is most efficient for the long wavelength (mid infrared, 6-18μm). The complementary technique for the shorter wavelength (visible and near infrared) is coronagraphy. In coronagraphy star light collected in single pupil is suppressed in the image plane. The latter can be achieved by light absorption (Lyot coronagraphy), light destructive interference (phase mask coronagraphy, interferometric coronagraph and Lyot coronagraphy as well), or virtually – changing the shape of the star PSF by reshaping the complex field in pupil (pupil apodized coronagraphy). The combination of the techniques as well as optical way to perform the light suppression result into a long list of coronagraphs, which is still growing.

In its classical sheme (see Fig. 2.1), a coronagraph is a combination of a low-frequencies filter (the coronagraph mask placed in the first focal plane) with a high-frequencies filter (so-called Lyot stop placed in the second pupil plane). The light distribution in the relayed pupil (second pupil plane) is different than in the input pupil. The light is diverted outside the geometric pupil. The action of the Lyot stop is precisely to select the geometric pupil (most of the time smaller) in which the on-axis starlight is rejected. Downstream, an image of the field can be formed with the starlight attenuated. In contrary, an off-axis object (companion) missing the effect of the coronagraph (low-frequencies filter) has its pupil unaltered and is re-imaged in the final detector plane.

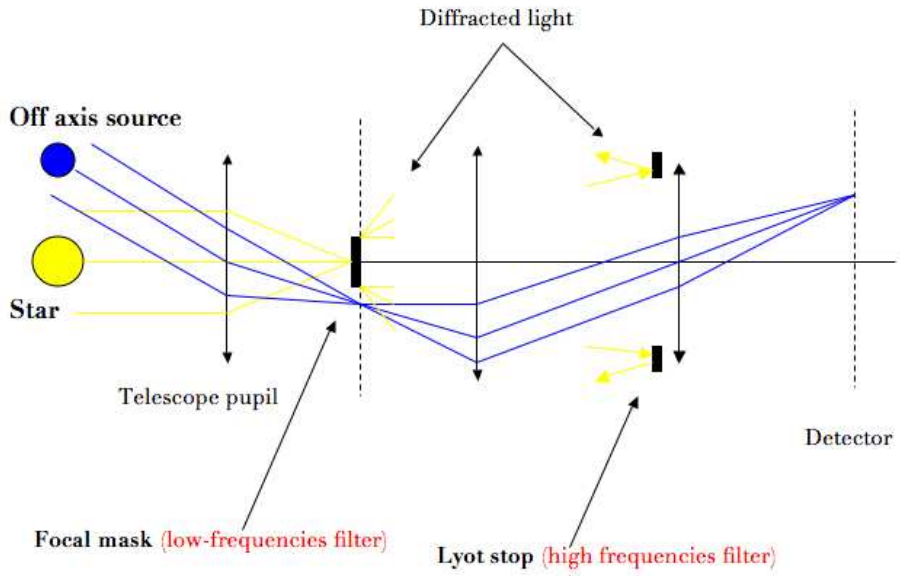

Figure 2.1: Classical sheme of the coronagraphy principle

Coronagraph concepts can be divided into four main families according to the optical principle of light suppression: multiple beams type (rejecting the light by interference beam combination at a beam splitter), pupil apodization (playing with light into a confined region of the image plane), amplitude mask and phase mask (light absorption or destructive interference in a sequence of Fourier spatial filters in the image and exit pupil plane). In the following, we describe the main coronagraph concepts. Obviously, it is a non-exaustive list.

2.1 Coronagraph general formalism

A common formalism can be used for a wide number of coronagraphs, the so-called focal plane coronagraphs. Here, we briefly describe this formalism while in the next section coronagraphs will be presented.

In the following, for the sake of clarity, we omit the spatial coordinates r and ρ (for the pupil plane and focal plane respectively). The coronagraphic process, corresponding to propagation from the telescope entrance aperture to the detector plane, is expressed in Eq. 2.1 to 2.5. Planes A, B, C and D correspond to the telescope aperture, the coronagraphic focal plane, the pupil stop plane and the detector plane respectively. The general setup is illustrated in Fig. 2.1.

- We denote by P the telescope pupil.
- The focal plane mask (FPM, hereafter) transmission is $1 - \varepsilon M$ where M described the mask function.
- The Lyot stop is denoted Π.

The coronagraphic process can be easily described using classical Fourier propagator (i.e a Fourier transform exists between each of the four planes). The Fourier transform of a function f is noted $\hat{f}$. The symbol $\otimes$ denotes the convolution product. The expression of the complex amplitude (ψ) in the successive planes A, B, C and D are:

In the pupil plane:

$$\psi_A = P\phi \tag{2.1}$$

The complex amplitude of the star is spatially filtered (low frequencies) by the FPM:

$$\psi_B = \hat{\psi}_A \times [1 - \varepsilon M] \tag{2.2}$$

The exit pupil image is spatially filtered (high frequencies) by the stop:

$$\psi_C = \hat{\psi}_B \times \Pi \tag{2.3}$$

$$\psi_C = [\psi_A - \varepsilon \psi_A \otimes \hat{M}] \times \Pi \tag{2.4}$$

The coronagraphic amplitude on the detector plane becomes:

$$\psi_D = \hat{\psi}_C = [\hat{\psi}_A - \varepsilon \hat{\psi}_A M] \otimes \hat{\Pi} \tag{2.5}$$

The effect of a coronagraph therefore appears in Eq. 2.4:

- The first term corresponds to the wave of the entrance pupil.
- The second term corresponds to the wave diffracted by the mask for which the light diffracted outside the geometric pupil in C has been removed.

Ideally a coronagraph cancel the on-axis starlight while preserving the light from an off-axis source. Therefore, for a star the two terms in Eq. 2.4 must interfere destructively while for the companion the second term only must cancels.

2.2 Amplitude-type coronagraphs

2.2.1 Lyot coronagraph

The first amplitude coronagraph is the Lyot coronagraph (Lyot 1939 [60]) initially used for the solar corona study (Fig. 2.2), could get a new interest on ELTs since these large telescopes relatively relax the constraint on the IWA. This device is a circular disk with no transmission inside its physical area. The diameter d of the device depends on the application (performance requirements with respect to the IWA constraint).

Figure 2.2: First utilization of the Lyot occulter for solar corona studies

2.2.2 Apodized Pupil Lyot Coronagraph

The apodized pupil Lyot coronagraph (APLC) is a direct improvement of the Lyot coronagraph (Aime et al. 2002 [9]); (Soummer et al. 2003 [89]). The APLC combines a variable radial transmission mask in the pupil plane with a small Lyot mask of the focal plane of the instrument, and strives to adapt the infinite support of the PSF to the finite support of the Lyot mask by reducing the PSF wings. As far as the energy conservation is concerned, the central core of the apodized PSF gets larger. This concept will be further detailed and analyzed in Chapter 5 where we will investigate the possibility of optimizing the apodizer/Lyot mask couple in regards of ELTs specificities.

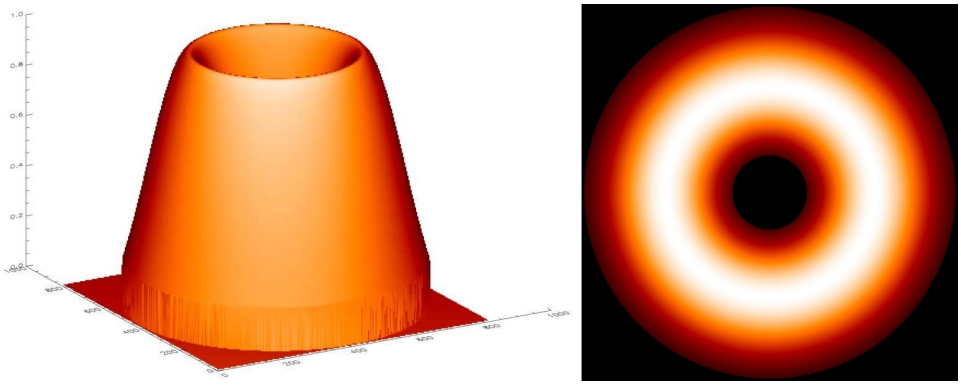

Figure 2.3: Amplitude function of an apodizer for APLC in 3D (left) and 2D (right) representation.

2.2.3 Multi-stage Apodized Pupil Lyot Coronagraph

Using the properties that the relayed pupil is apodized as the entrance aperture, the APLC can be implemented in cascade ($APLC_n$, Aime et Soummer 2004 [7]) using only one apodizer (in the first pupil plane) and successive Lyot mask (n) in n focal planes. The goal is therefore to produce deeper performance or relax IWA (i.e make a selection of smaller (n) Lyot masks reaching the same rejection rate in cascade as an APLC 1 stage with a larger Lyot mask diameter). A dedicated chapter (Chapter V) will be addressed on the suitability of the APLC cascade configuration.

2.2.4 Band-Limited coronagraph

As the APLC, Band-limited coronagraphs (BL) proposed by Kuchner et al. 2002 and 2005 [59, 58]. are direct improvement of the Lyot coronagraph. The principle is to limit the Fourier transform of the focal plane mask on a finite support. These are occulting mask which have mask shape functions that are band-limited in a Fourier sense (Fig. 2.4). In other words, the Fourier transform of such masks are band-limited. In perfect case, Band-limited coronagraphs can provide a perfect cancellation of an on-axis light. This concept will be further detailed and investigated in Chapter 6.

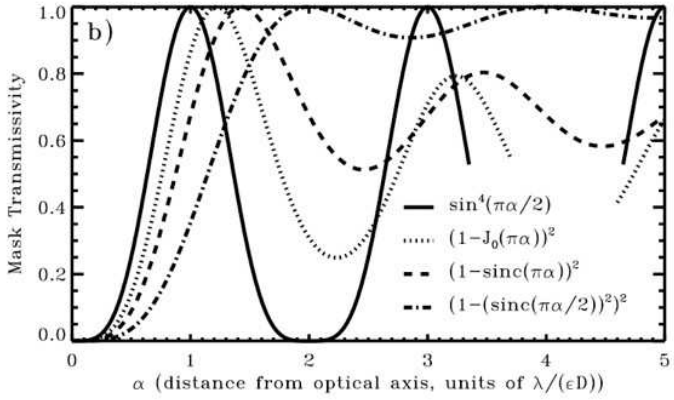

Figure 2.4: Example of band-limited functions. Image from Kuchner et al. 2002 [59]

2.3 Phase-type coronagraphs

2.3.1 Roddier Coronagraph

Proposed by Roddier & Roddier (1997) [82], the Roddier coronagraph (DPM hereafter, Disk Phase Mask) is the first concept using a phase shift instead of an amplitude approach on the mask in the focal plane. The principle is to change the sign of the complex amplitude by introducing a π phase shift in some area of the focal plane. The π phase shift is physically produced with a retardation of the wave at the focal plane by adding an optical path difference in the mask area. The thickness e of the mask is given by the following relation:

$$2(n_\lambda - 1)e = k\lambda \tag{2.6}$$

with n_λ the optical index of the layer, λ the wavelength and k the order. Since the mask has a circular geometry, the size of the device is calculated to balance the complex amplitude with positive and negative values. In other words, the size of the mask is calculated to provide an equalization of the complex amplitude inside and outside its physical area. The phase shift of half of the complex amplitude results in a destructive interference occurring inside the relayed pupil downstream of the focal plane. For a circular aperture with no obscuration, the radius of the mask is $0.53\ \lambda/D$.

2.3.2 Four Quadrants Phase Mask

The four quadrants phase mask (FQPM) was proposed by Rouan et al. 2000 [83] to solve the wavelenght dependence of the DPM regarding its size (geometrical chromatism). The nulling process is similar to that of the DPM (destructive interference occurring inside the relayed pupil downstream the focal plane) but the geometry of the device is fully different. The airy pattern is divided into four parts and a π phase shift is applied to half of them. In other words, the focal phase mask, shifts two out of the four quadrants of the image by π.

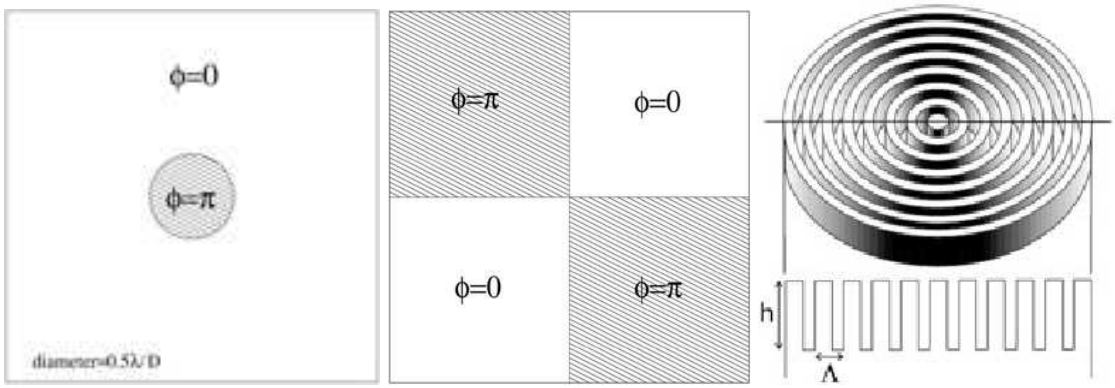

Figure 2.5: Some phase-type coronagraph designs, from left to right: DPM, FQPM and AGPM (image from Mawet et al. 2005 [68])

The FQPM has been tested in the laboratory like a lot of other concepts and it has been successfully installed and combined with Adaptive Optics system on a ground-based telescope (Boccaletti et al. 2004 [27]) and has provided scientific results (Gratadour et al. 2005 [44]); (Riaud et al. 2006 [80]).

2.3.3 Achromatic Phase Knife Coronagraph

Proposed by Abe et al. 2001 [4], the achromatic phase knife coronagraph (PKC) is an achromatic version of the FQPM where the π phase shift is performed in two steps. The idea is to separate spatially the wavelength in order to apply a space-variant phase shift. In practice, the phase shift can be implemented in the form of a prism with linearly increasing OPD along one axis. Prototype has been developed and tested in the lab (Abe et al. 2003 [2]) but in a monochromatic version. With a different optical design (using assembly of plates with different indexes instead of dispersive elements) it was tested on sky without achieving the expected results.

2.3.4 Annular Groove Phase Mask

The annular groove phase mask (AGPM) was proposed by Mawet et al. 2005 [68]. It is an achromatic solution derived on FQPM concept. It consists on an optical vortex induced by a space-variant surface relief sub-wavelength grating. It is made up with of a concentric circular surface-relief grating with rectangular grooves of depth h and equally separated by the period Λ. The period being smaller than the wavelength, this grating is actually a space-variant ZOG (Zero Order Grating). The period of such device is sufficiently small to avoid any diffraction of order up to 0 and by carefully controlling the geometry of the grating structure (Λ, h and the width of the grating ridges) it makes therefore the phase shift achromatic. The differential phase shift is induced between the local polarization components of the incident light. The AGPM behaves exactly like an achromatic FQPM except that the horizontal and vertical phase transitions are removed (blind zones). Therefore, the stellar environment is not attenuated by these λ/D-width dead zones. The AGPM has exactly the same performance and limitations as any achromatic FQPM. The manufacturing feasibility of AGPM is under evaluation.

2.3.5 Optical Vortex Coronagraphs

The optical vortex coronagraphs (OVC) proposed by Palacios et al. 2005 [76] are focal plane vortex phase masks as the AGPM. In polar coordinates (ρ, θ), the mask phase is equal to $m\theta$, where **m** is the topological charge. The AGPM coronagraph corresponds to the vortex phase of topological charge of 2. The topological charge directly dictates the null depth order of the concept (θ^2 law dependency for a topological charge of 2 and so). The order of the null rules the mask sensitivity to low-order aberrations near the optical axis and hence in practice directly impacts on aberrations level and pointing errors requirements.

2.3.6 Dual Zone Coronagraph

The dual zone coronagraph (DZ) proposed by Soummer et al. 2003 [90] is an achromatic version of the DPM. The achromaticity is obtained by combining circular phase masks with different sizes and different thickness. Prototypes were manufactured and are under testing by the Laboratoire d´Astrophysique de Marseille (LAM).

2.3.7 Apodized Pupil Dual Zone Coronagraph

The apodized Pupil dual zone coronagraph (APRC, initially the Apodized Pupil Roddier Coronagraph) is an improved version of the DZ where the entrance pupil is apodized to achieve a deeper rejection rate (Soummer et al. 2003 [90]). This concepts is also under further investigations by LAM. Prototype is currently under laboratory experiment at LESIA with DZ provided by LAM and apodizer provided by R. Soummer.

2.3.8 Optical Differentiation Coronagraph

The optical differentiation coronagraph (ODC) proposed by Oti et al. 2005 [75] combines a phase mask and amplitude mask and it is adapted from a wavefront sensing concept.

2.3.9 Multiple stage configuration

A wide number of phase mask can be used in cascade configuration with in the first order the intent to reach deeper starlight attenuation. So far, only the multiple-stage FQPM has been studied (Baudoz et al. 2007 [15]) and test in laboratory conditions. This concept is also consider in the EPICS consortium since cascade configuration of the FQPM reduces its sensitivity to the central obscuration, as well as providing an achromatic behavior.

2.4 Multiple beam concepts

2.4.1 Achromatic Interferometric Coronagraph

The Achromatic Interferometric Coronagraph (AIC) proposed by Gay et al. 1997 [39] and Baudoz et al 2000a,b [16, 17] has also been tested on ground-based telescope (OHP, CFHT) using adaptive optics system. On the contrary to the other concepts discussed hereabove, the AIC is intrinsically totally achromatic. However, this concepts has got its own intrinsic drawbacks: maintained the OPD and it symmetries images (each companion gives two images). The last limitation has been solved by the proposed concept of the Hybrid Interferometric Coronagraph (Baudoz et al. 2005 [14]) whom avoids the 180 deg ambiguity. Principle is schematically described in Fig. 2.6:

- Two identical telescope beams are created.
- One of them is π dephased and rotated.
- The two beams are recombined in the focal plane.
- Assuming that the central PSF is centro-symmetric, Starlight is perfectly cancelled.
- An off-axis source produces 2 equally bright images in the focal plane.

2.4.2 Visible Nulling Coronagraph

The visible nulling coronagraph proposed by Mennesson et al. 2003 [VNC 71] is indeed equivalent of a double-Bracewell interferometer. Two successive shear in perpendicular directions (X shear and Y shear) produce 4 beams that yield to a 4^{th} order null in the pupil plane when combined. The order null refer to the way coronagraph´ transmission evolve (as a power of θ, where θ is the angular separation from the optical axis). Therefore, transmission of the VNC varying as θ^4. Due to wavefront mismatches between the 4 beams, a spatial filtering stage using an array of single-mode waveguides is necessary to further suppress the stellar residual light.

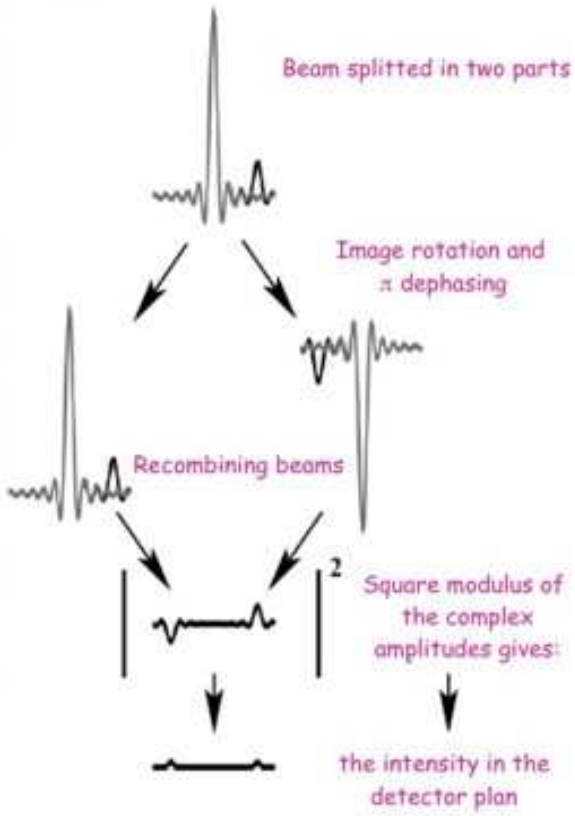

Figure 2.6: AIC shematic principle. Image from P. Baudoz

2.4.3 Pupil Swapping Coronagraph

The pupil swapping coronagraph proposed by Guyon et al. 2006 [49] consists on a pupil plane mask that subdivides the entrance pupil into four sub-pupils. A successive nulled against X swapped copy of the first four sub-pupils and Y swapped copy of the resulting after nulled with the X swapped copy yield a fourth order null.

2.5 Pupil Apodization

2.5.1 Conventional Pupil apodization and Shaped-Pupil

Conventional pupil apodization and Shaped pupil strive to modify the airy pattern using an amplitude mask in the pupil plane. These amplitude masks are either continuous (Jacquinot et al. 1964, Nisenson et al. 2001, Gonsalves et al. 2003, Aime 2005) [51, 73, 43, 6], or binary (Kasdin et al. 2003, Vanderbei et al. 2003a & b, Vanderbei et al. 2004) [55, 98, 99, 97, 6] (see Fig. 2.7). Apodization can be also produced using Mach-Zehnder type pupil plane interferometry (Aime et al. 2001 [8]) which was recently investigated (Carlotti et al. 2008 [29]).

2.5.2 Phase induced Amplitude Apodization Coronagraph

The Phase Induced Amplitude Apodization Coronagraph (PIAAC) has been proposed by Guyon et al. 2004 [47]. Using two mirrors, it achieves an achromatic apodization of the telescope pupil with a geometric redistribution of the light to allow a 100% throughput and no loss of angular resolution. This apodization differs from the one of the APLC since it concentrates most of the energy inside a single diffraction peak. The energy inside this peak is then

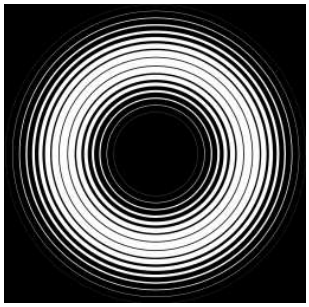

Figure 2.7: Example of shaped pupil coronagraph (binrary ring) optimized by L. Abe for a 30% central obscuration pupil using code based on Vanderbei et al .2003 [98]

occulted by a Lyot mask placed in the focal plane to efficiently remove star light. To remove the off-axis wavefront distortion introduced by the pupil remapping, the beam is de-apodized after the occulting mask.

PIAAC can be used as an imager (PIAA, see Fig. 2.8) proposed by Guyon et al. 2003 (originally before the PIAAC) [45] where the detection occurs directly in the first focal plane after the beam remapping. The PIAA concept is under intensive laboratory development for the Subaru telescope by O. Guyon.

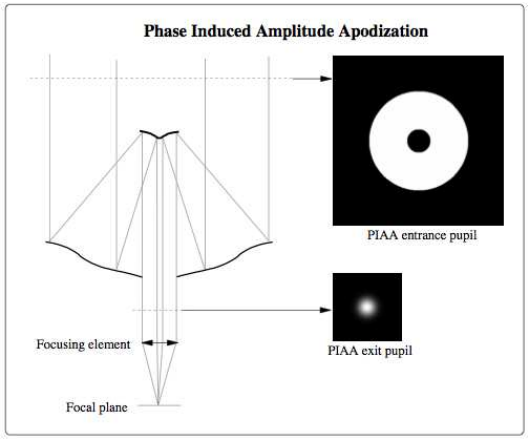

Figure 2.8: Shematic representation of PIAA principle from [45]

2.5.3 Phase Induced Zonal Zernike Apodization

The phase induced zonal zernike apodization (PIZZA) proposed by Martinache et al. 2004 [64], achieves the pupil amplitude apodization using phase contrast technique commonly used in microscopy or strioscopy (to control optics quality polishing). As the PIAA, there is no loss of off-axis resolution and high throughput.

2.6 Status of the coronagaphy approach

The list of coronagraphs presented above is not exhaustive but basically it is quite representative of most actual important concepts. In Table 2.1, status of these coronagraphic concepts is resumed. One can see that these last years has been fruitful in term of laboratory developments. However, sky observations are still limited to a few number of concepts.

Table 2.1: Status of the coronagraphy state-of-art

Coronagraph type	State of art		
	Laboratory tests	Sky observations	Scientific results
PHASE TYPE			
Roddier coronagraph	vis. / near IR	-	-
Four quadrant phase mask	vis. / near & mid IR	near IR	yes
Achromatic phase knife coronagraph	vis.	vis.	-
Annular groove phase mask	-	-	-
Optical vortex coronagraph	vis.	-	
Dual zone coronagraph	near IR	-	-
Apodized pupil Roddier coronagraph	near IR	-	-
Optical differentiation coronagraph	-	-	-
AMPLITUDE TYPE			
Lyot coronagraph	vis. / IR	vis. / IR	yes
Apodized Pupil Lyot Coronagraph	vis. / near IR	IR	-
Apodized Pupil Lyot Coronagraph (n)	near IR	-	-
Band-limited coronagraph 4^{th} order	vis.	-	-
Band-limited coronagraph 8^{th} order	vis.	-	-
INTERFEROMETRIC TYPE			
Achromatic interferometric coronagraph	vis. / near IR	near IR	yes
Visible nulling coronagraph	vis.	-	-
Pupil swapping coronagraph	-	-	-
PUPIL APODIZATION			
Pupil apodization and Shaped-pupil	vis.	-	-
Phase induce amplitude apodization	vis. / near IR	-	-
Phase induced zonal zernike apodization	-	-	-

2.7 Scientific results on the sky

Even if the last ten years have been rich in new coronagraphic concepts, only a few part of them have been developed and tested in laboratory conditions. The number of concepts implemented on telescopes is then really small. So far, only a small number of coronagaph has provided scientific results.

In this part, I will briefly present some sky results (not exhaustive list, of course) which are assumed to be representative of the actual possibilities of such devices. This part will also be an opportunity to recall that even if the ultimate goal of coronagraphy (at least in the background of this present thesis) is the direct detection of exo-planets (ideally down to earth-like planet), coronagraph combined with AO system can be a powerful tool for many other astrophysical targets as binary stars, circumstellar disk or AGNs.

2.7.1 Binary stars

Images on Fig. 2.9 (left) were obtained at the ESO Very Large Telescope using a FQPM coronagraph (Boccaletti et al. 2004 [27]) in 2004 on NACO (Rousset et al. 2003 [84]), the near-IR camera with adaptive optics at UT4. The FQPM was optimized for the *K* band. HIP 1306 is classified as a binary star (*Hipparcos* catalogue). The angular separations of components are 0.128" and 1.075" with magnitude differences of 1.6 and 3.5 respectively.

An other example (Fig. 2.9, right), has been obtained with a AIC (Baudoz et al. 2000 [17]) on the 1.52 meter OHP telescope in K band. The angular separations of the two components are 0.11" with magnitude difference of 3.5.

These two example shows the interest of coronagraph concepts that allow small IWA. Angular separations correspond to inaccessible area for Lyot coronagraph, for instance.

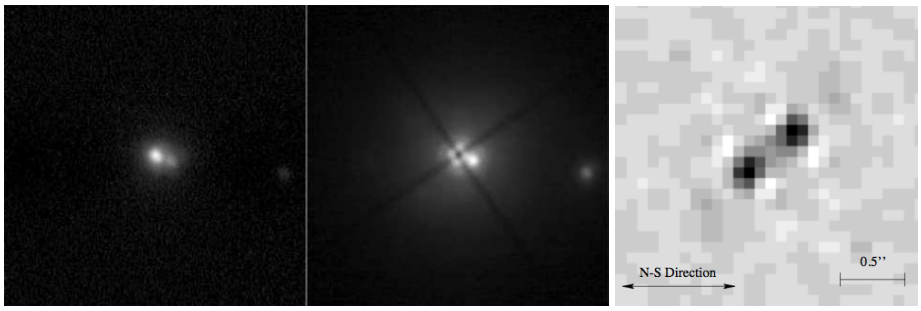

Figure 2.9: *Left*: HIP 1306 PSF and coronagraphic image (FQPM). Images from Boccaletti et al. 2004 [27]. *Right*: Image from Baudoz et al. 2000 [17] obtained with an AIC at OHP.

2.7.2 Low-mass companion

In Boccaletti et al. 2008 [23], it is demonstrated that coronagraphic observations of AB Doradus C can be more efficient than direct imaging, by improving contrast but more importantly by providing a better photometric estimation. These observations were carried out as part of a commissioning run of a new version of a coronagraph (FQPM) at the ESO/VLT using the AO-assisted near-IR camera NAOS-CONICA.

2.7.3 Circumstellar disks

Several circumstellar disks around relatively young stars have been discovered, most of them owing to the capabilities of a Lyot coronagraph (Smith et al. 1984, Jayawardhana et al. 1998, Augereau et al. 1999 [87, 52, 12]). In Fig. 2.10, a thick dust disk and a candidate star companion have been discovered around PSD 70 (Riaud et al. 2006 [80]).

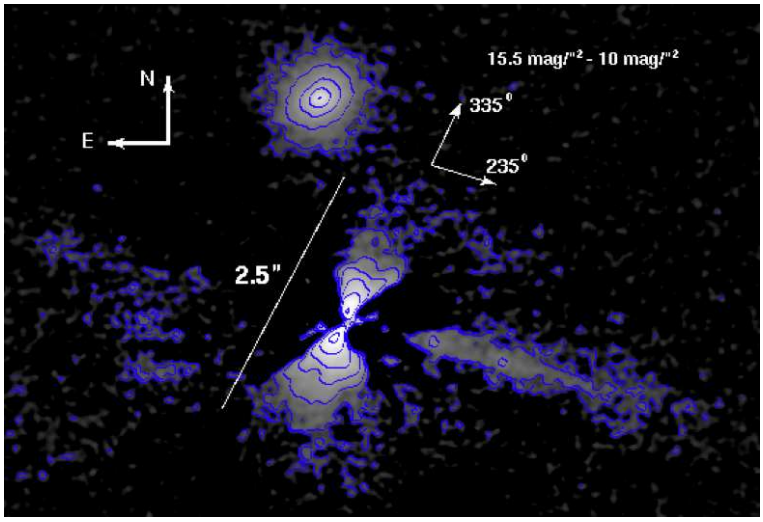

Figure 2.10: Final image of PDS 70 after data processing obtained with the VLT NACO adaptive optics combined with a FQPM which improve the dynamic range while preserving the high angular resolution. Image from Riaud et al. 2006 [80]

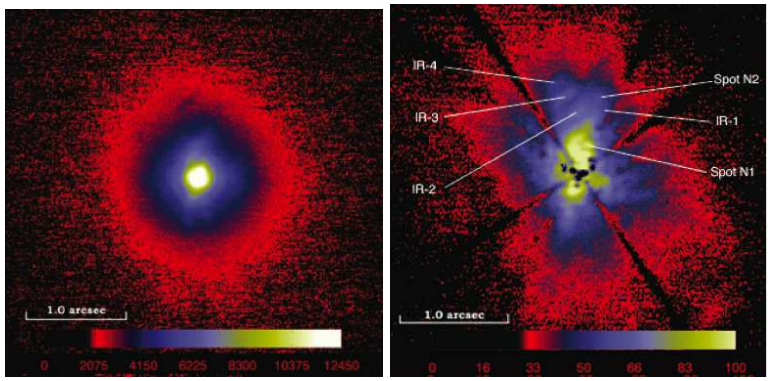

Figure 2.11: *Left*: NGC 1068, *Ks* band with NACO, without FQPM. *Right*: reference subtracted coronagraphic image of NGC 1068 in log-scale representation. Images from Gratadour et al. 2005 [44]

2.7.4 Extragalactic sources

In Fig. 2.11 Gratadour et al. 2005 [44] demonstrates the interest of coupling coronagraphy (FQPM, for instance) with AO system to study the close environment of the core of nearby active galactic nuclei (AGNs). This new approach allows to look for new structures that would otherwise be hidden by the PSF core. The FQPM avoids saturation and allows deeper integration and then a better signal-to-noise ratio.

2.8 Concepts analyzed in this thesis

As presented hereavove, the last ten years have been highly productive in producing new coronagraph designs. The coronagraphic Tree of Life is now quite important. Although it is difficult to consider all the existing coronagrahs, in this present thesis, we will further analyzed some of these concepts. In particular, we will consider, coronagraph concepts proposed to be implemented for planet finder project on actual telescope (SPHERE (Beuzit et al. 2006 [18]) and GPI (Macintosh et al. 2006 [61])) or potentially considered for next generation of planet finder project

with ELTs as EPICS (Kasper et al. 2007 [56]):

- Four Quadrant Phase Mask [FQPM]
- Annular Groove Phase Mask [AGPM]
- Apodized Roddier & Roddier Coronagraph (i.e Dual zone) [APRC]
- Lyot coronagraph [Lyot]
- Apodized Pupil Lyot Coronagraph [APLC]
- Band-limited [BL]
- Achromatic Interferometric Coronagraph [AIC]
- Binary pupil mask (shaped pupil coronagraph) [BM]

Indeed, this selection is quite representative of the main coronagraph families (phase, amplitude, interferometric and pupil apodization-type coronagraphs) presented above.

3

The need of a cross-optimization

Contents

Abstract - *We previously introduced coronagraph concepts. It is now convenient to have a look on constraints that coronagraphs will have to deal with. Ideally, telescope designs should be defined in strong relation with coronagraph weakness. A cross-optimization is critical to enhance the dynamic range, as began for the Terrestrial Planet Finder Coronagraph project (TPF-C, Traub et al. 2006 [92]) for space-based observations. However, it is not really the case for ground-based observations. Characteristics of these new generation of telescopes (ELTs) such as central obscuration ratio, primary mirror segmentation, and secondary mirror supports can have an impact on their high contrast imaging capabilities and impose strong limitations for many coronagraphs. In this part, we will introduce and discuss most of these telescope constraints. Their impact on coronagraph capabilities will be analyze in Part III and IV as the possibility of optimizing coronagraph with such constraints in Part II and V.*

3.1 Error sources in a coronagraphic telescope

Ground-based telescope and specifically ELTs, will have important constraints for high contrast imaging concepts. Coronagraphs will have to deal with the impact of 2 major categories of diffraction effects:

- The first category deals with amplitude variations : central obscuration, spiders, primary mirror segmentation, segment to segment reflectivity variation, pupil shear (misalignment of the coronagraph stop with respect to the instrument pupil).
- The second category is related to phase aberrations (segments aberrations, for instance).

Hereafter, we will list them and discuss the amplitude to consider through this present study.

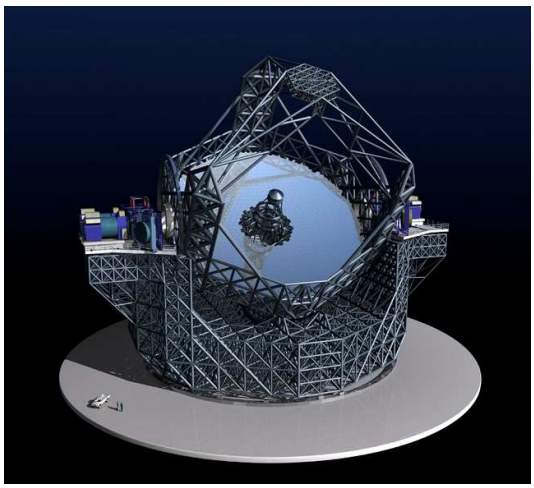

Figure 3.1: Baseline design (artist view) for the European-ELT as defined in March 2008

3.1.1 Segmented pupil: amplitude errors

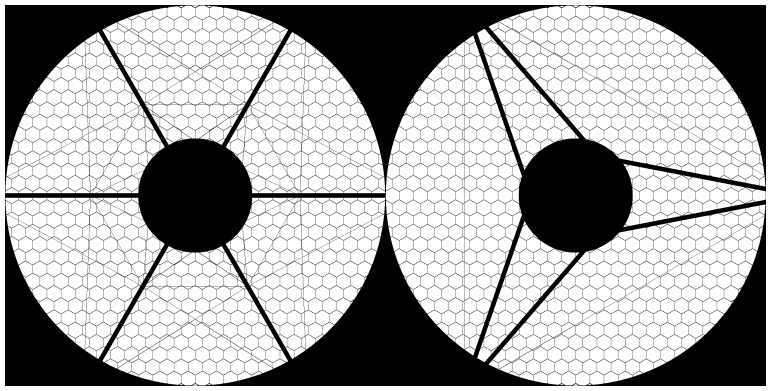

Figure 3.2: *Left*: OWL-like pupil, *Right*: E-ELT pupil proposed design 1. In both images some telescope parameters are illustrated: central obscuration (30%), spider vanes (6 of 60 cm width), cables and gaps (in grey levels).

Table 3.1: E-ELT main parameters (baseline design)

Parameter	Value
Telescope diameter	42 m
Central obscuration	30%
Segments shape	hexagons
Segments diameter	1.5 m
Number of segments	1148
Gaps	4 mm
Spider vanes number	6 - 8
Spider vanes thickness	60 cm

Central obscuration

Future ELTs will certainly have a large central obscuration to preserve reasonable telescope size (CFHT: 35%, VLT: 14%, E-ELT: 30%, TMT:15%). Specifically, the future European-ELT will have a non-negligeable one (30%). It is therefore important to study the suitability of coronagraph to this parameter. Moreover, some coronagraphs are well know to have a strong dependency to the central obscuration (phase mask, for instance). FQPM and AGPM are quite sensitive to this parameter since a significant part of the light diffracted by the central obscuration reappears in the relayed pupil. Nevertheless, given that, an optimization of the Pupil stop can mitigate this effect. Either the pupil stop is adapted to the entrance pupil with inner and outer diameter respectively oversized and undersized, or with the complementary shape of the diffracted light in the pupil plane as discussed in Boccaletti 2004 [21]. Therefore, we will investigate the efficiency of coronagraphs with a large range of central obscuration ratio, starting from 5% to 30%, and when it will not be specified, the default value of the central obscuration ratio through this thesis will be 30% (linear, E-ELT as a baseline).

Secondary support

We will analyze the impact of the spider vanes thickness considering most of the time a given secondary structure geometry. For this task, we will either consider six cable symmetric spiders (Fig. 3.1.1, left), or more recent proposed configuration for the E-ELT and check the impact of the spider arm width from 30 to 90 cm. The actual value for the E-ELT is 60 cm. In practice, for each case and for each coronagraph, pupil stop will be re-optimized to the entrance aperture including spider arms. Other mechanical structures can have an impact on coronagraphs (cables, for instance), but we assume that the effect of the spider vanes will be the major one. Hence, in simulation we will only consider spider vanes structures. Specifically, in Part II we will discuss how thickness of these mechanical structures and geometrical repartition (structure geometry) matter the optimization of a coronagraph and the selection of optimal parameters (APLC and BLs, for instance).

Segment reflectivity variations

Considering the size of the primary mirror, ELTs pupil will be segmented. An amplitude consecutive effect is the segment reflectivity variation due whether to the limitation of the optical coating on segments or by the mechanical segments positioning. The variation of reflectivity through an optical element induces wavefront amplitude variations that lead to potentially bright static speckles in the focal plane of the instrument (effect on the wings of the telescope Airy function pattern). Although these amplitude errors create speckles that have magnitudes that do not scale with wavelength, it is important to know how robust a coronagraph is to these defects. When analyzed in simulation, we will assume $\sim$ 750 hexagonal segments of 1.5 meters diameter (Fig. 3.3) and check the impact of a uniform distribution of segment variation reflectivity until 5% (peak-to-valley, hereafter ptv). Experience with the Keck telescope as discussed in Troy et al. 2003 [93] shows that segment-to-segment reflectivity variation of 5% (ptv) is in the order of what can be expected on a segmented telescope.

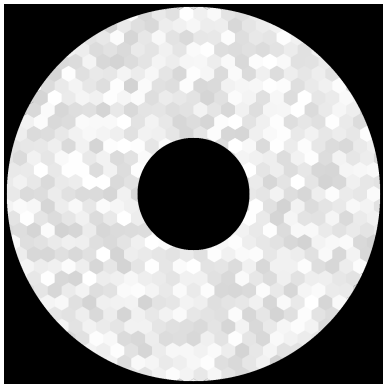

Figure 3.3: Pupil with reflectivity variations (levels are exagerated for sake of clarity).

Pupil shear

Most of coronagraphs include several optical components: apodizer, focal plane mask and pupil stop. As a result their performance also depends on the alignment of these components. In particular, the pupil stop has to accurately match the telescope pupil image. This condition is not always satisfied, and the telescope pupil may undergo significant mismatch which could amount to more than 1% of its diameter. The pupil shear is the mis-alignment of the pupil stop with respect to the telescope pupil image. It is an issue especially for ELTs for which mechanical constraints are important for the design. For example, the James Webb Space Telescope is expected to deliver a pupil image for which the position is known at about 3-4%. Therefore, the performance of the mid-IR coronagraph (Boccaletti et al. 2004 [26]) will be strongly affected. On SPHERE, the planet-finder instrument for the VLT (2010), the pupil shear was identified as a major issue and a dedicated Tip-Tilt mirror was included in the design to preserve the alignment stability at a level of 0.2% (Beuzit et al. 2006 [20]). Consider a range of misalignment between 0.1 and 0.5% of the pupil diameter seems therefore reasonable for the E-ELT and hence assumed through our simulations.

3.1.2 Segmented pupil: phase errors

Segment static aberrations

By static aberrations on segments of the primary mirror, we refer independently to low-order static aberrations (piston, tip-tilt, defocus and astigmatism, Fig. 3.4) that produce speckles that fall relatively near the image of the star in the final image plane and hence could potentially directly impact the IWA. Other order aberrations (higher orders) are less important. Although they have an impact on coronagraphic performance, it is generally with much lower amplitude.

For any ground-based telescope, the AO system will partially corrects both static and dynamic wavefront errors, and hence can correct for the Fourier components of the static wavefront errors that affect the field-of-view of interest delimited by the controlled spatial domain of the XAO. When using a XAO system (Chapter 8), we will further discuss that point.

Predict the level of low-order aberrations that ELTs will have to deal is quite difficult, nevertheless experience with Keck telescope (Chanan et al. 2000 [31]) shows that 10 nm rms is reachable. In practice, we will study each static aberration independently from each other using a large range of values (up to 30 nm rms most of the time).

3.1.3 Pointing errors and finite size of the star

The offset pointing error refers to the misalignment of the optical axis of the coronagraph to that of the star of interest. For instance, the goal with SPHERE (the planet instrument for the VLT) is to reach a pointing error of 0.5 mas rms, hence a direct translation of this requirements to a 42 meter telescope, would be a pointing error residual less than 0.1 mas rms. In practice, we will evaluate pointing error in between 0.1 and 0.5 mas rms.

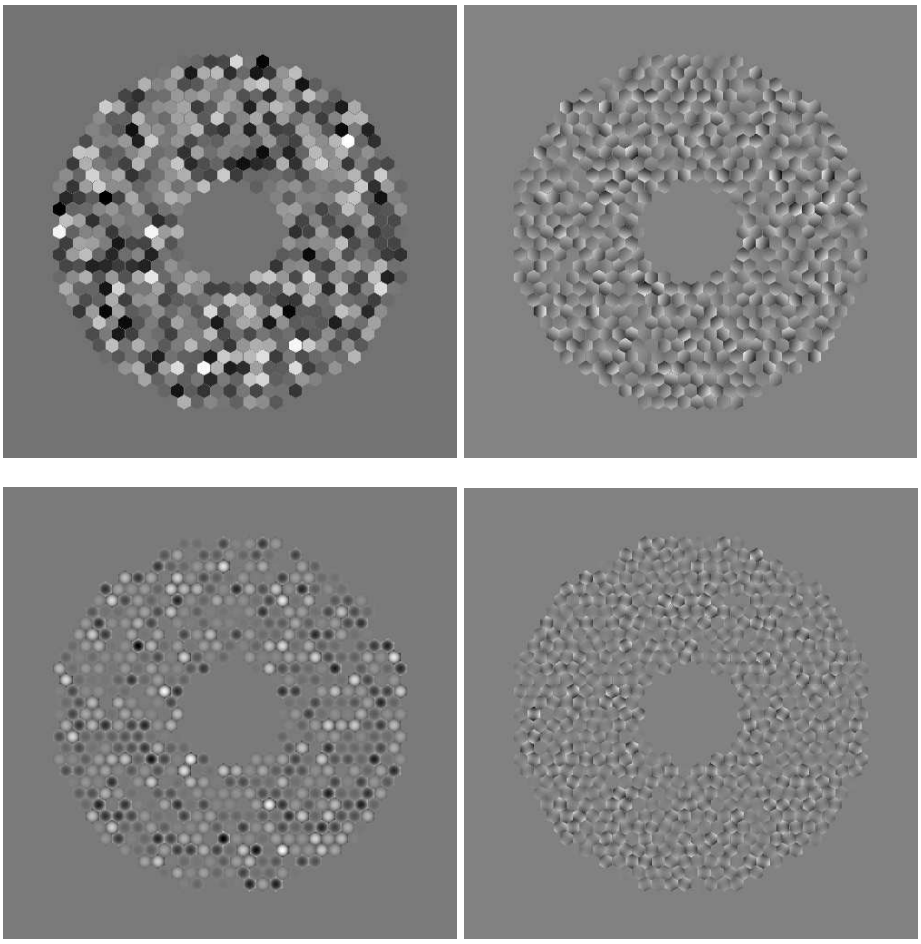

Figure 3.4: Example of segment phase errors: *top left*: piston, *top right*: tip-tilt, *bottom left*: defocus and *bottom right*: astigmatism.

The resolved stellar disk differs from a point source that it presents a sum of incoherent off-axis point sources (incoherent tilted wavefront to the telescope). Depending on the coronagraph, the sensitivity to these simultaneous wavefront will be different. As for the offset pointing error, coronagraph that allow a very small IWA will be more affected. The sensitivity to the finite stellar size is therefore a critical characteristic of coronagraph since the resulting error is not controllable by any given wavefront control system due to the incoherence of the arriving wavefront.

3.2 Resume

As a resume, through our study, we will further analyze the impact of the following parameters on coronagraphs:

- Central obscuration
- Spider vanes
- Segments reflectivity variations
- Segments phase aberrations
- Pupil shear

- Offset pointing
- Stellar diameter
- Chromatism

Impact of these parameters will be studied through three configurations: diffraction limited regime (Part III), Adaptive Optics (AO) residual limited regime (Chapter 8) and Differential Imaging (DI) quasi-static aberrations limited regime (Chapter 9). We will investigate for some coronagraphs, the possibility of optimizing their parameters regarding to these telescope limitations as well (Part. II) and impacts on the suitability of cascade concepts (Part. V).

4

Coronagraphic tools

Contents

Abstract - *At this point, it is convenient to define and discuss the metrics used to characterize the ability of a coronagraph to suppress the on-axis starlight. Moreover, with the number of publications related to coronagraphy, several parameters have been defined and are commonly used. Nevertheless, definitions are sometimes different. Hence, the purpose of this chapter is to present and define metrics we will consider through this present thesis in order to avoid any confusion.*

4.1 Common metrics

Several metrics can be used to quantify the capability of a coronagraph (Boccaletti 2004, Abe 2004 [21, 1], for instance). In this part, the common ones will be defined. In some specific parts of the thesis, we will define new ones, more appropriated to specific cases, and most of the time resulting from a modification or combination of the following metrics and common considerations presented in Sect. 4.2.

For sake of clarity, we denote by $\psi_{PSF}(\rho, \alpha)$ (where ρ and α are the polar coordinates) the intensity on the detector without the coronagraph ($\psi_{PSF}(0)$ hence will be the peak stellar intensity on the detector without the coronagraph) and $\psi_{CORO}(\rho, \alpha)$ is related to the intensity of the final image on the detector with the coronagraph.

4.1.1 Rejection rate

Total rejection rate

The total rejection rate (τ) corresponds to the ratio between the total intensity of an off-axis object to that of an on-axis object (blocked by the coronagraph):

$$\tau = \frac{\int_0^\infty \int_0^{2\pi} \psi_{PSF}(\rho, \alpha) \rho \, d\rho \, d\alpha}{\int_0^\infty \int_0^{2\pi} \psi_{CORO}(\rho, \alpha) \rho \, d\rho \, d\alpha} \quad > 1 \tag{4.1}$$

Peak rejection rate

The peak rejection rate (τ_0) is the ratio between the peak intensity of an off-axis object to that of an on-axis object (blocked by the coronagraph):

$$\tau_0 = \frac{\psi_{PSF}(0)}{max\left(\psi_{CORO}(\rho, \alpha)\right)} \tag{4.2}$$

4.1.2 Contrast evaluation

In the following, we describe several level of contrast evaluation metrics:

1/ The local contrast ($\mathscr{C}(\rho, \alpha)$) defined as:

$$\mathscr{C}(\rho, \alpha) = \frac{\psi_{CORO}(\rho, \alpha)}{\psi_{PSF}(0)} \tag{4.3}$$

2/ The contrast profile averaged azimuthally ($\mathscr{C}(\rho)$):

$$\mathscr{C}(\rho) = \frac{\int_0^{2\pi} \psi_{CORO}(\rho, \alpha) \, d\alpha}{2\pi \, \psi_{PSF}(0)} \tag{4.4}$$

3/ The averaged contrast in a annulus region ($\overline{\mathscr{C}}$) of the focal plane. it gives the contrast between the peak stellar intensity and an average intensity level in a region of the focal plane where an off-axis companion can be detected. The area of calculation in the focal plane can be well matched to the instrumental parameters (the width of the ring can be modified to match science requirements by changing the value of ρ_i and ρ_f, the short radii and the large radii defining the area of calculation for $\mathscr{C}$):

$$\overline{\mathscr{C}} = \frac{\left(\int_{\rho_i}^{\rho_f} \int_0^{2\pi} \psi_{CORO}(\rho, \alpha) \rho \, d\rho \, d\alpha\right) / \pi({\rho_f}^2 - {\rho_i}^2)}{\psi_{PSF}(0)} \tag{4.5}$$

It is convenient to moderate any contrast metrics by the overall coronagraphic throughput (herafter, $\mathscr{T}$, see Sect. 4.2.5). The overall throughput is mainly imposed by the optimization of the pupil stop and can be considered in a metric to avoid any over-estimation of the contrast and as a fair comparison between coronagraphs.

4.1.3 Detectability

When using a Differential imaging system (hereafter, DI system) a radial 5σ contrast metrics is appropriated (denoted $\mathscr{D}$) to compare coronagraphs:

$$\mathscr{D} = \frac{5 \times \sigma\left[\psi_{CORO_1}(\rho) - \psi_{CORO_2}(\rho)\right]}{\psi_{PSF}(0)} \tag{4.6}$$

Here, $\sigma[]$ is an operator which denote the azimuthal standard deviation measured in a ring of width λ/D on the subtracted image $\psi_{CORO_1} - \psi_{CORO_2}$. This final 5σ detectability is related to the ability of a coronagraph to peak out an off-axis companion at a given angular distance in a halo of residual speckles in the final image (the final image is obtained by subtracting intensity in the two channels of the DI system (ψ_{CORO_1} and ψ_{CORO_2})). The σ of the speckled halo is evaluated at a radius ρ with an azimuthal average of $\sim \lambda/D$ width scale normalized to the PSF peak intensity.

Although we use $\mathscr{D}$ through this study when using Differential imaging, more appropriate criteria adapted to the case of high contrast images have been developed recently by Marois et al. 2008 [63]. In the latter paper, Marois et al. discussed confidence level of such metrics for high contrast images.

4.2 Common considerations

This list of consideration is not exhaustive, but treats about some important factor we will further use in the next Chapters.

4.2.1 Inner Working Angle

The IWA is one way to describe quantitatively how close a coronagraph design allows the detection of a faint companion reaching a significant transmission. The IWA is commonly defined as the angular separation where a planet throughput reaches half of the peak throughput. Then in this present thesis, we define the IWA as the angular separation for which the diffraction peak of a planet is reduced by a factor of 2.

4.2.2 Outer Working Angle

The OWA define how far a planet can still be conveniently detectable. For most coronagraphs, the OWA is limited by optical design constraints. Only in few cases (shaped pupil, for instance), the coronagraph concepts itself imposes an OWA. In that case, the design of the coronagraph is optimized with respect to OWA (and IWA as well) generally sets by the control domain of the AO system.

4.2.3 Discovery space

The discovery is the focal plane region in which diffracted and scattered light are well suppressed by the coronagraph. This area may be restricted between the IWA and OWA as usable for planet detection.

4.2.4 Radial transmission

The radial transmission gives both information on the IWA and sensitivity of the concept to pointing error and stellar angular size. This behavior is important to analyze since coronagraphs do not radially attenuate in the same way an off-axis sources. For instance, Band-limited coronagraph have an off-axis attenuation depending on their mask functions. Hence, the choice of the function is quite important.

4.2.5 Throughput

The overall system transmission (denoted $\mathscr{T}$) refers to the transmission of the whole coronagraphic system (mainly imposed by the Pupil Stop throughput for most coronagraphs, times the mask transmission in the precise case of BLs).

4.2.6 Manufacturing issues

The choice of which coronagraph to implement in practice on a ELT will of course be driven by manufacturing considerations. Many programs aims to tackle critical point as chromaticity for instance, and can make us optimistic for the next years. We will further discussed about some manufacturing issue on coronagraphs we developed at ESO and tested on HOT in Chapter 12.

Part II

Optimizing coronagraph designs

Abstract - *In its general scheme, a coronagraph can be divided in two systems: a low-frequencies filter (amplitude or phase mask) and a high-frequencies filter (the so-called pupil stop). Therefore, the way that coronagraphs are optimized can be divided in two different approaches (most coronagraphs indeed need both optimizations). The first one aims at optimizing parameters of the low-frequencies filter considering the application (IWA constraint, spectral bandwidth or so) while the second one strives to optimize the coronagraph with the pupil stop (high frequencies filter) in the relayed geometrical pupil (to correctly remove contamination by the diffracted light).*

The total amount of the rejected light by a coronagraph strongly depends on the pupil stop size and shape. Most of the time, pupil stops are optimized to match the diffraction in the relayed pupil as defined in Boccaletti 2004 [21] and hence are well adapted to the way that each coronagraph deal with the diffracted light. This optimization is in practice balanced with angular resolution and off-axis throughput issues. Reducing the collecting area of the pupil stop help at producing deeper extinction (i.e attenuation) while conversely the angular resolution and throughput (transmitted flux) are degraded. However, when coupled to AO system, an optimization of the pupil stop must be tackled with respect to the level of the residual phase which could relax constraints on the pupil stop shape and throughput (as discussed for instance in Crepp et al. 2007 [34] for the Band-Limited case). This optimization depends on the dominant source of noise (diffracted light or uncorrected atmospheric scattered light). Hence, the optimization of the pupil stop is a critical work and depends on the application.

In that sense, phase mask such as FQPM, AGPM or DPM, and amplitude mask as the Lyot coronagraph are basically coronagraph that need to be optimized with the pupil stop. Although they have some internal parameters that required to be tuned according to the application: operating wavelength for phase masks, IWA for amplitude coronagraphs..., the main issue is the pupil stop optimization.

However, some of them (APLC and BLs, for instance) have additional and important opened parameters that are not trivial to define: apodizer/mask couple for APLC, bandwidth and order of the function for BLs. In the precise case of APLC, at first order the pupil stop optimization does not matter since in ideal conditions the pupil stop remains identical to the entrance pupil. In such a case, selection of the apodizer/mask couple prevails. The objective of the following part is precisely to focus on the optimization of these two particular concepts for which a dedicated Chapter (5 and 6) will be devoted.

Through these Chapters, we will study the possibility of optimizing these opened parameters with respect to ELT specificities and show that while some configurations appear optimal, some others are not suitable with such telescope geometries.

Finally, we will further have a look at the proposed configuration of APLC and BLs for EPICS, the planet finder project for the E-ELT.

5

Optimization of the Apodized Pupil Lyot Coronagraph

Contents

Abstract - *The Apodized Pupil Lyot Coronagraph (APLC) is potentially one of the more promising concepts for ELTs. Combining an apodizer in the pupil plane with a Lyot mask (FPM, hereafter) in the focal plane, its sensitivity to central obscuration is less critical than, e.g., for phase masks (Riaud et al. 2000, Mawet et al. 2005 [83, 68]) while still allowing small inner working angle (IWA) and high throughput if properly optimized. The potential of the APLC has been demonstrated for arbitrary apertures (Aime et al. 2002, Soummer et al. 2003 [9, 89]) and specific solutions for obscured apertures were proposed (Soummer 2005 [88]). However, the characteristics of ELTs may have an impact on its high contrast imaging capabilities. Parameters such as central obscuration, primary mirror segmentation, and large spider arms, usually impose strong limitations for many coronagraphs. It is therefore essential to indentify and evaluate the behavior of the APLC to these parameters. Specifically, in this Chapter, we investigate the possibility of optimizing the APLC with respect to parameters mentioned above. Optimization of the APLC refers to the selection of the apodizer/FPM combination. We will briefly revise the APLC formalism and define criteria for optimizing the coronagraph parameter space. Optimal configurations have been identified, and we will present how some telescope parameters may drive the choice of optimal apodizer/FPM couples.*

5.1 Apodization for centrally obscured pupils

5.1.1 Presentation

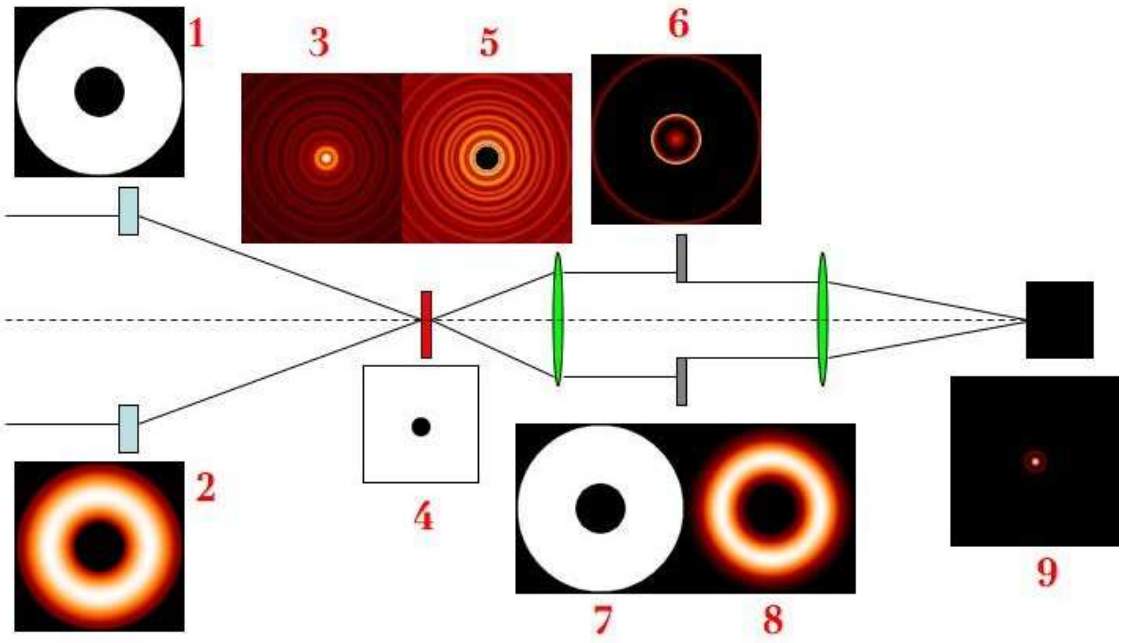

Figure 5.1: APLC coronagraphic process: Transmission of the entrance pupil (1) is modified by an apodizer (2). In the focal plane, the complex amplitude of the star (3) is spatially filtered (5, low-frequencies) by the Lyot mask (4). In the relayed pupil (6) a pupil stop (7) is filtering high frequencies and as a result the relayed pupil is attenuated (8) and proportional to the apodized entrance aperture. Finaly, the coronagraphic PSF is imaged on the detector (9).

The APLC is a direct improvement of the Lyot coronagraph, preventing for strong light presence in the relayed pupil resulting from the convolution of the telescope pupil with the Fourier transform of the hard-edge focal mask. To reduce starlight contamination in the relayed aperture, two philosophies are possible. Either adapt the Fourier transform of the Lyot mask to be with finite support as the telescope aperture (Band-limited approach, or at least use a quite large Lyot mask combine with smaller pupil stop but not favorable for faint planet detection close to their parent stars) or adapt the Fourier transform of the telescope pupil to be with finite support as the Lyot mask. The later is achieved through the use of an apodization of the pupil to attenuate the wings of the PSF. Apodization functions (Prolate spheroidal, for instance) have the particularity to have their Fourier transform truncated functions-like.

5.1.2 Formalism

In this section, we briefly revise the formalism of the APLC using the notation defined by Aime et al 2002 [9]. The APLC is a combination of a classical Lyot coronagraph (hard-edged occulting focal plane mask, FPM) with an apodization in the entrance aperture. In the following, for the sake of clarity, we omit the spatial coordinates r and ρ (for the pupil plane and focal plane respectively). The function that describes the mask is noted M (equal to 1 inside the coronagraphic mask and to 0 outside). With the mask absorption ε ($\varepsilon = 1$ for an opaque mask), the FPM is then equal to:

$$1 - \varepsilon M \tag{5.1}$$

P is the telescope aperture, and ϕ the profile of the apodizer. Π describes the pupil stop function, which is considered – in the initial approximation – to be equal to the telescope aperture ($\Pi = P$).

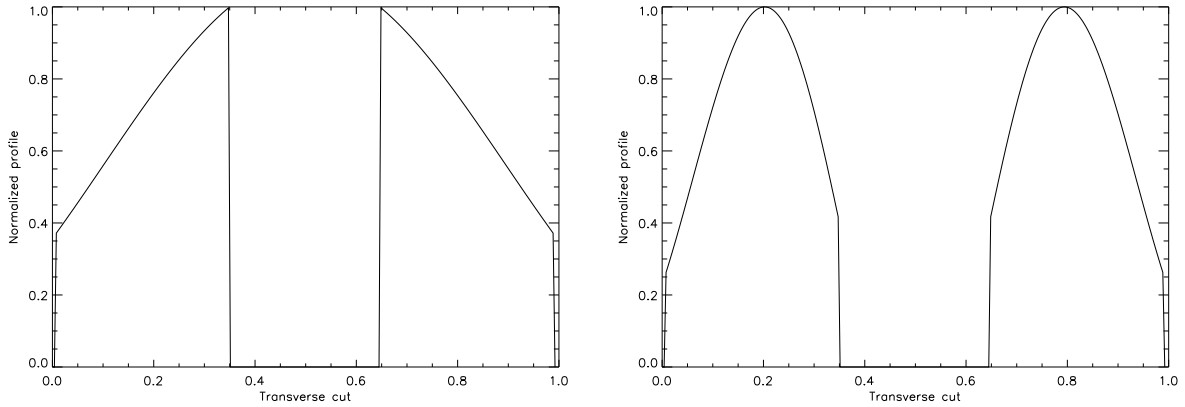

Figure 5.2: Typical apodizer shape for the bell regime (left) and the bagel regime (right). Central obscuration is 30%.

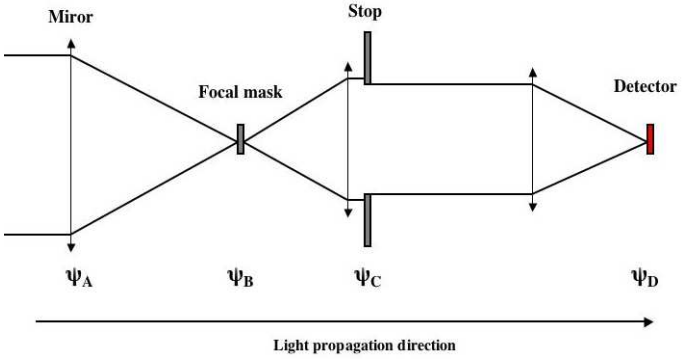

Figure 5.3: Sheme of a coronagraph showing the pupil plane containing the apodizer (ψ_A), the focal plane with the FPM (ψ_B), the pupil image spatially filtered by the stop (ψ_C) and the detector plane (ψ_D).

In practice the pupil stop of an APLC will be slightly reduced for alignment and chromatism issues, but theoretically this concept does not suffer from a restriction of the throughput compared to other concepts (amplitude and phase types as well). Hence, our approximation is justified.

The coronagraphic process, corresponding to propagation from the telescope entrance aperture to the detector plane, is expressed in Eq. 5.2 to 5.6. Planes A, B, C and D correspond to the telescope aperture, the coronagraphic focal plane, the pupil stop plane and the detector plane respectively as defined in Fig. 5.3. The Fourier transform of a function f is noted $\hat{f}$. The symbol $\otimes$ denotes the convolution product. The entrance pupil is apodized in the pupil plane:

$$\psi_A = P\phi \tag{5.2}$$

The complex amplitude of the star is spatially filtered (low frequencies) by the FPM:

$$\psi_B = \hat{\psi}_A \times [1 - \varepsilon M] \tag{5.3}$$

The exit pupil image is spatially filtered (high frequencies) by the stop:

$$\psi_C = \hat{\psi}_B \times \Pi \tag{5.4}$$

$$\psi_C = [\psi_A - \varepsilon\psi_A \otimes \hat{M}] \times \Pi \tag{5.5}$$

The coronagraphic amplitude on the detector plane becomes:

$$\psi_D = \hat{\psi}_C = [\hat{\psi}_A - \varepsilon\hat{\psi}_A M] \otimes \hat{\Pi} \tag{5.6}$$

The coronagraphic process can be understood as a destructive interference between two waves (Eq. 6.5): the entrance pupil wave $P\phi$, noted ψ_A and the diffracted wave by the mask (corresponding to $\varepsilon\psi_A \otimes \hat{M}$). In the non-apodized case ($\phi = 1$), the two wavefronts do not match each other, and the subtraction does not lead to an optimal starlight cancellation in the Lyot stop pupil plane. A perfect solution is obtained if the two wavefronts are identical (i.e., the diffracted wave by the mask (M) is equal to the pupil wave in amplitude). This latter case is obtained with the Apodized Pupil Phase Mask Coronagraph (Roddier & Roddier 1997, Aime et al. 2002, Soummer et al. 2003 [82, 9, 89]). For the APLC, the coronagraphic amplitude is minimized and proportional to the apodizer function but never cancelled.

Considering a pupil geometry, the apodization function is related to the size of the FPM. More precisely, the shape of the apodizer depends on the ratio between the extent of $\hat{M}$ and the central obscuration size (Soummer et al. 2005, Soummer et al. 2007 [88, 91]). If the extent of $\hat{M}$ is bigger than the central obscuration, the apodizer takes a "bell" shape (typically it maximizes the transmission near the central obscuration of the pupil (Fig.5.2, left). On the contrary, if the extent of $\hat{M}$ is smaller than the central obscuration, the apodizer takes a "bagel" shape reducing transmission in the inner and outer part of the pupil (Fig.5.2, right). Thus, the apodizer shape depends on both the FPM size and the central obscuration size.

Throughput (apodizer transmission/pupil transmission) as a function of the FPM size is given in Fig. 5.4 for different obscuration sizes (15 to 35%). These curves show a second maximum corresponding to the transition between the two apodizer regimes which depends on the central obscuration size. Since apodizer throughput does not evolve linearly with FPM diameter, it is not trivial to determine the optimal FPM/apodizer combination. Moreover, throughput might not be the only relevant parameter when optimizing a coronagraph.

A thorough signal-to-noise ratio analysis is definitely the right way to define the optimal FPM/apodizer system, but this would be too instrument-specific for the scope of this study. Here, we investigate a general case for any telescope geometry and derive the corresponding optimal FPM size.

5.1.3 APLC optimization criteria

Usually, in Lyot coronagraphy, the larger the FPM diameter the larger the contrast. However, in the particular case of the apodized Lyot coronagraph the transmission of an off-axis point-like object is not linear (Fig. 5.4) and a trade-off has to be made between contrast and throughput. This problem has been studied by Boccaletti 2004 [21] who evaluated optimal Lyot stops for any telescope pupil geometry and for any type of coronagraph. Based on this study, we propose a criterion adapted to the APLC to optimize the apodizer/ FPM combination. This criterion maximizes the coronagraphic performance while minimizing the loss of flux of the off-axis object. While not replacing a thorough signal-to-noise ratio evaluation, our criterion takes into account the modification of the off-axis PSF (in intensity and in shape) when changing the coronagraph parameters.

Several metrics can be used to quantify the capability of a coronagraph (e.g Boccaletti 2004 [21]). Here, we use 2 metrics:

1/ the total rejection (τ) corresponding to the ratio between the total intensity of an off-axis object ($\epsilon = 0$ in Eq. 5.6) to that of an on-axis object (blocked by the Lyot mask),

$$\tau = \frac{\int_0^{\infty}\int_0^{2\pi} \mid \psi_D(\rho,\alpha,\varepsilon=0) \mid^2 \rho\, d\rho\, d\alpha}{\int_0^{\infty}\int_0^{2\pi} \mid \psi_D(\rho,\alpha) \mid^2 \rho\, d\rho\, d\alpha} \tag{5.7}$$

2/ the contrast ($\mathscr{C}$) averaged over a range of angular radii.

$$\mathscr{C} = \frac{max\left(\mid \psi_D(\rho,\alpha)_{\varepsilon=0} \mid^2\right)}{\left(\int_0^{2\pi}\int_{\rho_i}^{\rho_f} \mid \psi_D(\rho,\alpha) \mid^2 \rho\, d\rho\, d\alpha\right)/\pi({\rho_f}^2 - {\rho_i}^2)} \tag{5.8}$$

where τ and $\mathscr{C}$ are expressed in polar coordinates ρ and α. We denote by ρ_i and ρ_f the short radii and the large radii, respectively, defining the area of calculation for $\mathscr{C}$.

In both cases, the attenuation of the off-axis object is given by the ratio of maximum image intensity with the apodizer only to that without the coronagraph, i.e., without the apodizer and the FPM. This quantity differs from

the throughput, since it also takes into account the modification of the PSF structure when changing the apodizer profile :

$$max\left(\frac{|\ \psi_D(\rho,\alpha)_{\varepsilon=0}\ |^2}{|\ \hat{P}(\rho,\alpha)\ |^2}\right) \tag{5.9}$$

Now, let us define the criterion C_τ as the product of τ and Eq. 5.9.

$$C_\tau = \tau \times max\left(\frac{|\ \psi_D(\rho,\alpha)_{\varepsilon=0}\ |^2}{|\ \hat{P}(\rho,\alpha)\ |^2}\right) \tag{5.10}$$

and the criterion $C_{\mathscr{C}}$ as the product of $\mathscr{C}$ and Eq. 5.9.

$$C_{\mathscr{C}} = \mathscr{C} \times max\left(\frac{|\ \psi_D(\rho,\alpha)_{\varepsilon=0}\ |^2}{|\ \hat{P}(\rho,\alpha)\ |^2}\right) \tag{5.11}$$

The first term of $C_{\mathscr{C}}$ (Eq. 5.8, which characterizes the performances of the coronagraphic system) is then adapted to the region of interest in the coronagraphic image and can be well matched to the instrument parameters while the first term of C_τ (Eq. 5.7) is a more localized information, typically identical in the case of APLC to the peak attenuation ratio value since the effect of the APLC is an homogenous down shift of the PSF. The second term (Eq. 5.9) takes into account the modification of the PSF structure when changing the apodizer profile and guarantees a reasonably moderate attenuation of the off-axis PSF maximum intensity (i.e, guarantees that when the coronagraph rejects the star it does not reject the planet as well). Although our criterion cannot replace a thorough signal-to-noise ratio analysis (no instrumental model, no noise terms), it presents a reasonable approach by assuming the residual light leaking through the coronagraph as noise. Our criteria allow us to investigate the trade-off between performance and throughput while keeping the study general and independent of a specific instrument setup.

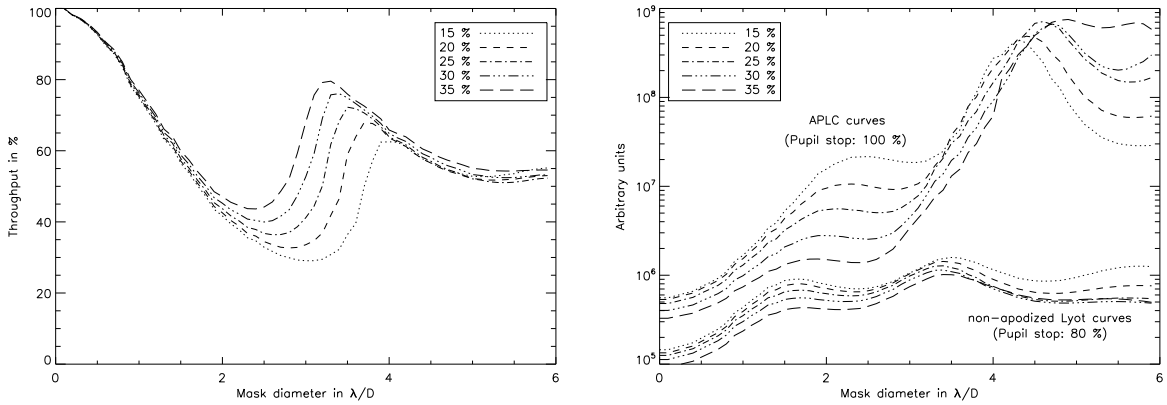

Figure 5.4: Left: Apodizer throughput (relative to full transmission of the telescope pupil) as a function of FPM diameter for different obscuration sizes. Right: $C_{\mathscr{C}}$ average between 3 and 100 λ/D as a function of the FPM diameter and obscuration sizes, in the case of the APLC and classical Lyot coronagraph.

Moreover, the validity of this criterion is supported by the pupil stop optimization study of Boccaletti 2004 [21] who faced a problem similar to ours, and also by the results presented and discussed in this study.

5.2 Sensitivity analysis

5.2.1 Assumptions

Based on the previously defined criterion, we now analyze the behavior of several telescope parameters as a function of the size of the FPM (and hence APLC characteristics) with the main objective of exploring possibilities

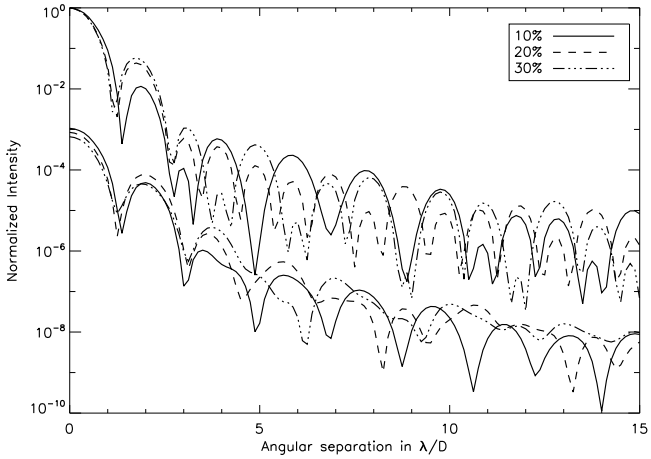

Figure 5.5: Radial profiles of PSFs and coronagraphic images obtained with optimal APLC (using $C_{\mathscr{C}}$) for several obscuration sizes.

Table 5.1: APLC mask diameter (and hence APLC characteristics) for several obscuration sizes.

	$C_{\mathscr{C}}$		C_τ		max. throughput	
Obstruction size	Mask (λ/D)	T(%)	Mask (λ/D)	T(%)	Mask (λ/D)	T(%)
10 %	4.3	59.4	4.6	55.9	4.1	62.2
15 %	4.3	58.3	4.7	53.6	4.0	62.4
20 %	4.4	55.8	4.8	51.9	3.8	65.5
25 %	4.6	52.7	4.9	50.1	3.6	67.9
30 %	4.7	51.2	5.0	48.9	3.5	68.7
35 %	4.9	49.4	5.1	48.5	3.3	70.4

of how to optimize the APLC configuration for a given ELT design. One advantage of $C_{\mathscr{C}}$ is that the area of optimization in the focal plane can be well matched to the instrumental parameters. For this reason, we will more focus on that criterion. We have limited the search area and investigated $C_{\mathscr{C}}$ only between $\rho_i = 3\lambda/D$ at small radii and $\rho_f = 100\lambda/D$ at large radii. These limits correspond to the IWA (distance at which an off-axis object reaches a significant transmission) and to the high-order Adaptive Optics (AO) cut-off frequency, respectively. At radii larger than the AO cut-off frequency, the coronagraph will only have a minor effect since atmospheric turbulence is not corrected and atmospheric speckles dominate.

For the simulations presented in the next sections, we assume a circular pupil with 30% central obscuration. The central obscuration ratio is left as a free parameter only in Sect. 5.2.2.0 where we evaluate its impact. The pupil stop is assumed identical to the entrance pupil including spider arms (Sivaramakrishnan & Lloyd 2005 [86]). Sect. 5.2.2.0, where the impact of the spider arms' size is analyzed, assumes a 42-m telescope. Elsewhere, simulation results do not depend on the telescope diameter. Apodizer profiles were calculated numerically with a Gerchberg-Saxton iterative algorithm [41]. The pixel sampling in the focal plane is 0.1 λ/D, and the pupil is sampled with 410 pixels in diameter. When phase aberrations are considered we adopt a wavelength of 1.6μm corresponding to the H-band in the near infrared.

5.2.2 Critical parameter impacts

In the following sub-sections, we study the impact of two major categories of diffraction effects. The first category deals with amplitude variations: central obscuration, spider arms, primary mirror segmentation, segment-to-

segment reflectivity variation, and pupil shear (misalignment of the coronagraph stop with respect to the instrument pupil). Inter-segment gaps and other mechanical secondary supports are not considered, since they would require finer pixel sampling in the pupil image, resulting in prohibitively large computation times with a non-parallel computer. In addition, some mechanical secondary supports can be much smaller than the main spider arms. At the first approximation, their effects can be considered to be similar to those produced by spider arms.

The second category is related to phase aberrations, which we assumed are located in the pupil plane (no instrumental scintillation). We only modeled low-order segment aberrations (piston, tip-tilt, defocus, astigmatism). Higher orders are less relevant for the optimization of the FPM size, but can have a significant impact on the coronagraphic performance.

The amplitude diffraction effect of gaps is partially accounted for (at least for infinitely small gaps) by the phase transition we are generating between primary mirror segments.

Central obscuration

The first parameter we evaluate is the central obscuration. High contrast instruments have to deal with central obscuration ratio which typically ranges from 10% to 35% (CFHT: 35%, HST: 33%, VLT: 14%). ELTs will likely have larger obscurations than current 8-m class telescopes to preserve a reasonable size for the telescope structure. In Fig. 5.5, the criterion $C_{\mathscr{C}}$ is shown for different obscuration sizes ranging from 10 to 35%. The curves show two maxima. The first is located near 2 λ/D and experiences a large contrast variation while the second (near 4λ/D) shows a smaller dispersion.

Table 1 summarizes these results and gives the position of the second maximum versus the obscuration size for the previously-mentioned criterion and for a criterion based solely on the maximum throughput (as in Fig. 5.4).

If we only consider the second maximum, which is more promising in terms of contrast and appears less sensitive, the optimal FPM diameter ranges from 4.3 to 4.9 λ/D for obscuration ratios between 10 to 35%. Here, our criterion $C_{\mathscr{C}}$ is more relevant than throughput, since it is better adapted to the region of interest in the coronagraphic image and to the modification of the PSF structure. We see a non-linear increase of optimum FPM size with the obscuration ratio because more starlight is redistributed in the Airy rings of the PSF. A solely throughput-based consideration shows the opposite behavior with a larger dispersion of the FPM size, which is not consistent with the effect on the PSF structure.

However, at small obscuration sizes (10%-15%), maximum throughput yields a similar optimal FPM diameter as $C_{\mathscr{C}}$. We consider this result to be evidence for the relevance of our criterion $C_{\mathscr{C}}$ to optimize the FPM size (and hence the APLC characteristics) with respect to the size of the central obscuration. Moreover, the validity of our criterion is also supported by the comparison of coronagraphic PSFs using an optimized APLC in Fig. 5.5. The optimized APLC allows for a contrast performance which is rather insensitive to the central obscuration size.

Spider arms

On an ELT, the secondary mirror has to be supported by a complex system of spider arms ($\sim$ 50 cm) and cables ($\sim$ 30-60 mm) to improve stiffness. Evaluating the influence of these supports is important in the context of coronagraphy.

The pixel sampling of our simulations limited by available computer power does not allow us to model the thinnest mechanical supports. However, the impact of these supports on the PSF structure will be similar to that of spider arms but at a reduced intensity level. Several configurations were considered as shown in Fig.5.8. As the number of spider arms increases from 3 to 7, the contrast gets worse (but no more than by a factor of 2). The curves in Fig. 5.6 (left) are almost parallel, indicating that the number of spider arms has no significant influence on the optimal FPM size. The second maximum of $C_{\mathscr{C}}$ peaks at 4.7 λ/D with a small dispersion of 0.2 λ/D.

Assuming a 6-spider arms configuration (OWL-like), we also analyzed the sensitivity to spider arm thickness from 15 cm to 93 cm (Fig. 5.6, right). The increasing width of the spider arms tends to flatten the profile of $C_{\mathscr{C}}$, making the selection of an optimal FPM more difficult (or less relevant) for very large spider arms. However, for the actual size of spider arms likely being of the order of 50 cm, the optimal size of the FPM (and hence APLC) is still 4.7 λ/D.

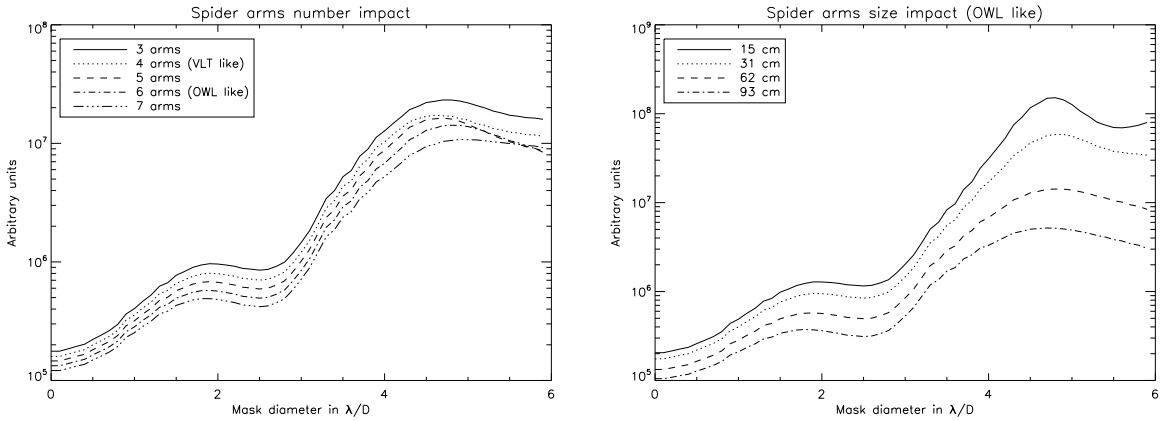

Figure 5.6: Left: $C_{\mathscr{C}}$ average between 3 and 100 λ/D as a function of the FPM diameter and number of spider arms. Spider thickness is set to 62 cm. Right: $C_{\mathscr{C}}$ average between 3 and 100 λ/D as a function of the FPM diameter and spider arm thickness. Number of spider arms is set to 6.

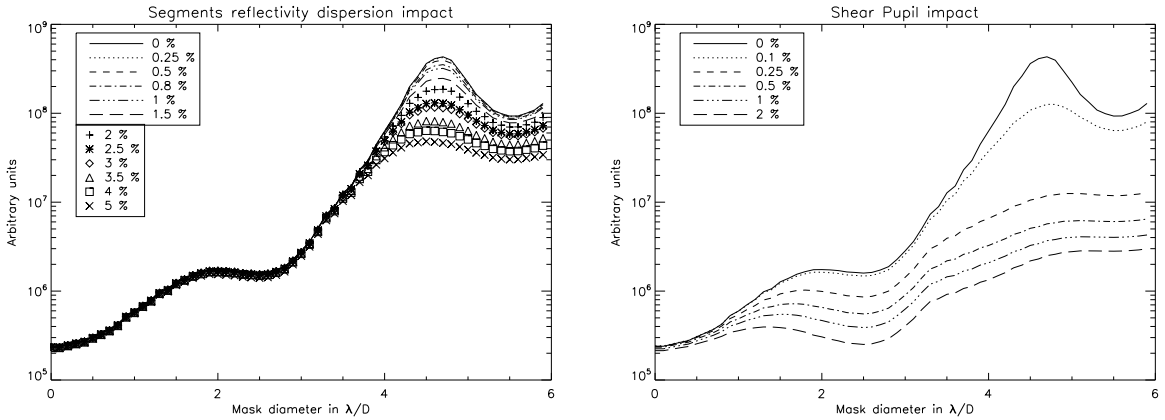

Figure 5.7: Left: $C_{\mathscr{C}}$ average between 3 and 100 λ/D as a function of the FPM diameter and reflectivity variations. Right: $C_{\mathscr{C}}$ average between 3 and 100 λ/D as a function of the FPM diameter and pupil shear.

Segments reflectivity variation

The primary mirror of an ELT will be segmented because of its size, and a potential resulting amplitude effect is segment-to-segment reflectivity variation. We show the APLC optimization sensitivity for segment reflectivity variation from 0 to 5% peak-to-valley in Fig. 5.7 (left). For this simulation, the primary mirror was assumed to consist of ~750 hexagonal segments. The criterion $C_{\mathscr{C}}$ is robust for FPMs smaller than 4 λ/D. A loss of performance with reflectivity variation is observed for larger FPM. However, the optimal FPM size remains located at 4.7 λ/D with a small dispersion of 0.2 λ/D.

Pupil shear

As mentioned above, an APLC includes several optical components: apodizer, FPM and pupil stop. The performance of the APLC also depends on the alignment of these components. In particular, the pupil stop has to accurately match the telescope pupil image. This condition is not always satisfied, and the telescope pupil may undergo significant mismatch which could amount to more than 1% of its diameter. The pupil shear is the misalignment of the pupil stop with respect to the telescope pupil image. It is an issue especially for ELTs for which

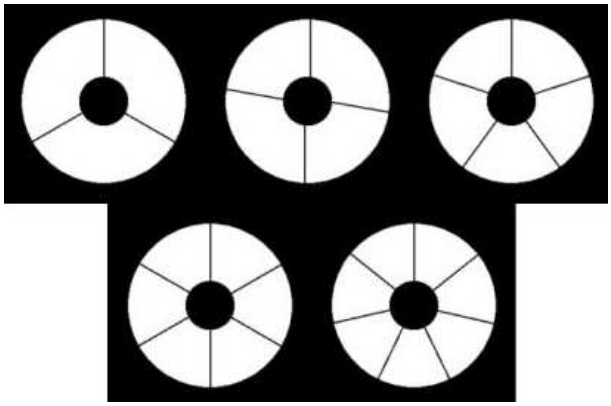

Figure 5.8: Pupil configurations considered in simulation.

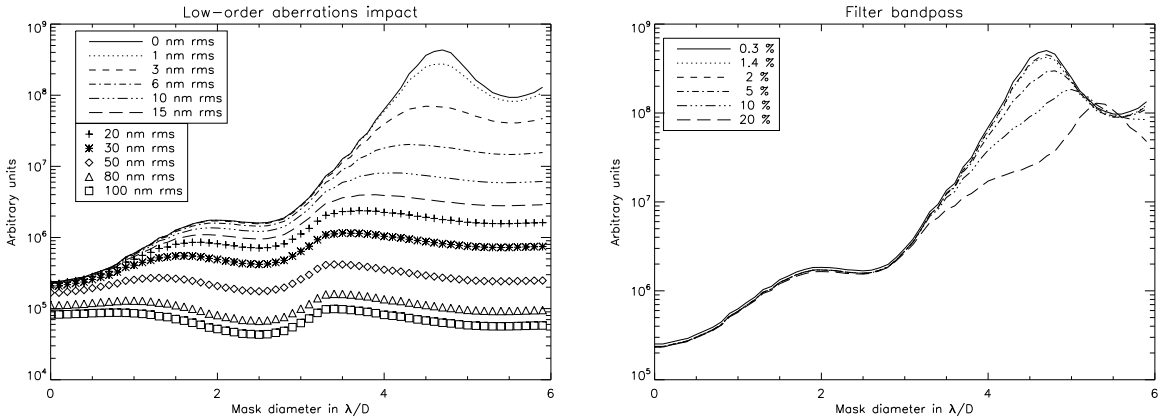

Figure 5.9: Left: $C_{\mathscr{C}}$ average between 3 and 100 λ/D as a function of the FPM diameter and low-order aberrations. Right: $C_{\mathscr{C}}$ average between 3 and 100 λ/D as a function of FPM diameter and the filter bandpass.

mechanical constraints are important for the design. For example, the James Webb Space Telescope is expected to deliver a pupil image for which the position is known at about 3-4%. Therefore, the performance of the mid-IR coronagraph (Boccaletti et al. 2004 [26]) will be strongly affected. On SPHERE, the planet-finder instrument for the VLT (2010), the pupil shear was identified as a major issue and a dedicated Tip-Tilt mirror was included in the design to preserve the alignment at a level of 0.2% (Beuzit et al. 2006 [20]).

The behavior of $C_{\mathscr{C}}$ in Fig. 5.7 (right) is somewhat different from that seen with the previous parameters. The loss of performance is significant even for small FPM.

However, the criterion is still peaking at 4.7 λ/D with a variation of about 0.2 λ/D although above 4.5 λ/D the curves are rather flat indicating that a larger FPM would not improve performance.

Static aberrations

Here, static aberrations refer to low-order aberrations on the segments of the large primary mirror. We separately investigated the effect of piston, tip-tilt, defocus and astigmatism, and found the behavior to be similar for all these aberrations. In contrast to the other defects, both the performance and the optimal FPM diameter (optimal APLC) are very sensitive to low-order aberrations.

As the amplitude of aberrations increases, the dependency of $C_{\mathscr{C}}$ on FPM diameter becomes flatter and the optimal FPM size gets smaller (Fig. 5.9). A larger FPM would not decrease performance enormously. For values

larger than 15nm, there is no longer clear evidence of an optimal size beyond ~ $3.5\lambda/D$. The performance is rather insensitive to the actual FPM size.

Even though low-order aberrations strongly affect APLC performance, their presence has virtually no impact on the optimized configuration. The fairly constant performance in the presence of larger low-order aberrations indicates that low-order aberrations are not a relevant parameter for the optimization of the APLC.

Chromatism

All previous analysis was performed for monochromatic light at λ_0. However, as with the classical Lyot coronagraph, the APLC performance should depend on the ratio between FPM size and PSF size and therefore on wavelength. Hence, the impact of chromatism on the APLC optimization must be evaluated. We note that the chromatism of the APLC can also be mitigated by a slight modification of the standard design (Aime et al. 2005 [5]).

Figure 5.9 and Table 5.2 present the results of the simulations for several filter bandpass widths ($\Delta\lambda/\lambda$) when using the standard monochromatic APLC. As long as the filter bandpass is smaller than 5%, the optimal FPM size and performance are nearly the same as in the monochromatic case.

The values displayed in Cols. 4 and 5 of Table 5.2 quantify the loss of contrast due to chromaticity with respect to the monochromatic case for the APLC being optimized to the filter bandpass (F_1) and to the central wavelength of the band (F_2). These two factors begin to differ significantly from each other at a filter bandpass larger than 5%. Hence, optimization of the APLC for chromatism is needed for a filter bandpass exceeding this value.

An efficient way of optimizing an APLC for broad band application is to optimize it for the longest wavelength of the band, which leads to results that are within $0.1\lambda/D$ of the true optimal FPM size. This behavior can be explained by the non-symmetrical evolution of the residual energy in the coronagraphic image around the optimal FPM size at λ_0 (Soummer et al. 2003 [89]). Another way to minimize chromaticity would be to calculate the apodizer profile for the central wavelength and only optimize the FPM diameter considering the whole bandpass. We compared the behavior of both methods for $\Delta\lambda/\lambda = 20\%$: they are in fact very comparable in terms of performance.

Table 5.2: Chromatism effects synthesis

$\Delta\lambda/\lambda$ **(%)**	$FPM(\lambda/D)$	$FPM_{\lambda_{max}}(\lambda/D)$	F_1	F_2
0.3	4.70	4.70	1.0	1.0
1.4	4.70	4.73	1.1	1.1
2	4.70	4.75	1.1	1.1
5	4.80	4.82	1.6	1.6
10	5.00	4.94	2.6	3.7
20	5.30	5.20	3.7	14.6
50	5.90	5.87	26.3	180.9

Table 5.3: APLC optimization for an obscuration of 30%

Parameters	Value range	Optimal APLC configuration (FPM range in λ/D)
Obscuration	30%	4.7
Spider (arm)	3 - 7	4.6 - 4.8
Spider (size)	15 - 90 cm	4.6 - 4.8
Shear pupil	0.5 - 2 %	4.7 - 4.9
Segment reflectivity	0.25 - 5 %	4.5 - 4.7
Low-order aberrations	1 - 100 nm rms	3.5 - 6.0
Chromatism ($\Delta\lambda/\lambda$)	1.4 - 5 %	4.7 - 4.8
Chromatism ($\Delta\lambda/\lambda$)	5 - 20 %	4.8 - 5.3

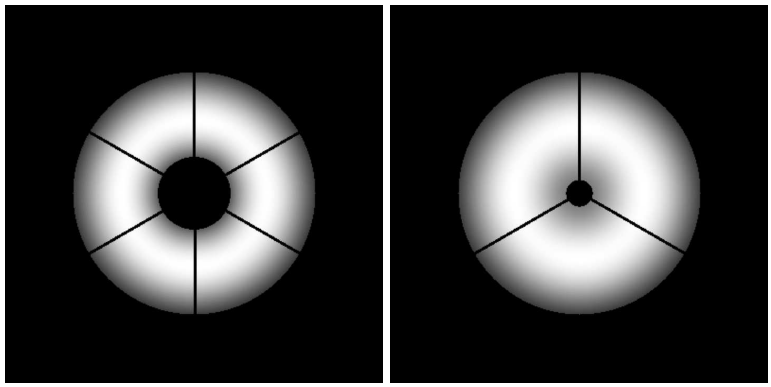

Figure 5.10: Optimized apodized E-ELT apertures: telescope design 1 (left), telescope design 2 (right).

5.2.3 Summary

In this part, Table 5.3 summarize the results obtained with the previous system analysis. Most of these results concerned a 30% central obscuration pupil geometry (E-ELT). However, as we can see, the central obscuration ratio is determining (most of the optimal configuration derived from other parameters are not really far from the one constrained by the central obscuration). Hence, results for different pupil geometries can be easily derived from this study. In Chapter 12 results for the VLT-like pupil (mimics on HOT the High order Testbench developed at ESO) will be presented since they determine the choice of the apodizer/FPM couple to develop in practice.

5.3 Application to ELT pupils

In this section, we apply the tools and results from the APLC optimization study discussed in the previous section to the two telescope designs proposed for the E-ELT. The objective is to confirm our optimization method and to produce idealized contrast profiles which admittedly must not be confused with the final achievable contrast in the presence of a realistic set or instrumental errors.

5.3.1 Starting with telescope designs

We assume a circular monolithic primary mirror of 42 meters in diameter. Segmentation errors are not taken into account, although we note that the E-ELT primary mirror consists of hexagonal segments with diameters ranging from 1.2 to 1.6 meters in its current design. Two competing telescope designs are considered: a 5-mirror arrangement (design 1) and a 2-mirror Gregorian (design 2). For our purpose, the two designs differ by their central obscuration ratios and the number of spider arms. Design 1 (Fig. 5.10 left) is a 30% obscured aperture with 6 spider arms of 50 cm and design 2 (Fig. 5.10 right) is a 11% obscured aperture with 3 spider arms of 50 cm. These numbers are likely to be subject to change as the telescope design study is progressing. Mechanical supports (non-radial cables of the secondary mirror support) and intersegment gaps are not considered for the reasons mentioned in Sect. 5.2.2.0.

In such conditions and taking into account the previous sensitivity analysis on central obscuration, spider arms, and chromatism ($\Delta\lambda/\lambda = 20\%$) we found optimal APLC configurations with:

- the apodizer designed for 4.8 λ/D and with a FPM size of 5 λ/D for design 1.
- the apodizer designed for 4.3 λ/D and with a FPM size of 4.3 λ/D for design 2.

[86] has demonstrated that optimization or under-sizing of the pupil stop is not necessary with the APLC. We independently verified and confirm this result using our criterion applied to the stop rather than to the mask.

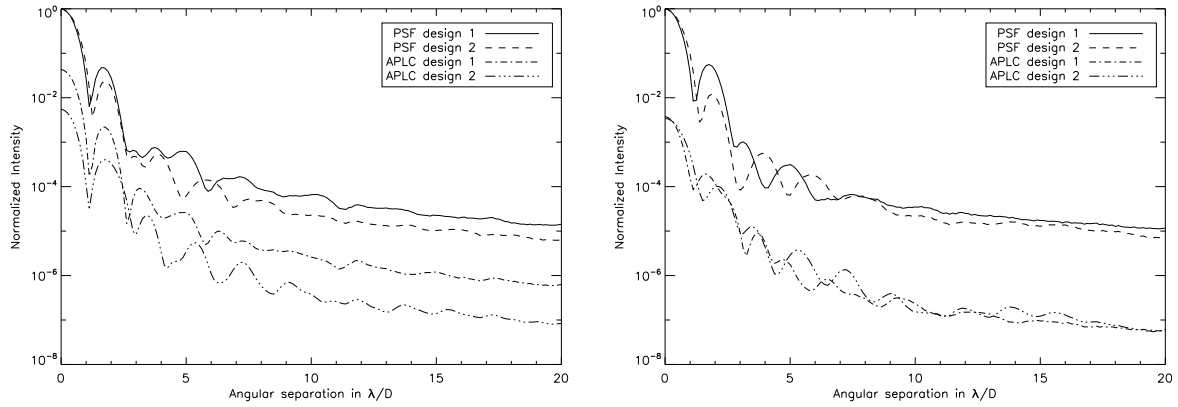

Figure 5.11: Radial profiles of PSFs and coronagraphic images ($\Delta\lambda/\lambda = 20\%$) for the 2 designs considering throughput optimization (left) or $C_{\mathscr{C}}$ optimization (right).

5.3.2 Radial contrast

As shown in Sect. 5.2.2.0, the optimal APLC configuration with our criterion is different to the optimal configuration considering throughput as a metric. We can now demonstrate this difference using contrast profiles. Figure 5.11 compares the coronagraphic profiles based on throughput optimization (apodizer and FPM size are 3.5 and 4.1 λ/D for design 1 and 2, see Fig. 5.4) with that obtained from optimization with our criterion.

For design 2, the optimization with both methods leads to similar APLC configurations (4.3 and 4.1 λ/D). Hence, the contrast performance between them differs by only a factor of 3. On the other hand for design 1, the gain by using our criterion for the optimization is a factor of 10. In addition, the plot shows that APLC contrast performance only weakly depends on the telescope geometry with this optimization method. This is an important result, which means that the APLC can efficiently accomodate with a large variety of telescope designs.

5.4 General conclusion

The APLC is believed to be a well suited coronagraph for ELTs and for the search of extrasolar planets with direct imaging. The high angular resolution of such large telescopes relaxes the constraints on the IWA of a coronagraph which is an important issue for high contrast imaging instruments on 8-m class telescopes. Hence, coronagraphs with a relatively large IWA such as the APLC present an interesting alternative to the small IWA coronagraphs such as the phase mask coronagraphs.

The objective of this study is to analyze the optimization of APLC in the context of ELTs. We defined a criterion ($C_{\mathscr{C}}$) similar to that used by Boccaletti 2004 [21] for the general problem of Lyot stop optimization in coronagraphy. We then analyzed the behavior of this criterion as a function of the FPM diameter in the presence of different telescope parameters. The optimal FPM is determined by the maximum value of the criterion. A sensitivity analysis was carried out for the several telescope parameters such as central obscuration, spiders, segment reflectivity, pupil shear, low-order static aberrations and chromatism. Some of these parameters are not relevant for APLC optimization such as low-order aberrations which provide a pretty flat response of the criterion to FPM diameter when applied at reasonably large amplitudes. However, ELTs are not yet well enough defined to predict the level of static aberrations that coronagraphs will have to deal with.

The parameter which has the largest impact on the optimum FPM diameter is the central obscuration. An obscuration ratio of 30% leads to an optimal APLC of 4.7 λ/D. In most cases, the optimal sizes derived for other telescope parameters are quite consistent with that imposed by the central obscuration. The dispersion of the FPM size is no larger than 0.2λ/D given the range of parameters we have considered. We also demonstrated that APLC optimization based on throughput alone is not appropriate and leads to optimal FPM sizes which decrease with increasing obscuration ratios. This behavior is opposite to that derived using our criterion. The superior quality of

our criterion is supported by the comparison of contrast profiles obtained with both optimization methods in Sects. 5.3.2 and 5.2.2.0.

5.5 Limits of this study

- This study can not be generalized to telescope without central obscuration. In that case the problematic is totally different: there is only one apodizer regime (bell regime) and the transmission of an off-axis evolves linearly with the mask diameter since the apodization gets stronger. The bigger the FPM, the stronger the apodizer, the lower the throughput. The choice is then driven by performance (contrast level requirements, throughput and IWA considerations). It is more a trade-off analysis rather than optimization.
- Although the idealized simulations presented in this study do not consider atmospheric turbulence and instrumental defects, they allow us to find the optimal APLC configuration and PSF contrast for each case. Cavarroc et al. 2006 [30] show that the ultimate contrast achievable by differential imaging (speckle noise suppression system to enhance the contrast for exo-planet detection topics, for instance, Racine et al. 1999; Marois et al. 2000; Baba et al. 2003; Guyon et al 2004 [78, 62, 13, 46]) with a perfect coronagraph is not sensitive to atmospheric seeing but depends critically on static phase and amplitude aberrations. Our results therefore present the possibility of extending this study to the more realistic case of a real coronagraph taking into account relevant effects releated to telescope properties. However, it is important to analyse how telescope parameters will matter the coronagraph with respect to the atmosphere residual phase left by an AO system (depend on science program objectives, for instance imaging of the vicinity of elongated object (AGN or so) is a totally different than imaging Earth-like planet and hence required different approaches and considerations). Hence, these results must be considered carefully, since when operating on a telescope (i.e in realistic conditions) undistinguished contrast between different apodizer/FPM combination can be delivered, and could therefore potentially give more weight to throughput consideration.

5.6 APLC optimization for EPICS

5.6.1 Context

In the context of the future planet hunter project for the E-ELT (EPICS: Exo-Planets Imaging Camera and Spectrograph), a comparison study between coronagraphs has been initiated between different institutions : LAM, LESIA, FIZEAU and ESO. The goal of this first step was to provide optimal parameters for a large number of coronagraphs with respect to diffraction from the proposed pupils of the E-ELT and chromatism. LAM is responsible of the Dual-zone, LESIA of AGPM and multi-4QPM, FIZEAU of binary pupil mask and two mirrors apodization techniques and ESO/LESIA of APLC and Band-limited. Through this part, we will only present optimized parameter for APLC and some basic results in diffraction limited regime. Optimized parameters for BLs will be presented in Chapter 6. Note that this comparison study is only the first step of a more complex and general study that aims to finely analyze the whole system (telescope + AO residual + instrument + coronagraph + speckle calibration + data processing) in a End-to-End simulator (Vérinaud et al. 2007 [100]) in order to fairly compare coronagraphs at a level close to the level of detection.

5.6.2 Assumptions

Pupil designs

At this time, two main pupil designs were into competition for the future E-ELT as shown on Fig. 5.12. These two designs differs from the geometry of the spider vanes. Central obscuration is in each case 30%.

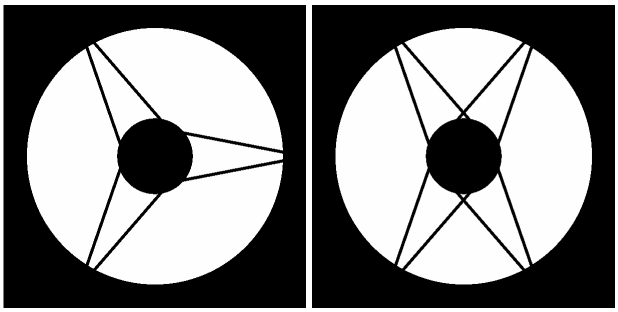

Figure 5.12: Two pupil designs proposed for the E-ELT differing by the configuration of the spider vanes

Spectral bandwidth

For this first step optimization, three spectral bandwidths have been defined:

- 0.8 μm ± 100 nm (R = 25%)
- 1.25 μm ± 100 nm (R = 16%)
- 1.6 μm ± 100 nm (R = 12.5%)

5.6.3 Proposed APLC and first results

Assuming results of the previous study, a 4.7 λ/D APLC has been proposed for each design. Nevertheless, in that case the apodizer has been calculated without the presence of spider vanes in the pupil. Spider vanes structures usually start to alter the shape of the apodizer for mask size of about 5 λ/D (apodizer more complex, not rotationnally symmetric, lower throughput) as discussed in Soummer et al. 2007 [91]. However, in some cases depending on the pupil geometry (as Design 1 & 5, see Fig. 5.12) spider vanes start to modify the apodizer at smaller mask

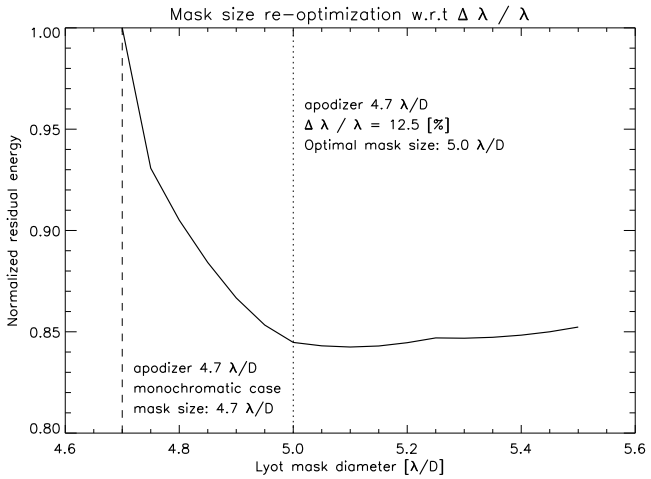

Figure 5.13: Lyot mask size re-optimization for APLC to mitigates chromatism effects here for R = 12.5%. The optimal one is the one which minimize the residual energy at R=12.5%.

size. A study is required to determine which configuration is better. This has been started and potentially could lead to a re-optimization. This issue will be further discussed in Sec. 5.6.5.

As discussed in Sec. 5.2.2.0, the nominal mask size of the Lyot can be re-optimized to mitigates chromatism impact (see Fig. 5.15 as example for R = 12.5% where the optimal size is the one that minimize the residual energy). Apodizer designed for a $4.7\lambda/D$ mask diameter combined with a $4.7\lambda/D$ mask diameter is the optimal point for a monochromatic case (at least until R = 5%, seeTable. 5.2). In a case of a limited bandwidth with a central wavelength λ_0, the apodizer profile calculated for a mask $4.7\lambda_0$/D, is not optimal for other wavelength, simply because the mask size for this wavelength is different:

$$4.7\left(\frac{\lambda_0}{\lambda}\right)\frac{\lambda}{D} \tag{5.12}$$

For apodizer corresponding to the $4.7\lambda_0$/D, the optimal Lyot mask size for a limited bandwidth $\Delta\lambda$ is a mask actually corresponding to a minimal wavelength from the band:

$$\frac{4.7}{1-\frac{\Delta\lambda/\lambda_0}{2}}\times\frac{\lambda_0}{D} \tag{5.13}$$

Hence, considering the spectral bandwidth, the 4.7 λ/D Lyot mask has been re-optimized to:

- 5.0 λ/D for R = 12.5%
- 5.1 λ/D for R = 16%
- 5.4 λ/D for R = 25%

Note that in each case the pupil stop has been also optimized to mitigates chromatism effects as well. The outer diameter has been slightly reduced, the inner diameter and spider vanes have been slightly increased. For instance, the physical size of the spider vanes has been oversized by a factor of 2.

In Fig. 5.14, results of this optimization are presented. Note the fairly constant of contrast of the polychromatic coronagraphic PSFs owing to the mask and stop optimization.

5.6.4 Chromatism dependency

Monochromatic case

Using numerical fitting function applied on Fig. 5.15 (left, resulting from simulation), an empirical relation can be defined for the chromatism dependency of APLC. In that case the 4.7 λ/D (no mask size re-optimization) is

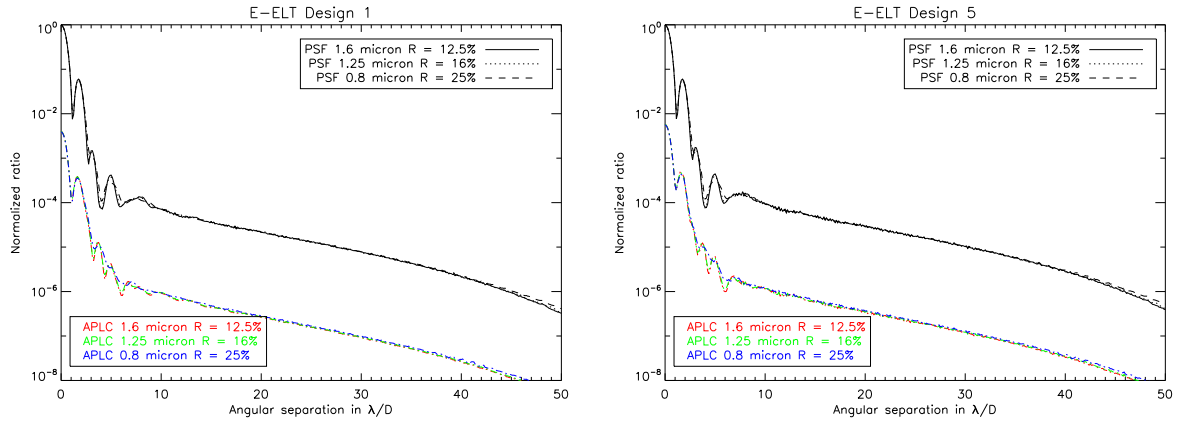

Figure 5.14: Coronagraphic PSF of optimized APLC (apodizer 4.7 λ/D with mask size of 5.0, 5.1, 5.4 for R = 12.5, 16 and 25 % respectively (pupil stop is also re-optimized)

considered, and 51 wavelengths have been simulated (R = 33%) to optimize fitted function coefficients. We found more convenient to express the empirical relation as function of λ_0/λ where λ_0 is the nominal operating wavelength (monochromatic case) and λ the effective wavelength:

$$\tau(\frac{\lambda_0}{\lambda}) = C_0 \times e^{-\left(\frac{\frac{\lambda_0}{\lambda}-C_1}{\sqrt{2}C_2}\right)^2} + C_3 + C_4 \times \frac{\lambda_0}{\lambda} + C_5 \times (\frac{\lambda_0}{\lambda})^2 \tag{5.14}$$

Owing to the later equation, the total rejection (τ_λ) can be determined when $\lambda \neq \lambda_0$ where:

C_0 = 0.6841 (weight of the gaussian)
C_1 = 1.0 (center of the gaussian)
C_2 = 0.0347 (standard deviation)
C_3 =- 3.8735 (constant term)
C_4 = 6.7805 (linear term)
C_5 = -2.6292 (quadratic term)

As we said, this case only show the chromatic behavior of a 4.7 λ/D APLC when the mask size is not re-optimized with respect to the spectral bandwidth. A re-optimization of the mask size for a given spectral bandwidth is obviously mandatory (see Table 5.4) for large spectral bandwidth. In Fig. 5.15, we compare the two cases by plotting on the left side Eq. 5.14 chromatism dependency when mask size is not re-optimized and on the right side the chromatic behavior when the mask size is re-optimized (both case for R = 33When $\lambda_0/\lambda < 1$, so to say at longer wavelengths, the 4.7λ/D mask appears smaller which indeed explains the strong decreasing of the curve (Fig. 5.15, left). On the opposite, when $\lambda_0/\lambda > 1$, corresponding to the case of shorter wavelengths, the mask appears bigger, and hence the decreasing of the left curve is not so important (Fig. 5.15, left). In the later case, although the mask diameter differs from the nominal one, it gets larger and therefore has a better efficiency from a Lyot coronagraph point of view. In other words, the 4.7λ/D APLC will be more efficient at shorter wavelengths because even if the mask size does not correspond to the apodizer shape, it gets bigger. It is precisely the reason why the mask size is re-optimized to a bigger one (5.6λ/D at $\lambda = \lambda_0$) for R = 33%: at the longest wavelength for which the mask appears smaller, it will get its nominal size and increase up at shorter wavelengths. Hence, chromaticity has been mitigated (Fig. 5.15, right).

Polychromatic case

Here, we are interesting on the total rejection rate efficiency when using the APLC on a spectral bandwidth ($\lambda_0/\Delta\lambda$). To do so, we simulated polychromatic coronagraphic PSF using 11 wavelengths. We compare the efficiency of

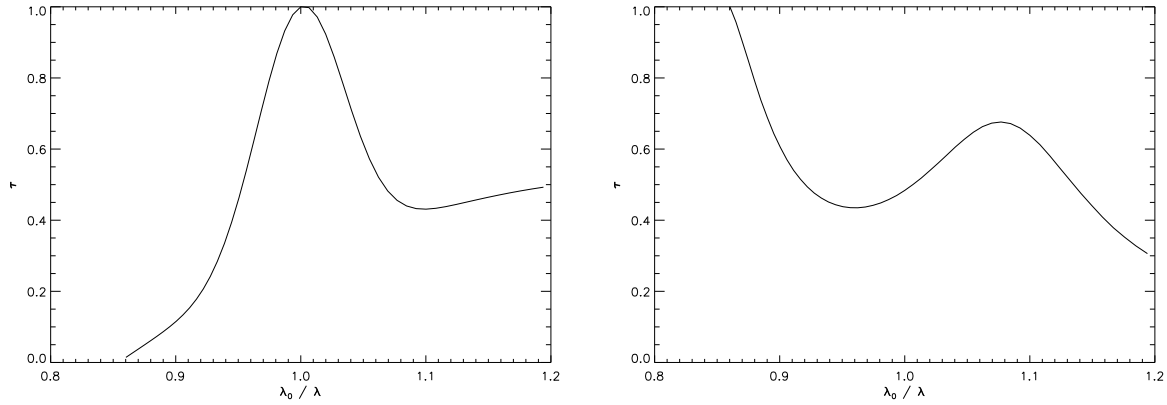

Figure 5.15: Chromatism dependency of APLC: *Left* total rejection rate behavior (normalized) for a $4.7\lambda/D$ APLC as function of the operating wavelength through the ratio λ_0/λ, *Right* $4.7\lambda/D$ APLC with re-optimization of the mask size ($5.6\lambda/D$) for $R = 3$

the APLC in its nominal configuration ($4.7\ \lambda/D$) to that when the mask size is re-optimized with respect to the spectral bandwidth. Note that in each case, the pupil stop remains identical to the entrance pupil (a re-optimization of the pupil stop can help to further mitigate chromaticity). Results are resumed in Table 5.4 and show the critical interest of re-optimizing the mask size. Note that the total rejection rate is better by $\sim 78\%$ for $R = 33\%$, for instance. Obviously, re-optimizing the mask size impacts the IWA, but it is not really critical considering that in the worst case ($R = 33\%$) the mask increases only by $0.9\lambda/D$ and that we are dealing with ELTs for which the angular resolution is usually confortable.

Table 5.4: Total rejection rate of $4.7\lambda/D$ APLC as function of the spectral bandwidth ($\lambda_0/\Delta\lambda$) for the nominal (τ, d) and optimized configuration ($\tau_{optimized}$,$d_{optimized}$)

R [$\lambda_0/\Delta\lambda$]	100	50	25	20	10	7	5	3
d [λ/D]	4.7	-	-	-	-	-	-	-
$d_{optimized}$ [λ/D]	4.7	4.7	4.9	4.9	5.0	5.1	5.4	5.6
τ	1195	1178	1112	1068	796	583	376	158
$\tau_{optimized}$	1195	1178	1114	1101	835	782	757	731
Gain [%]	-	-	0.28	3.00	4.68	25.45	50.33	78.38

5.6.5 Reserves: the spider vanes impact

In this last section, we discussed interest of optimizing (calculation) the apodizer with respect to the spider vanes of the pupil. Simulations discussed hereafter are preliminary and will be further developed in the context of EPICS. As discussed above, spider vanes structures usually start to alter the shape of the apodizer for mask size about 5 λ/D (apodizer more complex, not rotationnally symmetric, lower throughput) as discussed in Soummer et al. 2007 [91]. The way it impacts the apodizer is determined by the ratio between the mask size and the spider vanes thickness. Here, we will show that the way spider vane structures impact the apodizer is not only determined by the spider vanes thickness vs. the mask size but also by the geometrical repartition of the spider structures across the entrance pupil. Specifically, some pupil geometries make the calculation of the apodizer with respect to the spider vanes useless because of the poor performance they allow compared to that without taking into account the spider vanes.

- When the geometrical repartition of the spider vanes remains homogeneous across the pupil diameter, alteration of the apodizer only start from $5\lambda/D$. Given that, conclusions presented in Sec. 5.2.2.0 remain relevant assuming that we are only looking at APLC configurations not higher than 6 λ/D. Apodizers in such range of mask size are not highly modified.

- When the geometrical repartition of the spider vanes are not homogeneous across the pupil diameter (Pupil design 1 and more specifically design 5, for instance), the alteration of the apodizer start before $5\lambda/D$ (it is already visible from $4\lambda/D$, see Fig. 5.6.5) and modification of the profile is quite important: apodizer complex, not rotationnally symmetric, low throughput (see Table 5.5).

- The way that the spider vanes (in a non-homogeneous configuration) are dispatched has a strong impact on performance, making the optimization of the apodizer with respect to the spider vanes useless (poor performance) for some of them. Note in Table 5.5, the loss of throughput compared to that non-optimized case, and differences between design 1 and 5 results ($\sim$ 20% transmission difference).

- Using non-optimized apodizer on aperture with spider structures strongly impacts APLC in a 2 stages configuration while 1 stage is efficient enough (Fig. 5.6.5, top).

- For small mask size (<$4.5\lambda/D$), using optimized apodizer on Design 1 allows good performance even in 2 stages configuration while on Design 5 performance are really bad (Fig. 5.6.5, bottom left).

- Whatever the repartition of the spider vanes (pupil 1 or 5), from $\sim 5\lambda/D$ performance of APLC with optimized apodizer are not enough important compared to non-optimized APLC (Fig. 5.6.5, bottom right).

As shown in simulations, there is a strong relation between the repartition of the spider vane structures across the pupil and the interest of optimizing APLC apodizer with these later. These optimized complex apodizer do not appear favorable in terms of performance and add additional constraints (alignment and manufacturing issues).

Table 5.5: Apodizer throughput [%] as function of the mask size and impact of the pupil design on the calculation of the corresponding apodizer.

	optimized w.r.t spider vanes			
	no		yes	
Mask size [λ/D]	Design 1	Design 5	Design 1	Design 5
4.0	65.3	65.3	48.2	23.2
4.5	57.2	57.2	39.1	20.1

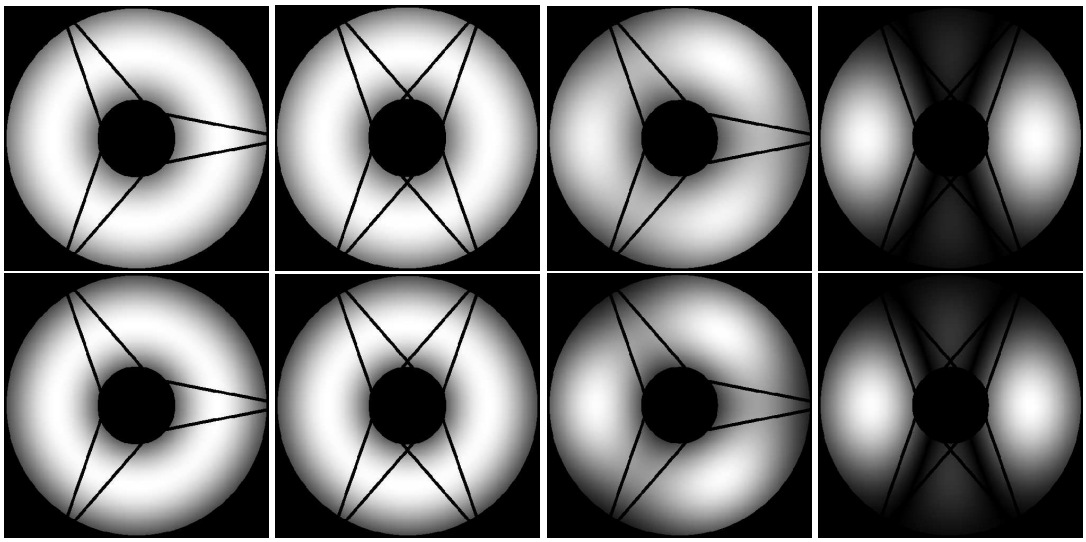

Figure 5.16: Apodized pupils: $firstline$: 4.0λ/D APLC, *secondline*: 4.5λ/D APLC. *Column* 1 & 2: apodizer calculated without the presence of the spider vanes and applied on design 1 & 5 respectively. *Column* 3 & 4: apodizer calculated with respect to the corresponding pupil design. Corresponding throughput are in Table 5.5

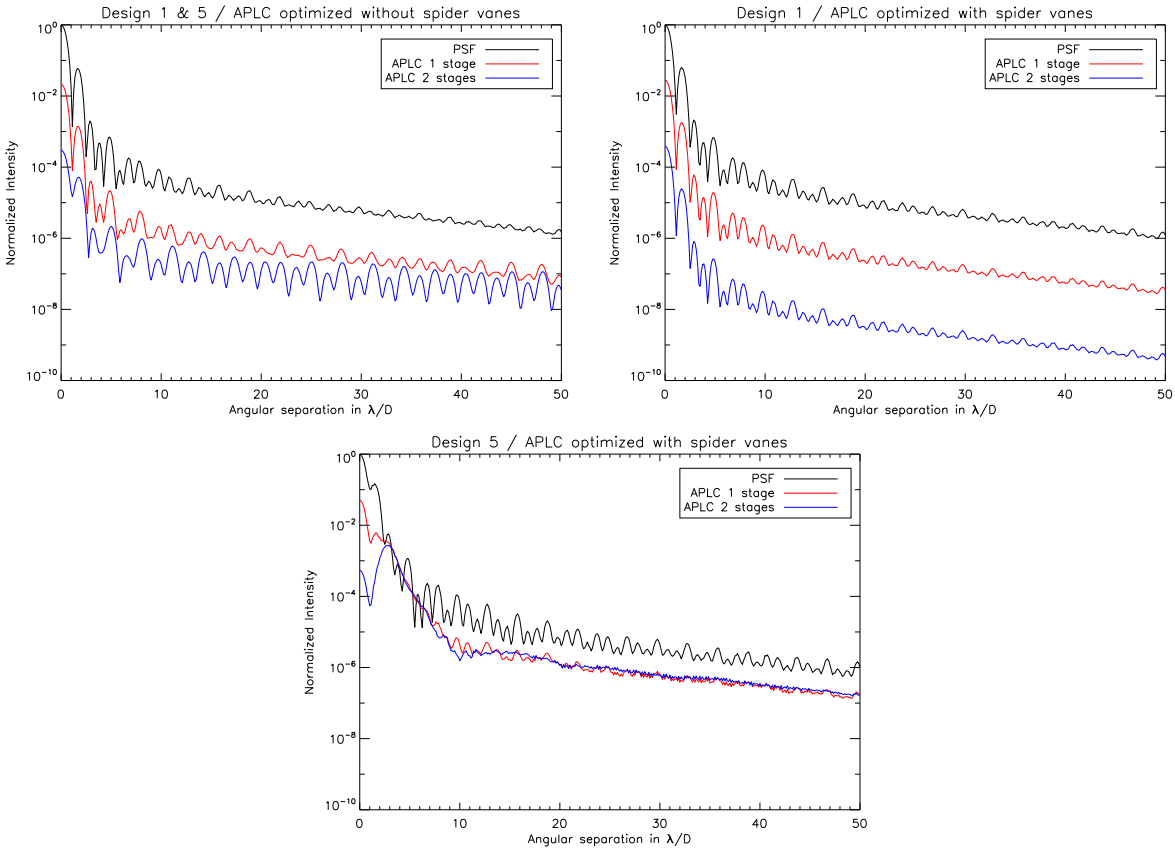

Figure 5.17: Monochromatic PSF and coronagraphic PSF with a $4.0\lambda/D$ APLC. *Top*: apodizer calculated without the presence of spider vanes (T=65.3%) and applied on pupil design 1 & 5. *Bottom left*: apodizer calculated with respect to the pupil design 1 (T=48.2%). *Bottom right*: apodizer calculated with respect to pupil design 5 (T=23.2%). As a fair comparison, curves are pondered by the T.

6

Optimization of Band-limited coronagraphs

Contents

Abstract - *Band-limited coronagraphs are considered as promising coronagraphs for space-based observations (TPF-C, Traub et al. 2006 [92], for instance). These series of band-limited image masks are built to provide an insensitive-like behavior to pointing errors and other low-spatial-frequency optical aberrations. A large variety of band-limited functions exists, with different mask throughputs, orders, and associated pupil stops. The order of a band-limited coronagraph dictates the sensitivity of the mask to optical aberrations. In this Chapter, we will investigate the suitability of such device considering some important specificities of ELTs that can potentially severely restrict the interest of high order band-limited function. From a simple system analysis and by only considering some parameters as the IWA and the pupil stop shape and throughput, we will underline the fact that most of the telescope geometry parameters impact on the choice of the order of these function to implement on ELTs in practice. This analyzis will be further investigated in Chapter 8 and 9, where we combine band-limited coronagraphs (with different orders) with XAO system and speckle calibration system respectively.*

6.1 Band-limited coronagraphs for arbitrary apertures

6.1.1 Presentation

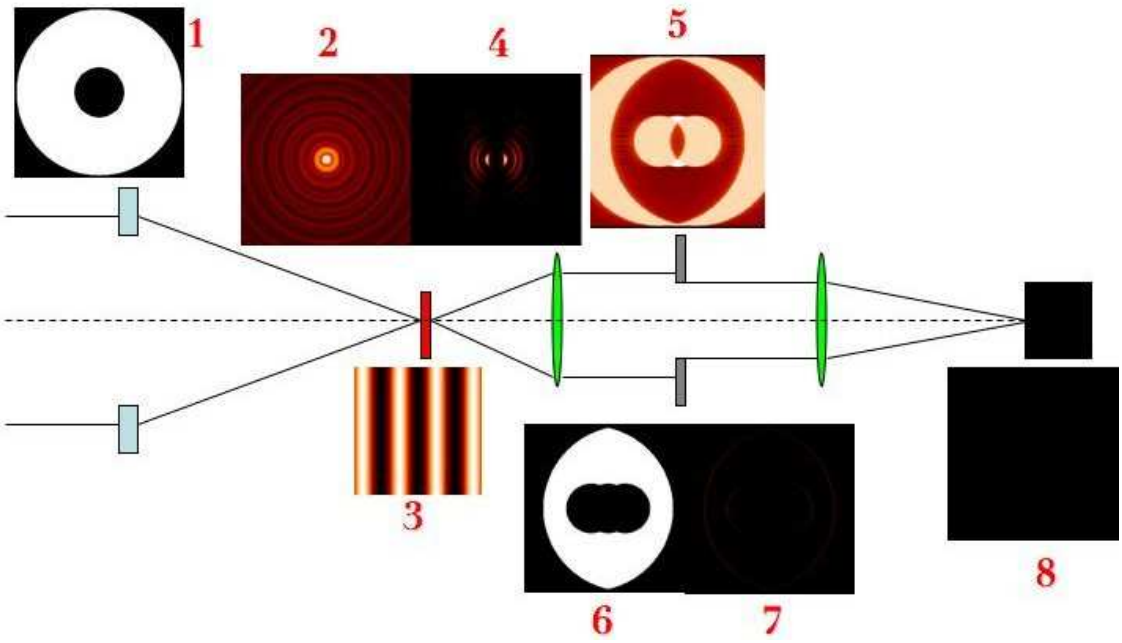

Figure 6.1: BL coronagraphic process : Entrance pupil (1). In the focal plane, the complex amplitude of the star (2) is spatially filtered (4, low-frequencies) by the Lyot mask (3). In the relayed pupil (5) a pupil stop (6) is filtering high frequencies and as a result in the relayed pupil diffraction light is canceled (7). Finaly, the starlight is suppressed and not imaged on the detector (9).

The BL is a direct improvement of the Lyot coronagraph which prevents for the starlight to propagate in the geometric area of the relayed pupil (resulting from the convolution of the telescope pupil with the Fourier transform of the mask). To reduce starlight contamination in the relayed aperture, it is then required to use a quite large Lyot mask combine with a reduced pupil stop. However, this configuration is not favorable for planet detection close to their parent stars. The philosophy of the BL coronagraph is to adapt the Fourier transform of the mask to be with finite support as the telescope aperture in a way to reduce the oscillation of the mask Fourier Transform. In other words, the Fourier transform of the BL mask is band-limited.

6.1.2 Formalism

In this Section, we briefly remind the formalism of the Band-limited coronagraph (mostly based on Kuchner et al. 2002 and Kuchner et al. 2004 [59, 57] and adapted to the case of arbitrary apertures). Band-limited coronagraphs are image mask function that are band-limited in a Fourier sense. As discussed above, these devices are direct improvement of the Lyot coronagraph that strive to adapt the amplitude mask support to be infinite as the PSF. In other words, the Fourier transform of such masks are band-limited, defined on a finite support.

In the following, for the sake of clarity, we omit the spatial coordinates r and ρ (for the pupil plane and focal plane respectively). The function that describes the amplitude mask is noted M. The classical coronagraphic process, corresponding to propagation from the telescope entrance aperture to the detector plane, is expressed in Eq. 6.1 to 6.5. Planes A, B, C and D correspond to the telescope aperture, the coronagraphic focal plane, the pupil stop plane and the detector plane respectively. The Fourier transform of a function f is noted $\hat{f}$. The symbol $\otimes$ denotes the convolution product. The entrance pupil is noted P in the pupil plane:

$$\psi_A = P \tag{6.1}$$

The complex amplitude of the star is spatially filtered (low frequencies) by the mask:

$$\psi_B = \hat{\psi}_A \times M \tag{6.2}$$

The exit pupil image is spatially filtered (high frequencies) by the stop:

$$\psi_C = \hat{\psi}_B \times \Pi \tag{6.3}$$

$$\psi_C = [\psi_A \otimes \hat{M}] \times \Pi \tag{6.4}$$

The coronagraphic amplitude on the detector plane becomes:

$$\psi_D = \hat{\psi}_C = [\hat{\psi}_A M] \otimes \hat{\Pi} \tag{6.5}$$

In Kuchner et al. 2002 [59], Kuchner & Traub proposed to use a focal plane mask shape function M which is band-limited and will block all the light from an on-axis source to angle within the clear area defined by the pupil stop (i.e $\psi_A \otimes \hat{M} = 0$). Following the notation of Kuchner et al. 2004 [57] expressed for uniform entrance aperture, we will further develop Eq. 6.4 in 1D. To do so, we can write ψ_A as a difference of Heaviside functions, $\mathscr{H}(\rho)$:

$$\psi_A(\rho) = \mathscr{H}(\rho + \frac{1}{2}) - \mathscr{H}(\rho + \frac{\alpha}{2}) + \mathscr{H}(\rho - \frac{\alpha}{2}) - \mathscr{H}(\rho - \frac{1}{2}) \tag{6.6}$$

Assuming that the entrance aperture is opaque for $|\ \rho\ | > 1$ and inside the central obscuration as well, $|\ \rho\ | < \alpha$ where $\alpha < 1$ (α is the width of the central obscuration regarding the entrance aperture scale unit). By $\mathscr{D}$, we refer to the domain where $\Pi(\rho) = 1$ including $|\ \rho\ | < \frac{(1-\epsilon)}{2}$ and $|\ \rho\ | > \frac{(\alpha+\epsilon)}{2}$ where $\epsilon < 1$.
Then, since the convolution with an Heaviside function is equivalent to indefinite integration, we can write:

$$\psi_A(\rho) \otimes \hat{M}(\rho) = \mathscr{M}(\rho + \frac{1}{2}) - \mathscr{M}(\rho + \frac{\alpha}{2}) + \mathscr{M}(\rho - \frac{\alpha}{2}) - \mathscr{M}(\rho - \frac{1}{2}) \tag{6.7}$$

Where $M(\rho) = \frac{d\mathscr{M}(\rho)}{d\rho}$. Hence, to remove all the starlight within the clear area of the pupil stop, Eq. 6.4 requires to satisfy:

$$\mathscr{M}(\rho + \frac{1}{2}) + \mathscr{M}(\rho - \frac{\alpha}{2}) = \mathscr{M}(\rho - \frac{1}{2}) + \mathscr{M}(\rho + \frac{\alpha}{2}) \ \ \forall \rho \in \mathscr{D} \tag{6.8}$$

Now, if we consider the case where $\alpha = 0$ (uniform entrance aperture), Eq. 6.8 becomes:

$$\mathscr{M}(\rho + \frac{1}{2}) = \mathscr{M}(\rho - \frac{1}{2}) \ \ \forall \rho \in \mathscr{D} \tag{6.9}$$

And, considering factors added in Eq. 6.4 by the presence of the central obscuration, a trivial solution would requires to satisfy both Eq. 6.9 and the following:

$$\mathscr{M}(\rho - \frac{\alpha}{2}) = \mathscr{M}(\rho + \frac{\alpha}{2}) \ \ \forall \rho \in \mathscr{D} \tag{6.10}$$

Conditions of Eq. 6.9 and 6.10 are respected with a simple solution:

$$\mathscr{M}(\rho) = constant \ \ \forall \rho \in \mathscr{D} \tag{6.11}$$

To do so, this condition about $\mathscr{M}(\rho)$ translates into two requirements on $\hat{M}$: the Fourier transform of the mask shape function have to satisfy the following properties as defined in Kuchner et al. 2004 [57]:

$$\hat{M}(\rho) = 0 \ \ \forall \rho \in \mathscr{D} \ \ (|\ \rho\ | < \epsilon/2) \tag{6.12}$$

$$\int_{-\epsilon/2}^{\epsilon/2} \hat{M}(\rho) d\rho = 0 \tag{6.13}$$

A family of mask functions satisfy Eq. 6.12 and 6.13. Such mask function typically consist of a series of dark rings or stripes as described for instance in Fig. 6.2 and can be designed in 1D or 2D where ϵ is the bandwidth of the mask.

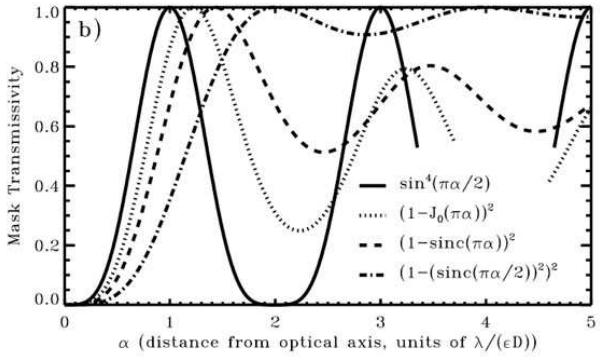

Figure 6.2: Example of band-limited functions. Image from Kuchner et al. 2002 [59]

6.1.3 Band-limited parameters

We will show through this section that band-limited coronagraphs have opened parameters that depends on the application. An optimization of these parameters can not be done in the same way as APLC (Chapter 5). In that sense, BLs optimization is close to the non-apodized Lyot coronagraph case. The choice of BLs parameters is actually largely driven by considerations such as IWA, aberration and pointing errors requirements.

Bandwidth of the function

In the previous part (Sec. 6.1.2), we introduce the parameter ϵ as the bandwidth of the band-limited mask function. This parameter is in a certain way comparable to the one that controls the physical size of a Lyot mask: the diameter. This means that the choice of the ϵ value will directly impact the IWA of the coronagraph and hence control the pupil stop throughput to combine with the mask in practice. In other words, a given ϵ will impose an effective IWA, pupil stop throughput and angular resolution. So, the choice of the optimal value for ϵ is determined by sciences requirements.

Order of the function

The order of a band-limited mask can be well understood by expanding the amplitude transmission function of an ideal band-limited mask into Taylor series about the origin. Given that, we can describe the way that the mask attenuates sources near to the optical axis.

$$M(r) = m_0 + m_1 r + m_2 r^2 + m_3 r^3 + ... \tag{6.14}$$

Assuming the case for which the mask is opaque at the center and symmetric, we can state that m_0, m_1, m_3...= 0. Hence, the first term in this expansion is quadratic in r, in 4^{th} power for the second term and so on. Since the corresponding intensity transmission is $\mid M(r)^2 \mid$, the intensity attenuation will then vary as r^4 for the first term, r^8 for the second term and so on, by multiple of 4. Hence a mask that produces as a first term a 4^{th}, 8^{th} or 12^{th} power dependency will be called a fourth order, eighth order or twelfth order BL mask respectively. By analogy to inteferometry, we can say that such masks produces fourth, eighth or twelfth order null respectively.

The order of the null sets the mask sensitivity to low-order aberrations near the optical axis and hence directly impact on aberrations and pointing errors requirements. The higher the order, the lower the requirements. This order-sensitivity behavior has been numerically verify in Shaklan et al. 2005 [85].

BLs can be build to have different order, starting with 4. A eight-order band-limited mask is designed to eliminate the quadratic term in Eq. 6.14 owing to the following properties that imposes m_2 to be equal to 0:

$$\frac{d^2}{dr^2} M(r) = 0 \quad for \quad r = 0 \tag{6.15}$$

The interest of a high order band-limited mask is then obvious. However, an important drawback due to the level of the order is the pupil stop throughput. For a given IWA (i.e ϵ), the higher the order, the lower the pupil stop thoughput. This inconvenience is quite acceptable in the case of full entrance aperture, but may become problematic for centrally obscured aperture since the pupil stop is necessarily already reduced to block the additional diffraction light in the relayed pupil. In other words, while for space-based observations (off-axis aperture as the TPF-C, Traub et al. 2006 [92]) a high order BL can be useful (to relax pointing requirements for instance), its interest may be severely restricted for ground-based observations because of the telescope geometry that will restrict the collecting area of the pupil stop and hence decrease the angular resolution. Hence, the pupil stop is a critical issue for this coronagraph. This issue will then be addressed along the following parts of this Chapter.

6.2 Assumptions

Here, we describe the assumptions for simulations presented along the next parts of this Chapter. We will consider two 1D band-limited mask functions with fourth and eighth order. We do not consider higher order since conclusions derived from this study will underline the fact that eighth order BLs already have a restricted interest for ELTs. Note that these results will be supported by the analysis performed in Parts III and IV.

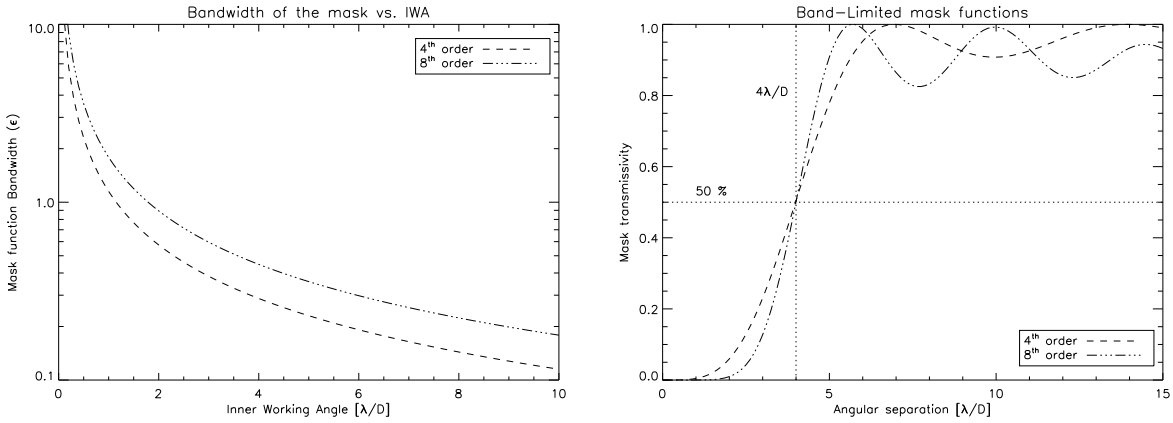

Figure 6.3: *Left*: Bandwidth of the mask vs. IWA for a four and eight order mask function. *Right*: Off-axis throughput as function of the angular separation for a four and eight order mask function with IWA = 4 λ/D

6.2.1 Mask functions and orders

Here, we briefly present band-limited coronagraph functions and properties for the fourth and eighth order masks respectively:

$$M(r)_{4^{th}} = 1 - sinc^2(\frac{\epsilon r D}{\lambda}) \tag{6.16}$$

$$M(r)_{8^{th}} = N\left[\frac{l-m}{l} - sinc^l\frac{\pi r\epsilon}{l\lambda f} + \frac{m}{l}sinc^m\frac{\pi r\epsilon}{m\lambda f}\right] \tag{6.17}$$

Where f is the focal ratio at the mask, λ is the wavelength at which the mask is supposed to operate, N is a normalization factor, l and m are integer exponent parameters. These latter, controls the ringing of the mask (i.e their effective throughput). Using larger values for l and m helps to reduce the ringing but at the cost of a lower Pupil stop throughput. In the following, we will consider the fourth order mask (Eq. 6.16) and the eighth order mask (Eq. 6.17 with $m = 1$ and $l = 3$). Note that the eighth order is simply a linear combination of two fourth order masks build such that the quadratic term in the amplitude transmission cancels.

6.2.2 Bandwidth of the function vs. IWA

In Fig. 6.3 (*left*), we plot the relation between the bandwidth of the mask (ϵ) and the inner working angle (IWA, defined at half-maximum of the intensity transmission profile of the mask function) in the case of the fourth and eighth order mask. In Fig. 6.3 (*right*), the intensity profile of these two order masks is plotted for a given IWA ($4\lambda/D$, for instance). Note that we choose mask functions with a good effective throughput (high transmission in critical region where planet are potentially observable). Moreover, these two masks have been proposed for TPF-C. The choice of the parameter ϵ is then drive by sciences requirements and hence upon the application. An optimization as we did for the APLC by defining criteria is not relevant for that reason. Moreover, as the Lyot coronagraph, BLs are coronagraphs that need to be optimized with the pupil stop.

6.3 The pupil stop problem

For the Lyot, the larger the mask, the higher the performance, the higher the pupil stop throughput (starlight contamination in the geometrical pupil gets finely localized when the mask gets larger). For BLs, problematic is identical except that at each bandwidth of the mask, performance will be identical (perfect rejection in ideal conditions, i.e if properly optimized, the pupil stop cancels all starlight contamination in the relayed geometrical pupil), while throughput of the pupil stop will evolve as a function of ϵ. The smaller the bandwidth (ϵ), the larger the IWA, the higher the pupil stop throughput. Hence, it is clear that an optimization of BLs is mainly concern with the optimization of the pupil stop, and will be set by throughput considerations and IWA as well.

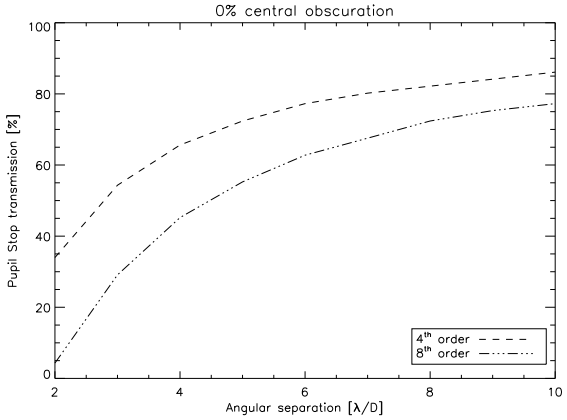

Figure 6.4: Pupil stop throughput as function of the IWA for a four and eight order mask function. Central obscuration is 0%.

6.3.1 IWA & order of the function vs. Pupil stop throughput

Some analytical expressions of the pupil stop throughput have been defined through the large number of paper dedicated to BLs (Kuchner et al. 2004, Crepp et al. 2006 [57, 33]). The simple and somehow optimistic one states that the throughput of a 1D linear mask BLs is equal to $1-\epsilon$. In simulation, in the case of full entrance aperture, throughput is generally consistent to this later relation within 5 - 10%. For the following simulations, pupil stop have been optimized in perfect case to reach a perfect attenuation of the on-axis star.

In Fig. 6.4, we compare the pupil stop throughput of the fourth and eighth order mask as function of the IWA (i.e ϵ, the bandwidth of the mask). On this plot this comparison is performed for a full pupil (0% central obscuration). From this plot, we can derive some conclusions:

- Conformed with theory, the larger the IWA, the higher the throughput

- Eighth order is less transmissive than four order, the difference gets smaller when IWA gets larger
- Throughput difference is about 20% for small IWA and 10% for large IWA
- For very small IWA ($\sim 2\ \lambda/D$), eighth orders are poorly suited considering the throughput

6.3.2 Telescope geometry impact

For most coronagraphs, telescope specificities such as the central obscuration or the secondary mechanical structures (spider vanes) directly impact the shape and the throughput of the pupil stop since additional diffracted light remains in the geometrical relayed pupil. In the problematic of BLs, these effects matter the interest of a high order BL.

Central obscuration impact

In Fig. 6.5, we compare for two IWA configuration ($4\lambda/D$ and $10\lambda/D$) the impact of the central obscuration ratio on the pupil stop thoughput for the fourth and eighth order BL masks. From these two plots, we can derive some conclusions:

- Conform to theory, a large IWA is more favorable in term of pupil stop throughput
- Throughput differences between a fourth and eighth order is less critical for large IWA
- For small IWA, throughput decreases in the same way whatever the order
- For large IWA, throughput starts to matter for 20% central obscuration whatever the order

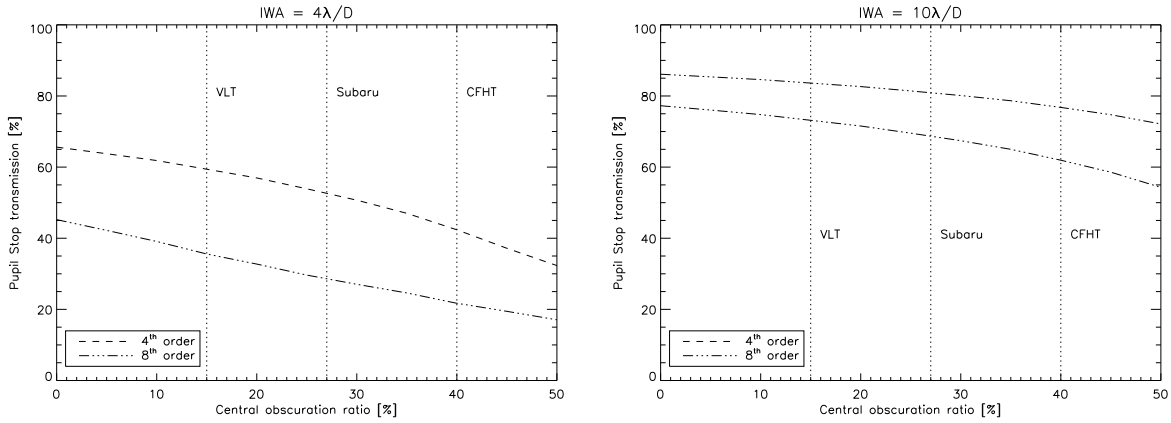

Figure 6.5: *Left*: Pupil stop throughput as function of the central obscuration ratio (linear) for a four and eight order mask function with IWA = 4 λ/D. *Right*: Same a the previous one with IWA = 10 λ/D

Again, high orders (eighth or higher) are poorly suited when the IWA is small ($4\lambda/D$, for instance). The example of the Subaru telescope shows that a fourth order pupil stop will have ~52% throughput while a eighth order will only reach ~28%. This results will actually be worse in reality since a pupil stop is necessarily reduced for spider vanes diffraction effects (see Sec. 6.3.2.0), chromatism (see Sec. 6.3.3), alignement and manufacturing issues.

Spider vanes impact

As discussed in Sivaramakrishnan et al. 2005 [86], the impact of the presence of spider vanes influences more BLs than APLC, since the additional diffracted light remaining in the geometrical relayed pupil is more diffused around the spider diffraction pattern while finely localized in the case of APLC. Hence, these effects require an additional reduction of the pupil stop collecting area around the spider vanes. Examples of pupil stop optimized for centrally obscured pupil with spider vanes will be shown in Sec. 6.4.

6.3.3 Spectral bandwidth impact

BLs are not highly chromatic as phase mask, for instance. However, pupil stop need to be optimized with respect to the spectral bandwidth in order to mitigate chromatic effects. The bandwidth of the mask is proportional to λ while the bandwidth of the pupil stop is independent of λ. Therefore, a combination of mask / Pupil stop will work at all wavelengths shorter than the one for which it was designed (but it only have optimum throughput at one wavelength). Given that, the pupil stop must be optimized to the longest wavelength considered for the application. In Fig. 6.6, we compare the impact of the spectral bandwidth ($R = \Delta\lambda/\lambda$) on the pupil stop throughput for a fourth and eighth order masks as function of the IWA of the mask. From these plots, we can derive some conclusion:

- The impact is independent of the order of the mask
- A re-optimization of the pupil stop w.r.t the spectral bandwidth is more critical for small IWA than large IWA
- For small IWA ($4\lambda/D$, for instance), the impact on the throughput is $\sim$ 5% for R = 20% and $\sim$ 10% for R = 50%.
- For large IWA ($8\lambda/D$, for instance), the impact on the throughput is $\sim$ 2% for R = 20% and $\sim$ 5% for R = 50%

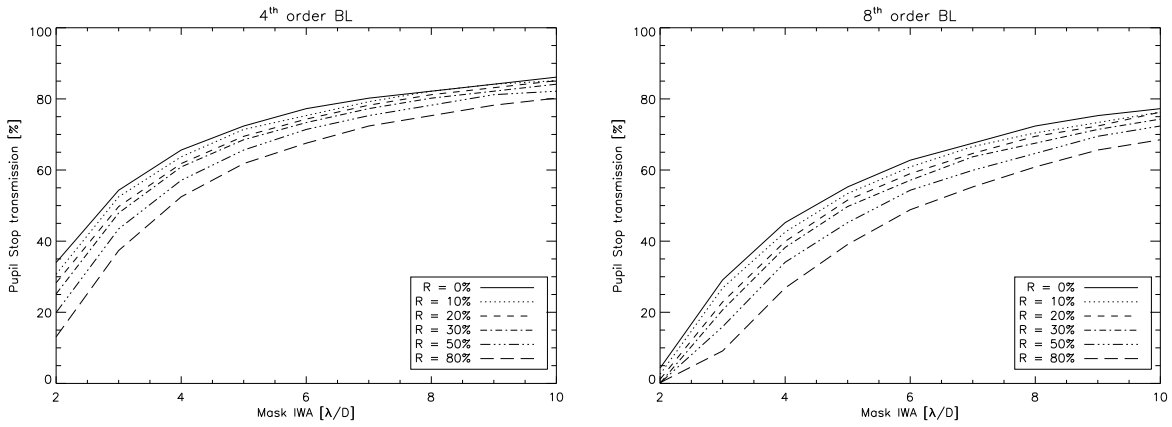

Figure 6.6: Pupil stop throughput as function of the spectral bandwidth for a four (*left*) and eight (*right*) order mask functions

6.4 An example: optimization for EPICS

As presented in Chapter 5.6, an optimization of coronagraphs in diffraction limited regime has been initiated in the context of EPICS. Here, we are dealing with the optimization of BLs. In Fig. 6.7, pupil designs are shown again, and we recall bellow the spectral bandwidth considered for this optimization:

- 0.8 μm ± 100 nm (R = 25%)
- 1.25 μm ± 100 nm (R = 16%)
- 1.6 μm ± 100 nm (R = 12.5%)

In Fig. 6.8 we show the evolution of the total rejection rate as a function of the pupil stop throughput for BL4 and BL8 with a $4.0\lambda/D$ fixed IWA. This simulation was done on the pupil design 5 (monochromatic simulations) and pupil stop are optimized to match the diffraction pattern (all starlight canceled). Curves clearly show that high

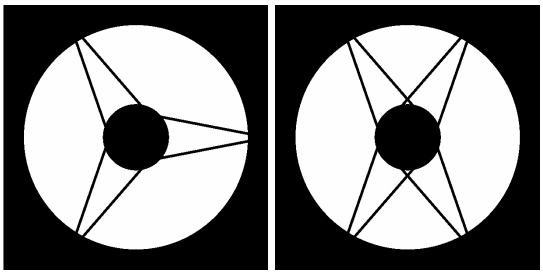

Figure 6.7: Two pupil designs proposed for the E-ELT differing by the configuration of the spider vanes

Table 6.1: Pupil stop throughput when optimized for design 1 and 5 with respect to the spectral bandwidth.

	Pupil stop throughput [%]			
	$IWA = 5$		$IWA = 10$	
R [%]	Design 1	Design 5	Design 1	Design 5
12.5	25.8	19.5	53.0	46.5
16	25.1	18.8	52.4	45.8
25	23.3	17.2	50.9	44.2

coronagraphic efficiency of a BL is strongly related to the pupil stop. From 20% pupil stop throughput BL4 and BL8 provide identical rejection. High rejection rate require very low throughput. Given that, for EPICS we revised some choice:

- We choose a 4^{th} order band-limited function
- Instead of a function as $1 - sinc(r)^2$ we adopt a $1 - sinc(r)$ a little bit more transmissive
- Two configuration have been defined: IWA = $5\lambda/D$ and IWA = $10\lambda/D$ to maximize pupil stop throughput
- Expected performance have been decreased to increase throughput (10^{-8} contrast at IWA for the $5\lambda/D$ configuration and under 10^{-10} contrast at IWA for the $10\lambda/D$ configuration)

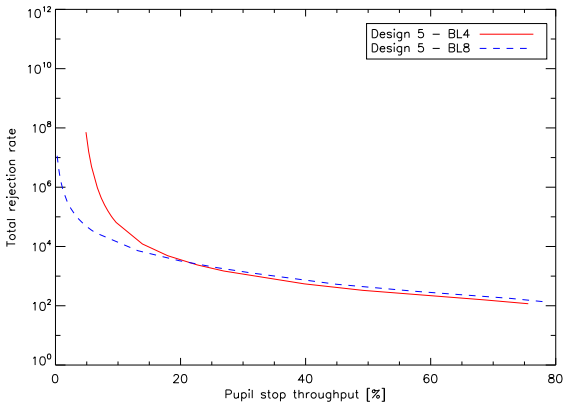

Figure 6.8: Pupil stop throughput behavior as function of the total rejection rate for a 4^{th} and 8^{th} order band-limited coronagraphs.

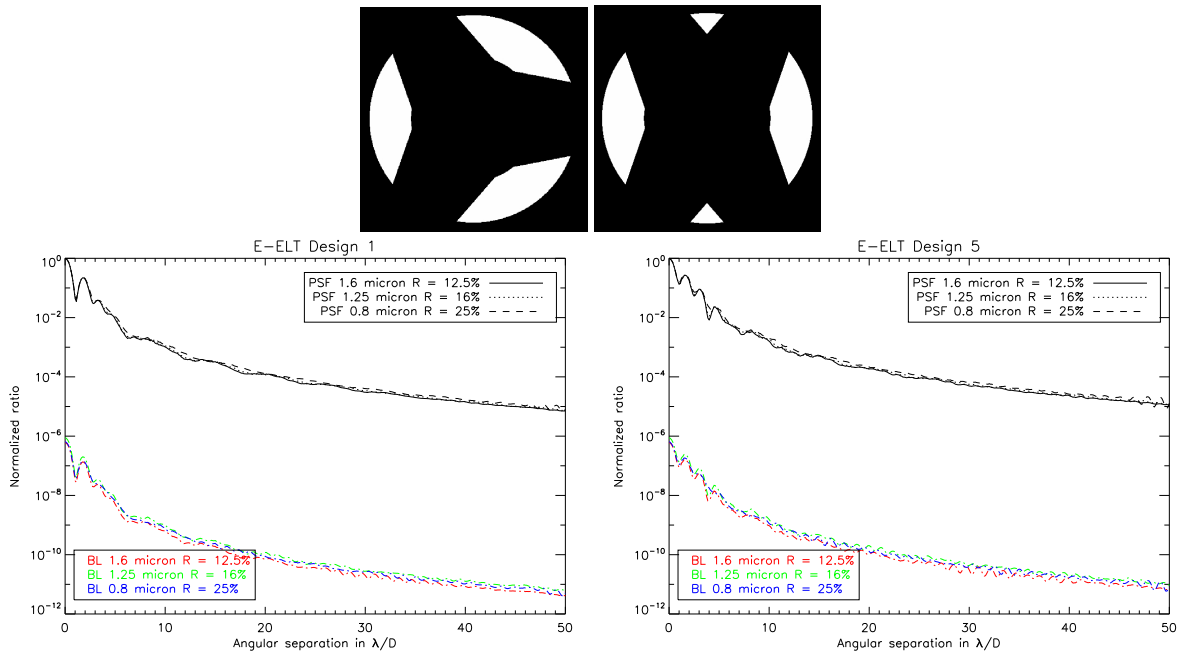

Figure 6.9: BL 4^{th} order in $5\lambda/D$ IWA configuration: *top left*: pupil stop for design 1, *top right*: pupil stop for design 5, *bottom left*: polychromatic coronagraphic PSFs (design 1), *bottom right*: polychromatic coronagraphic PSFs (design 5).

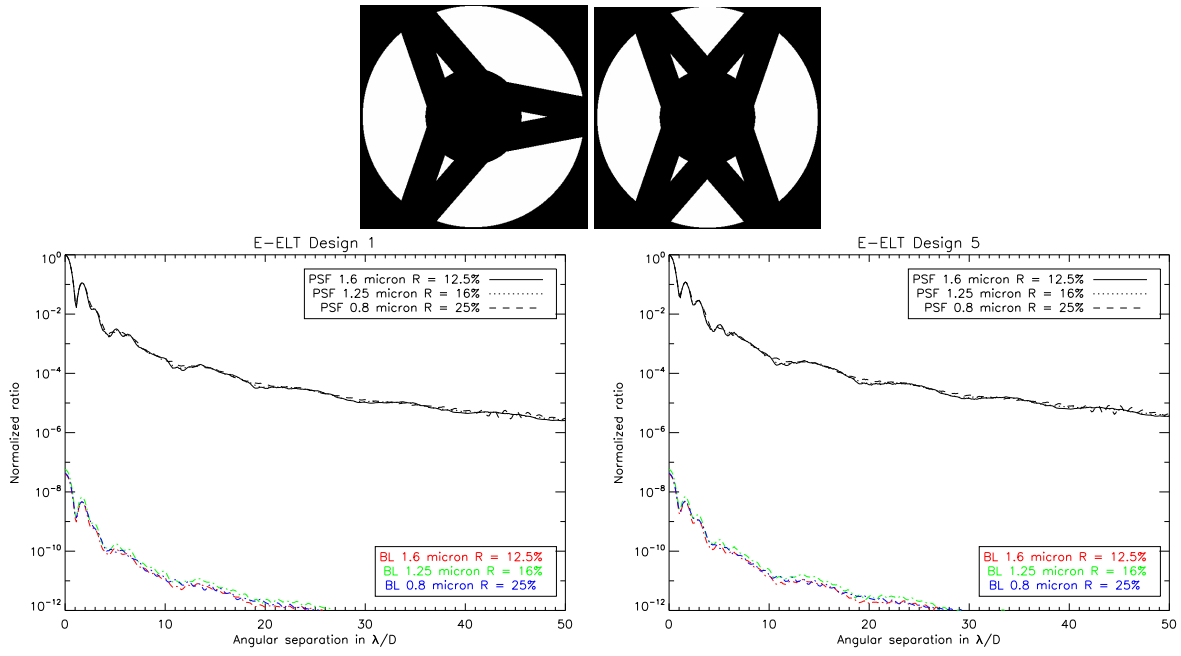

Figure 6.10: BL 4^{th} order in $10\lambda/D$ IWA configuration: *top left*: pupil stop for design 1, *top right*: pupil stop for design 5, *bottom left*: polychromatic coronagraphic PSFs (design 1), *bottom right*: polychromatic coronagraphic PSFs (design 5).

6.5 conclusion

This first analyzis in diffraction limited regime enables to underline that high order (higher than 4) BLs are poorly suited for ground-based observation with an ELT. Here, we only focus on the limitation imposed by the pupil stop optimization (throughput) and show that most of the ELT specificities such as the central obscuration or the spider vanes strongly drive this choice. Higher order than 4 should be relegated to situation where the IWA constraint can be largely relaxed and hence they are not favorable for exoplanet purpose. Of course, we can make the choice to support low-order aberration sensitivity (i.e higher order BLs) at a cost of throughput, nevertheless in that case pupil stop are quite abrupt (which is already the case for the 4^{th} order BL with $5\lambda/D$ IWA, see Fig. 6.9). In the precise case of BLs, an aggressive pupil stop will be problematic: even if it provides very deep contrast in perfect situation when phase aberrations are negligible (i.e Strehl = 100%) it is no longer the case in realistic condition, even at high Strehl ratio. This is obviously true for any concepts but the decrease of performance between the perfect and realistic situations is even more abrupt with the BL 8^{th} order (see Part. 8). On the other hand, in realistic conditions, an optimization of the pupil stop depends on the dominant source of noise (diffracted light or uncorrected atmospheric scattered light) and may potentially relax the shape and throughput of such device. However, through the next Chapters, this analyzis will be supported by comparison of 4^{th} and 8^{th} order BL when combining with AO system and differential imaging system (see Part. 8).

Part III

Preliminary system analysis

7

First order sensitivity analysis

Contents

Abstract - *It is very likely that any coronagraph will not provide directly a 10^{-10} contrast at close angular distance. Coronagraphs are not perfect even for those which are able to provide perfect starlight cancellation in idealistic simulations (as a result of intrinsic defects from manufacturing limitations, alignment issues...). Although a large number of coronagraphs that have been studied and developed for the last 10 years were designed to work on ground-based telescopes, limitations will be set by telescope aberrations, instrument aberrations and so on. The intent of this part is to start a simple sensitivity analysis of aberrations, pointing errors, telescope parameters in ideal conditions (without modeling turbulence nor a thorough instrument design). This first step will give a basis for coronagraphs sensitivity-order and initiates a first order of comparison for ground-based observations. Further investigations will be address in Chapter 8 and 9 where similar analysis will be performed when coronagraphs are combined either with an eXtreme Adaptive Optics system or a Differential Imaging system.*

Table 7.1: Parameters of coronagraphs optimized for a central obscuration of 30%. d is the Lyot focal mask diameter, ϵ the BL bandwidth parameter (m and l are complementary BL8 function parameters), lp is the AGPM topological charge and $\mathscr{T}$ the overall transmission.

Coronagraph type	Specifications		
	IWA (λ/D, ± 0.1)	$\mathscr{T}$ (%)	Parameters
FQPM	0.9	82.4	-
AGPM	0.9	82.7	lp=2
AIC	0.4	50.0	-
Lyot	3.9	62.7	$d = 7.5\lambda/D$
APLC	2.4	54.5	$d = 4.7\lambda/D$
APRC	0.7	74.5	$d = 1.06\lambda/D$
BL4	4.0	22.4	$\epsilon = 0.21$
BL8	4.0	13.8	$\epsilon = 0.6$, m=1, l=3
BM	×	38.0	Discovery space: 7 to $30\lambda/D$

7.1 Preamble

In this Chapter, we perform a first order sensitivity analysis of several coronagraph concepts presented in Chapter 2 to investigate the impact of major error sources that occur in a coronagraphic telescope (central obscuration, secondary supports, low-order segment aberrations, segment reflectivity variations, pointing errors, stellar angular size...). This analysis is performed in a perfect case (when only performance limitations are set by the studied parameters).

We consider, the following coronagraph concepts: Lyot coronagraph [Lyot], Apodized Pupil Lyot Coronagraph [APLC], Apodized Roddier & Roddier Coronagraph (i.e Dual zone) [APRC], Four Quadrant Phase Mask [FQPM], Annular Groove Phase Mask [AGPM], Band-limited [BL], Achromatic Interferometric Coronagraph [AIC] and a Binary pupil mask (shaped pupil coronagraph) [BM]. Coronagraphs parameter space is defined in Table 7.1.

In the whole Part III, we will consider the following metrics (defined in Chapter 4):

- Total rejection rate (τ)
- Peak rejection rate (τ_0)
- Azimuthally averaged contrast estimation ($\overline{\mathscr{C}}$): from 4 (IWA limit imposed) to $60\lambda/D$ except for BM which will be estimated in its discovery space (from 7 to $30\lambda/D$).

7.2 Four Quadrants Phase Mask - Annular Groove Phase Mask

7.2.1 Central obscuration

One of the main limitation of the FQPM/AGPM is its sensitivity to the central obscuration, since a significant part of the light diffracted by the central obscuration reappears in the relayed pupil. P. Riaud analytically evaluated the residual flux (F_r) in the relayed pupil resulting from the presence of a central obscuration:

$$F_r = \frac{R_{obs}^2}{R_{tel}^2 - R_{obs}^2} \tag{7.1}$$

where R_{tel} and R_{obs} represent the telescope radius and the telescope central obscuration radius respectively. For instance, the residual flux for the VLT configuration is 2% while for the E-ELT case (where the central obscuration is $\sim$ 30%), the residual flux is about 10%. This effect can be mitigates by adequately optimizing the Pupil stop: either by reproducing the shape of the entrance pupil assuming inner and outer diameter respectively oversized and undersized or by matching the complementary shape of the diffracted light in the pupil plane as discussed in Boccaletti 2004 [21]). However, since a significant part of the residual flux remains in the relayed pupil, this concept (FQPM and AGPM as well) can no longer yields to a perfect starlight cancellation (see right plot of Fig. 7.1, where the black curve (0% central obscuration) only reveals the residual numerical noise). In Fig. 7.1 (left), one can see that the impact on the peak (peak rejection rate) and on the halo (contrast evaluation) is identical. The effect on the coronagraphic PSF is actually an homogeneous-like up shift behavior (Fig. 7.1, right). For instance, by comparing the VLT and E-ELT central obscurations (14% and 30% respectively), one can see that an increase of 8% of the residual flux in the relayed pupil is responsible of one order of magnitude performance degradation.

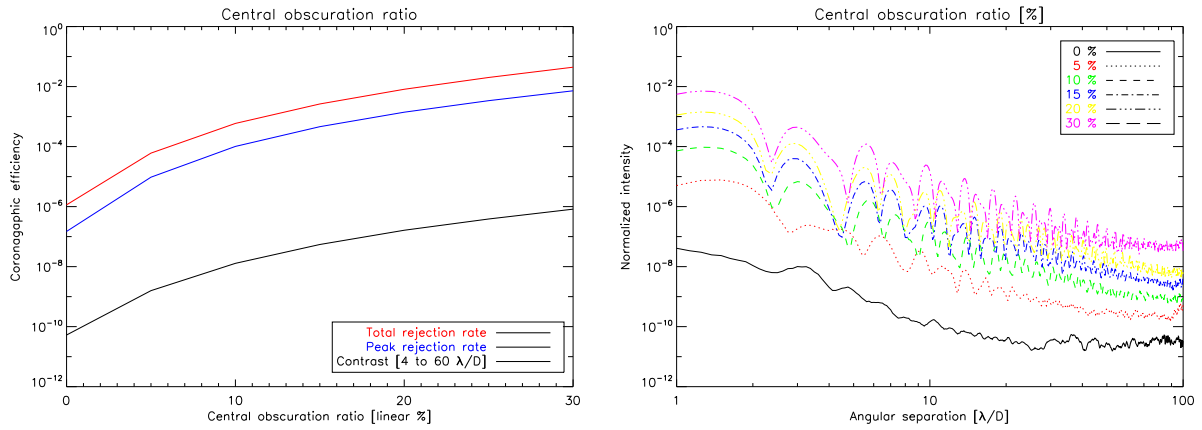

Figure 7.1: FQPM/AGPM sensitivity to the central obscuration ratio - *left*: impact on the coronagraphic efficiencies, *right*: impact on the coronagraphic PSF.

7.2.2 Spider vanes

Owing to an optimization of the pupil stop regarding to the presence of the spider vanes in the entrance aperture, their impact on the coronagraphic efficiency can be largely mitigates (see Fig. 7.2).

7.2.3 Segment reflectivity

In diffraction limited regime, the segment-to-segment reflectivity variation has no effect on the performance of the FQPM/AGPM, even for a high value (10%). However, this is no longer true when the central obscuration ratio is equal to 0% (i.e full-filled pupil). In such a case, performance are theoretically perfect and hence segment-to-segment reflectivity matters. In the precise case of 30% central obscuration ratio, the central obscuration itself sets the limitation.

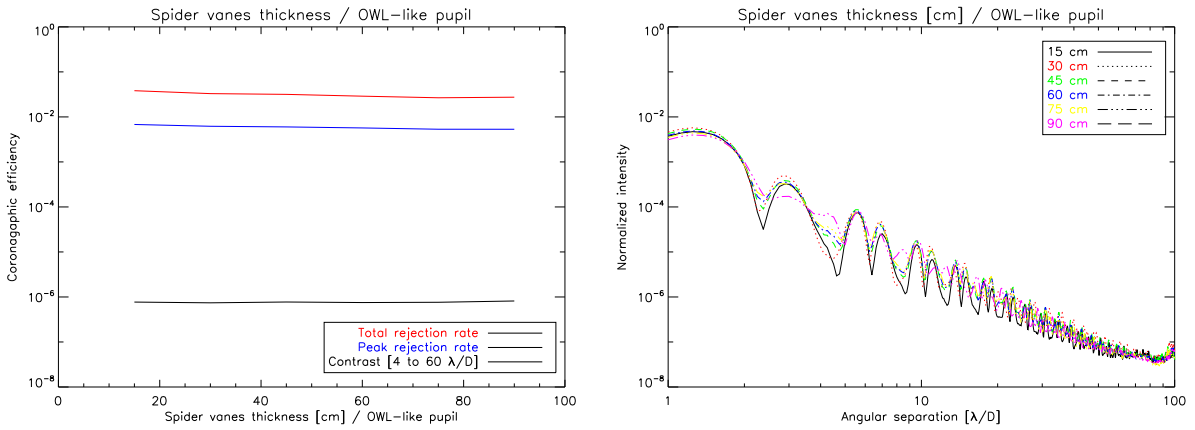

Figure 7.2: FQPM/AGPM sensitivity to the spider vanes thickness (OWL-like pupil as a baseline) - *left*: impact on the coronagraphic efficiencies, *right*: impact on the coronagraphic PSF.

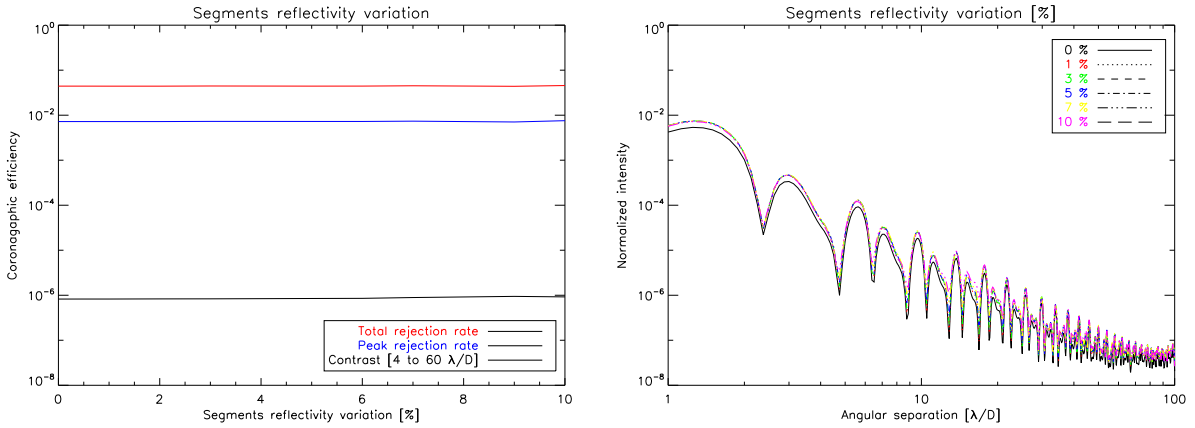

Figure 7.3: FQPM/AGPM sensitivity to the segment reflectivity - *left*: impact on the coronagraphic efficiencies, *right*: impact on the coronagraphic PSF.

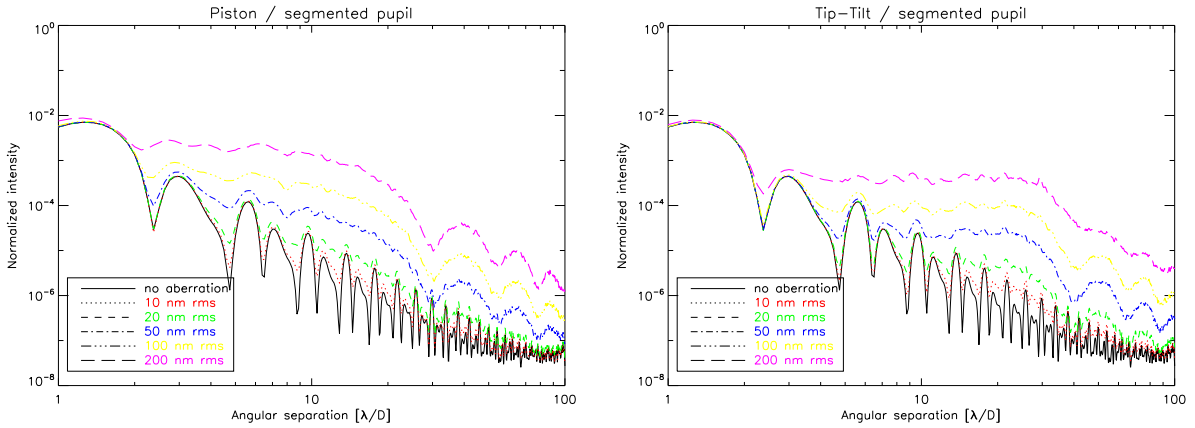

Figure 7.4: FQPM/AGPM sensitivity to low-order aberrations (piston and tip-tilt here) through their impact on the coronagraphic PSF.

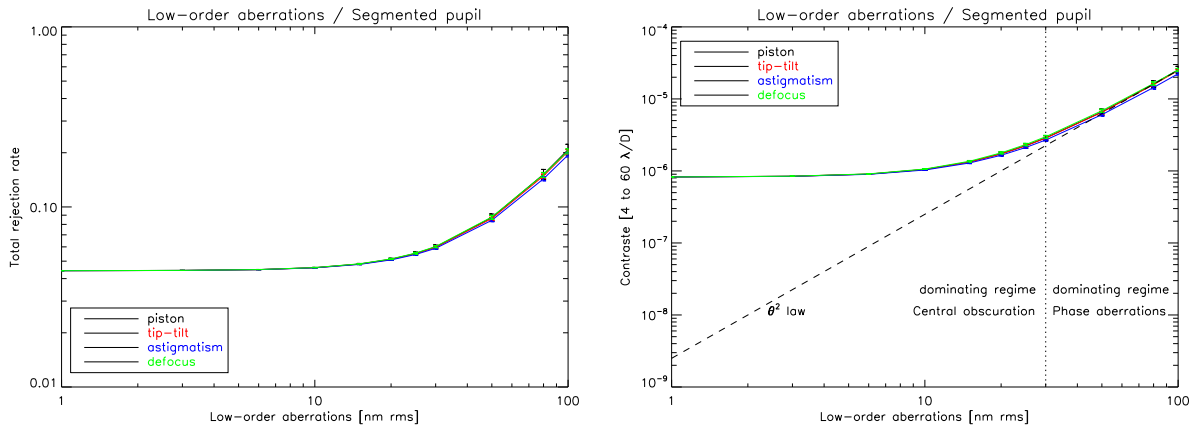

Figure 7.5: FQPM/AGPM sensitivity to low-order aberrations - *left*: impact on the total rejection rate, *right*: impact on the coronagraphic halo. 10 phase aberrations realizations have been used in simulations.

7.2.4 Segment static aberrations

In the following (which is ever true for any forthcoming coronagraph analysis of the Chapter III), phase aberrations have been considered until a very high amplitude value for the sake of clarity. Obviously, when operating on a telescope, phase aberrations will not be that high and will be AO-corrected as well.

Segment aberrations degrade performance much larger on the halo than on the peak (Fig. 7.4, bottom left and right). This is a consequence of the principal frequency (first order diffraction) of segment halos where speckles will appear. This principal frequency is on the order of the ratio of the pupil diameter by a segment width (42/1.5 = 28 in λ/D units). This results is actually not really the best favorable case when one aims at detecting companions at some λ/D from the on-axis star. It shows the critical importance of controlling and reducing static aberrations level.

In Fig. 7.4 (left and right), impact of segment aberrations (piston, tip-tilt, defocus and astigmatism) are plotted as a function of the total rejection rate (left) and contrast in the halo (right). Most of these low-order aberrations have roughly the same impact on performance. Two regimes can be identified:

- The first one where curves are about flat, where the central obscuration (30%) is the dominant source of limitation (before $30\lambda/D$, see Fig. 7.5 (right) where the dotted line identify these two regimes).
- The second one where the phase aberrations are the dominant source of limitation (above $30\lambda/D$, curves are decreasing). For this later, the sensitivity of the AGPM/FQPM follows a quadratic dependency (illustrated by the dashed line in Fig. 7.5, right).

7.2.5 Pointing errors

The range of the offset pointing we considered does not really impact FQPM/AGPM coronagraphic performance (Fig. 7.6). The limitation is actually again set by the central obscuration.

7.2.6 Stellar angular size

The rejection factor due to a partially resolved star has been defined in Riaud et al. 2001 [79] by:

$$\tau(r) = \frac{r^2}{2}\left[\int_0^r (1 - exp(-r^2/1.16))rdr\right]^{-1} \tag{7.2}$$

As a result, the impact of the stellar angular size can be estimated for the FQPM/AGPM. In Fig.7.7, the impact seems to be important only above 0.1 λ/D. The reason is that the limitation is mostly imposed by the central obscuration (30%) when the stellar size is small. In other words, FQPM/AGPM appears insensitive to the stellar

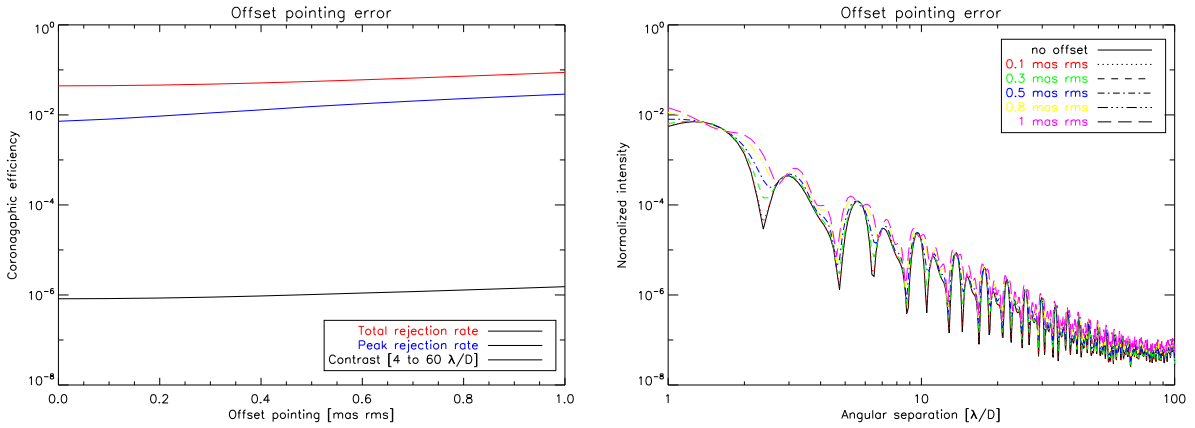

Figure 7.6: FQPM/AGPM sensitivity to the offset pointing errors - *left*: impact on the coronagraphic efficiencies, *right*: impact on the coronagraphic PSF

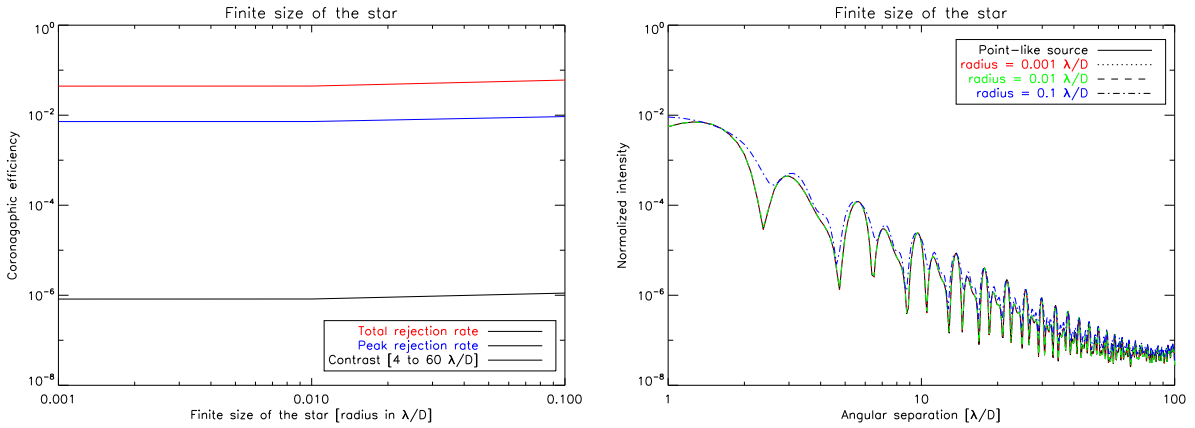

Figure 7.7: FQPM/AGPM sensitivity to the stellar angular size - *left*: impact on the coronagraphic efficiencies, *right*: impact on the coronagraphic PSF

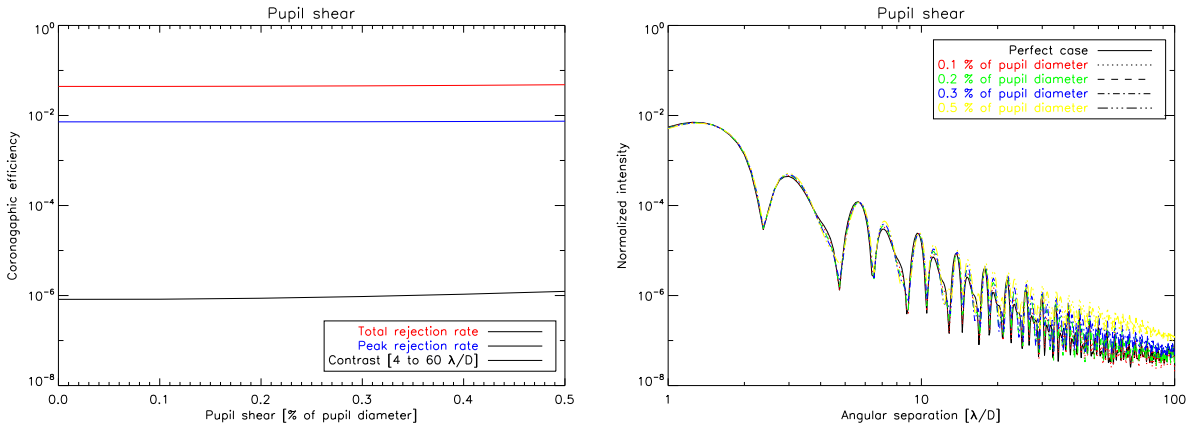

Figure 7.8: FQPM/AGPM sensitivity to the misalignment of the pupil stop - *left*: impact on the coronagraphic efficiencies, *right*: impact on the coronagraphic PSF.

angular size until $0.1\lambda/D$ because the limit sets by the 30% central obscuration ratio impact is dominant. For instance, in the case of a full-filled pupil (hence performance in ideal case yield to a perfect cancellation of a point-like on-axis source), the limit on the total rejection rate sets by a 0.1 λ/D resolved object is ~236 instead of a perfect rejection.

7.2.7 Pupil shear

Alignment of the pupil stop only matters performance at large angular distance (above 30 λ/D) with a tiny impact indeed. This impact can be mitigates for any coronagraph by relaxing constraints on the optimization of the pupil stop shape. Simulation presented here assumes the diffracted light as the source of noise while in realistic conditions (on ground-based observations), sensitivity of the pupil shear will varies upon the dominant source of noise (either the diffraction light or the uncorrected atmospheric speckles).

7.3 Achromatic Interferometric Coronagraph

The AIC is intrinsically advantageous since performance does not depend on the pupil telescope characteristics such as the central obscuration or the secondary support as long as the pupil remains centro-symmetric. And even with non-centro-symmetric secondary supports geometry, by using a suitable mask in an intermediate pupil plane, vignetting effect can be avoided by restoring a centro-symmetric distribution in the pupil plane.

7.3.1 Segment reflectivity

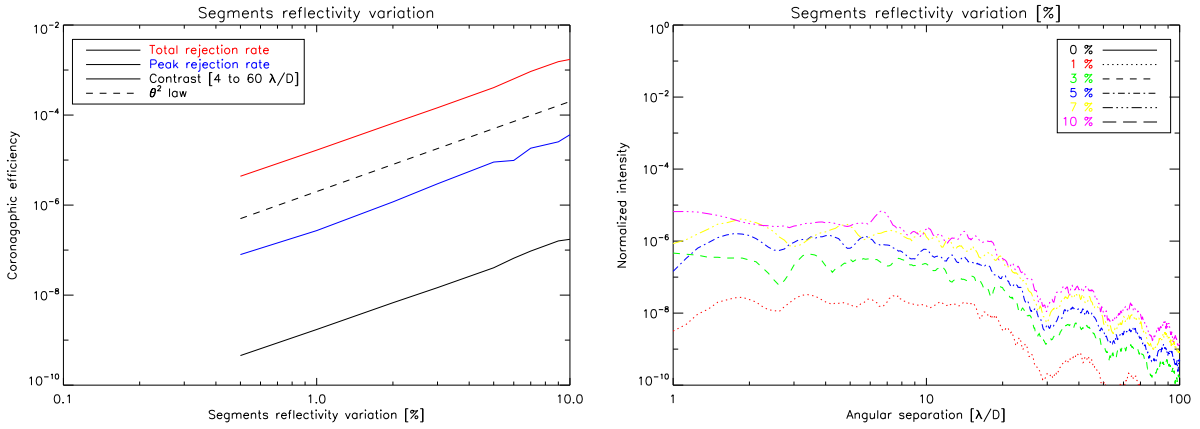

Figure 7.9: AIC sensitivity to the segment reflectivity - *left*: impact on the coronagraphic efficiencies, *right*: impact on the coronagraphic PSF.

Since AIC yields to perfect starlight cancellation even with a 30% central obscured telescope pupil, unlike AGPM/FQPM, segment to segment reflectivity variations matters. From the core of the PSF to $20\lambda/D$ (Fig. 7.9, right), contrasts are set to 10^{-8} only with 1% segment reflectivity (ptv). 5% (ptv, i.e $\sim$ 1.4% rms) sets contrasts at 10^{-6} until $20\lambda/D$ and to 10^{-8} above. Therefore, the effect is non-negligeable for the AIC. As described with arbitrary value in Fig. 7.9 (left), AIC has a quadratic dependency to segment reflectivity variations, where θ is the amplitude of the reflectivity in % ptv.

7.3.2 Segment static aberrations

In Fig. 7.10, impact of phase aberrations on a segmented pupil is presented. The perfect case (no aberrations, black curve) yield to perfect extinction (under 10^{-10} contrast). As a small IWA concept, AIC is highly sensitive to phase aberrations: 10 nm rms tip-tilt limits contrasts from IWA to $30\lambda/D$ at $\sim 10^{-6}$. Above $30\lambda/D$, contrasts are set to $\sim 10^{-7} - 10^{-8}$. Controlling and reducing for these static aberrations is therefore an issue for the AIC.

In Fig. 7.11 (left and right), impact of segment aberrations (piston, tip-tilt, defocus and astigmatism) is plotted as a function of the total rejection rate (left) and contrast estimation in the halo (right). Most of these low-order aberrations have the same impact on performance (simulations toke into account 10 different realizations of aberrations, error bars are plotted as well). In each case, the AIC sensitivity to segment phase aberrations follows a quadratic dependency that can be expresed as:

$$\tau(\theta) = 2.5\ 10^{-5} \times \theta^2 \tag{7.3}$$

$$\overline{\mathscr{C}(\theta)} = 2.5\ 10^{9} \times \theta^2 \tag{7.4}$$

where θ is the low-order phase aberrations amplitude in nm rms.

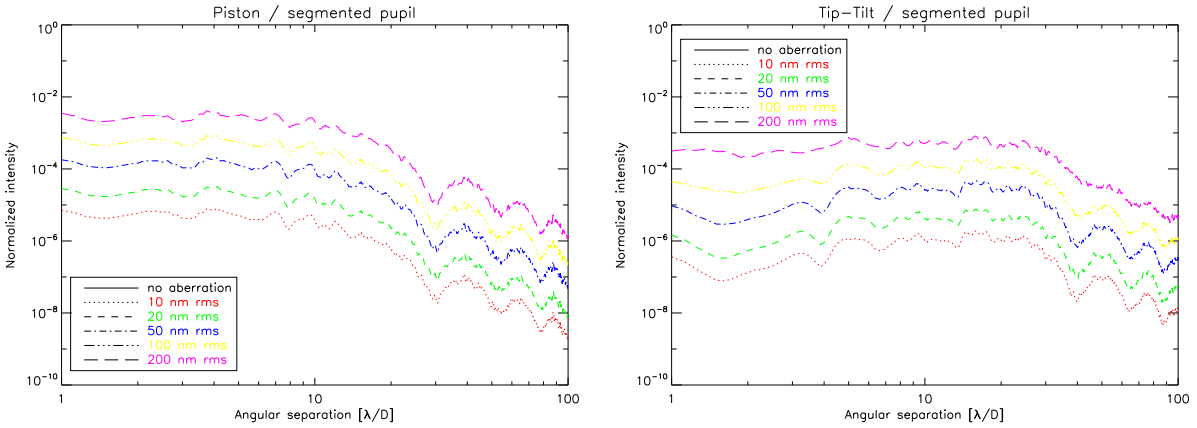

Figure 7.10: AIC sensitivity to low-order aberrations (piston and tip-tilt here) - impact on the coronagraphic PSF.

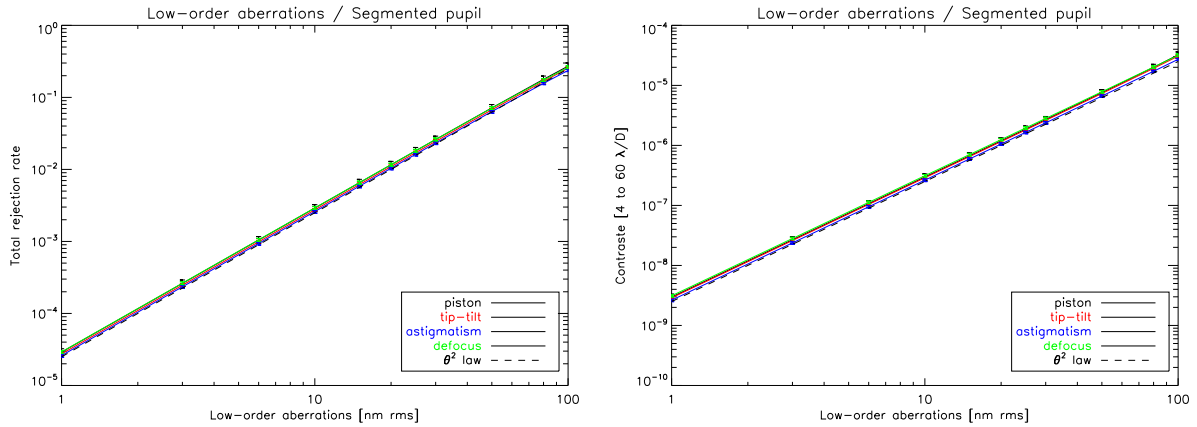

Figure 7.11: AIC sensitivity to low-order aberrations - *left*: impact on the total rejection rate, *right*: impact on the coronagraphic halo.

7.3.3 Pointing errors

Like every small IWA concepts, the AIC suffers from its sensitivity to pointing errors (Fig. 7.12, top). For instance, 0.1 mas rms pointing error (direct translation of the SPHERE requirements to the E-ELT case) decreases AIC performance from infinite contrast to 10^{-3} on the peak, 10^{-6} at $10\lambda/D$ and 10^{-8} at $30\lambda/D$. AIC has a quadratic power-law dependency to pointing errors:

$$\tau(\theta) = 0.16 \times \theta^2 \tag{7.5}$$

$$\overline{\mathscr{C}(\theta)} = 3.3\ 10^{-6} \times \theta^2 \tag{7.6}$$

where θ is the offset pointing error amplitude in mas rms.

7.3.4 Stellar angular size

Like for the offset pointing effect, AIC has a quadratic power-law dependency to the stellar angular size: In Fig. 7.12, the impact of the resolution of the star is plotted as a function of some metrics (left) while the right plot shows coronagraphic PSFs. One can see the huge degradation of performance (with point-like source the AIC yields to a perfect starlight cancellation).

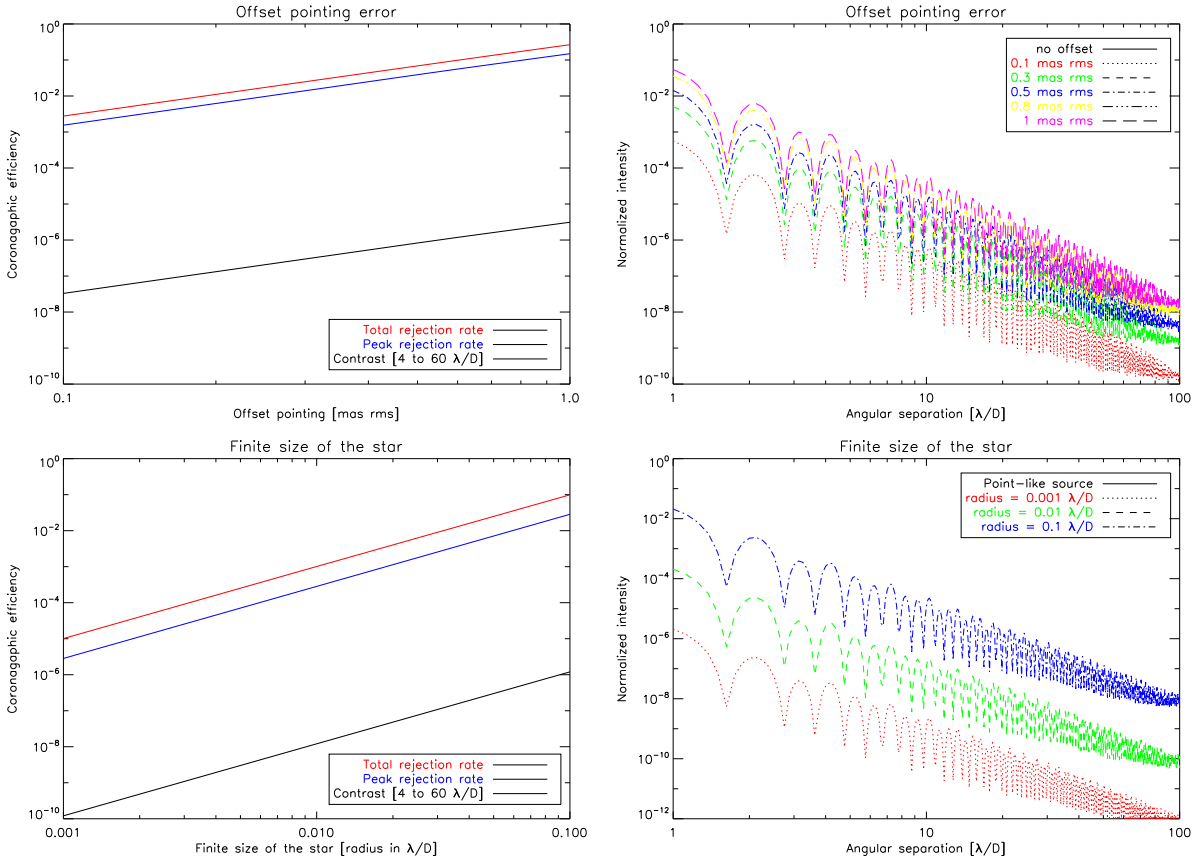

Figure 7.12: AIC sensitivity to offset pointing errors (top) and the stellar angular size (bottom) - *left*: impact on the coronagraphic efficiencies, *right*: impact on the coronagraphic PSF.

7.4 Apodized Pupil Roddier Coronagraph

The Apodized Pupil Roddier Coronagraph (Dual zone) has like the AIC, the advantage of being insensitive to the presence of the central obscuration. However, as all the small IWA concepts, the APRC suffers from its sensitivity to phase aberrations, pointing errors and stellar angular size.

7.4.1 Spider vanes

In theory, the APRC does not require more than a pupil stop like the entrance pupil. However, simulations presented hereafter, revealed a non negligible impact on performance when spider vanes thickness increase. From 15 cm to 90 cm, two orders of magnitude have been lost. Assuming a typical value for the E-ELT (60 cm), contrasts would be severely restricted. However, these results can be largely mitigates by oversizing the spider vanes thickness in the pupil stop at the cost of slightly degrade throughput.

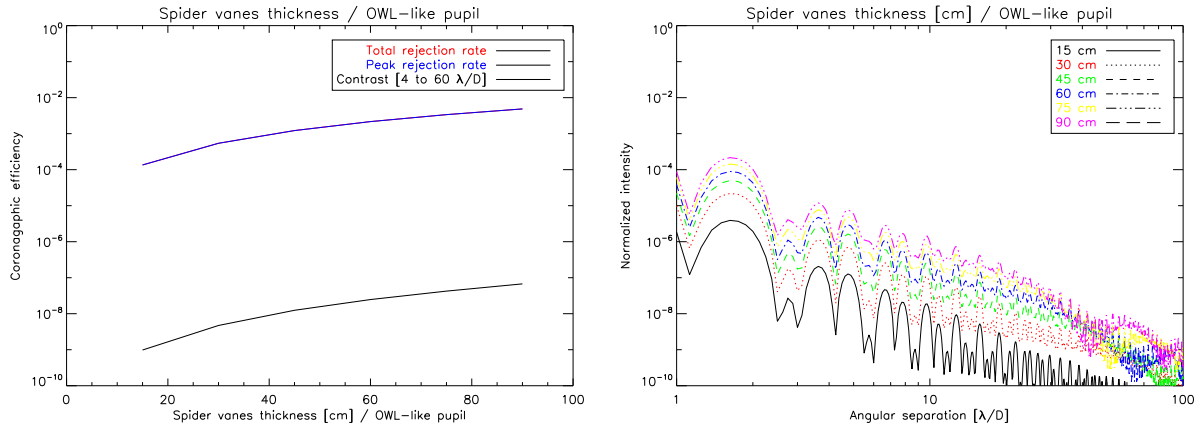

Figure 7.13: APRC sensitivity to the spider vanes thickness (OWL-like pupil as a baseline) - *left*: impact on the coronagraphic efficiencies, *right*: impact on the coronagraphic PSF.

7.4.2 Segment reflectivity

As the AIC, the APRC yield to perfect starlight cancellation even with a 30% central obscured telescope pupil, and therefore, unlike AGPM/FQPM segment to segment reflectivity matters. From the core of the PSF to $20\lambda/D$ (Fig. 7.14, right), contrasts are set to $\sim 10^{-8}$ when only 1% segment reflectivity (ptv) is considered. 5% (ptv, i.e $\sim 1.4\%$ rms) sets contrasts at $10^{-6} - 10^{-7}$ until $20\lambda/D$ and to $10^{-8} - 10^{-9}$ above. Therefore, the effect is non-negligeable for the APRC as for the AIC. As described with arbitrary values in Fig.7.14 (left, where θ is the amplitude of the reflectivity in % ptv), APRC has a quadratic power-law dependency to segment reflectivity variations.

7.4.3 Segment static aberrations

In Fig. 7.15, impact of segment phase aberrations is presented. The perfect case (no aberrations, black curve) yields to perfect extinction (under 10^{-10} contrast). As a small IWA concept, APRC is highly sensitive to phase aberrations: 10 nm rms tip-tilt limits contrasts from IWA to $30\lambda/D$ to $\sim 10^{-6} - 10^{-7}$. Above $30\lambda/D$, contrasts are set to $\sim 10^{-7} - 10^{-8}$. Controlling and reducing for these static aberrations is an issue for the APRC. In Fig. 7.11 (left and right), impact of segment aberrations (piston, tip-tilt, defocus and astigmatism) is plotted as a function of the total rejection rate (left) and contrast estimation in the halo (right). Most of these low-order aberrations have roughly the same impact on performance (simulations toke into account 10 different realizations of aberrations, error bars are plotted as well). In each case, the APRC sensitivity to segment phase aberrations follows a quadratic power-law:

$$\tau(\theta) = 10^{-6} \times \theta^2 \tag{7.7}$$

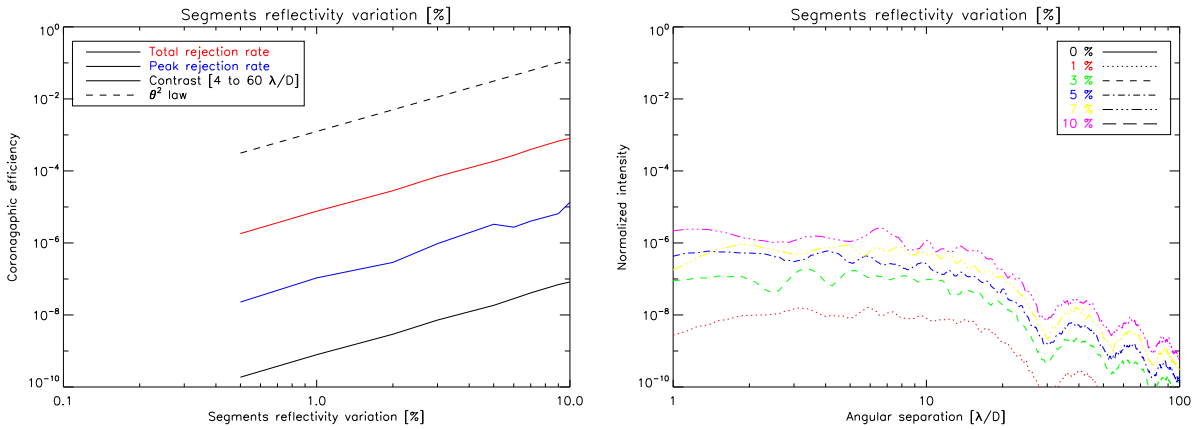

Figure 7.14: APRC sensitivity to the segment reflectivity - *left*: impact on the coronagraphic efficiencies, *right*: impact on the coronagraphic PSF.

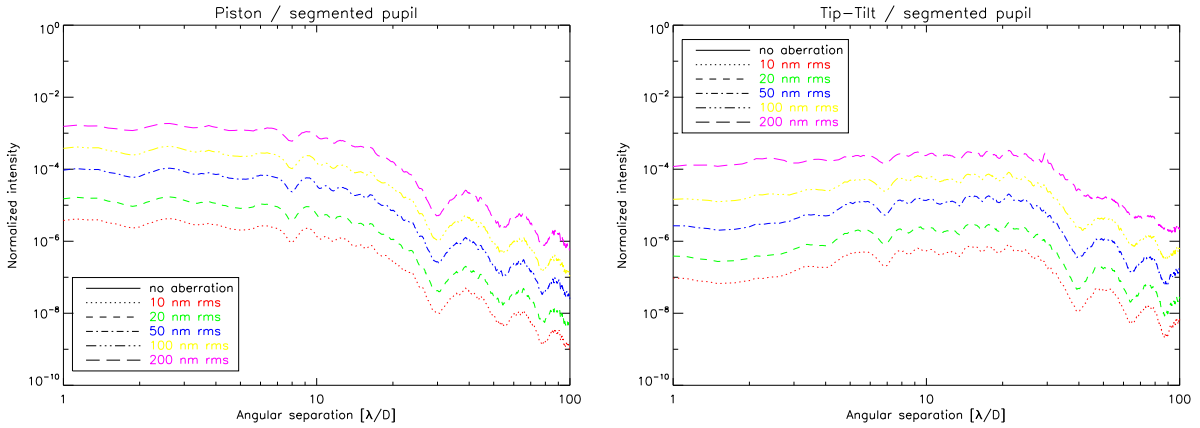

Figure 7.15: APRC sensitivity to low-order aberrations (impact on the coronagraphic PSF for piston and tip-tilt only).

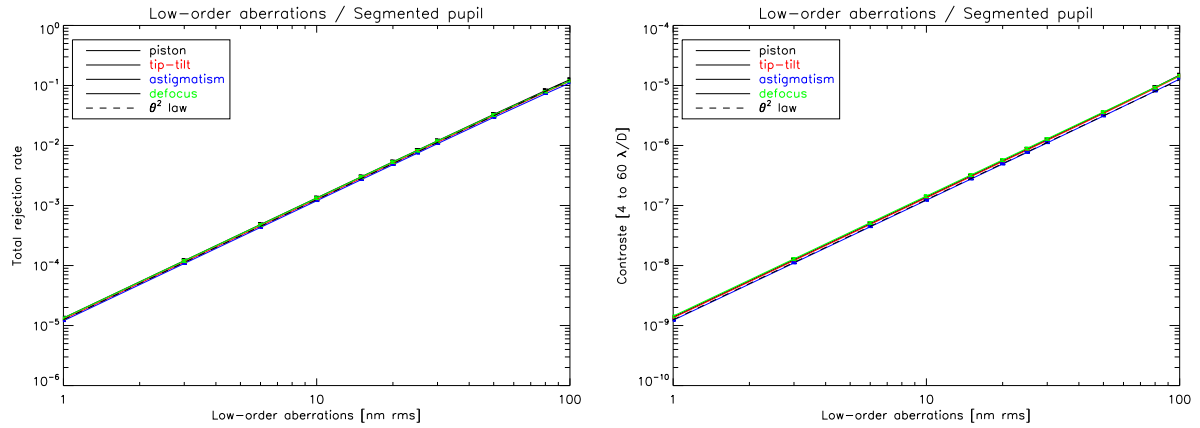

Figure 7.16: APRC sensitivity to low-order aberrations - *left*: impact on the total rejection rate, *right*: impact on the coronagraphic halo.

$$\overline{\mathscr{C}(\theta)} = 10^{-9} \times \theta^2 \tag{7.8}$$

where θ is the phase aberration amplitude in nm rms.

7.4.4 Pointing errors

Like every small IWA concepts, the APRC suffers from its sensitivity to pointing errors (Fig. 7.17, top). For instance, 0.1 mas rms pointing error (direct translation of the SPHERE requirements to the E-ELT case) decreases APRC performance from infinite contrast to $\sim 10^{-4}$ on the peak, $\sim 10^{-7}$ at $10\lambda/D$ and 10^{-8} at $30\lambda/D$. APRC has a quadratic power-law dependency (see Fig. 7.17, top left):

$$\tau(\theta) = 4.10^{-2} \times \theta^2 \tag{7.9}$$

$$\overline{\mathscr{C}(\theta)} = 4.10^{-7} \times \theta^2 \tag{7.10}$$

where θ represent the offset pointing amplitude in mas rms.

7.4.5 Stellar angular size

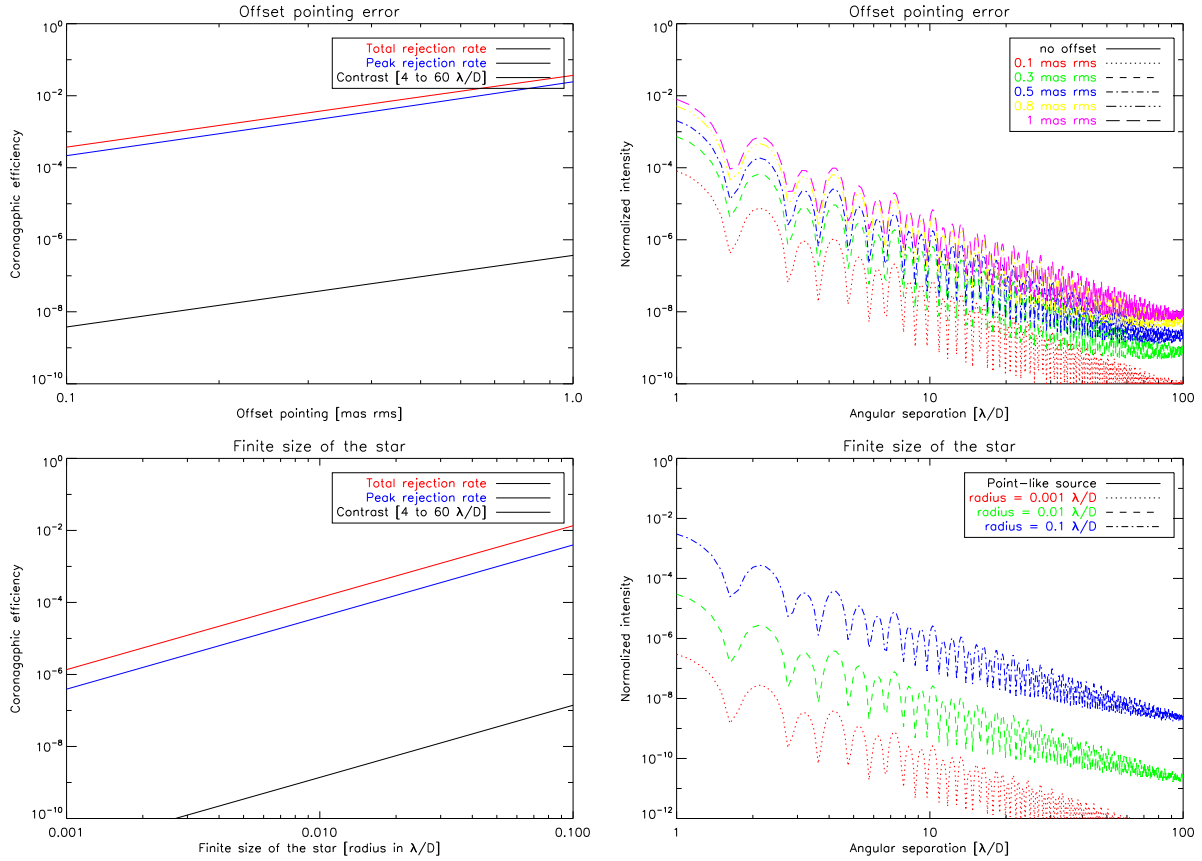

Figure 7.17: APRC sensitivity to offset pointing errors (top) and the stellar angular size (bottom) - *left*: impact on the coronagraphic efficiencies, *right*: impact on the coronagraphic PSF.

Like for the offset pointing effect, APRC has a quadratic dependency to the stellar angular size:

$$\tau(\theta) = 0.9 \times \theta^2 \tag{7.11}$$

$$\overline{\mathscr{C}(\theta)} \sim 3.3\ 10^{-7} \times \theta^2 \tag{7.12}$$

where θ represent the stellar radius in λ/D. In Fig. 7.17 (bottom), the impact of the resolution of the star is plotted as a function of some metrics (left) while in the right plot shows coronagraphic PSFs. One can see the huge degradation of performance (with point-like source the APRC yield to a perfect starlight cancellation).

7.4.6 Pupil shear: pupil stop alignment

The misalignment of the pupil stop ranges from 0.1 to 0.5 % of the pupil diameter. The APRC sensitivity to this error source is following a quadratic power-law as described in Fig. 7.18 where the dashed line describes the evolution of a θ^{-2} law.

$$\tau(\theta) = 1.6\ 10^{-2} \times \theta^2 \tag{7.13}$$

$$\overline{\mathscr{C}(\theta)} = 1.2\ 10^{-6} \times \theta^2 \tag{7.14}$$

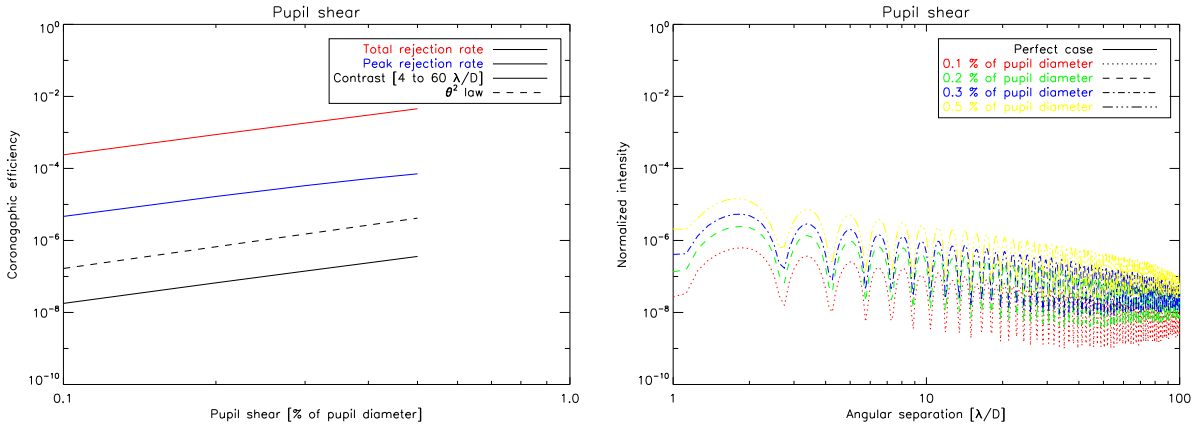

Figure 7.18: APRC sensitivity to the misalignment of the pupil stop - *left*: impact on the coronagraphic efficiencies, *right*: impact on the coronagraphic PSF.

7.5 Lyot Coronagraph

In the following, the Lyot coronagraph has a mask diameter of $7.5\lambda/D$. Its IWA is therefore much larger than for phase mask (e.g AGPM). Hence, its sensitivity to pointing errors and aberrations will therefore be less critical.

7.5.1 Central obscuration

Performance are not really sensitive to the central obscuration ratio (Fig. 7.19, left and right). It is actually only a matter of pupil stop optimization. Assuming an adequate optimized pupil stop, Lyot coronagraphs can be implemented even with large central obscured telescope apertures.

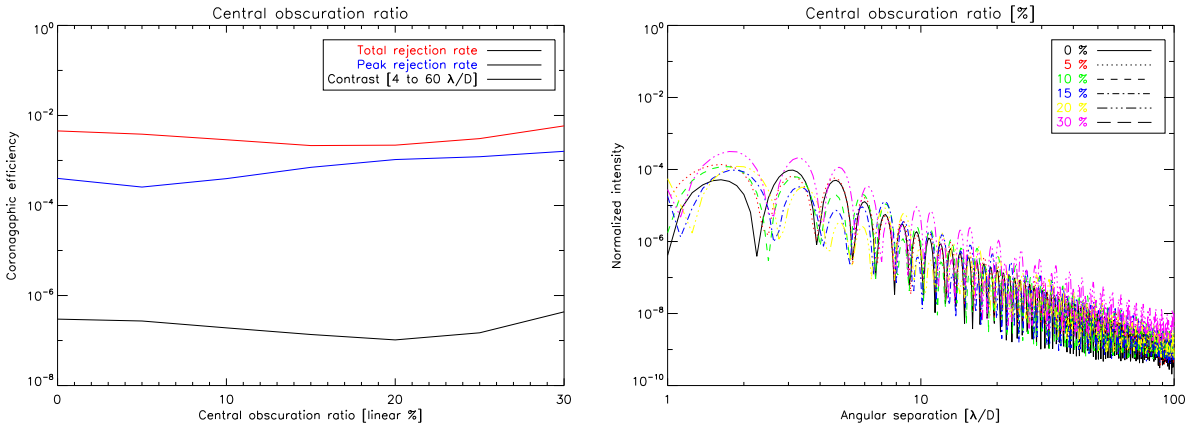

Figure 7.19: Lyot sensitivity to the central obscuration ratio - *left*: impact on the coronagraphic efficiencies, *right*: impact on the coronagraphic PSF.

7.5.2 Spider vanes

Like for the central obscuration ratio, assuming a dedicated optimized pupil stop taking into account the presence of the spider vanes in the pupil aperture, this parameter is not critical.

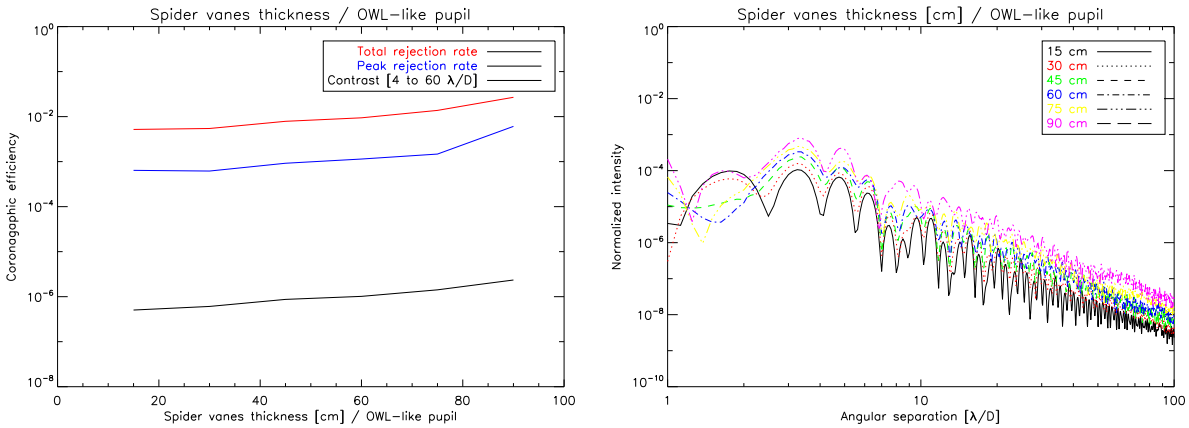

Figure 7.20: Lyot sensitivity to the spider vanes thickness (OWL-like pupil as a baseline) - *left*: impact on the coronagraphic efficiencies, *right*: impact on the coronagraphic PSF.

7.5.3 Segment reflectivity

Segment reflectivity has no impact on the Lyot performance (Fig. 7.21). This results only reveals that performance of the Lyot are not deep enough to reach the level of contrast where the reflectivity of segments starts to matter.

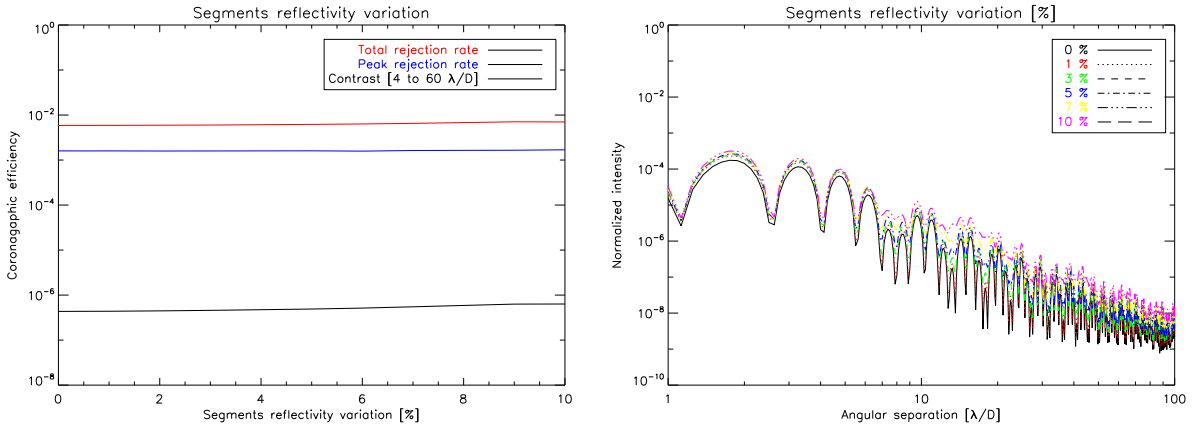

Figure 7.21: Lyot sensitivity to the segment reflectivity - *left*: impact on the coronagraphic efficiencies, *right*: impact on the coronagraphic PSF.

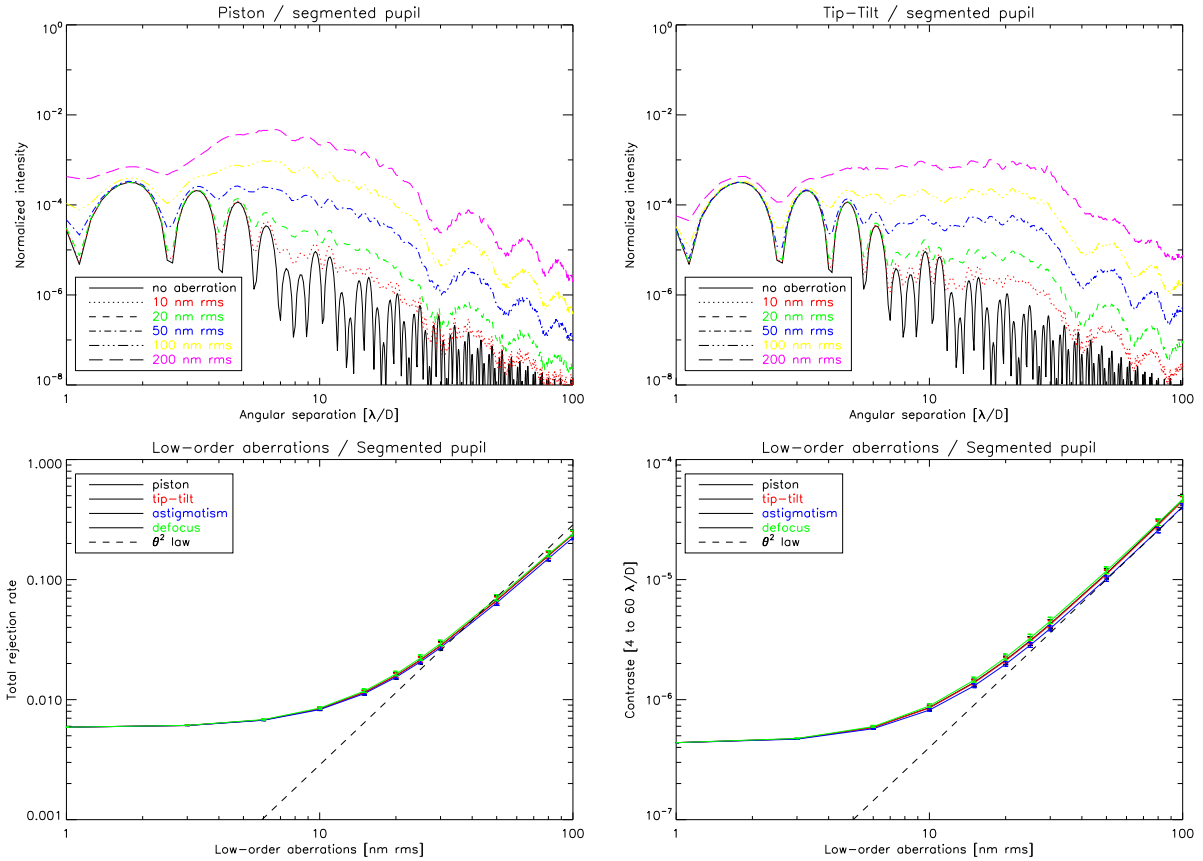

Figure 7.22: Lyot sensitivity to low-order aberrations (piston and tip-tilt here) - Top - impact on the coronagraphic PSF. - Bottom - *left*: impact on the total rejection rate, *right*: impact on the coronagraphic halo.

7.5.4 Segment static aberrations

The impact of phase aberrations on a segmented pupil is described in Fig.7.22, top left and right. Although the large focal mask diameter, segments aberrations highly degrades performance on the halo. This is a consequence of the principal frequency (first order diffraction) of segment halos where speckles appear (28 in λ/D units). This result actually shows the critical importance at controlling and reducing for these segment static aberrations.

In Fig. 7.22 (bottom left and right), impact of segment aberrations (piston, tip-tilt, defocus and astigmatism) is plotted as a function of the total rejection rate (left) and contrast in the halo (right). Most of these low-order aberrations have the same impact on performance. Two regimes can be identified:

- The first one where curves are about flat, where the central obscuration (30%) is the dominant source of limitation (before $20\lambda/D$).
- The second one where the segment phase aberrations are the dominant source of limitation (above $20\lambda/D$, where curve are decreasing). For this later, the sensitivity of the Lyot follows a quadratic power law (illustrated by the dashed line in Fig. 7.22, bottom, where θ represent the amplitude of aberrations in nm rms).

7.5.5 Pointing errors

Owing to the large Lyot mask (7.5 λ/D in diameter), the Lyot is not sensitive to pointing errors (assuming the range of values we used in simulation).

7.5.6 Stellar angular size

As for the pointing error, the Lyot coronagraph (assuming the configuration we used, i.e mask diameter) is quite favorable for observing large angular size sources. However, this results must be mitigates by the fact that this ability at working well with a large range of resolved sources is balance by a non-accessibility to very close region around the star (IWA). The Lyot coronagraph does not allow observation in the very close environment of the star which is detrimental for a large topics of planet finder.

7.5.7 Pupil shear: pupil stop alignment

In Fig. 7.24, impact of the pupil shear is analyzed with performance metrics (left) and with coronagraphic PSF (right). Assuming the range of pupil shear (until 0.5% of the pupil diameter), not impact on the Lyot performance has been revealed.

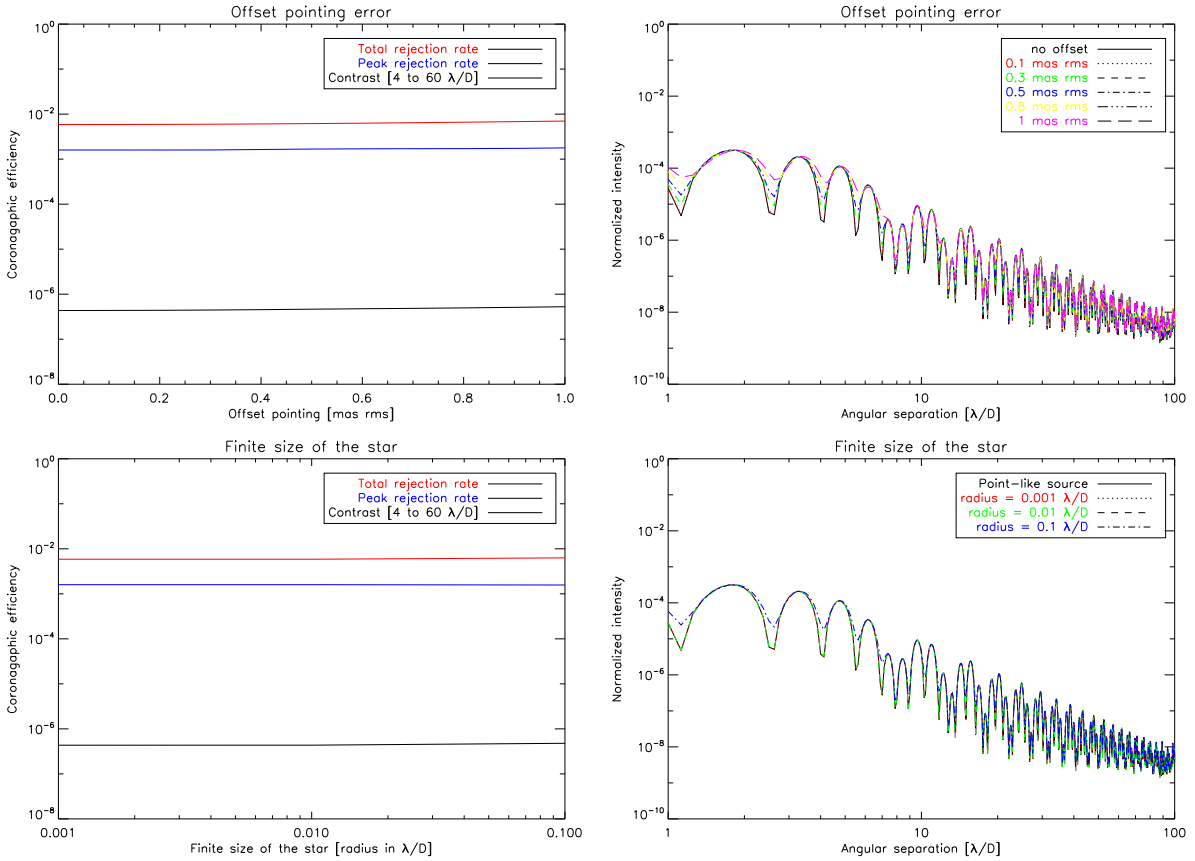

Figure 7.23: Lyot sensitivity to offset pointing errors (top) and the stellar angular size (bottom) - *left*: impact on the coronagraphic efficiencies, *right*: impact on the coronagraphic PSF.

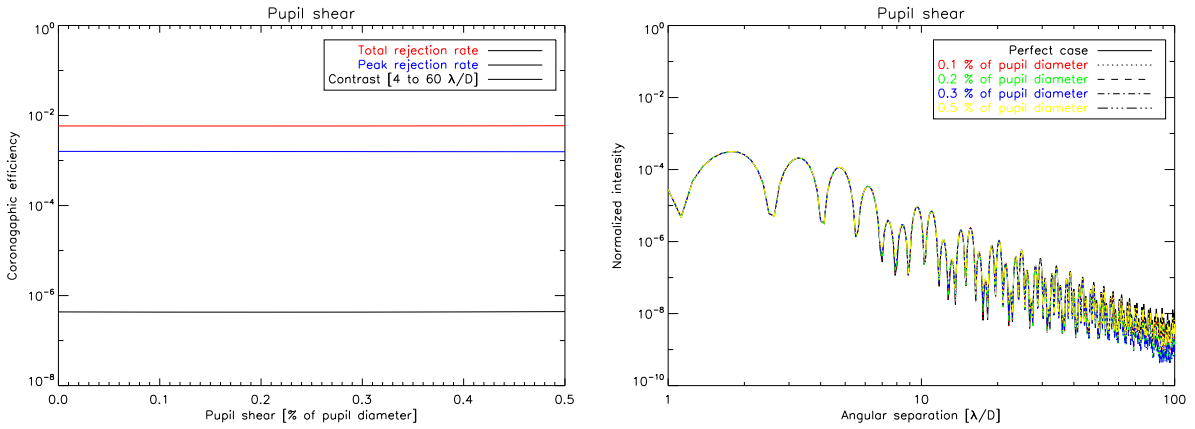

Figure 7.24: Lyot sensitivity to the misalignment of the pupil stop - *left*: impact on the coronagraphic efficiencies, *right*: impact on the coronagraphic PSF.

7.6 Apodized Pupil Lyot Coronagraph

The Apodized Pupil Lyot Coronagraph has been previously studied in Chapter 5 in the context of its optimization for an implementation on ELTs. We defined some metrics to select the optimal apodizer/Lyot mask combination for a given telescope. We performed a sensitivity analysis to different telescope parameters and analyzed how our metrics responded. Here, we perform a sensitivity analysis of the optimal APLC configuration to a large set of important parameters as we did in the previous chapters of Part III for the AGPM, APRC, AIC and Lyot coronagraphs.

7.6.1 Central obscuration

As demonstrated in Chapter 5, optimal APLC configurations are mainly driven by the central obscuration ratio. Therefore, for each value of the central obscuration, assuming that the APLC operates with its optimal configuration, performance are roughly insensitive to the ratio of the central obscuration (Fig. 7.25). The case of a full-filled aperture is particular, since the APLC regime is different (bell regime instead of bagel regime) which was out of our previous study (Chapter 5). In this precise case, performance are better while throughput is lower ($\sim$ 20%). Locally, $\sim$ 4 orders of magnitude are lost because of the central obscuration presence (Fig. 7.25, right).

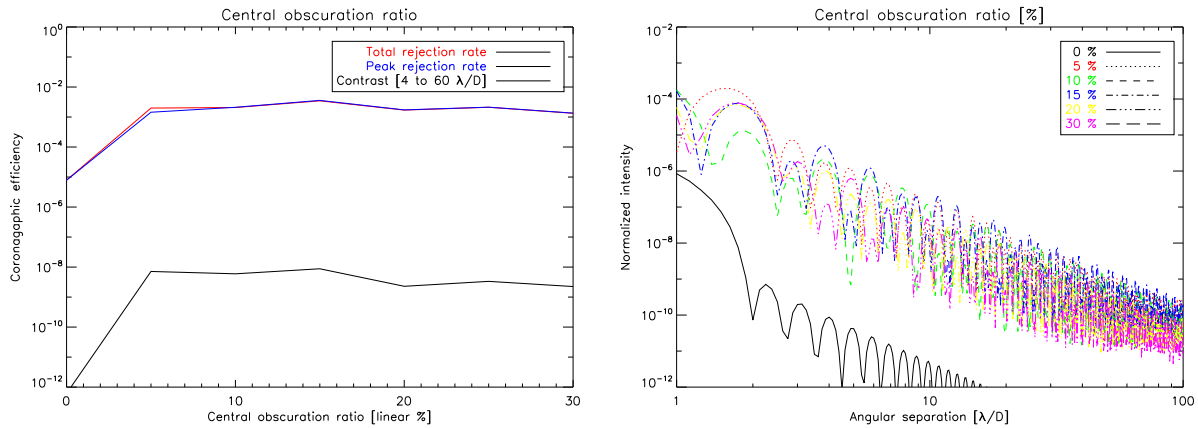

Figure 7.25: APLC sensitivity to the central obscuration ratio - *left*: impact on the coronagraphic efficiencies, *right*: impact on the coronagraphic PSF.

7.6.2 Spider vanes

As for the APRC, in theory, the APLC does not require more than a pupil stop like the entrance pupil. However, simulations presented hereafter, reveale a non negligible impact on performance when spider vanes thickness increase. From 15 cm to 90 cm, two orders of magnitude have been lost. Assuming the typical value for the E-ELT (60 cm), contrasts would be severely restricted. These results can largely be mitigates by oversizing the spider vanes thickness in the pupil stop (which reduces slightly its throughput).

7.6.3 Segment reflectivity

1% (ptv) segment reflectivity slightly impacts coronagraphic PSF (Fig. 7.27, right) while 5% (ptv) sets contrasts to 10^{-6} at $10\lambda/D$ and 10^{-7} at $20\lambda/D$. Average contrast has actually a quadratic power-law dependency (Fig. 7.27, left, where θ describes the amplitude of reflectivity in ptv) with segment reflectivity. Therefore, the effect is non-negligeable for the APLC.

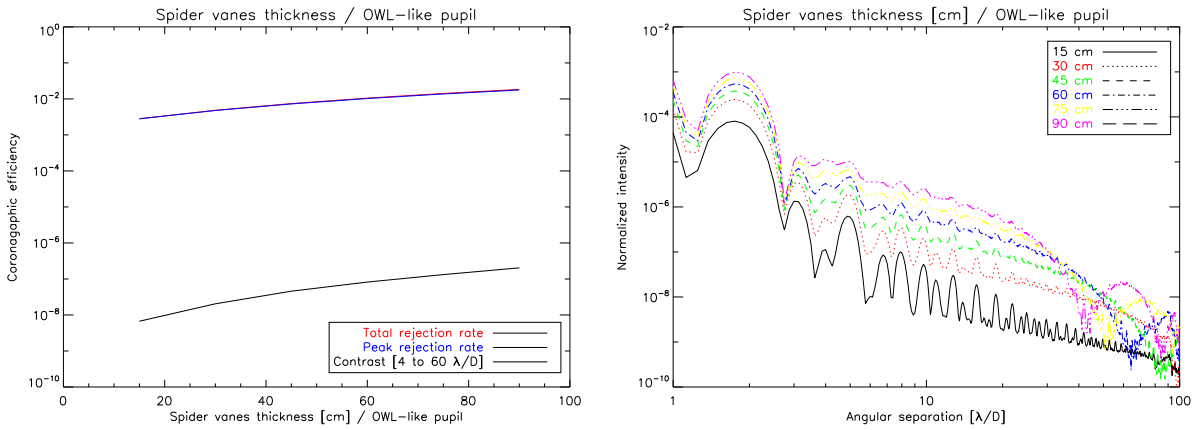

Figure 7.26: APLC sensitivity to the spider vanes thickness (OWL-like pupil as a baseline) - *left*: impact on the coronagraphic efficiencies, *right*: impact on the coronagraphic PSF.

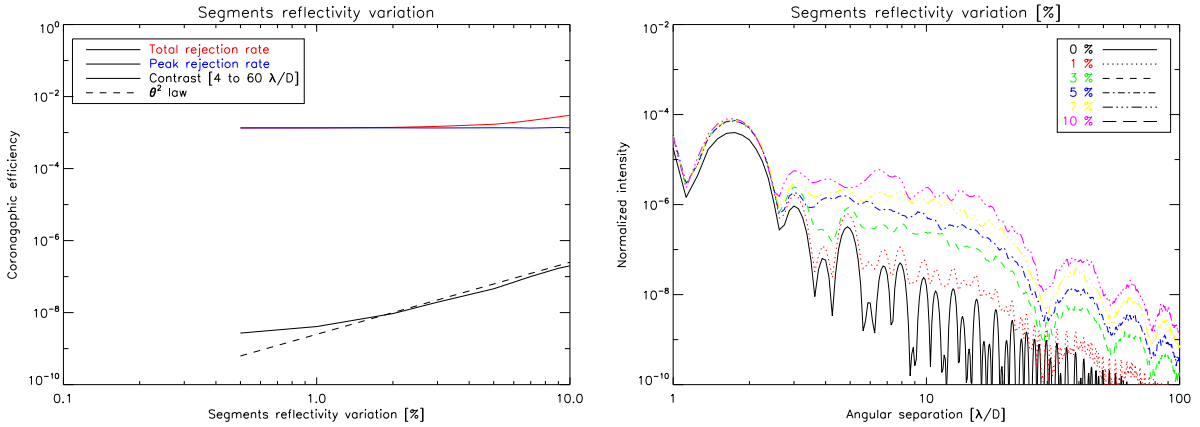

Figure 7.27: APLC sensitivity to the segment reflectivity - *left*: impact on the coronagraphic efficiencies, *right*: impact on the coronagraphic PSF.

7.6.4 Segment static aberrations

The impact of phase aberrations on a segmented pupil is described in Fig.7.28, top left and right. Segment aberrations degrade performance much larger on the halo. In Fig. 7.28 (bottom left and right), impact of segment aberrations (piston, tip-tilt, defocus and astigmatism) is plotted as a function of the total rejection rate (left) and contrast in the halo (right). Most of these low-order aberrations have roughly the same impact on performance.

With the contrast evaluation metrics, phase aberrations are the dominant source of limitation, where the APLC sensitivity follows a quadratic dependency. This is also true when the rejection rate metrics is used except that the central obscuration is the dominant source of limitation for small level of phase errors (smaller than ~ 10 *nm rms*). 10 nm rms actually sets contrasts to 10^{-6} until $30\lambda/D$. The quadratic power-law dependency can be expressed as follow:

$$\tau(\theta) = 2.8\ 10^{-5} \times \theta^2 \quad \theta > 10\ nm\ rms \tag{7.15}$$

$$\overline{\mathscr{C}(\theta)} = 3.3\ 10^{-9} \times \theta^2 \tag{7.16}$$

where θ is the low-order phase aberrations amplitude in nm rms.

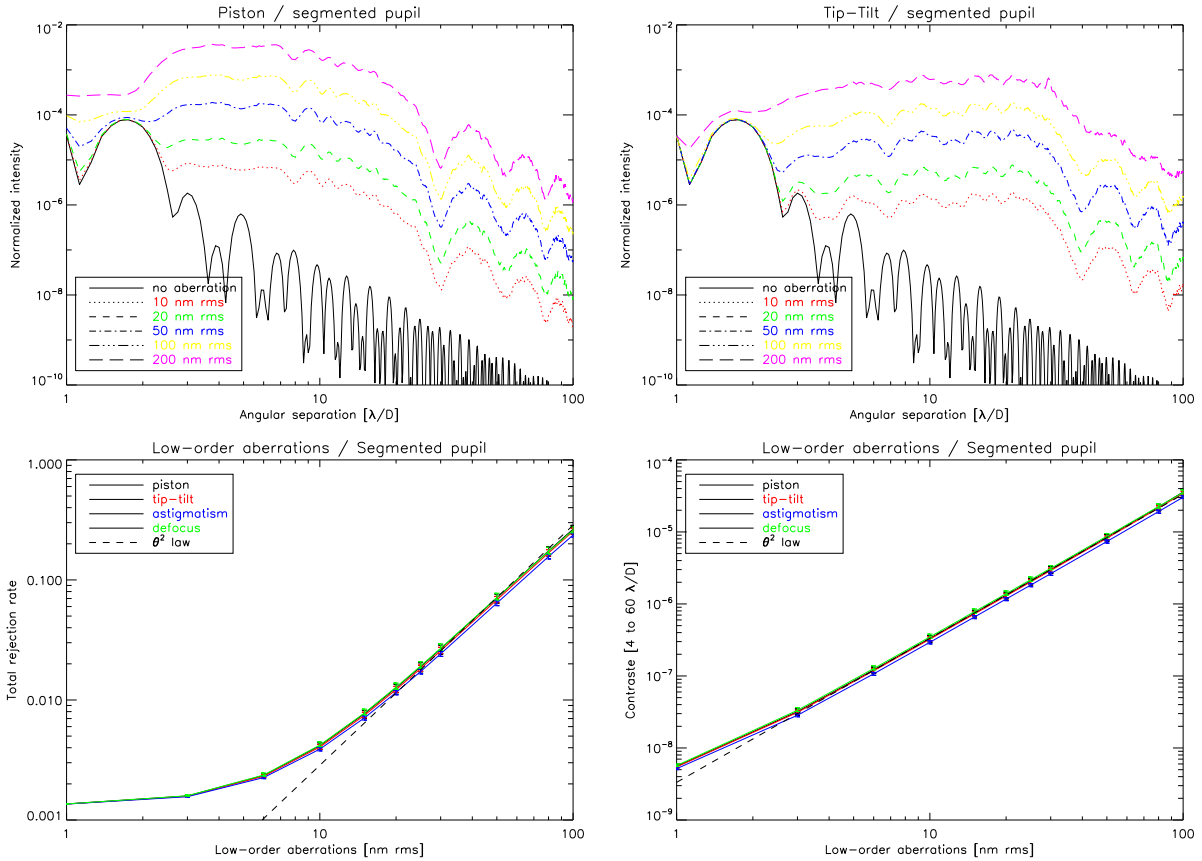

Figure 7.28: APLC sensitivity to low-order aberrations (piston and tip-tilt here) - Top - *left*: impact on the coronagraphic PSF. - Bottom - Impact of low-order aberrations (piston, tip-tilt, defocus and astigmatism) on the total rejection rate (*left*) and on the coronagraphic halo (*right*).

7.6.5 Pointing errors

Considering the range of the offset pointing we simulated (Fig. 7.29, top) and owing to its Lyot mask ($4.7\lambda/D$), APLC is not sensitive to the offset pointing error. Obviously, this result is Lyot mask diameter dependent. Most of the effect is localized in the halo and specifically affects performance at large angular distances (above $30\lambda/D$ for 5 mas rms).

7.6.6 Stellar angular size

As for the offset pointing error, the size of the Lyot mask balance the APLC sensitivity to the resolved star impact. Considering our APLC, performance start to be affected for stellar radius of $0.1\lambda/D$ (Fig. 7.29, bottom).

7.6.7 Pupil shear: pupil stop alignment

The pupil shear has somehow an important impact on the contrast (Fig. 7.30, right). Contrasts are set to 10^{-6} *to* 10^{-7} in the middle range of frequencies.

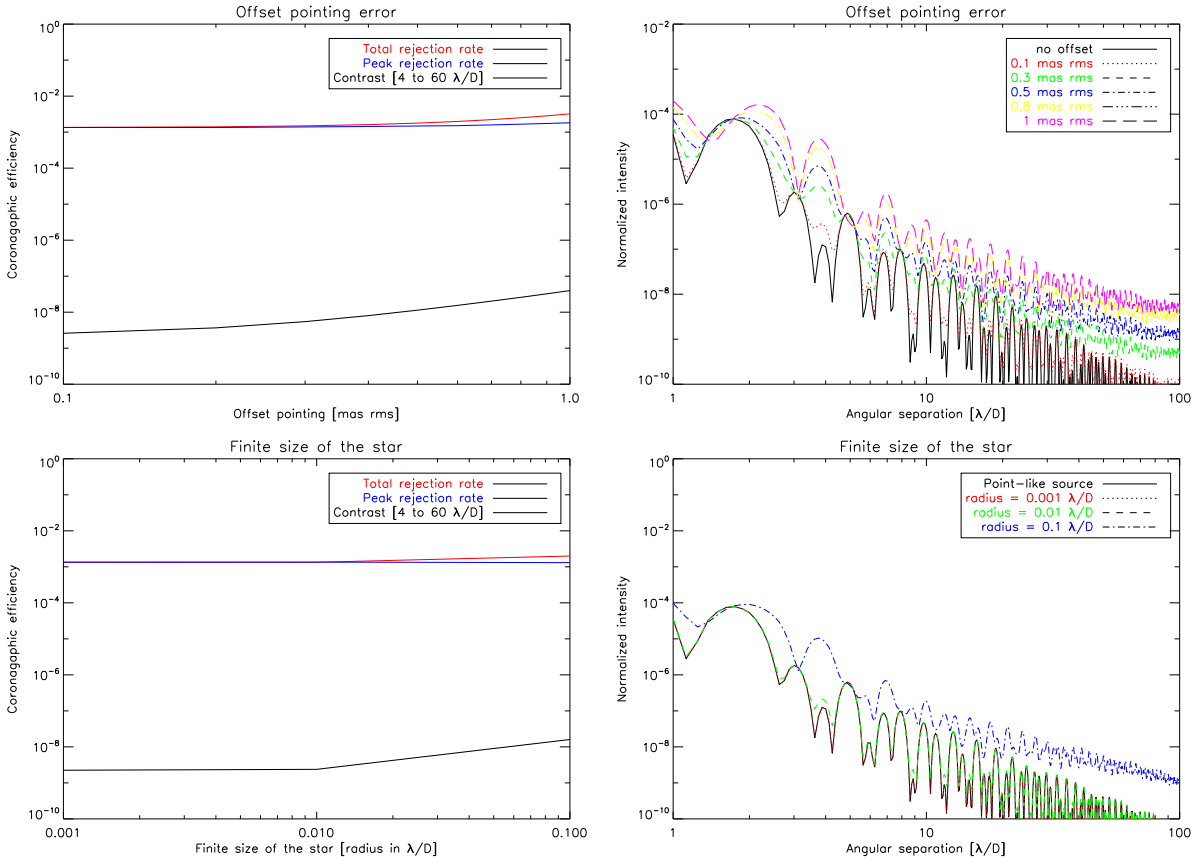

Figure 7.29: APLC sensitivity to offset pointing errors (top) and the stellar angular size (bottom) - *left*: impact on the coronagraphic efficiencies, *right*: impact on the coronagraphic PSF.

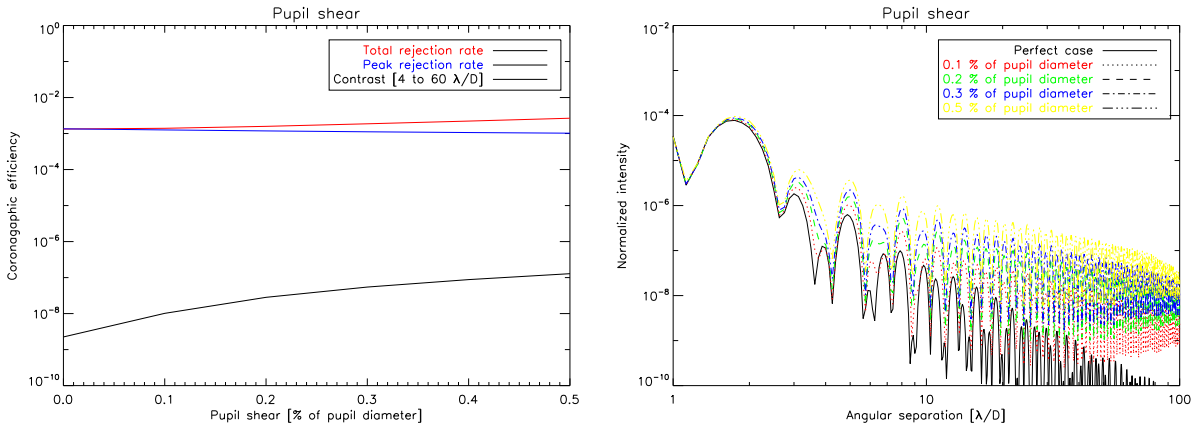

Figure 7.30: APLC sensitivity to the misalignment of the pupil stop - *left*: impact on the coronagraphic efficiencies, *right*: impact on the coronagraphic PSF.

7.7 Band-Limited 4^{th} order

Band-limited coronagraphs have been already studied from an optimization point of view in a dedicated part (Chapter 6). Therefore, some telescope characteristics (such as the central obscuration and the spider vanes) have already been discussed. Here, we focus on parameters not yet analyzed.

7.7.1 Segment reflectivity

In Fig. 7.31 (left), it appears that BL4 has a quadratic dependency to the segment reflectivity variations. From Fig. 7.31 (right), one can see that 1% (ptv) reflectivity already sets contrasts to $\sim 10^{-8}$ until $20\lambda/D$, while 5% (ptv, i.e 1.4% rms) limits the contrast to $\sim 10^{-6} - 10^{-7}$ in the same range of frequencies. Segments reflectivity has therefore a strong effect on BL4 performance.

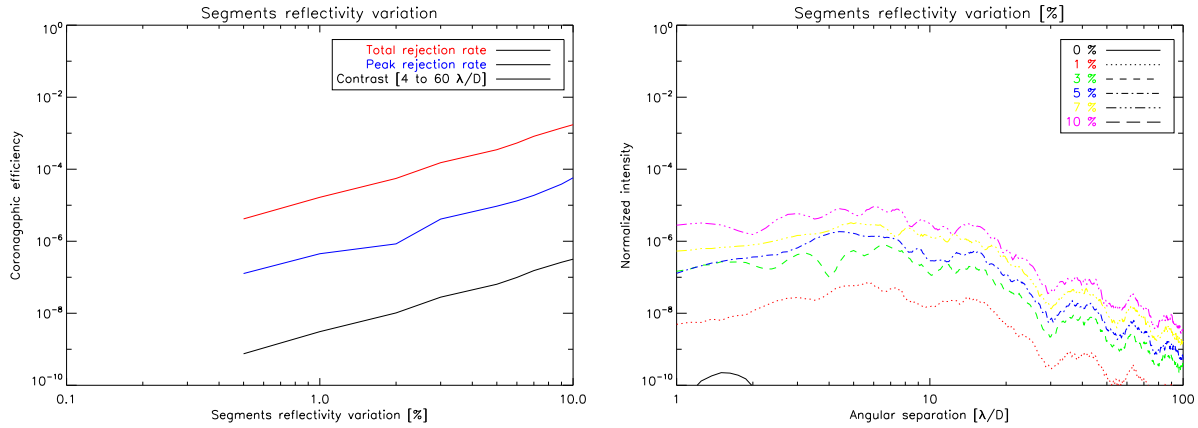

Figure 7.31: BL4 sensitivity to the segment reflectivity - *left*: impact on the coronagraphic efficiencies, *right*: impact on the coronagraphic PSF.

7.7.2 Segment static aberrations

In this section we will discuss the impact of phase aberrations on BL4 performance. We will focus not only on segment phase aberrations but on monolithic pupil phase aberrations as well. Although, the two cases are not comparable (frequencies distributions are different), it is important to understood that unlike for monolithic pupil, the dependency law to segment phase aberrations is not anymore related to the order of the band-limited mask function. Most of the time, for monolithic pupil, the choice of the band-limited mask function (i.e order of the function) is selected as a function of the phase aberration budget error. A 4^{th} order mask will demonstrate a 4^{th} order dependency to tip-tilt for instance, which is advantageous compared to other coronagraphs that most of the time exhibit a quadratic dependency. This advantage falls off in the context of segment phase aberrations.

One can see in Fig. 7.32 (middle row and bottom row) that:
1/ when the pupil is monolithic the fourth order mask demonstrates:

- fourth-order dependence on tip-tilt and astigmatism.
- quadratic dependence on defocus.

These results are consistent with the ones obtained by Shaklan et al. 2005 [85], except that the sensitivity to astigmatism was found to be quadratic dependent and not with a fourth-order. However, even if the order of the BL is the same, mask functions we used are different and the optimization of the pupil stop might have an impact since additional aberration rejection can comes at the expense of pupil stop further reduction. Actually, the flat behavior of some curves (tip-til and astigmatism) for small aberrations level (therefore insensitive behavior), reveals the best achievable performance sets when optimizing the pupil stop. BLs pupil stops were optimized with the goal

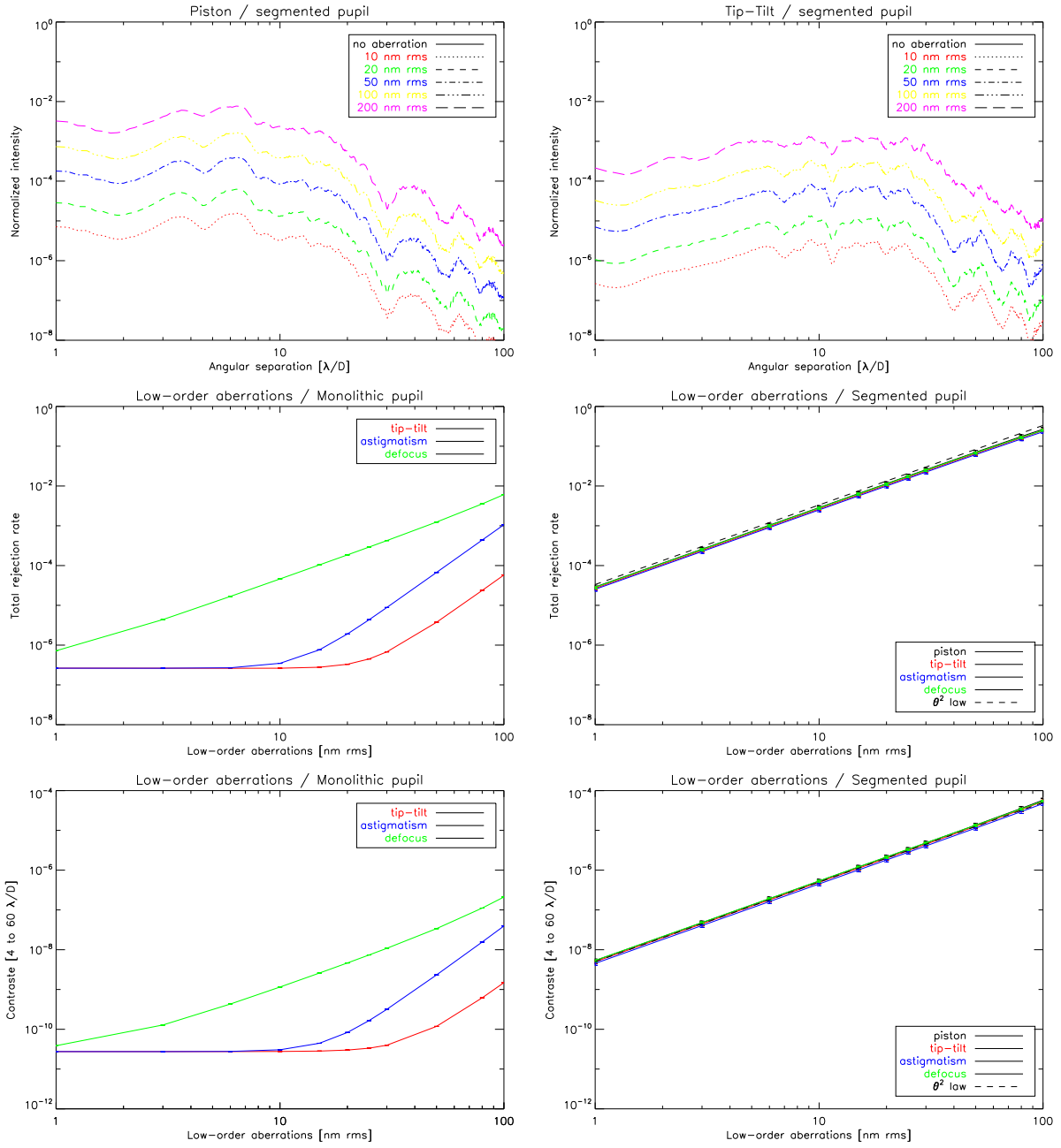

Figure 7.32: BL4 sensitivity to low-order aberrations - Upper row - *left*: impact on the coronagraphic PSF (piston), *right*: impact on the coronagraphic PSF (tip-tilt). - Middle row - impact on the total rejection rate: monolithic pupil (*left*) and segmented pupil (*right*). - Bottom row - impact on the coronagraphic halo: monolithic pupil (*left*) and segmented pupil (*right*).

to provide better contrast than 10^{-10} while preserving as far as possible the throughput. 2/ when the pupil is segmented the fourth-order mask demonstrates a quadratic dependence to piston, tip-tilt, astigmatism and defocus as well. The dependency to segment phase aberrations can be expressed as follow:

$$\tau(\theta) = 3.3\ 10^{-5} \times \theta^2 \tag{7.17}$$

$$\overline{\mathscr{C}(\theta)} = 5.10^{-9} \times \theta^2 \tag{7.18}$$

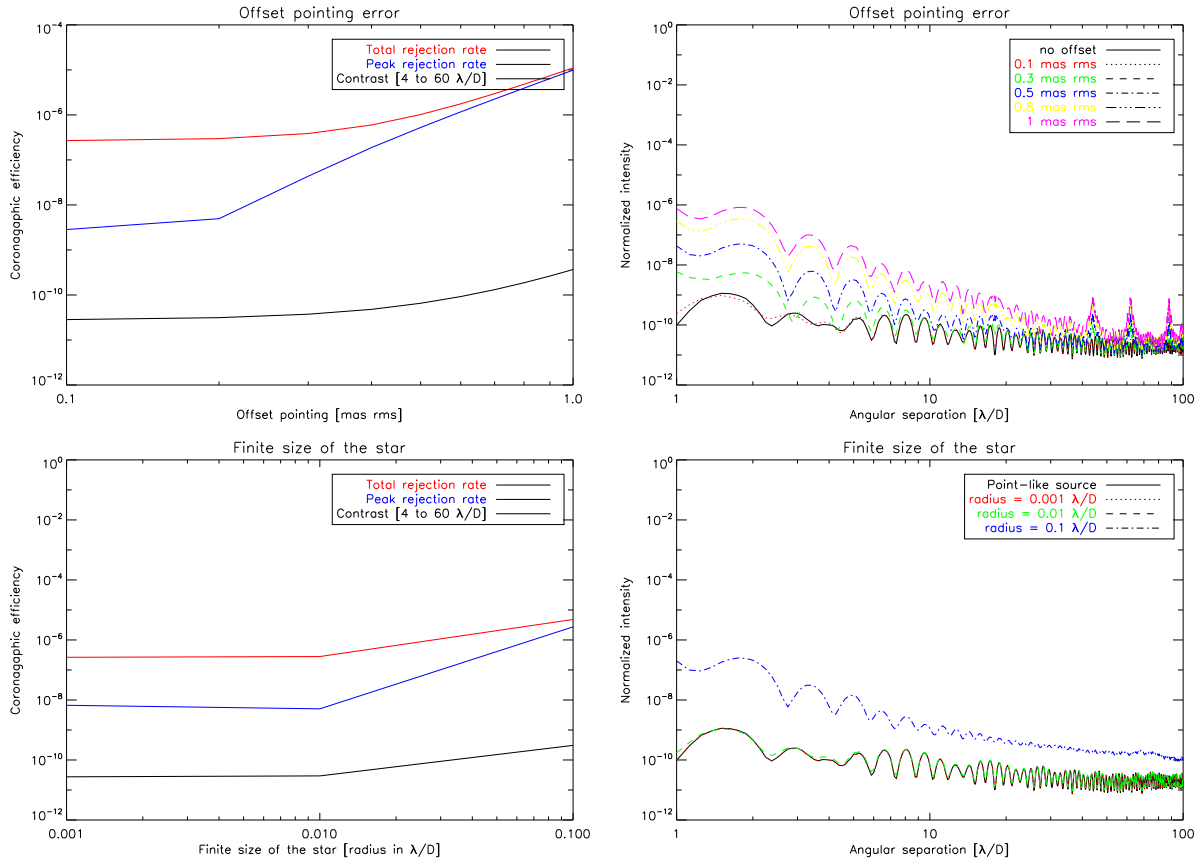

Figure 7.33: BL4 sensitivity to offset pointing errors (top) and the stellar angular size (bottom) - *left*: impact on the coronagraphic efficiencies, *right*: impact on the coronagraphic PSF.

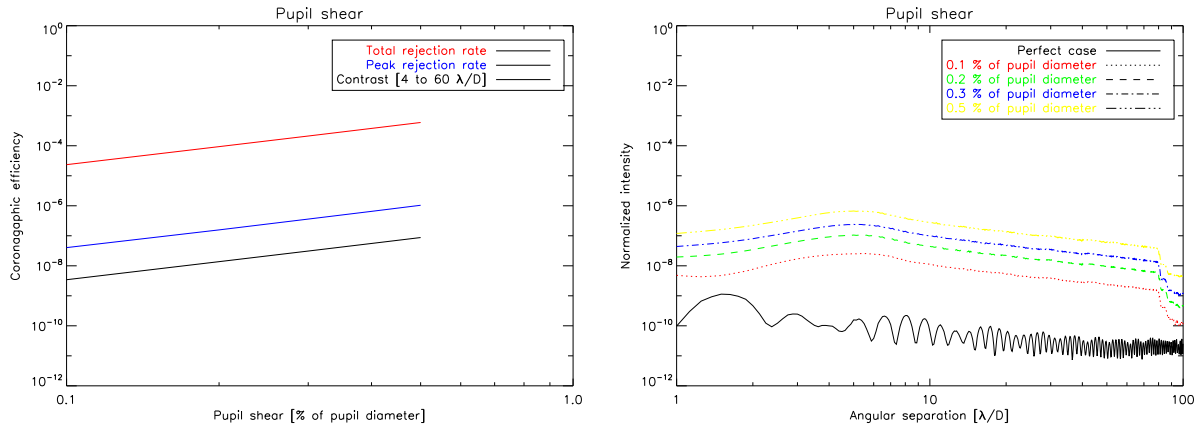

Figure 7.34: BL4 sensitivity to the misalignment of the pupil stop - *left*: impact on the coronagraphic efficiencies, *right*: impact on the coronagraphic PSF.

where θ is the low-order phase aberrations amplitude in nm rms.

7.7.3 Pointing errors

Considering the range of values of the offset pointing (Fig. 7.33, top) and owing to the BL4 IWA ($4\lambda/D$), BL4 is not highly sensitive to the offset pointing error. Obviously, this result is quite dependent of the choice of the mask bandwidth. Most of the effect is localized in the halo and specifically affects performance at angular distance before $20\lambda/D$. The small range of offset pointing does not allow to derive power-law dependency (supposed to be a fourth-order dependency), but the sensitivity to the offset pointing is very similar to the case of the stellar angular size (next section).

7.7.4 Stellar angular size

The fourth-oder mask is supposed to demonstrates a fourth-order dependence to the stellar angular size (Fig. 7.33, bottom). The halo is actually not affect until a stellar radius of $0.1\lambda/D$.

7.7.5 Pupil shear: pupil stop alignment

The fourth-order band-limited mask demonstrates a quadratic dependence on the pupil shear. 0.1% misalignment already sets contrasts to 10^{-8} at most of the angular distance (fig. 7.34). Controlling the alignment of the pupil stop will therefore be an issue to reach deep contrasts.

7.8 Band-Limited 8^{th} order

As for the BL4, we focus on parameters not yet analyzed in Chapter 6.

7.8.1 Segment reflectivity

In Fig. 7.31 (left), it appears that BL8 has (like BL4) a quadratic-like dependency to the segment reflectivity variations. From Fig. 7.31 (right), one can see that 1% (ptv) reflectivity already sets contrasts to $\sim 10^{-7}$ until $20\lambda/D$. Segment reflectivity has therefore a strong effect on BL8 performance.

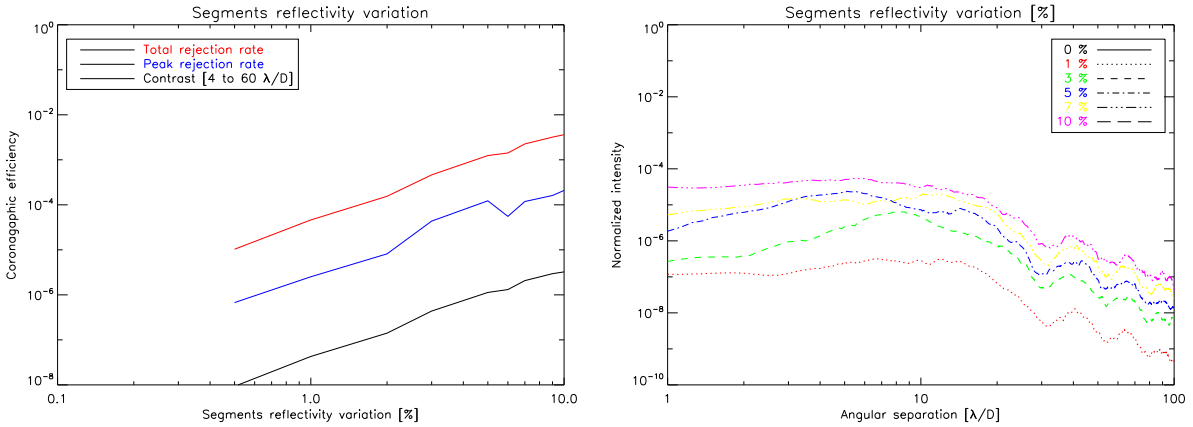

Figure 7.35: BL8 sensitivity to the segment reflectivity - *left*: impact on the coronagraphic efficiencies, *right*: impact on the coronagraphic PSF.

7.8.2 Segment static aberrations

As for BL4, the major result of simulations presented hereafter is that the impact of segment aberrations is quite important (Fig. 7.36, upper row). Even if it is for some aberrations difficult to clearly derive power-law in Fig. 7.36 (middle row and bottom row), one can interpolates that:
1/ when the pupil is monolithic the eighth order mask demonstrates:

- eighth-order dependence on tip-tilt and astigmatism.
- fourth-order dependence on defocus.

These results are consistent with the ones obtained by Shaklan et al. 2005 [85], except that the sensitivity to astigmatism was found to be fourth-order dependent and not with a eighth-order dependency. Same reserves can be expressed as already done for the BL4 case (Section 7.7.2). 2/ when the pupil is segmented the eighth-order mask demonstrates a quadratic dependence to piston, tip-tilt, astigmatism and defocus. The dependency to segment phase aberrations can be expressed as follow:

$$\tau(\theta) = 1.10^{-4} \times \theta^2 \tag{7.19}$$

$$\overline{\mathscr{C}(\theta)} = 1.10^{-7} \times \theta^2 \tag{7.20}$$

where θ is the low-order phase aberrations amplitude in nm rms.

7.8.3 Pointing errors

Considering the range of the offset pointing (Fig. 7.37, top) and owing to the BL8 IWA ($4\lambda/D$) and mask order, BL8 is not sensitive to the offset pointing error. Obviously, this result is quite dependent of the choice of the mask bandwidth. 0.5 mas rms offset pointing still allow a contrast of about 10^{-10} at all angular distance.

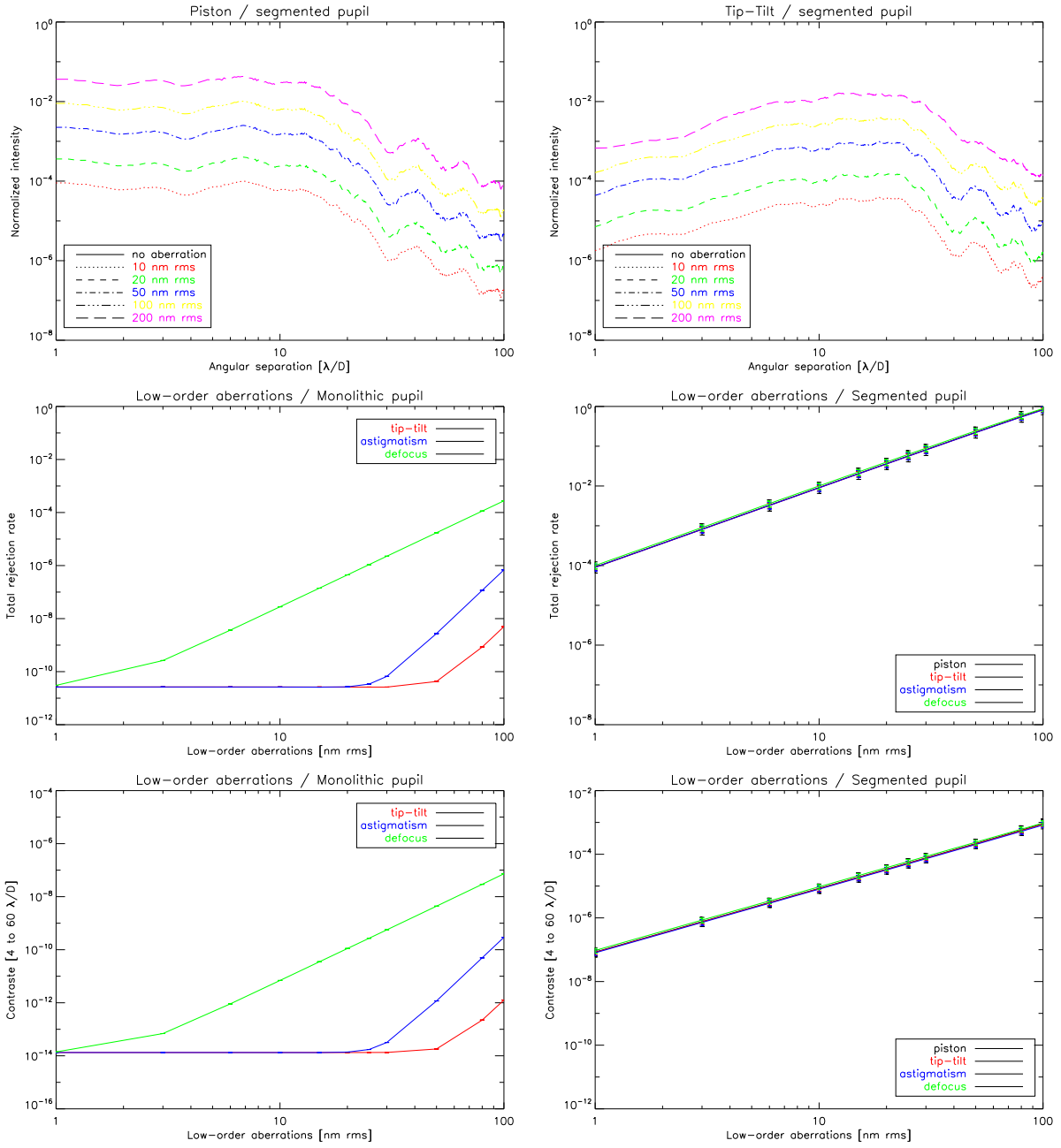

Figure 7.36: BL8 sensitivity to low-order aberrations - Upper row - *left*: impact on the coronagraphic PSF (piston), *right*: impact on the coronagraphic PSF (tip-tilt). - Middle row - impact on the total rejection rate: monolithic pupil (*left*) and segmented pupil (*right*). - Bottom row - impact on the coronagraphic halo: monolithic pupil (*left*) and segmented pupil (*right*).

7.8.4 Stellar angular size

The eighth-oder mask demonstrates an ability to keep contrasts under 10^{-10} for each value of the stellar size considered in simulation.

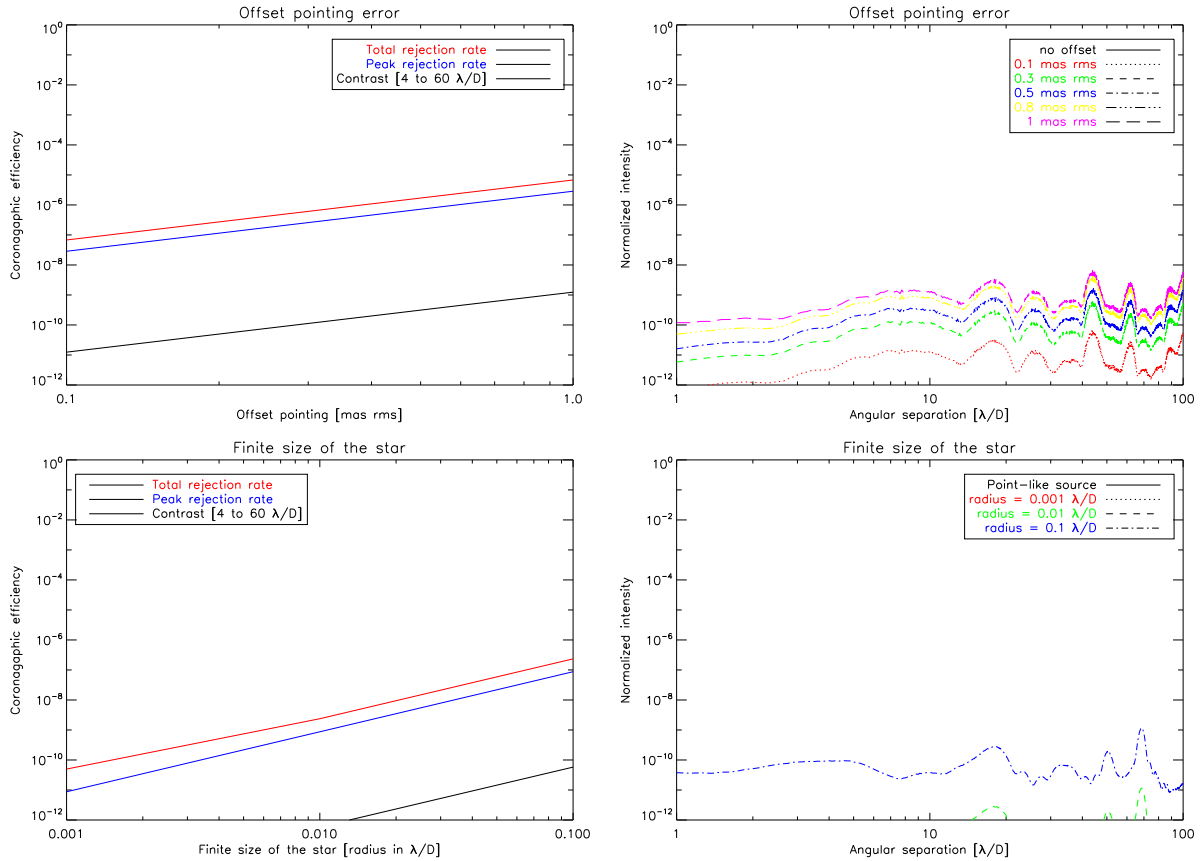

Figure 7.37: BL4 sensitivity to offset pointing errors (top) and the stellar angular size (bottom) - *left*: impact on the coronagraphic efficiencies, *right*: impact on the coronagraphic PSF.

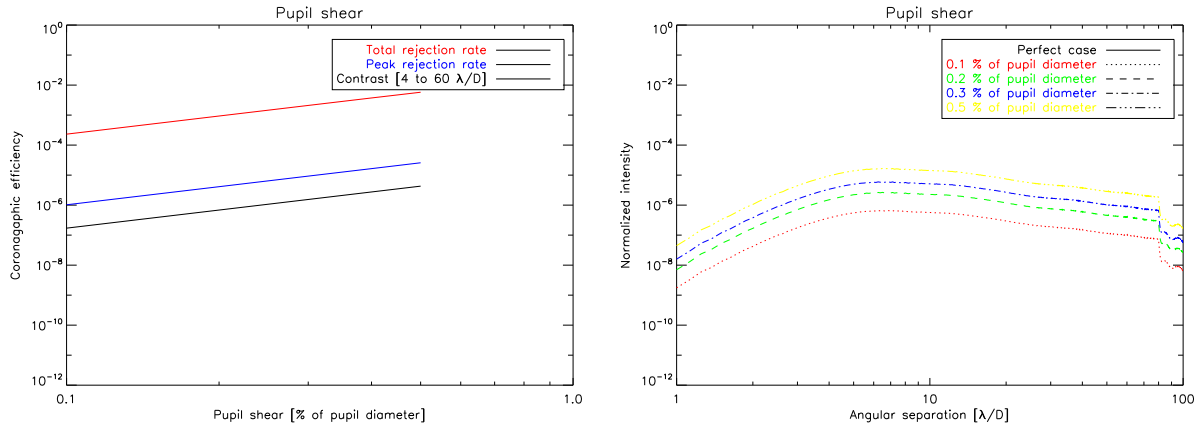

Figure 7.38: BL8 sensitivity to the misalignment of the pupil stop - *left*: impact on the coronagraphic efficiencies, *right*: impact on the coronagraphic PSF.

7.8.5 Pupil shear: pupil stop alignment

The eighth-order band-limited mask demonstrates a quadratic dependence on the pupil shear. 0.1% misalignment already sets contrasts to 10^{-7} at most of the angular distance (fig. 7.38). Controlling the alignment of the pupil stop will therefore be an issue to reach deep contrast.

7.9 Binary Mask (Checkerboard mask)

The Checkerboard mask (binary apodization mask, BM hereafter) is designed to allow a 10^{-8} contrast between 7 to 30 λ/D. It is based on the one designed and optimized by L. Abe for the EPICS consortium in the context of a coronagraphic trade-off study for the future planet finder instrument for the E-ELT. Unlike the other coronagraphs, the BM has a limited discovery space where planets can be observed. This restricted region in the image where diffracted and scattered light can be suppressed by the BM (between IWA and OWA) is defined when optimizing the design of the mask, as well as the achievable contrast. Therefore, the present BM design coronagraphic capabilities used hereafter must not be confused with the best performance reachable with such techniques but only as an example to derive sensitivity order dependence. BM can be design whatever the central obscuration ratio. Here, the central obscuration is 30%. No further investigations of this coronagraph will be presented than the ones of this section (i.e only in ideal conditions).

7.9.1 Spider vanes

The BM has been designed for a spider-less pupil. Therefore, the presence of spider vanes matters the achievable contrast (Fig. 7.39, left). 15 cm already limits contrasts between 10^{-5} and 10^{-6}. Therefore, more than 2 orders of magnitude have been lost compared to the case without any spider vanes.

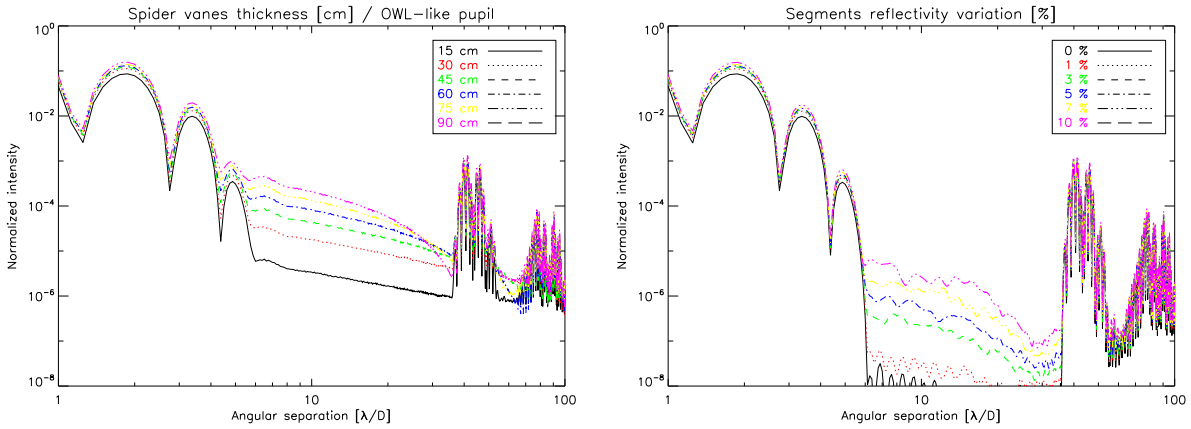

Figure 7.39: *Left*: BM sensitivity to the spider vanes thickness (OWL-like pupil as a baseline). *Right*: sensitivity to the segment reflectivity.

7.9.2 Segment reflectivity

The BM seems to demonstrate a quadratic dependence to the segment-to-segment reflectivity variations (Fig. 7.39, right). 5 % (ptv, i.e 1.4 % rms) already sets contrast at 10^{-6} at 7 λ/D (2 orders of magnitude lost), 10^{-7} at 20 λ/D (1 order of magnitude lost). Therefore, the impact of the segment reflectivity is important.

7.9.3 Segment static aberrations

Like the other coronagraphs previously considered, the BM demonstrates a quadratic dependence to the segment phase aberrations (Fig. 7.40, right). 2 orders of magnitude is lost when considering 10 nm rms of tip-tilt (Fig. 7.40, left).

7.9.4 Pointing errors

Pointing error does not impact at all the BM. No contrast degradation has been revealed (Fig. 7.41, left)

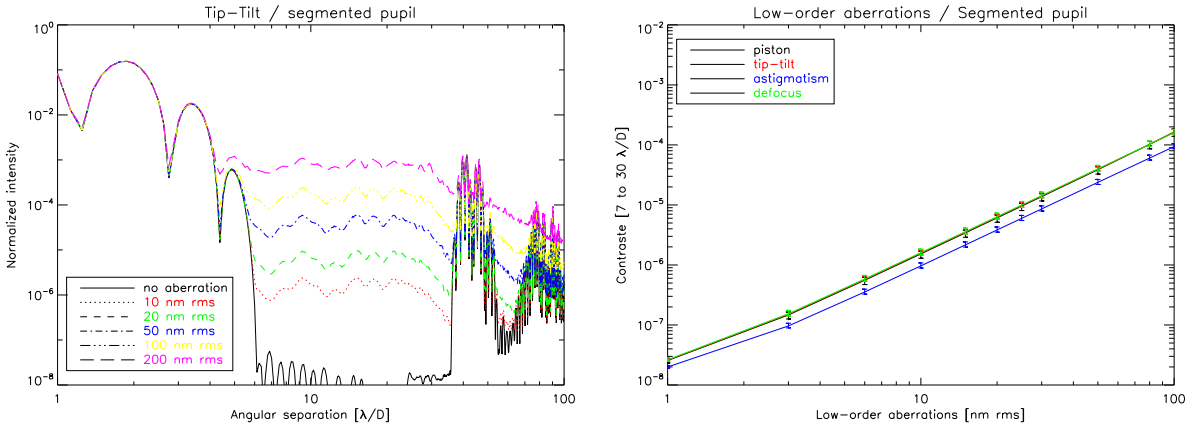

Figure 7.40: BM sensitivity to low-order aberrations. *Left*: impact on the coronagraphic PSF (segmented pupil). *Right*: impact on the coronagraphic halo (average contrast estimation from 7 to 30 λ/D).

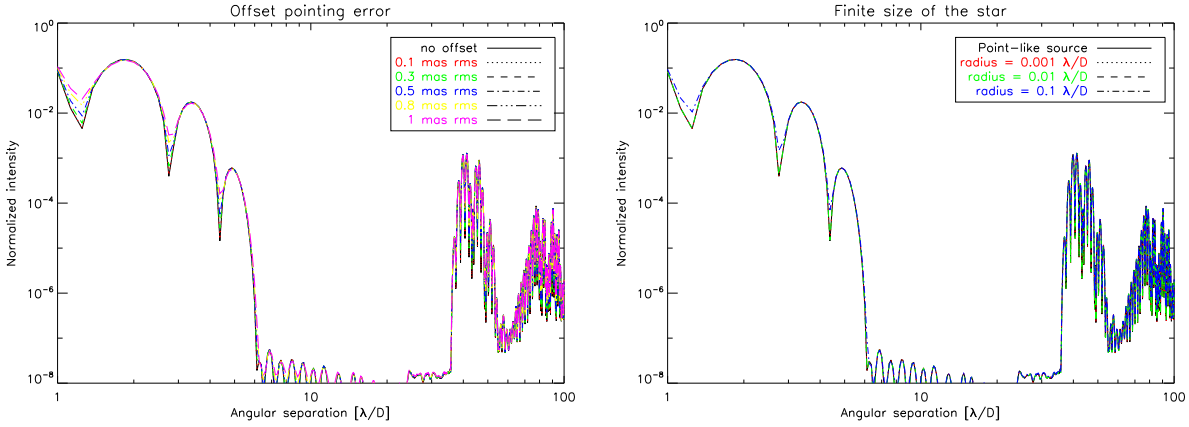

Figure 7.41: BM sensitivity to offset pointing errors (left) and the stellar angular size (right).

7.9.5 Stellar angular size

As for the offset pointing error, no impact on the coronagraphic PSF has been revealed (Fig. 7.41, right), which is the main advantage of this concept.

Table 7.2: Part III results resume assuming the E-ELT configuration.

Parameter	Coronagraph							
	AGPM/FQPM	AIC	APRC	Lyot	APLC	BL4	BL8	BM
Contrast of 10^{-10} achievable	no	yes	yes	no	no	yes	yes	yes
Contrast of 10^{-8} achievable	no	yes	yes	no	yes	yes	yes	yes
Central obscuration	+++	–	–	++	+	–	–	–
Spider vanes	+	–	+	+	+	+	+	+
Segment reflectivity	-	θ^2	θ^2	-	θ^2	θ^2	θ^2	θ^2
Segment phase aberrations	θ^2	θ^2	θ^2	θ^2	θ^2	θ^2	θ^2	θ^2
Offset pointing error	-	θ^2	θ^2	-	-	θ^4	-	–
Star resolution	+	θ^2	θ^2	-	+	-	-	–
Pupil shear	-	×	θ^2	-	θ^2	θ^2	θ^2	×

7.10 Resume

In Table 7.2, we briefly gather and resume results of Part III with the following qualitative notations:

- +++ highly sensitive
- ++ sensitive
- + slightly sensitive
- - not sensitive
  - the limitation is either set by an other parameter (central obscuration, for instance)
  - or the coronagraph is not sensitive assuming a reasonable amplitude value of the error
- – intrinsically not sensitive
- × does not concern the coronagraph
- θ^2: quadratic dependancy
- θ^4: fourth-order dependancy

Results presented assume the E-ELT configuration (30% central obscuration). Some coronagraph apparent non-sensitivity to a given parameter might be only a result as a strong dependency to an other parameter (most of the time the central obscuration indeed).

1/ Telescope mechanical characteristics mostly affect coronagraphs because of the central obscuration which is quite high for the E-ELT. This parameter will put severe performance restriction on FQPM/AGPM and Lyot as well. Solutions to mitigates its effect on phase masks would be mandatory: either by using of a small Lyot mask on the center of the phase mask or by using a multiple stages configuration (as studied in Baudoz et al. 2007 [15]).

2/ Segment amplitude and phase aberrations impacts in a same way any coronagraph. All coronagraphs exhibit θ^2 power-law dependence to low-order phase aberrations and segment reflectivity as well. Actually, BL coronagraphs are well appreciated for space-based observation for their power-law dependence to low-order phase aberrations, which is in the case of monolithic pupil, somehow related to the order of the band-limited mask. This advantage disappear for segmented pupil telescope. Hence, even if their low sensitivity to pointing error is not negligible, their interest for ground-based observations is questionable from a segment phase aberration point of view.

3/ It is possible somehow to improve the pointing of a telescope to very high accuracy (a fraction of *mas* indeed). However, the angular size of the star cannot be reduced and is about $1mas$ for most potential exoplanet targets. Therefore, even with accurate pointing and wavefront correction, the amount of light that will leaks through any coronagraphs will be dominated by the angular size of the parent star. All the small IWA coronagraph concepts exhibit a quadratic behavior to pointing error/stellar size. Therefore, Lyot coronagraphs and their avatars can be preferable since they can be tuned to be less sensitive (but this tuning comes at the price of a larger IWA which prohibits sources to be observed in the close environment of the parent star).

Part IV

Coronagraphs characterization/comparison in realistic conditions

Abstract - *A large review of the different families of coronagraph was performed in Guyon et al. 2006 [48] and optimal concepts were proposed in the context of space-based observations. Results of this study can not be generalized for ground-based observations as the problematic is different. Contrast level and inner working angle requirements are relaxed while telescopes characteristic constraints are stronger. Here, our purpose is precisely to investigate in the general case of ELTs.*

Our problematic is definitely different from the one tackles in Guyon et al. 2006 [48]:

- *We are dealing with ground-based observations instead of space-based observations, thus the interest of a coronagraph will depend within the foreseen capability of the next generation of XAO systems correction. Therefore, the selection of a coronagraph must take into account its ability to generate a deep contrast with respect to the level of wavefront control.*
- *We are dealing with ELT characteristics (central obscuration ratio, secondary support, segmentation...) instead of an off-axis configuration telescope. In this context, a coronagraph must be able to play with these important constraints.*
- *Since we are working with 30-42 meters telescopes, constraints on the IWA and contrast requirements are relaxed.*

In Guyon et al. 2006 [48], the Phase Induced Amplitude Apodization Coronagraph (PIAAC, Guyon et al. 2004 [47]) has been proposed as a major useful concept even if it is one of the more complex coronagraph to implement in practice. Using two mirrors, it achieves an achromatic apodization of the telescope pupil by geometric redistribution of the light with full throughput and no loss of angular resolution. This apodization differs from the APLC's one since it concentrates most of the energy inside a single diffraction peak. The few part of the energy outside this peak is then occulted by a Lyot mask placed in the focal plane to efficiently remove star light. To remove the off-axis wavefront distortion introduced by the pupil remapping, the beam is de-apodized after the occulting mask.

Appropriated to off-axis telescopes, performance of this concept will suffer from the impact of large central obscuration and the shadow in the pupil from the presence of spider vanes (structures that supports the secondary mirror) to correctly apodize the telescope pupil (i.e to achieve the contrast performance requirements) because of the highly aspherical surfaces needed. Although some recent works strive to minimize spider vanes effects (Abe et al. 2006 [3] and the spider removal plate concept produce by Guyon for the Subaru telescope pupil that translates the spider vanes part of the beam closer together to reduce the gap), we decided to not simulate this concept for our study. This choice is justified by the later points and to avoid an heavy study that would required in a first time to analyze the physical feasibility of the two mirros deformation considering the telescope pupil, and in a second time to tune the focal mask.

8

Characterization/comparison with eXtreme Adaptive Optics system

Contents

Abstract - *A variety of astrophysical topics (low-mass companions, circumstellar disks, ...) has driven the next generation of high contrast instruments like SPHERE and GPI (Beuzit et al. 2006, Macintosh et al. 2006 [18, 61]) expected in 2011, or EPICS (Kasper et al. 2008 [56]) for the longer term (~ 2018). Coronagraphy is a mandatory technique for these instruments and is therefore a critical sub-system.*

We have previsously studied coronagraphs sensitivity to a wide range of error sources in ideal conditions (i.e Strehl ratio of 100%). Here, the objective is to investigate the trade-off for coronagraphy in the general context of ELTs in more realistic conditions. On ground-based telescopes equipped with extreme Adaptive Optics systems (XAO), coronagraphs are expected to attenuate significantly the on-axis star. However, even at a high level of correction (Strehl ratio > 90%) a significant fraction of the star flux remains in the focal plane (<10%). The residual light sets the photon noise contribution for high contrast imaging. The estimation of this level is thus one byproduct of our study (as shown in Cavarroc et al. 2006 [30]) The intent of this Chapter is twofold: 1/ determine limiting parameters and ideally derive specifications at the system level, 2/ initiate a general comparison of coronagraphs to identify valuable concepts and field of application. For that, we have run intensive numerical simulations accounting for the most critical sub-systems of an high contrast instrument. This trade-off was carried out at the level of the coronagraphic image assuming atmospheric wavefront residuals left by the AO system

A similar study (Chapter 9) is also performed after differential imaging (assuming this technique is independent of the coronagraph concept). In these cases, we considered infinitely long exposures (photon noise is not considered since we are dealing only with the limitation by systematics).

Table 8.1: Parameters of coronagraphs optimized for a central obscuration of 30%. d is the Lyot focal mask diameter, ϵ the BL bandwidth parameter (m and l are complementary BL8 function parameters), lp is the AGPM topological charge and $\mathscr{T}$ the overall transmission.

Coronagraph type	Specifications		
	IWA (λ/D, ± 0.1)	$\mathscr{T}$ (%)	Parameters
FQPM	0.9	82.4	-
AGPM	0.9	82.7	lp=2
AIC	0.4	50.0	-
Lyot	3.9	62.7	$d = 7.5\lambda/D$
APLC	2.4	54.5	$d = 4.7\lambda/D$
APRC	0.7	74.5	$d = 1.06\lambda/D$
BL4	4.0	22.4	$\epsilon = 0.21$
BL8	4.0	13.8	$\epsilon = 0.6$, m=1, l=3

8.1 Purposes

In this Chapter we compare several coronagraph concepts presented in Chapter 2 and investigate the impact of major error sources that occur in a coronagraphic telescope (central obscuration, secondary support, low-order segment aberrations, segment reflectivity variations, pointing errors). This analysis is performed under residual phase left uncorrected by an eXtreme Adaptive Optics system (XAO) for a large range of Strehl ratio. We derive critical parameters that each concept will have to deal with by order of importance. We evidence three coronagraph categories as a function of the accessible angular separation and proposed optimal one in each case. Most of the time amplitude concepts appear more favorable and specifically, the Apodized Pupil Lyot Coronagraph gathers the adequate characteristics to be a baseline design for ELTs.

8.2 Assumptions

In these following subsections we describe all the assumptions we consider through this analysis. We consider, the following coronagraph concepts: Lyot coronagraph, Apodized Pupil Lyot Coronagraph, Apodized Roddier & Roddier Coronagraph (i.e Dual zone), Four Quadrant Phase Mask, Annular Groove Phase Mask, Band-limited, Achromatic Interferometric Coronagraph.

8.2.1 Constraint on IWA

The Inner Working Angle (IWA) describes quantitatively how close a coronagraph design allows the detection of a faint companion. In this paper we define the IWA as the angular separation for which the diffraction peak of a planet is reduced by a factor of 2.
The AIC, FQPM/AGPM, APRC have a very small IWA owing to their intrinsic properties. On the opposite, amplitude concepts (Lyot, APLC, and BLs) have a larger IWA depending on coronagraph parameters (d, diameter of the focal mask or ϵ, bandwidth of the mask function that actually depends on the application).

Since we are dealing with ELTs, the angular resolution of such large telescopes is relaxing the constraint on the IWA and hence the problematic is different than for planet finder instruments on 8-m class telescopes. As a baseline, we fixed the limit of the IWA to the reasonable value of $4\lambda/D$. For instance, at 1.6 μm (H-band), $4\lambda/D$ correspond to 30 mas and 165 mas respectively for a 42 and a 8 meters telescope.

In the next simulations, the Lyot coronagraph has a mask size of $7.5\lambda/D$ (i.e a corresponding IWA of 3.9 λ/D). The APLC has a $4.7\lambda/D$ mask diameter (i.e IWA = 2.4 λ/D). This size is the result of the optimization performed in Martinez et al. 2007 [65]. We also consider two band-limited masks with different orders: a 4^{th} order (sin^4 intensity mask with $\epsilon = 0.21$, Kuchner et al. 2002 [59]) and a 8^{th} order (m=1, l=3 and $\epsilon = 0.6$, Kuchner et al. 2005 [58]). BLs parameter ϵ both control the IWA and Lyot stop throughput.

8.2.2 Pupil stop optimization

The total amount of the rejected light by a coronagraph strongly depends on the pupil stop size and shape. In this paper, pupil stops are optimized to match the diffraction in the relayed pupil as defined in Boccaletti 2004 [21] and hence are well adapted to the way that each coronagraph deal with the diffracted light. However, in forthcoming simulations we generate a large different range of wavefront errors, hence an optimization of the pupil stop with respect to the level of the residual phase could relax constraints on the pupil stop shape and throughput (as discussed for instance in Crepp et al. 2007 [34], for the Band-Limited case). This optimization depends on the dominant source of noise (diffracted light or uncorrected atmospheric speckles).

In practice, we optimized pupil stops in the ideal case (no wavefront error) since the final comparison is made after differential imaging when the uncorrected atmospheric speckles have been removed. Pupil stops are assumed to be perfectly aligned except when we evaluate the impact of its misalignment (pupil stop throughput and coronagraph parameters are summarized in Table 8.1).

8.2.3 XAO hypothesis

As a baseline we consider a 42 meters ELT with 30% (linear) central obscuration ratio as expected for the European ELT (E-ELT, Gilmozzi et al. 2008 [42]), except when we evaluate its impact. As for the wavelength, we adopt a baseline of $\lambda = 1.6\mu m$ (centre of the H-band), a good compromise between angular resolution and AO correction. This spectral band is also recognized as a scientific baseline, at least for giant gazeous planets. The spectral features of CH_4 for instance, are favorable to differential imaging.

Our simulations make use of simple Fraunhofer propagators between pupil and image planes, which is implemented as fast Fourier transforms (FFTs) generated with an IDL code. The image plane is sampled with $0.125\lambda/D$ per pixel.

Since we are concerned with ELTs, we consider an eXtreme Adaptive Optics system (XAO) with a large number of actuators. Table 8.2 shows the characteristics for the simulations of the XAO phase residuals. As we want to analyze the behavior of coronagraph under realistic conditions we generate many phase screens with different Strehl ratios (from 84% to 96%). For that, we modify the atmospheric seeing (from 1.0" to 0.4") while leaving the XAO system unchanged. As a fair comparison, all coronagraphs have been affected by the same set of phase screens. We are using 100 phase realizations, and check that it was sufficient to produce long exposures at the contrast level we are dealing with. The Fried parameter (r_0) varies from 10 to 30 cm when Strehl ratio evolves from 84% to 96%.

Phase screens are generated with a tool (from ONERA, thanks to T. Fusco) based on the approach introduced by Rigaut et al. 1998 [81], Jolissaint and Veran 2002 [54] where analytical expressions of the PSD of residual phase are obtained for various effect affecting the AO system (fitting, aliasing, temporal...). The resulting global AO PSD is compute as the sum of the individual PSD of each error sources, and used to compute the AO corrected phase screens. It also includes fitting errors, servo lag and photon noise on the wavefront sensor (Shack-Hartmann).

8.2.4 Comparison metric

In the following, we describe metrics used to evaluate efficiency of coronagraphs. Caution: none of these metrics are weighted by the overall coronagraphic system transmission ($\mathscr{T}$). This throughput is set by the pupil stop transmission (times the mask transmission for BLs). The system transmission (presented in Table. 8.1) basically remains a physical limitation that must influence the decision for which coronagraph to implement in practice (integration time issue), but here we are more interested on upper limit of coronagraphs for comparison clarity in regards with external limitations.

Several metrics can be used to quantify the capability of a coronagraph Boccaletti 2004 [21], for instance. At the level of the coronagraphic image we have identified two metrics. The first one, $C_{CORO}(\rho)$ is the contrast profile averaged azimuthally and the second one $\overline{C_{CORO}}$ gives the contrast between the star peak and an average intensity in an annular region of the focal plane where an off-axis companion are expected to be detected. These metrics read :

Table 8.2: Values and amplitudes of parameters used in the simulation.

	XAO simulation
Input parameters	
telescope diameter	42 m
seeing at 0.5 μm	1.0" - 0.4"
wind speed	15 m/s
outerscale of turbulence L_0	20 m
number of actuators	2.10^4
inter-actuator distance	26 cm
AO frequency	2.5 KHz
wavelength	1.6 μm
average Strehl ratio	83% - 96 %
delay	0.04 s
focal sampling	0.125 λ/D / pixel
central obscuration default value	30%
Studied parameters	
central obscuration	10 - 30 [%]
spider vanes thickness	30 - 75 [cm]
segments reflectivity (~750 of 1.5m diameter)	1 - 5 [% ptv]
segments static aberrations (~750 of 1.5m diameter)	6 - 30 [nm rms]
pointing errors	0.1 - 0.5 [mas rms]
pupil shear	0.1 - 0.5 [%]

$$C_{CORO}(\rho) = \frac{\int_0^{2\pi} \psi_{CORO}(\rho,\alpha)\, d\alpha}{2\pi\, \psi_{PSF}(0)} \tag{8.1}$$

$$\overline{C_{CORO}} = \frac{\left(\int_{\rho_i}^{\rho_f} \int_0^{2\pi} \psi_{CORO}(\rho,\alpha)\rho\, d\rho\, d\alpha\right) / \pi({\rho_f}^2 - {\rho_i}^2)}{\psi_{PSF}(0)} \tag{8.2}$$

Where ρ_i and ρ_f are the inner and outer radii of the annular region; $\psi_{PSF}(0)$ is the maximum intensity of the star image on the detector (without the coronagraph, except for the APLC and APRC for which this term includes the apodizer transmission); $\psi_{CORO}(\rho,\alpha)$ is related to the intensity of the coronagraphic image on the detector.

We use these metrics to study the variation of performance with respect to telescope parameters and as a function of the Strehl ratio.

The area of calculation in the focal plane for $\overline{C_{CORO}}$ can be well matched to the instrumental parameters (the width of the ring can be modified to match science requirements). For most results presented hereafter, the search area is bounded at $\rho_i = 4\lambda/D$ for short radii (IWA requirement) and at $\rho_f = 80\lambda/D$ for large radii (XAO cut-off frequency). These limits translate to 30mas and 0.63" respectively at 1.6μm, and allow coronagraphs comparison over a large region of interest while keeping the study general and independent of a specific science requirement. The impact of ρ_i and ρ_f values will be further discussed.

8.3 Parameters sensitivity vs. residual atmospheric speckles

8.3.1 The wavefront correction quality

Influence of the XAO correction

We first started to compare the coronagraphic performance as a function of the Strehl ratio (S) with the $\overline{C_{CORO}}$ metric. The objective of this first analysis is to assess the raw contrast delivered for each coronagraph considering only the diffraction by the edges of the pupil and the residual atmospheric phase aberrations which is leaking through the XAO system. Therefore, these defects will produce a perfectly averaged halo of speckles which sets

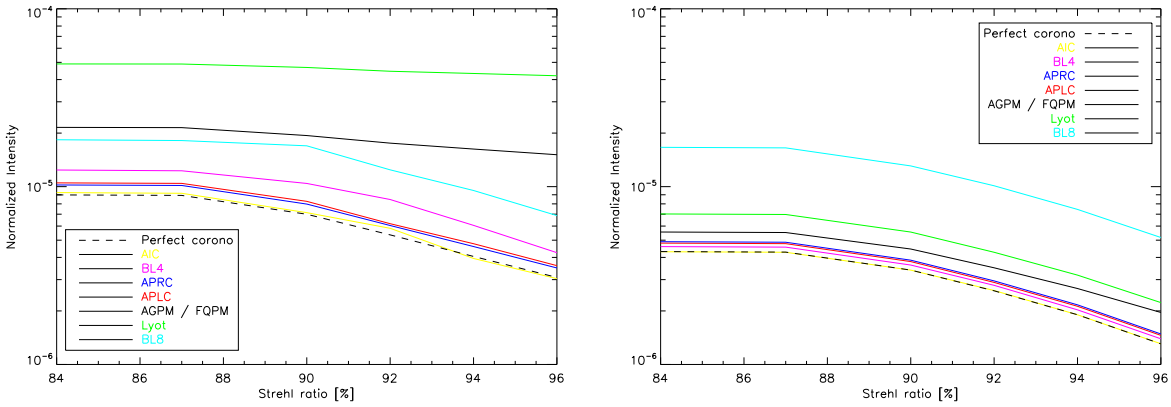

Figure 8.1: Variation of $\overline{C_{CORO}}$ as a function of the Strehl ratio for all coronagraph concepts. Left: at $4\lambda/D$ (IWA), Right: averaged from $4\lambda/D$ (IWA) to $80\lambda/D$ (AO cut-off frequency).

the level of the photon noise in the coronagraphic image plane. Obviously the contrast level must be much better than this coronagraphic halo but this noise contribution estimate will be necessary to investigate the signal to noise ratio achievable for detecting exoplanets with ELTs in further studies.

Figure 8.1 shows $\overline{C_{CORO}}$ as a function of the Strehl ratio for two locations in the coronagraphic image. At the left, for an angular separation of $4\lambda/D$=IWA and to the right, averaged in between the IWA and the AO cut off frequency ($\mathscr{F}_{AO} = 80\lambda/D$). In each case, $\overline{C_{CORO}}$ for a perfect coronagraph is plotted as a dashed line. This ideal model is helpful since it reveals the limitations from the residual aberrations that are leaking through the XAO system only (i.e by principle there is no pupil edges diffraction contribution since all the coherent part of the light has been removed). The actual contribution on the limitations sets by the diffraction of the edges of the pupil is actually revealed by the difference of departure of real coronagraph $\overline{C_{CORO}}$ curves to that of the ideal model. Two regimes can be identified:

- where $\overline{C_{CORO}}$ of a coronagraph follows $\overline{C_{CORO}}$ of the ideal model, which corresponds to the speckle dominated regime where coronagraphs perform much better than the XAO and so the performance is set by the XAO itself. In other words, improving the XAO correction is necessary to improve final performance. In such a case, contrast increases with S and a substantial gain in starlight suppression imposes to reach a high level of wavefront correction (S ~94%). For the considered range of S values (84 - 96%) all the coronagraphs considered are in this regime (Fig. 8.1, right) except for the AGPM/FQPM and the Lyot but only when $\overline{C_{CORO}}$ is evaluated at the IWA (Fig. 8.1, left).

- the diffraction dominated regime appears when $\overline{C_{CORO}}$ of a coronagraph does not anymore follow $\overline{C_{CORO}}$ of the ideal model and is about flat, i.e phase aberrations are small enough to reveal the actual limitation of the coronagraphs and so the limitation is mostly set by the diffraction by the edges of the pupil. In other words, improving the XAO correction is useless since the limitation comes from the coronagraph (AGPM/FQPM and Lyot cases previously underlined at IWA).

The particular case where $\overline{C_{CORO}}$ is about flat while still following the ideal model (below $S = 88\%$) corresponds to a case where the limitation comes from the residual phase aberrations that are present in a so large amount that improving the XAO correction (from 84 to 88%) does not yield to an improvement of the performance.

The AGPM/ FQPM and Lyot coronagraphs have a strong dependency with the area where $\overline{C_{CORO}}$ is evaluated which indicates that most of the residual energy is actually localized near the image center in contrary to other coronagraphs. This is a consequence of the diffraction by the central obscuration which is not favorable to such designs. At angular distances larger than $4\lambda/D$, the AGPM/FQPM and the Lyot perform as well as other designs. Thus, the choice for the value of ρ_i and ρ_f allows a more homogeneous comparisons of coronagraphs.

The contrast achieved with the BL8 is significantly worse than with other coronagraphs. To operate with a 30% central obscuration and a somewhat small IWA of $4\lambda/D$ the BL8 requires a very aggressive pupil stop

($\mathscr{T}$ = 13.8). Although, this optimization provides a very deep contrast in a perfect situation when phase aberrations are negligible (S = 100%) it is no longer the case in a realistic condition, even at high Strehl ratios. This is obviously true for any concepts but the decrease of contrast between the perfect and realistic situations is even more abrupt with the BL8.

8.3.2 Parameter dependency

Figure 8.2 and 8.3 analyze in detail the impact of each parameters defined in Table 8.2 first using $\overline{C_{CORO}}$ as function of the Strehl ratio (left column) and second for the particular case of S=90% using $C_{CORO}(\rho)$ the coronagraphic contrast as a function of the angular separation (right column). The variation of each parameter is represented with error bars indicating the dispersion of contrast. For instance, for figures on the left column, each curve presents a value of $\overline{C_{CORO}}$ of telescope parameter and the sensitivity of $\overline{C_{CORO}}$ to this parameter within a given range is shown as an error bar. The range is given in the legend close to the nominative value. For figures on the right column, for the sake of clarity, only the sensitivity to the parameter is plotted (i.e no nominative value are presented).

For each case, the limit of detection achievable with a perfect coronagraph is plotted as a dashed line. The left column of Fig. 8.2 and 8.3 shows the same quantity as in Fig. 8.1 but for the several parameters independently. The variation of contrast as a function of the Strehl ratio is identical for all parameters and all coronagraphs. In other words, the curves are parallel in between each others and parallel to that of Fig. 8.1. This simply means that the contrast is most of the time dominated by the XAO halo and the diffraction by the edges of the pupil. For all coronagraphs but AIC, APRC and APLC, the parameters impacts the contrast at various levels.

In the following, we describe the impact for each coronagraph in the case of S=90% (right column):

AGPM / FQPM – At distances shorter than $3\lambda/D$, the image is dominated by the diffraction of the central obscuration while beyond the contrast limit is set by the spider diffraction spikes. For the worst values of the dominating parameter the contrast reaches 2.10^{-4} at $4\lambda/D$ and only improves by a factor of 2 at $10\lambda/D$. Achievable contrast is quite far from the ideal model (dashed line).

AIC – In that case, pupil diffraction is negligible as far as it is centro-symmetrical, but pointing errors are clearly dominating the contrast up to $20\lambda/D$. The impact is as large as that of the central obscuration for the AGPM/FQPM. At larger distances, the performance of the AIC is identical to that of a perfect coronagraph. At $4\lambda/D$ the contrast is 7.10^{-5} while at $10\lambda/D$ it is improved to 2.10^{-5}.

APRC – $10\lambda/D$ sets the limit between pointing error dominated regime and pupil shear dominated regime. At $4\lambda/D$ the contrast reaches 4.10^{-5} and 9.10^{-6} at $10\lambda/D$.

Lyot – Spider diffraction limits the contrast at any angular radius. However, the impact is not that much important. The central obscuration has also a significant signature. At $4\lambda/D$ (near the mask edges) the contrast is only 1.10^{-4} but it improves by a factor of 10 at $10\lambda/D$.

APLC – The dispersion of contrast is negligible in that case for any parameter. The APLC achieves the same performance as the perfect coronagraph beyond the IWA and does not feature a dominant parameter. At $4\lambda/D$ the contrast reaches $\sim 1.10^{-5}$ and 5.10^{-6} at $10\lambda/D$.

BL4 – As for the APLC, the contrast is very close to the perfect case and the dispersion of contrast is small with however a dominance of the spider diffraction spikes. At $4\lambda/D$ the contrast is 2.10^{-5} while at $10\lambda/D$ it is improved to 6.10^{-6}.

BL8 –The spider diffraction dominates significantly at any angular separations. The contrast is much worse than for the BL4 and reaches 2.10^{-4} at $4\lambda/D$ and 5.10^{-5} at $10\lambda/D$. The BL8 suffers from a severe reduction of the pupil stop therefore distorting the off-axis PSFs while reducing the throughput. High order BLs are actually not suited for ELTs.

The impact of spider diffraction must be mitigated since contrast profile are azimuthally averaged and therefore some image areas feature larger contrasts. Planets could be observed within the clear areas between the spider spike diffractions. This choice depends on the observing strategy.

For all coronagraphs, amplitude and phase aberrations on segments in the considered range have much less impact than the diffraction by the pupil edges (central obscuration and spiders). For the small IWA coronagraphs, the pointing error is the most dominant factor.

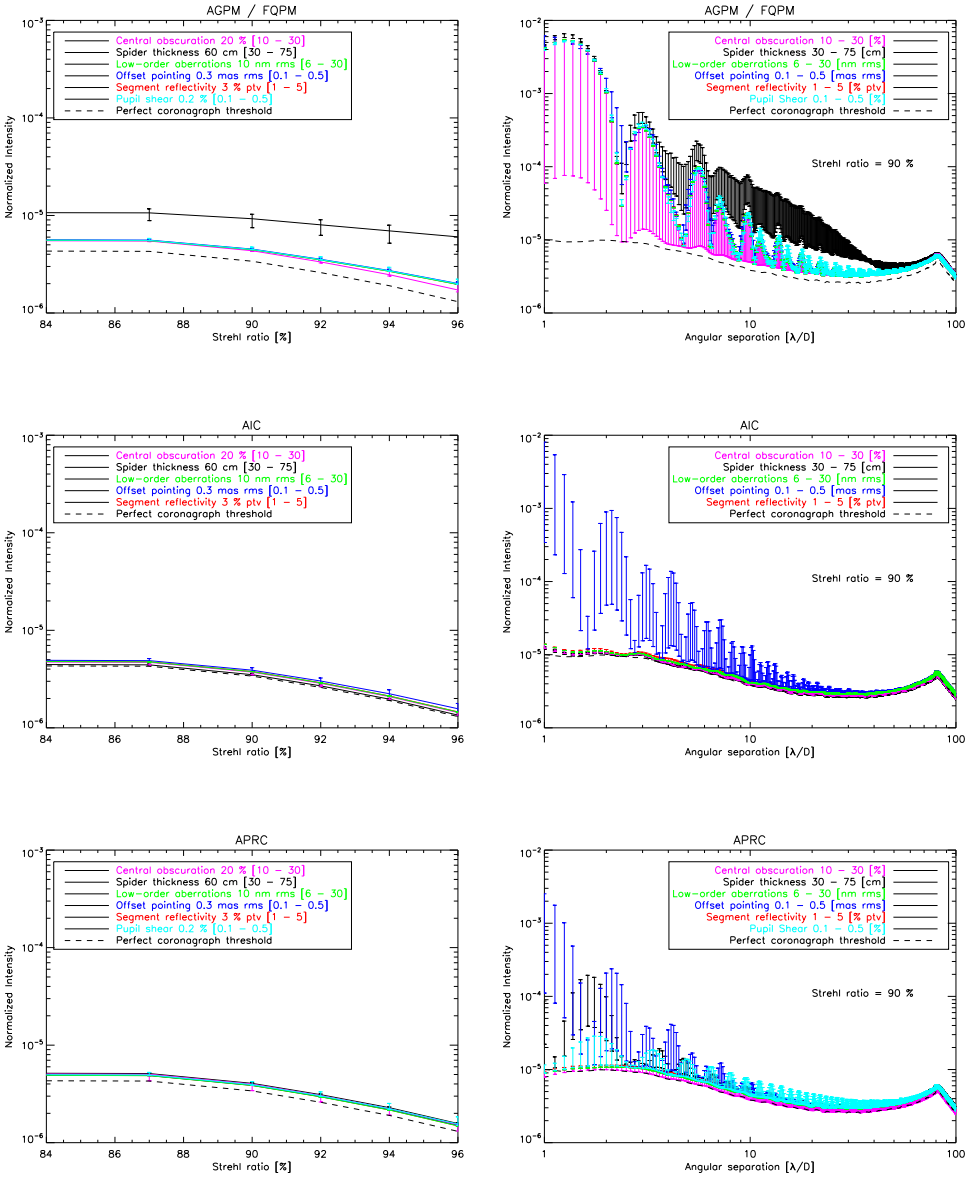

Figure 8.2: Averaged contrast $\overline{C_{CORO}}$ (left) and contrast profile $C_{CORO}(\rho)$ (right) for the different parameters and for the following coronagraphs: AGPM/FQPM, AIC, and APRC. The Strehl ratio on the right plots is 90 %. Error bars indicates the amplitude of the contrast variation. The dashed line stands for the ideal case.

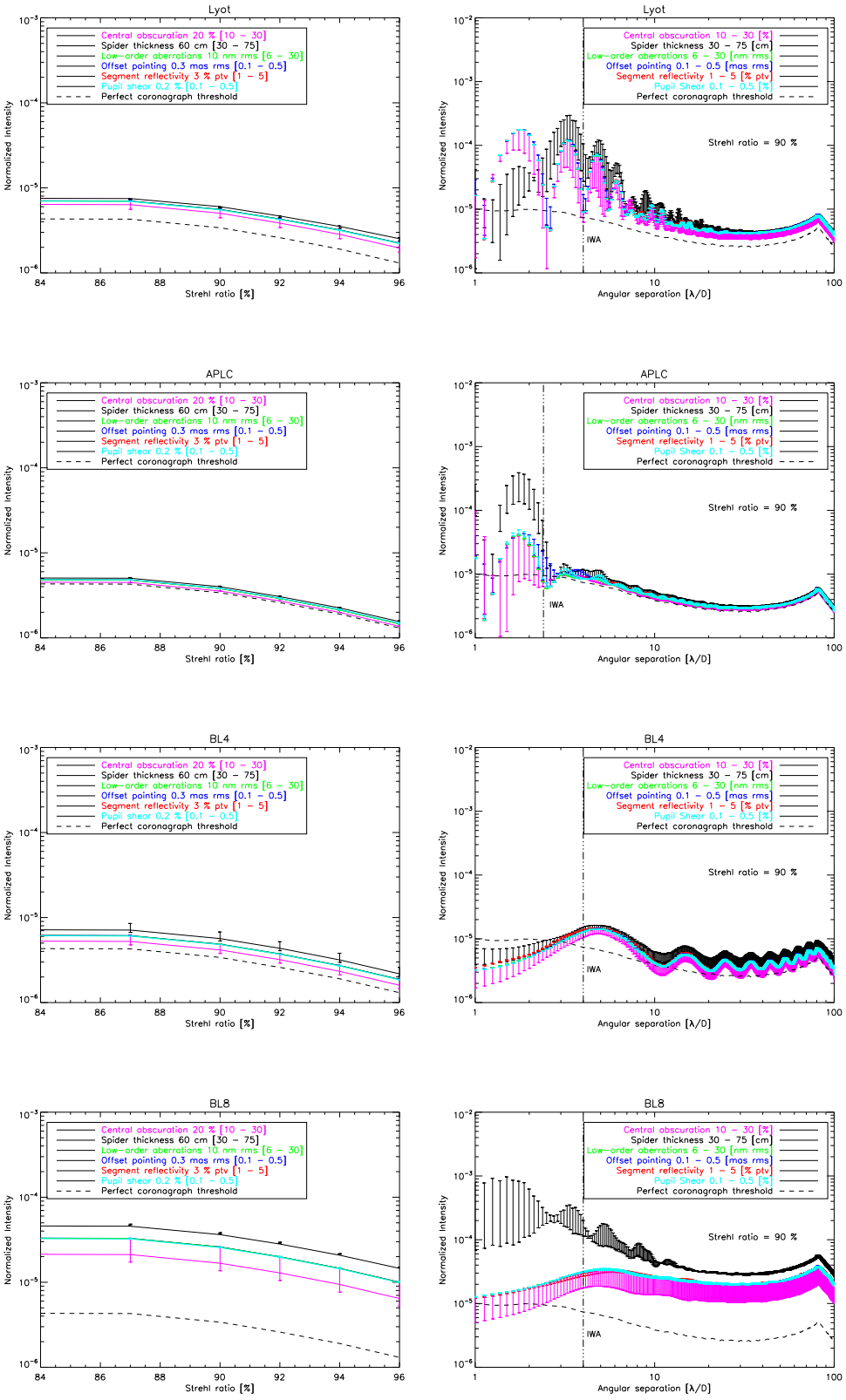

Figure 8.3: The same as Fig. 8.2 but for the following coronagraphs: Lyot, APLC, BL4 and BL8

9

Characterization/comparison with Differential Imaging system

Contents

Abstract - *The presence of a residual atmospheric wavefront perturbation even if corrected with a XAO system is limiting the contrast behind a coronagraph to about* 10^4 - 10^6*. The first series of simulations to assess the impact of telescope parameters on coronagraph performance were carried out at this level (Chapter 8). However, it is important to perform the same analysis at the level of contrast which is adequate for planet detection (*10^8 - 10^{10}*) to evaluate how the sensitivity of coronagraph propagates. To enhance the contrast, a second step is required to suppress the speckle noise (composed of dynamical and static aberrations). On SPHERE and GPI, specke calibration is implemented in the form of spectral and polarimetric differential imaging (Racine et al. 1999, Marois et al. 2000, Baba et al. 2003 [78, 62, 13]). A larger contrast is then achievable through appropriate data reduction. Here, for the sake of generality we consider a simple model of differential imaging system to derive first order conclusions.*

9.1 Purposes

In this Chapter we compare coronagraph concepts discussed in Chapter 8 and investigate the impact of major error sources that occur in a coronagraphic telescope (central obscuration, secondary support, low-order segment aberrations, segment reflectivity variations, pointing errors) as in the latter chapter but this time the analysis is performed after a general and simple model of speckle calibration, assuming common phase aberrations between the XAO and the coronagraph (static phase aberrations of the instrument) and non-common phase aberrations downstream of the coronagraph (differential aberrations provided by the calibration unit). We derive critical parameters that each concept will have to deal with by order of importance and compared to the analysis performed after XAO correction.

9.2 Assumptions

Most of the assumptions are identical to the ones made in Chapter 8, but for the sake of clarity we briefly recall them.

9.2.1 Constraint on IWA

We define the IWA as the angular separation for which the diffraction peak of a planet is reduced by a factor of 2. As a baseline, we fixed the limit of the IWA to the reasonable value of $4\lambda/D$.

In the next simulations, the Lyot coronagraph has a mask size of $7.5\lambda/D$ (i.e a corresponding IWA of 3.9 λ/D). The APLC has a $4.7\lambda/D$ mask diameter (i.e IWA = 2.4 λ/D). We also consider two band-limited masks with different orders: a 4^{th} order (sin^4 intensity mask with $\epsilon = 0.21$) and a 8^{th} order (m=1, l=3 and $\epsilon = 0.6$). BLs parameter ϵ both control the IWA and Lyot stop throughput. Other coronagraphs considered here (FQPM/AGPM, AIC, APRC) have intrinsic properties that lead to very faint IWA. All the coronagraph parameters are resumed in Table 8.1.

9.2.2 Differential Imaging hypothesis

As in Chapter 8 we consider a 42 meters ELT with 30% (linear) central obscuration ratio as expected for the European ELT (E-ELT, Gilmozzi et al. 2008 [42]), except when we evaluate its impact. As for the wavelength, we adopt a baseline of $\lambda = 1.6\mu m$ (centre of the H-band). The image plane is sampled with $0.125\lambda/D$ per pixel. Here, for sake of generality we assume a general and simple scheme of Differential Imaging (DI, Fig. 9.1). A

Figure 9.1: General principle of the differential imaging simulations: δ_c is the common aberrations upstream of the coronagraph and δ_{nc} the non-common aberrations downstream of the coronagraph.

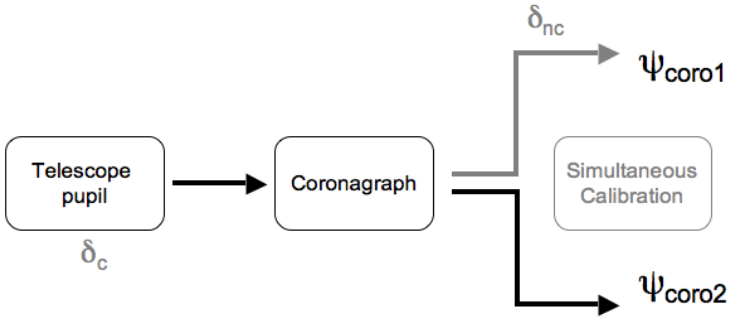

detailed analysis of contrast performance for ELTs with DI has been performed by Cavarroc et al. 2006 [30]. For the reader´s convenience we repeat in the following the main assumptions and results used in this present study. We consider two images taken simultaneously using two channels downstream of the coronagraph (same spectral band, same polarization state). In such a case, the contribution to the wavefront error is made of two terms :

Table 9.1: Values and amplitudes of parameters used in the simulation.

	DI simulation
Input parameters	
telescope diameter	42 m
wavelength	1.6 μm
focal sampling	0.125 λ/D / pixel
static aberrations upstream of the coronagraph	10 nm rms
static aberrations downstream of the coronagraph	0.3 nm rms
central obscuration default value	30%
Studied parameters	
central obscuration	10 - 30 [%]
spider vanes thickness	30 - 75 [cm]
segments reflectivity (~750 of 1.5m diameter)	1 - 5 [% ptv]
segments static aberrations (~750 of 1.5m diameter)	6 - 30 [nm rms]
pointing errors	0.1 - 0.5 [mas rms]
pupil shear	0.1 - 0.5 [%]

- the static common aberrations (δ_c) in the instrument upstream of the coronagraph.
- the non-common aberrations (δ_{nc}) downstream of the coronagraph. The latter corresponds to differential aberrations since the light goes through two different optical paths.

Here, the residual phase left uncorrected by the XAO system is omitted since it will be averaged to an azimuthally constant pattern over time and be suppressed by subtraction in the two channels (if the photon noise is neglected). Therefore, the detectability for an infinitely long exposure only depends on δ_c and δ_{nc}. The static aberrations δ_c and δ_{nc} are described by PSDs with f^{-2} variation (f is the spatial frequency). Since aberrations are critical at close angular separations, we assume that the PSDs at low frequencies were "shaped" (flat in the range $0 < f < f_c/4$, with f_c the cut-off frequency of the XAO.

Many combinations of δ_c, δ_{nc} are possible to reach the desired contrast level. But, as we are interested in the DI performance rather than the technique itself we adopt an arbitrary amplitude of 10 nm rms and 0.3 nm rms for δ_c and δ_{nc} respectively. A contrast level of 10^9 is thus achievable which is consistent with EPICS science contrast requirements (Kasper et al. 2008 [56]). In Table 9.1 we resume most of the input parameter assumptions as well as the studied parameters values.

9.2.3 Comparison metric

When using a DI system implying some image subtraction, the average contrast is no longer suited. Results will be presented as radial contrast plots (5σ normalized contrast vs. angular separation) to compare coronagraphs:

$$C_{DI}(\rho) = \frac{5 \times \sigma\left[\psi_{CORO_1}(\rho) - \psi_{CORO_2}(\rho)\right]}{\psi_{PSF}(0)} \tag{9.1}$$

Here, $\sigma[]$ is an operator which denote the azimuthal standard deviation measured in a ring of width λ/D on the subtracted image $\psi_{CORO_1} - \psi_{CORO_2}$. C_{DI} quantifies the ability to pick out an off-axis companion at a given angular distance.

Here, we adopt that simple metric for sake of clarity but we note that more appropriate criteria adapted to the case of high contrast images have been developed by Marois et al. 2008 [63]. Caution: this metric is not weighted by the overall coronagraphic system transmission ($\mathscr{T}$). This throughput is set by the pupil stop transmission (times the mask transmission for BLs). The system transmission (presented in Table. 8.1) basically remains a physical limitation that must influence the decision for which coronagraph to implement in practice (integration time issue), but here we are more interested on upper limit of coronagraphs for comparison clarity in regards with external limitations. This point will be further discussed in Sec. 9.3.2.

9.3 Parameters sensitivity vs. quasi-static speckles

9.3.1 Results

First of all, compared to the study with XAO (Chapter 8), the parameters that limit the contrast of a given coronagraph are the same except that at large angular distances the AO halo is no longer dominant and then the dispersion of parameters is much larger.

AGPM / FQPM – A clear limit is seen at $3\lambda/D$ between a central obscuration limited regime and a spider diffraction limited regime. Also, beyond $20\lambda/D$, the impact of the pupil shear becomes predominant. The level of detectability is rather flat between 4 and $10\lambda/D$ achieving 2.10^{-7}.

AIC – All symmetrical defects are quite small compared to the pointing errors. At $4\lambda/D$ the performance is similar to that of the AGPM/FQPM and improves to 7.10^{-8} at $10\lambda/D$ although being far from the ideal model.

APRC – The separation between pointing errors and pupil shear limited regime has moved from 10 to $20\lambda/D$ with respect to Fig. 8.2 (Chapter 8). At $4\lambda/D$ the detectability reaches 3.10^{-8} while at $10\lambda/D$ is improves to 7.10^{-9}. A gain of 1 order of magnitude is reached compared to AGPM/FQPM and AIC concepts.

Lyot – The spider diffraction still dominates the contrast which reaches 1.10^{-7} at $4\lambda/D$ and improves by a factor of 10 at $10\lambda/D$. Considering its simplicity, the Lyot coronagraph is suitable for ELTs.

APLC – It features one of the best detectability level with the BL4. In contrary to Fig. 8.3 (Chapter 8), it is dominated by the spider diffraction (and pupil shear at very large angular separation, i.e after $50\lambda/D$) but achieves at $4\lambda/D$ a level of 1.10^{-8} and 8.10^{-9} at $10\lambda/D$.

BL4 – Very high contrast can be achieved close to the limit imposed by static aberrations. The sensitivities to the parameters are rather small. The level of detection is identical at 4 and $10\lambda/D$: 2.10^{-9}.

BL8 – For the same reasons expressed in Chapter 8, BL8 is not as efficient as BL4. Up to $50\lambda/D$ the dominating parameter is the spider diffraction, and at larger angular separations the pupil shear is dominating. Compared to BL4, the performance degrades by about 2 orders of magnitude in the middle range of frequencies and about 1 order of magnitude at very large angular separations. At $4\lambda/D$ the detectability reaches 1.10^{-7} while at $10\lambda/D$ it improves to 7.10^{-8}.

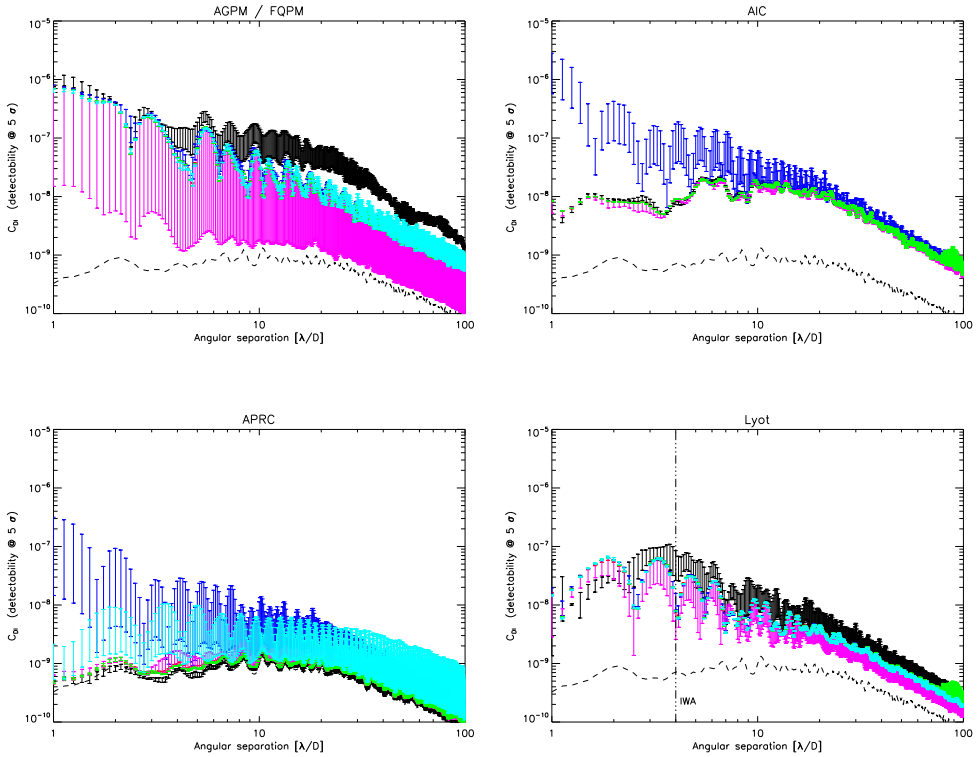

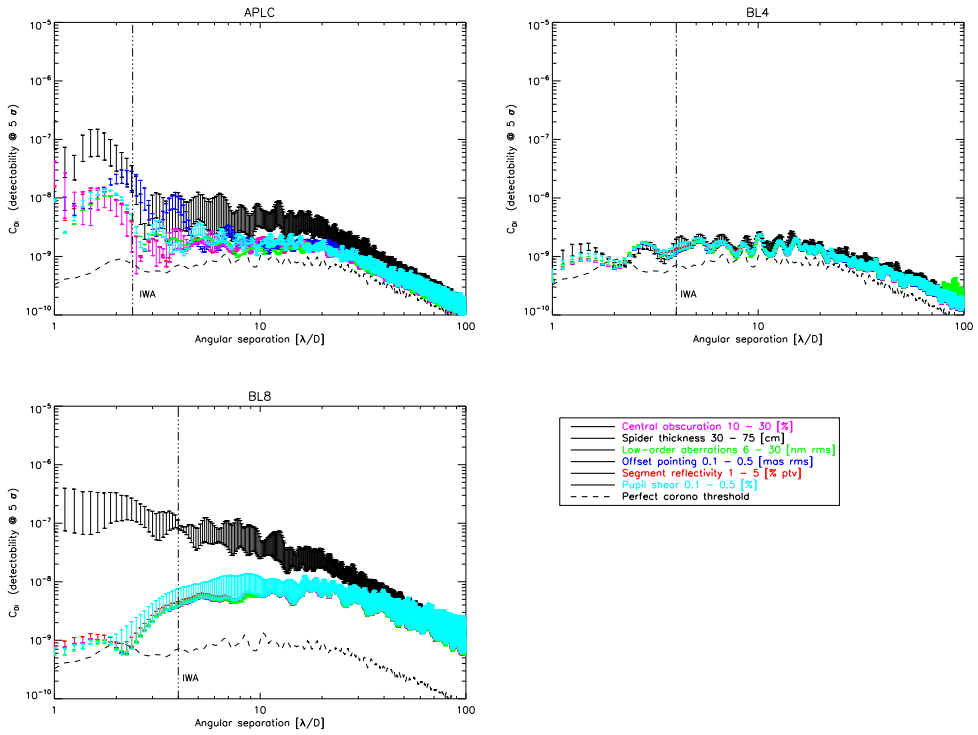

Figure 9.2: Contrast profile at 5σ, $C_{DI}(\rho)$, for the different parameters and for each coronagraph. Error bars indicates the amplitude of the contrast variation. The dashed line stands for the ideal case and was obtained for static aberrations $\delta_c = 10$ nm rms, $\delta_{nc} = 0.3$ nm rms.

9.3.2 Further comparison between APLC and BL4

In previous sections, the APLC focal mask diameter ($4.7\lambda/D$, IWA=$2.4\lambda/D$) results from an optimization based on the size of the central obscuration while the mask of the BL4 is optimized for an IWA of $4\lambda/D$. This sections compares these two designs in more details for a similar IWA.

Figure 9.3 presents a DI simulation when both the APLC and the BL4 are optimized for IWA=$2.4\lambda/D$ For that, the BL4 was re-optimized ($\epsilon = 0.33$, $\mathscr{T} = 12.5\%$) while APLC has remain the same ($\mathscr{T} = 54.5\%$). Here, we only present the worst case corresponding to the largest values of parameters (except for the spider thickness, sets to 60cm, E-ELT as baseline). The net effect of a smaller IWA for the BL4 is a less transmissive pupil stop, and as a result pupil shear becomes the dominant effect. From 2.4 to $20\lambda/D$, the BL4 has a lower sensitivity to parameters, and beyond $20\lambda/D$ both are quite comparable.

However, if we assume a comparable system transmission for these coronagraphs, the APLC will then deliver a better performance. This can be done either with a more aggressive APLC pupil stop and hence the achievable contrast is increased or conversely with a more transmissive BL4 stop. Even if the performance of the BL4 with a small IWA is close to that of a perfect coronagraph, its interest is questionable since the transmission is a factor of 4 lower than that of the APLC. A signal to noise ratio analysis including fundamental noises (photon, read-out) is needed here to evaluate how many stars could be observed with a low throughput at such a level of contrast.

Same analysis was performed for an IWA of $4\lambda/D$. In that case the APLC has been re-optimized to $7.5\lambda/D$ ($\mathscr{T} = 50.0\%$) while the BL4 is identical to previous sections ($\epsilon = 0.21$, $\mathscr{T} = 22.4\%$). In such a case, the transmission is still favorable for APLC by a factor 2. Conclusions on contrast performance are identical than in the previous case.

The interest of the BL4 for ELTs would be deserved either to very bright objects or to large IWA to relax system transmission but in that case further analysis would be needed to compare its performance to that of the Lyot mask.

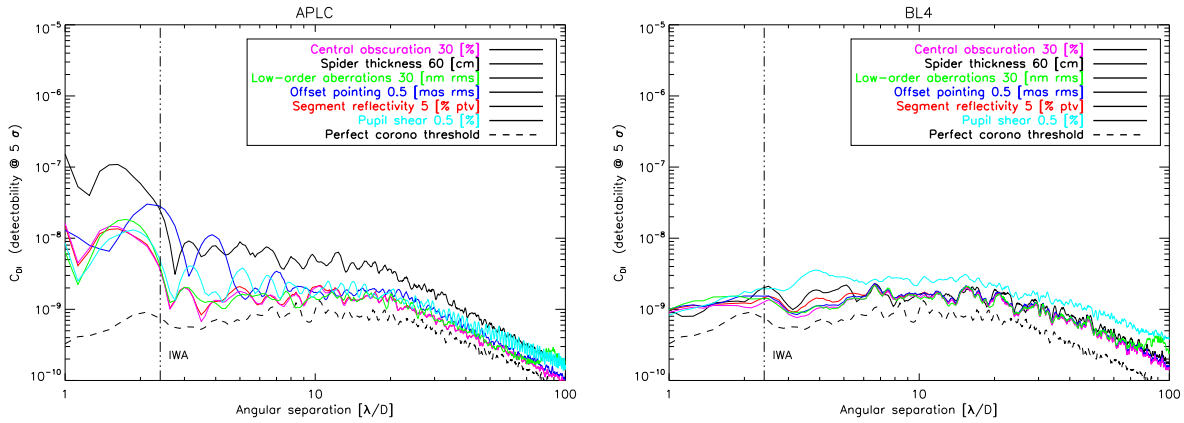

Figure 9.3: C_{DI} (5σ detectability (δ_c = 10 nm rms, δ_{nc} = 0.3 nm rms)) vs. error sources for APLC (left) and BL4 (right) optimized for IWA = $2.4\lambda/D$

Table 9.2: Preliminary parameters specification to reach best performance (set by 30% central obscuration) for each coronagraph within the simulated space parameters. Results are based on DI simulations for 30% central obscuration configuration. It is assumed that within specifications coronagraphs do not delivered the same detectability.

Coronagraph	Acceptable parameter error values				
	Spider	Segment error		Offset pointing	Pupil shear
	[cm]	Phase [nm rms]	Reflectivity [% ptv]	[mas rms]	[%]
AGPM/FQPM	30	30	5	0.5	0.5
AIC	75	30	5	0.2	-
APRC	75	30	5	0.2	0.3
Lyot	45	30	5	0.5	0.5
APLC	45	30	5	0.5	0.5
BL4	60	30	5	0.5	0.5
BL8	30	30	5	0.5	0.2

9.3.3 Limitations imposed by the quasi-static common aberrations

In this part, we discuss the impact of δ_c on the detectability in presence of some error sources. Previously we fixed the level of δ_c and δ_{nc} to 10 and 0.3 nm rms respectively. At this point, it is difficult to predict the level of quasi-static aberrations upstream and downstream of the coronagraph that it is possible to reach. However it is known from Cavarroc et al. 2006 [30] that the detectability has a quadratic dependence on δ_c and a linear dependence on δ_{nc}. On GPI, 1 nm rms is expected for δ_c. Therefore, it is important to investigate coronagraph behavior to a lower value of δ_c which could potentially allow to relax the value of δ_{nc} (a level of 0.3 nm rms is a severe constraint in practice). The problematic is therefore to know if coronagraphs can reach deeper detectability if δ_c is reduced with respect to the limitation imposed by the error sources previously considered.

To tackle this problem, we compared the 5σ detectability reach by each coronagraph by varying the level of δ_c form 20 to 0.1 nm rms and by imposing some error sources. We restrict the study to the impact of the central obscuration ratio, and the offset pointing since they are representative of the minor (in the sense that the central obscuration signature sets the limit by the diffraction of the pupil) and major issue respectively. The objective is to define the level of δ_c from which an improvement is useless because detectability is dominating by other parameters. Results are resumed in Table. 9.3.

By considering the central obscuration ratio only, most of the coronagraph (except FQPM / AGPM for 30%) reach the diffraction-limited regime only at δ_c = 0.1 nm rms. Thus, a deep improvement compared to results with δ_c = 10 nm rms is reachable and therefore mandatory.

Nevertheless, if we focus on pointing errors (the major issue) an improvement of δ_c is questionable for some

Table 9.3: Influence of the quasi-static aberration upstream of the coronagraph

Coronagraph	Level of δ_c [nm] from which improvement is useless (δ_{nc} = 0.3 nm)			
	central obscuration [%]		Pointing errors [mas rms]	
	10	30	0.1	0.5
FQPM / AGPM	0.1	20	10	20
AIC	0.1	0.1	0.1	20
APRC	0.1	0.1	0.1	20
APLC	0.1	0.1	0.1	0.1
Lyot	1	1	1	1
BL4	0.1	0.1	0.1	0.1
BL8	0.1	0.1	0.1	0.1

coronagraphs. Actually, there is an important difference between amplitude-type and other concepts: for 0.5 mas rms poiting error (SPHERE requirements), only amplitude concepts (APLC, Lyot, BL4 and BL8) yield to a smaller value of δ_c (1 or 0.1 nm rms, for instance) owing to their larger IWA. This confirm that an important effort to smaller pointing error (0.1 mas rms, for instance) is making sense.

However, it is difficult to predict if an improvement of δ_c is useful or not in reality since a wide number of error sources will interfere, therefore the effect of an improvement on δ_c might be a compromise. A complete knowledge of the telescope limitations is crucial.

10

Coronagraphs characterisation/comparison conclusion

Contents

Abstract - *This last Chapter of Part IV closes the comparison study we carried out. We give here some interpretations of the XAO and DI results obtained and draw conclusions. Specifically, we underline three coronagraph categories as function of the accessible angular separation and propose optimal one in each case. Along our study, most of the time, amplitude concepts appeared more favorable, and the Apodized Pupil Lyot Coronagraph specifically gathers the adequate characteristics to be a baseline design for ELTs.*

10.1 Interpretation of XAO and DI results

When considering the XAO halo, most coronagraphs (except BL8) provide roughly the same performance at mid angular radii (Fig. 8.1). Throughput consideration and sensitivity to parameters are then mandatory to make a difference. In this section we summarize the most important results of the study we carried out.

For each coronagraph, the sensitivity to parameters propagates similarly between the raw coronagrahic images (XAO) and Differential images. The limiting factors are the same at these two contrast levels.

As for band-limited, increasing the order of the mask (beyond the fourth order) is not advantageous since the Lyot stop throughput is severely restricted by the central obscuration and spiders. The Lyot stop throughput places a limit on the order of the mask that can be implemented on an ELT. Fourth order are preferable to eighth (or higher) order. This result confirms the one obtained by Crepp et al. 2007 [34] where they compared Lyot type coronagraphs combined with AO system using a filled circular pupil. As already mentioned here above, the BL8 is very efficient for perfect optics but its interest is questionable in the context of ELTs.

Coronagraphs with small IWA (AGPM/FQPM, AIC) are not able to reach the ultimate level sets by static aberrations. This is either a result of a high sensitivity to pointing errors (AIC) or an effect of the large residual amount of diffracted light by the pupil central obscuration which is not sufficiently suppressed (AGPM/FQPM). We note that solution exist to improve the peak suppression and pointing error sensitivity in the precise case of phase mask, such as the combination of a small Lyot mask placed in the center of the phase mask. A trade-off analysis would be mandatory to select the diameter of this additional Lyot mask.

For all coronagraphs, the signature of the central obscuration appears at the lowest contrast level but still can be a limitation. For instance, with the AGPM/FQPM, the other aberrations are pinned to the contrast level imposed by the central obscuration at small angular distances. Also, pointing errors and spider diffraction are critical for most coronagraph concepts (AGPM/FQPM, AIC, APRC, Lyot, BL8)

Among the concepts we have studied here, some are able to provide good and homogenous performances, namely the APRC, the APLC, the Lyot and the BL4.

To further improve the contrast level, the main effort will have to be made on the pointing errors (telescope vibrations and stability of the XAO environment) and on the pupil shear (alignment issue). The impact of the spider diffraction shows either the importance of a coronagraph that is not sensitive to this effect (APRC, BL4, AIC), or the necessity of a specific system that can remove their impacts (Abe et al. 2006 [3]).

Achieving a deep contrast imposes a concept of coronagraph which can accommodate some telescope characteristics while preserving a reasonable throughput. Amplitude concepts like the APLC and the BL4 appear the most suited in that case. The APLC is foreseen as the baseline design for EPICS and independent studies have shown that it is more suited to focal plane wavefront correction, a mandatory technique for EPICS. In the next Section, impact of the design (IWA) on these concepts and throughput considerations will be addressed.

Finally, the simulation in Fig. 9.2 allows us to put a specification to each parameter of the simulation (within the range of values we considered) corresponding to the best contrast achievable with a given coronagraph (presented in Table. 9.2). This ultimate contrast level is driven in most cases by the central obscuration that we took equal to 30% in this analysis. A coronagraph that potentially reaches high contrasts close to the level imposed by static aberrations also requires a more severe constraints on the parameters while conversely, specifications can be relaxed for a less efficient coronagraph.

10.2 Conclusion

The objective of the study we carried out was to assess the impact of system parameters on several coronagraph concepts and to start a first order comparison in the context of ELTs. We have selected a few coronagraphs (or families) and we evaluate the behavior of the delivered contrast with respect to the main sources of degradations that occur in a coronagraphic telescope at two levels of contrast when:

- considering the residuals of an XAO system.
- a calibration of this halo is performed by the use of a differential imaging system. In that case, the residuals are set by the static aberrations.

The contrast plots that are presented in this paper are preliminary in the sense that we have considered a simple model of image formation with a limited number of parameters of which most are not yet fully defined.

It is understood that a detailed study would involve signal to noise ratio estimation considering different type of astrophysical objects as it was done for SPHERE/VLT (Boccaletti et al. 2005, 2006 [24, 25]). A parallel analysis has been initiated for the EPICS project (Vérinaud et al. 2007 [100]). We also note that some coronagraph concepts analyzed through this study can deliver better performance when implemented in cascade (Aime et al. 2004, Baudoz et al. 2007 [7, 15]). Performance resulting from these configurations in the precise case of ELTs must be investigated further as already started for EPICS. Involving a large number of existing coronagraph designs is mandatory as well (Phase Induced Amplitude Apodization Coronagraph (Guyon et al. 2004 [47]), Checkerboard-Mask Coronagraphs (Vanderbei et al. 2004 [97]), for instance).

The study – preliminary results of system level specification are shown in Table. 9.2 – is then one step toward this ultimate goal. Under these assumptions, we can derive three categories of coronagraphs:

- those adapted for short angular separations, but conversely sensitive to pointing errors: AGPM, AIC, APRC. In that case, the APRC delivers the more robust performance since it is less sensitive to system parameters.
- those adapted for intermediate angular separations: APLC and Lyots where the APLC has the advantage to provide better performance with smaller IWA and low sensitivities to system parameters.
- those adapted for large angular separations: BL4 and APLC.

More specifically, the APLC gathers the adequate characteristics to be a baseline design in the case of ELTs. In addition, more sophisticated implementations are possible (Aime et al. 2004 [7]) with the goal to provide deeper contrast and/or relax IWA constraint. Potentially, it can be upgraded (although with a particular optical system) to feature a 100% throughput (using two mirrors apodization system based on the Phase Induced Amplitude Apodization principle, PIAA Guyon et al. 2003 [45, 47], to generate the apodizer through beam redistribution).

Chromatic effects can seriously drive the choice of which coronagraph to implement. Actually, amplitude concepts are again more favorable for producing low chromatic dependencies. For instance, APLC focal plane mask size can be easily re-optimized to mitigates bandwidth effects. In the same time, many programs are striving to make other concepts achromatic, as the AGPM or the multi-FQPM (Mawet et al. 2005a,b and Baudoz et al. 2007 [67, 68, 15]), achromatic and improved versions of the FQPM.

However, to fully take advantage of a coronagraph the most demanding parameters is clearly the level of the XAO residuals and then a lot of efforts has to be made to provide very high Strehl ratios on ELTs.

Finally, the manufacturing feasibility of coronagraphs is also a critical issue in the development of an high contrast instrument for ELTs. In that perspective, we have started to prototype several designs (APLC, FQPM, Lyot and BL, Martinez et al. 2008 [66]) to be tested on the High Order Test-bench developed at the European Southern Observatory (Vernet et al. 2006, Aller Carpentier et al. 2008 [101, 10]). Results of these technical aspects will be presented in forthcoming papers (see Part VI).

Part V

Interest of multiple stages coronagraph

11

Suitability of Apodized Pupil Lyot Coronagraph n steps

Contents

Abstract - *In this Section we analyze the interest of the APLC in a cascade configuration (Aime et al. 2004 [7]); the so-called $APLC_n$, where n describe the number of stage. Cascade configuration is an attractive solution to reach deeper starlight extinction. Multiple-stage configuration is currently studied for EPICS through the multi-FQPM concept (Baudoz et al. 2007 [15]). It features several advantages: it decreases the wavelength dependency and reduces the central obscuration impact. Here, we investigate the interest of multiple-stage configuration for the Apodized Pupil Lyot Coronagraph. We limit this study to the case of $n = 2$ which is sufficient enough to derive conclusions. Therefore we compare $APLC_1$ and $APLC_2$ in presence of either telescope parameters as already done in Part III for $n = 1$ or external error sources such as chromaticism, residual phase error that are leaking through the XAO system (as used in Part IV, Chapter 8), common and non-common static aberrations when using a DI system (as defined in Part IV, Chapter 9).*

11.1 General interest of APLC n steps for arbitrary apertures

11.1.1 Problematic

APLC in multiple-stage configuration has been proposed by Aime & Soummer 2004 [7]. $APLC_n$ is in practice implementable for any aperture types (obstructed or filled apertures). However, problematic is slightly different if either the pupil is designed with a central obscuration due to the secondary mirror or not. This is a result of the existing apodizer regime(s) for each case.

In the case of a filled aperture, as already discussed in Chapter 5, there is only one apodizer regime (the so-called bell regime). In such a case, the choice of the apodizer/Lyot mask is driven by performance considerations (starlight suppression efficiency vs. throughput). Optimal configurations (in the sense of the former study described in Chapter 5) do not exist. In such a case, increasing the coronagraphic efficiency requires to increase the Lyot mask diameter and to increase at the same time the apodization effect (i.e leading to a stronger apodizer).

Unlike for the case of obsctructed pupil, for full-filled pupil, increasing the APLC diameter always decreases the throughput since the apodizer becomes stronger. When a single APLC (i.e one stage configuration) is used, to obtain a deep enough starlight rejection, it is necessary to use a large Lyot mask diameter which correspond to a strong apodization. As a result, for filled apertures, at least an APLC of $\sim 3.5\lambda/D$ is required to reach a good contrast. Throughput of such configuration is not favorable (i.e $\sim$ 20%). This requirement can be relaxed if several APLCs are used in cascade. In other words, an $APLC_n$ can increases starlight extinction and/or relaxes the choice of the $APLC_1$ configuration for throughput.

In the case of obstructed pupil, two apodizer regimes exist and throughput does not evolve linearly with the Lyot diameter. Optimal configurations derived from a former study (Chapter 5) gather good performance (constant with the central obscuration ratio) and higher throughput ($>$ 50% indeed). In such a case, the main concern is rather to increase performance instead of relaxing constraint on the 1^{st} stage configuration initially selected. This is especially true when dealing with ELTs, where contrast requirements are extremely high and challenging.

11.1.2 Principle

In this section, we briefly recall the formalism of the $APLC_n$ on the basis of development performed in Chapter 5. The APLC is a combination of n classical Lyot coronagraph (hard-edged occulting focal plane mask, FPM, placed in n focal planes) with an apodization in the entrance aperture. In the following, for the sake of clarity, we omit the spatial coordinates r and ρ (for the pupil plane and focal plane respectively). We also restrict development to $APLC_2$ following Fig. 11.1. The coronagraphic process, corresponding to propagation from the telescope entrance aperture to the detector plane, is expressed in Eq. 11.1 to 11.11. Planes A, B, C, D, E and F correspond to the telescope aperture, the coronagraphic first focal plane, the pupil stop plane and the second coronagraphic focal plane, the second pupil plane and the detector plane respectively. The Fourier transform of a function f is noted $\hat{f}$. The symbol $\otimes$ denotes the convolution product.
The entrance pupil is apodized in the pupil plane:

$$\psi_A = P\phi \tag{11.1}$$

The complex amplitude of the star is spatially filtered (low frequencies) by the FPM:

$$\psi_B = \hat{\psi}_A \times [1 - \varepsilon M] \tag{11.2}$$

The exit pupil image is spatially filtered (high frequencies) by the stop:

$$\psi_C = \hat{\psi}_B \times \Pi \tag{11.3}$$

$$\psi_C = [\psi_A - \varepsilon\psi_A \otimes \hat{M}] \times \Pi \tag{11.4}$$

The coronagraphic complex amplitude (output of an $APLC_1$) is:

$$\psi_D = \hat{\psi}_C = [\hat{\psi}_A - \varepsilon\hat{\psi}_A M] \otimes \hat{\Pi} \tag{11.5}$$

The latter coronagraphic complex amplitude is not imaged on the detector but is again spatially filtered (low frequencies) by the second FPM:

$$\psi_D = [\hat{\psi}_A - \varepsilon\hat{\psi}_A M] \otimes \hat{\Pi} \times [1 - \varepsilon M] \tag{11.6}$$

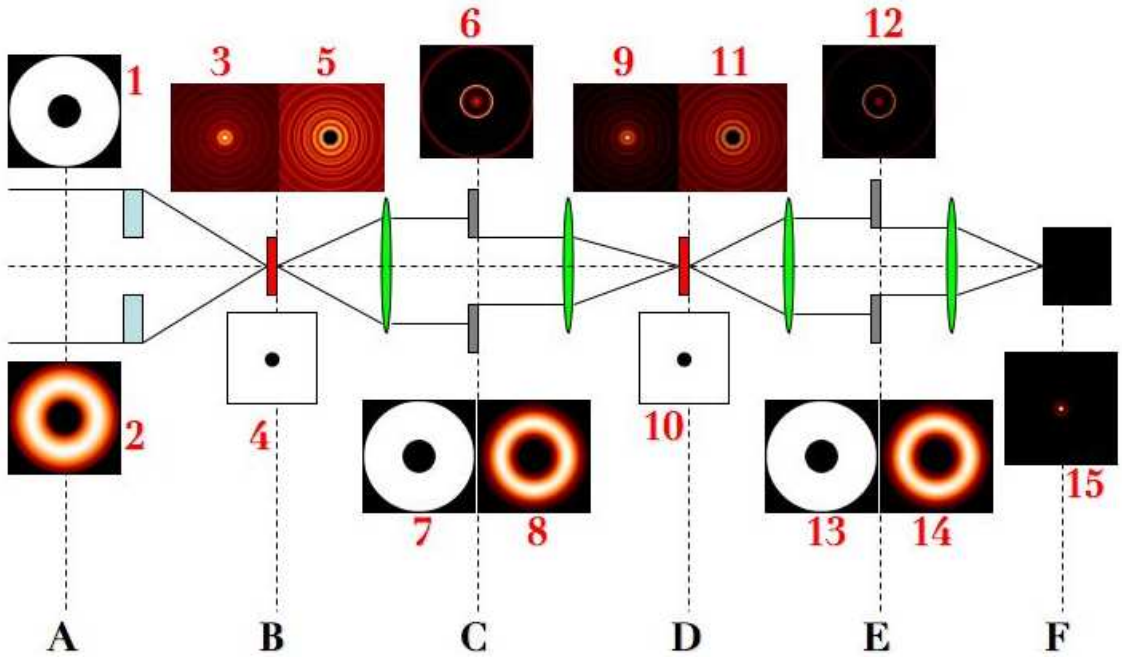

Figure 11.1: APLC 2 stages ($APLC_2$) coronagraphic process : Transmission of the entrance pupil (1) is modified by an apodizer (2). In the first focal plane, the complex amplitude of the star (3) is spatially filtered (5, low-frequencies) by the Lyot mask (4). In the relayed pupil (6) a pupil stop (7) is filtering high frequencies and as a result the relayed pupil is attenuated (8) and proportional to the apodized entrance aperture. The first stage coronagraphic PSF is for the second time spatially filtered by the second Lyot mask (10, 11), identical to the first one). In the second relayed pupil (12) a second pupil stop (13) is filtering high frequencies and finally the 2 stages coronagraphic PSF is imaged on the detector (15).

The second exit pupil image is spatially filtered (high frequencies) by a second stop (in principle identical to the first one):

$$\psi_E = \hat{\psi}_D \times \Pi \tag{11.7}$$

$$\psi_E = \left[\left((\psi_A - \epsilon\psi_A \otimes \hat{M}) \times \Pi - \epsilon(\psi_A - \epsilon\psi_A \otimes \hat{M}) \times \Pi \otimes \hat{M}\right)\right] \times \Pi \tag{11.8}$$

$$\psi_E = (\psi_C - \epsilon\psi_C \otimes \hat{M}) \times \Pi \tag{11.9}$$

The coronagraphic amplitude on the detector plane becomes:

$$\psi_F = \hat{\psi}_E = (\hat{\psi}_C - \epsilon\hat{\psi}_C \times M) \otimes \hat{\Pi} \tag{11.10}$$

$$\psi_F = (\psi_D - \epsilon\psi_D \times M) \otimes \hat{\Pi} \tag{11.11}$$

Obviously, performance of second stage (Eq. 11.11) depends on the output of the first stage (Ψ_D, Eq. 11.5). As described in Fig. 11.1, APLC makes possible its use in multiple-stage owing to the particular properties of the apodizer functions (prolate functions). Prolate functions have characteristics of being invariant by Fourier finite transform. This means that the Fourier transform of the central part of a prolate function (i.e on in the pupil domain, actually pseudo-prolate functions in the precise case of obscured apertures) is an infinite function similar to the original truncated one. Therefore, owing to the properties of prolate functions, the diffracted amplitude in the relayed pupil (i.e pupil stop plane, 6 and 12 in Fig. 11.1) is an infinite prolate function as well. Its shape is similar to the initial prolate apodization function used at the entrance pupil (2, Fig. 11.1). As a result the wave amplitude in plane C is itself apodized which permits to use plane C as an entrance apodized pupil for a second stage. This second APLC stage is therefore made without any additional loss of transmission since it avoids the use of a second apodizer. Therefore, several identical coronagraphs (FPM) can be used in cascade with only one apodizer at the entrance aperture.

11.2 Coronagraphic efficiency vs. budget error

The intent of the next sections is to compare $APLC_1$ and $APLC_2$ configuration assuming error sources in the coronagraphic system. By error sources we refer to telescope characteristics (central obscuration, spider vanes), misalignments (pupil shear, offset pointing), segmentation effects (segment amplitude and phase errors), bandpass filter, atmospheric residual aberrations that are leaking through an XAO system as well as static common and non-common aberrations (using a differential imaging system). All these defects matter high contrast imaging capabilities of any coronagraph. The question behind these simulations is to evaluate how relevant a mulitple-stage is in practice. As previously said, the advantage of APLC in regards with cascade configuration is that each pupil plane (next to the entrance pupil plane) is itself apodized, avoiding the use of multiple apodizers that would strongly decrease throughput. However, it is understood that each error parameter that will impact somehow the coronagraphic process prior to the second focal plane will affect the second stage. Some error sources could modify somehow the energy distribution in the first pupil plane prior to the pupil stop. A misalignment of the pupil stop itself is enough to impact on the second stage capabilities since it will truncated not symmetrically the prolate function, which is in essence the apodizer of the second stage. Therefore, one could expect that apodization function in the *n* relayed pupil plane will be strongly modified as *n* increases when error sources are considered in the system. Modification of the apodization function in the *n* relayed pupil will then impact on the *n* coronagraphic stage(s) efficiency.

As a baseline the central obscuration is 30% and the APLC is a 4.7 λ/D. When changing the central obscuration ratio, APLC operates with its optimal configuration (defined in the former study, Chapter 5).

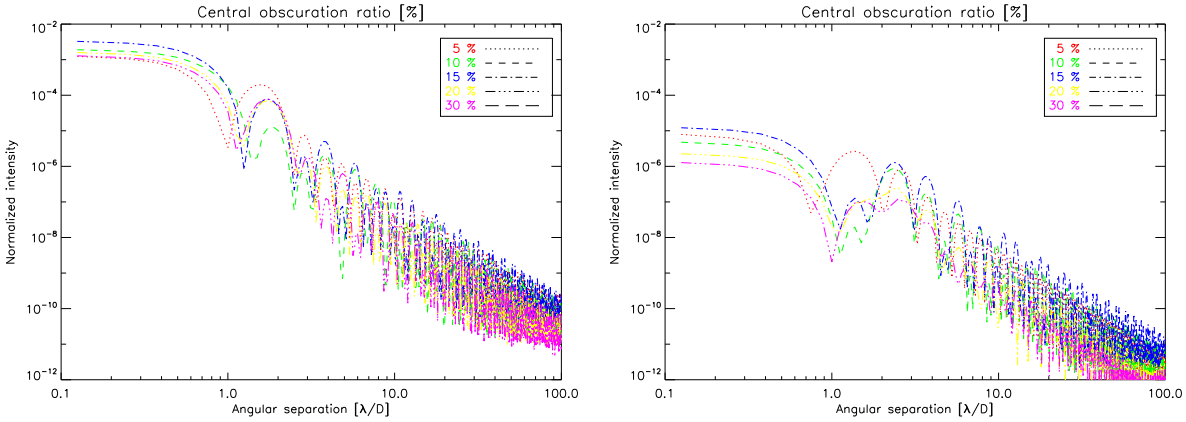

Figure 11.2: $APLC_1$ (left) and $APLC_2$ (right) coronagraphic PSFs assuming different central obscuration ratios.

11.2.1 Coronagraphic telescope characteristics impact

Central obscuration

These first series of simulation (Fig. 11.2) demonstrate the efficiency of the cascade configuration. From a former study on the optimization of APLC (Chapter 5) we derive one important conclusion: when APLC operates with its optimal configuration (mainly drives by the central obscuration indeed) it can efficiently cope with a large variety of telescope designs (i.e central obscuration ratio). That is precisely what Fig. 11.2 (left) reminds: performance are rather insensitive with the central obscuration ratio. This is also true in cascade configuration (Fig. 11.2, right) even if there is slightly more dispersion on the peak. For instance, in the case of 30% central obscuration, peak rejection is 10^{-3} with $APLC_1$ while in 2 stages peak rejection is 10^{-6}. At, $2\lambda/D$, contrasts are $\sim$ 10−4 ($APLC_1$) and $\sim 10^{-7}$ ($APLC_2$). At $10\lambda/D$, contrasts are $\sim$ 10−7 ($APLC_1$) and $\sim 10^{-10}$ ($APLC_2$). Peak attenuation of $APLC_2$ with respect to $APLC_1$ is similar to that of $APLC_1$ with respect to the PSF without coronagraph. Improvement of contrast between $APLC_1$ and $APLC_2$ at a given angular distance is equivalent in gain to the first stage peak rejection (10^3). In other words, improvement of $APLC_2$ with respect to $APLC_1$ is constant and on the order of the

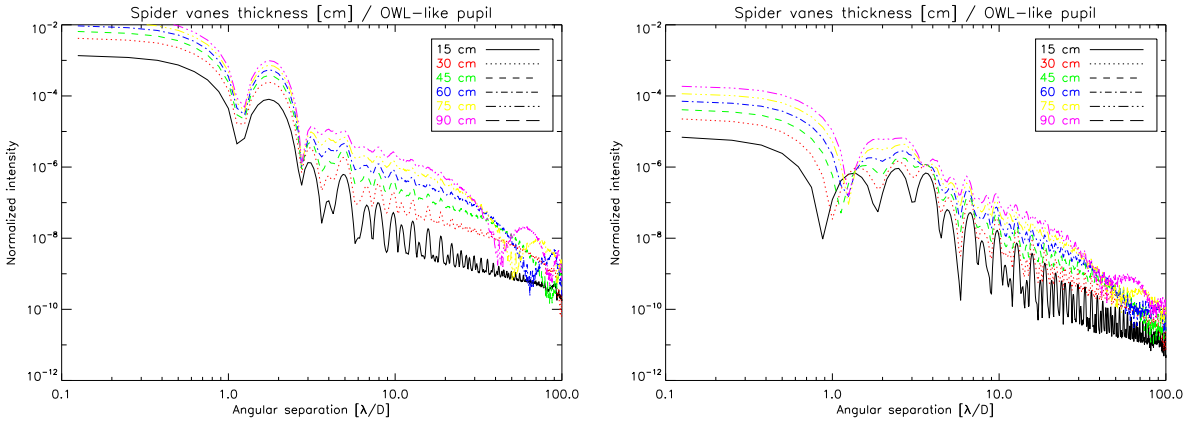

Figure 11.3: $APLC_1$ (left) and $APLC_2$ (right) coronagraphic PSFs as function of spider vanes thickness (assuming six symmetrical spiders configuration and 30% central obscuration, e.g former OWL design).

peak attenuation in between them which is also equal to the first stage peak attenuation. The gain is conserved through stages, at least for two stages.

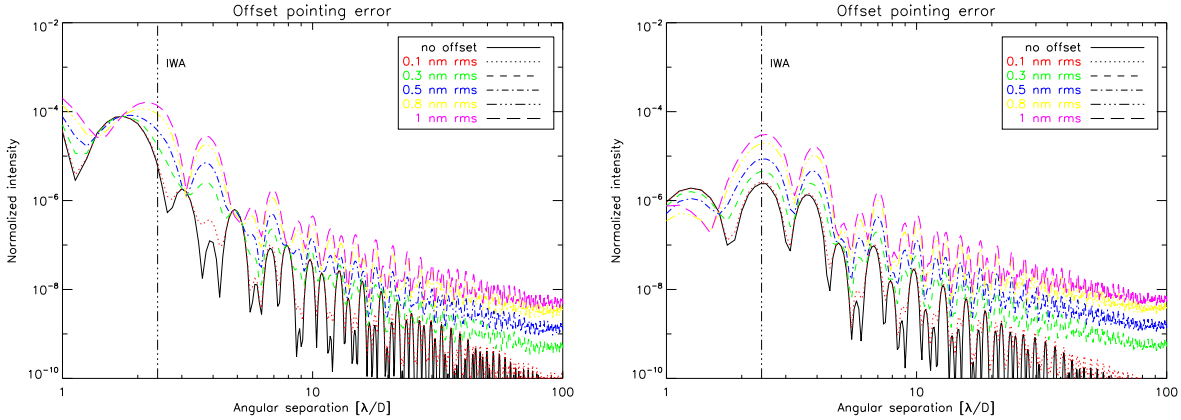

Figure 11.4: $APLC_1$ (left) and $APLC_2$ (right) coronagraphic PSFs as function telescope offset pointing error.

Spider vanes

The analysis for the spider thickness is made for one configuration where six symmetrical cables are used to maintain the secondary support. The thickness varies from 15 to 90 cm. For each case, the pupil stop(s) are identical to the entrance pupil including spider vanes.

The purpose here is not to discuss the decrease of performance due to the presence of the secondary support. It is well understood that spider vanes matter at some point performance of any coronagraphic devices.

We carried out these simulations to analyze whether or not the gain in between $APLC_1$ and $APLC_2$ is affected. By principle, the gain is supposed to be equivalent to that of the $APLC_1$ with respect to the non-coronagraphic PSF. For instance, looking at 60 cm configuration, the peak rejection is $\sim 10^{-2}$ and $\sim 10^{-4}$ for $APLC_1$ and $APLC_2$ respectively. At $10\lambda/D$, contrasts are $\sim 10^{-6}$ and $\sim 10^{-8}$ for $APLC_1$ and $APLC_2$ respectively. Hence, the first stage gain (10^2) is identical to that of the second stage with respect to the first stage. Spider vanes do not affect the interest of multiple stages.

Offset pointing

In Fig. 11.4, the effect of the offset pointing error is compared between $APLC_1$ and $APLC_2$ for values ranging from 0.1 to 1 nm rms. From 0.3 nm rms the halo level of the two configuration is roughly comparable (from IWA to $100\lambda/D$). Of course, peak attenuation is still important (before IWA) but it is more a detector saturation and exposure time concerns rather than coronagraphic efficiency at angular separation where faint objects are expected to be observed. For instance, with SPHERE the goal is 0.5 mas rms. In such a case, $APLC_2$ has no interest. The direct translation of the SPHERE requirement to a 42 meters telescope, would be a 0.1 mas rms pointing error. In such a case, coronagraphic PSF is pinned the one without offset pointing error. As a result, multiple stage would make sense.

Pupil Shear

As for the offset pointing, there is a level of pupil shear for which implementation of multiple stage does not make sense (except for preventing detector saturation and allowing longer integration time). For this simulation we consider a range of misalignment between 0.1 and 0.5% of the pupil diameter. Caution: in this simulation, only the first pupil stop is affected by the pupil shear. Hence, we are in a favorable situation. In practice, both pupil stop will be affected. In Fig. 11.5, one can see that from 0.2 or 0.3 % misalignment, the gain from a second stage is severely limited. However, solutions exist to preserve the alignment at 0.2%. For instance, for SPHERE a dedicated Tip-Tilt mirror was included in the design to prevent from misalignment higher than 0.2%.

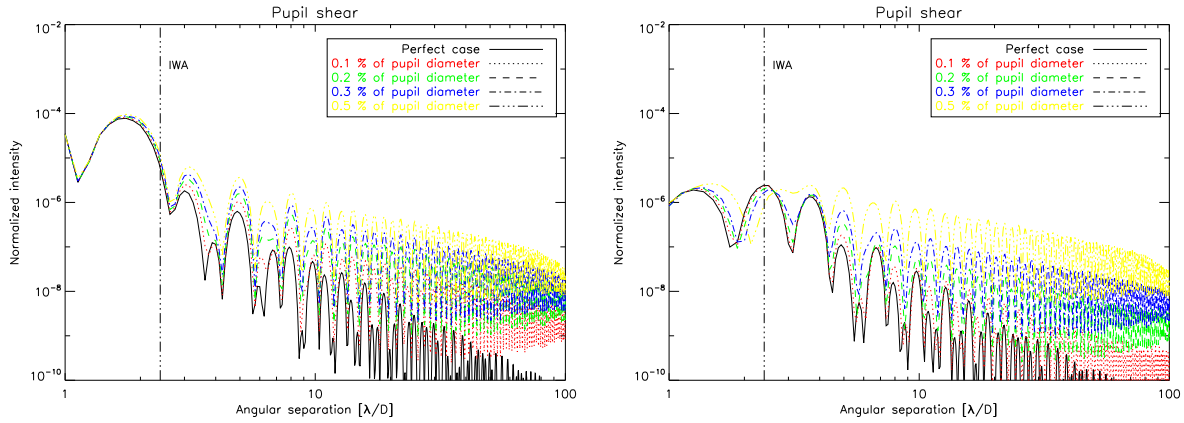

Figure 11.5: $APLC_1$ (left) and $APLC_2$ (right) coronagraphic PSFs as function of pupil shear (expressed in % of pupil diameter).

Segment reflectivity variation

Segment reflectivity variation of 1% ptv is enough to rule out the interest of a second stage (Fig. 11.6) assuming that segment reflectivity is dominating error source that therefore matters coronagraphic performance (i.e for Strehl ratio of 100%, for instance).

In Chapter 8, we have shown that segment reflectivity was not a dominating parameter with respect to the residual phase aberrations that are leaking through an XAO system. But in that situation phase residual aberrations will set a limit on the interest of cascade configuration.

Segment static aberrations

In the following, we consider 10 realizations of 4 low-order static aberrations on segments (piston, tip-tilt, defocus and astigmatism). Segments are hexagonal with diameter of 1.5 meter. In Fig. 11.7 impact of these aberrations are described assuming the total rejection rate as a metric while in Fig. 11.8 a contrast metric is used (evaluated between IWA and $60\lambda/D$). Interest of a second stage is only revealed when the level of aberrations stay at least

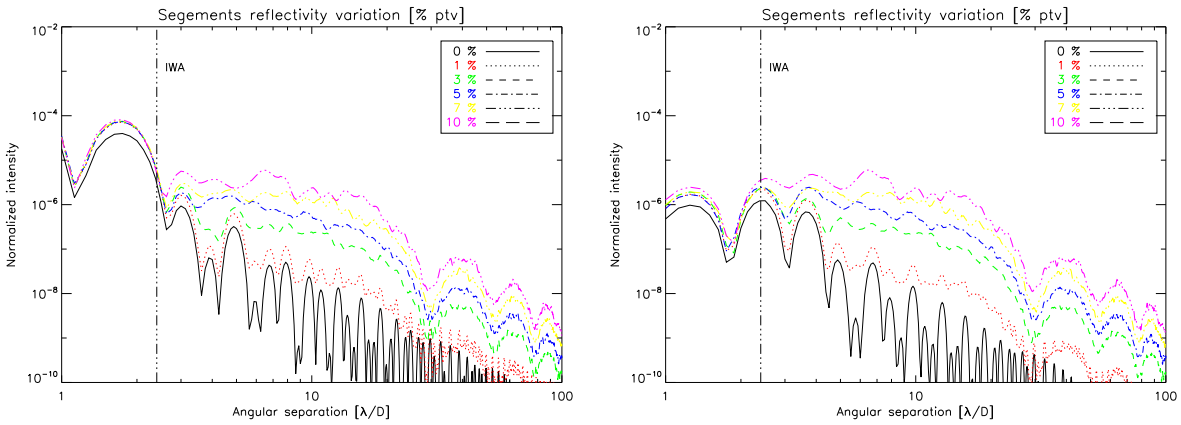

Figure 11.6: $APLC_1$ (left) and $APLC_2$ (right) coronagraphic PSFs as function of segment reflectivity variation (ptv).

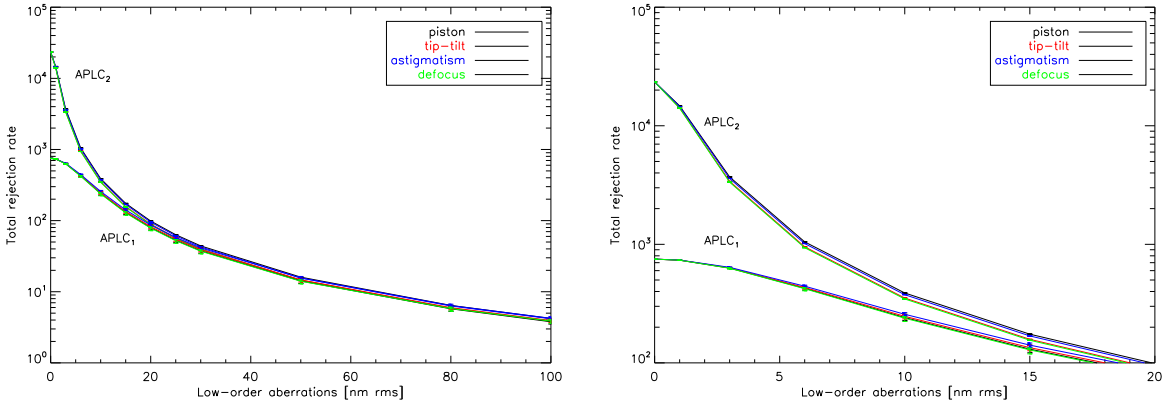

Figure 11.7: $APLC_1$ and $APLC_2$ total rejection rate as function low-order segment static aberrations (assuming 10 realizations for each aberration). Right figure is a zoom of left figure (between 0 and 20 nm rms).

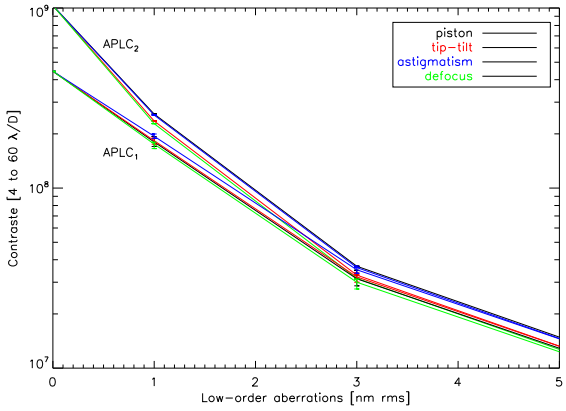

Figure 11.8: $APLC_1$ and $APLC_2$ contrast evaluation of the halo (i.e between IWA and $60\lambda/D$) as a function of low-order segment static aberrations (assuming 10 realizations for each aberration).

Table 11.1: $APLC_1$ performance (τ_1) compared to $APLC_2$ (τ_2) as a function of the bandpass filter. τ_{Ref} represent the total rejection for the minimal bandpass filter (i.e 1%).

Total rejection	Bandwidth filter [%]						
	1	1.5	2	5	10	20	50
τ_1	1185	1178	1169	1065	809	412	92
τ_i lost w.r.t τ_{Ref} [%]	-	0.6	1.4	10	32	65	92
τ_2	539804	303841	188501	32275	7976	1794	219
τ_i lost w.r.t τ_{Ref} [%]	-	43	65	94	98	99	~100

under 5 nm rms, while for the halo contrast a level less than 1 nm rms is mandatory. As a result, interest of multiple stages regarding to segment phase aberrations will lead to severe requirements.

11.2.2 Wavelength dependence

In Table 11.1, we resume chromatism effect using different bandpass filter on multiple-stage configuration compared to one stage. The metric used is the total rejection rate (τ). For $APLC_1$ and $APLC_2$ the decrease of τ with respect to the monochromatic case (i.e $\Delta\lambda/\lambda = 1\%$) is expressed and can be compared. One can see that even if $APLC_2$ outperform $APLC_1$ it has a high sensitivity and a fast reduction of performance when bandpass filter increases. For instance, for $\Delta\lambda/\lambda = 2\%$, 65% of the monochromatic performance has been lost while this rate is 1.4% for $APLC_1$. This is a consequence of the modification of the apodizer function in the relayed pupil du to chromatism (see Fig. 11.9, profiles are rescaled).

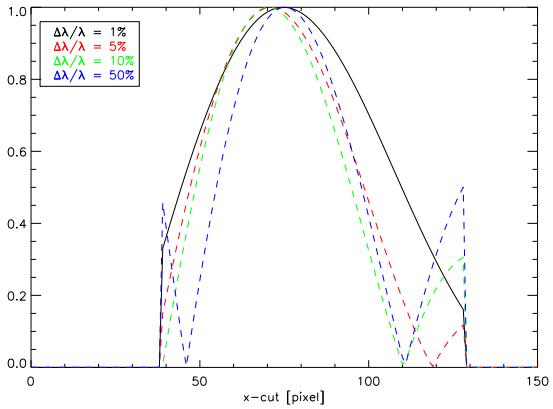

Figure 11.9: Amplitude profile of the energy in the relayed geometric pupil after Pupil stop filtering as function of the spectral bandwidth.

11.2.3 Interest in presence of atmospheric residual phase

Here, we briefly discuss interest of cascade configuration when APLC operates on telescope combined with AO system. As we have shown in Chapter 8, $APLC_1$ has, in presence of residual phase aberrations, a performance close to the "ideal" model. Its dependency to parameters analyzed in previous chapters is favorable compared to other coronagraphs (e.g phase mask). By looking at some figures presented in Chapter 8, it is obvious that a second stage will not be required, except for preventing detector saturation and allowing longer integration time. Halo performance will not be highly improved by multiple-stage configuration. In Fig. 11.11, we compare $APLC_1$ and $APLC_2$ with a contrast metric evaluated over an annular region from IWA to the XAO cut-off frequency ($80\lambda/D$).

XAO hypothesis are identical to the ones used in Chapter 8, expect that we are looking over a larger range of Strehl ratio: from 60 to 100% (Strehl ratio is modified by changing the site seeing conditions). As one can see, multiple-stage is here totally useless.

11.2.4 Interest when using a DI system

Using same assumptions as in Chapter 9 where we combine coronagraph to a simple model of differentiel imaging system, we compare $APLC_1$ with $APLC_2$ (simulation assumes 10 nm rms of common static aberrations and 0.3 nm rms non-common static aberrations). We use a 5σ detectability metrics in the following. In Fig. 11.10, we investigate parameters impact separately from each other (for a given value wrote in the legend) for these two configurations. Every parameter effect that matters $APLC_1$ has been reduced in intensity through the second

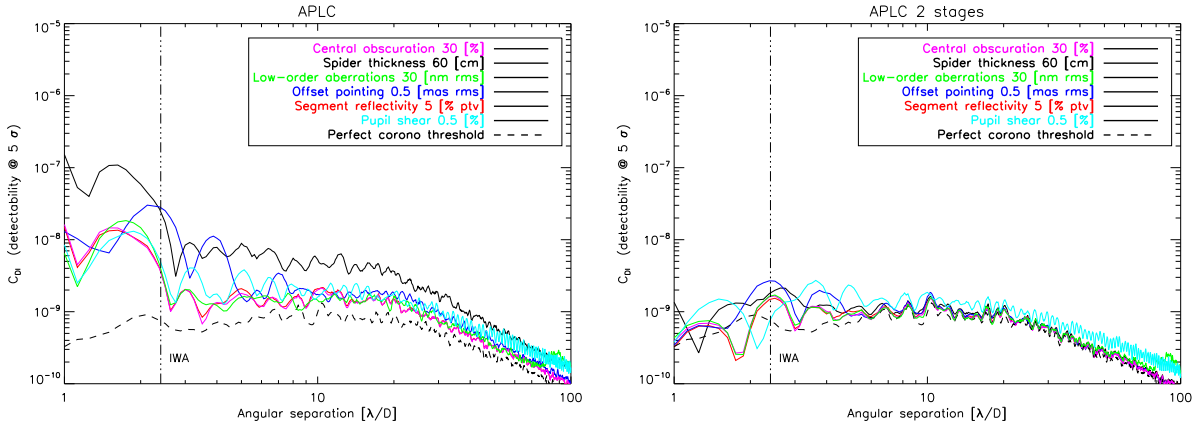

Figure 11.10: Impact of several parameter on $APLC_1$ (left) and $APLC_2$ after differential imaging assuming 10 nm rms common static aberrations and 0.3 nm rms non-common static aberrations.

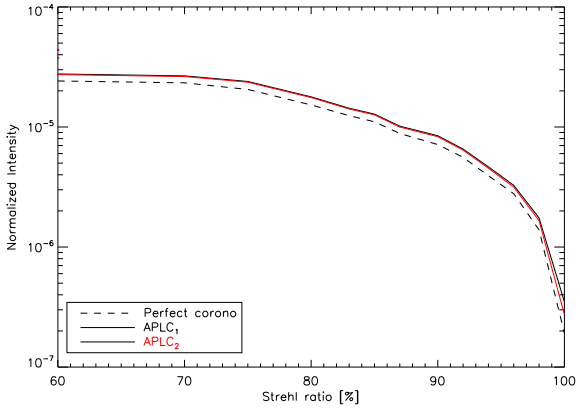

Figure 11.11: Contrast evaluation as function of the Strehl ratio over a large annular area of interest (from IWA to $80\lambda/D$, i.e XAO cut-off frequency.

stage. Specifically, spider vanes are now at the same level as every other parameters (i.e roughly at the same intensity) and hence with an impact which is quite negligible. The improvement is not that much compared to the first stage (except for the spider vanes impact) but allow a detectability very close to the ideal model.

11.3 Conclusion

Through these relatively simple simulations we underline the fact that although multiple-stage configuration for APLC is an attractive solution to reach deeper starlight extinction, it is not obvious that in practice it will deliver expected performance (i.e gain in ideal conditions). Of course, the central peak will be highly reduced preventing from detector saturation and allowing longer integration time which is not negligible. However, to be competitive on the halo contrast with respect to a single APLC, it will set strong requirements on the segment error (amplitude and phase), pointing error and so. As the number of stages increases, the number of pupil stops increases. At each level, the ability to maintain a very low level of misalignment will be mandatory. For instance, we shown that 0.2% misalignment of the first pupil stop (the second one was considered perfectly aligned) already sets a limit on the interest of a second stage.
Although this study was performed on the precise case of APLC, one can expect that most of these conclusions are valid for any coronagraph used in cascade configuration (e.g the FQPM, Baudoz et al. 2007 [15]). Therefore, a strong effort on different intrinsic critical points (compacticity, alignment) will be mandatory as well as on external errors (pointing errors, segement aberrations).

Part VI

Laboratory demonstration

Abstract - *A coronagraph used in conjonction with an AO system can improve the sensitivity of an imaging system to faint structure surrounding a bright source. These devices block the core of the image of an on-axis source and suppress the bright diffraction pattern, removing light that would otherwise reduce the dynamic range of the imaging. The state-of-the-art of coronagraphy has impressively envolved during the last ten years. Coronagraphs are now able to provide a very large on-axis exctinction as demonstrated in laboratory conditions. But their capabilities during sky observations are damped by the large amount of residual phase aberrations that are left uncorrected by the AO system. Coronagraphy is a mandatory technique to suppress on-axis starlight, but a coronagraph can only reduce the contribution of the coherent part of the light. Hence, their capabilities on sky are in strong relation with AO efficiencies. Any high contrast instrument concepts for large ground-based telescopes such as SPHERE, GPI, PFI (TMT planet finder instrument) or EPICS for the future E-ELT use a combination of XAO and a coronagraph. Therefore, implementation of coronagraphs on HOT, the High Order Testbench provide an ideal environment to assess the contrast delivered by each device considering the diffraction by the edges of the pupil and the residual phase aberrations that are leaking through the AO system. We have produced several coronagraphs to compare them in this advantageous environment. Hopefully, outputs of this comparison will present the possibility to extend this study to the case of Extremely Large Telescopes.*

In Chapter 12, we report laboratory development of coronagraphic devices to be implemented on the High Order Testbench (HOT) to compare their performance and sensitivities at a high Strehl ratio regime. The high order test bench implements extreme adaptive optics with realistic telescope conditions reproduced by star and turbulence generators. A 32×32 actuator micro deformable mirror, one pyramid wave front sensor, one Shack-Hartmann wave front sensor and the ESO SPARTA real-time computer. This will enable characterization and comparative study of different types of coronagraphs in realistic conditions. We have developed several prototypes of promising coronagraphs concepts: Four Quadrant Phase Mask, Lyot coronagraphs and Apodized Pupil Lyot Coronagraph. We will describe the design of the IR coronagraphic path on HOT, prototyping processes used for each coronagraph and discuss quality control and first results obtained on a IR coronagraphic testbench (Strehl ratio 94%).

Unfortunately, as a result of delays in the delivery of coronagraph prototypes resulting either from difficulties to reach specifications or, in the particular case of the APLC apodizer manufacturing, as a result of a change of the manufacturing technique itself (since the baseline one was unsuccessful), we are only currently implementing them on HOT. Forthcoming experiments will then enable comparison of these coronagraphs under realistic telescope conditions . However, as a balance of this disappointment, we investigated and successfully validated a new technology approach for manufacturing apodizer mask (Chapter 13)

12

Coronagraphs prototyping

Contents

Abstract - *In this Chapter, we describe coronagraphs we have developed for HOT. As a baseline, we have produced three coronagraphs (phase and amplitude type): FQPM, Lyot and APLC. These coronagraphs have been actually selected for SPHERE. Specifically Lyot and APLC have been proposed for GPI and the Lyot project [74]. Manufacturing process as specification aspects will be adressed. The ESO AO testbench (HOT) will be described, and we will have a specific look at the IR coronagraphic path.*

12.1 The High Order Testbench (HOT)

12.1.1 HOT General presentation

The High Order Testbench (HOT, see Fig. 12.1) implements an XAO system on the MACAO (Multi Application Curvature Adaptive Optics) test bench which includes star and turbulence generators to mimic realistic conditions at a telescope. The bench is installed at ESO/Garching. Responsibilities are split between ESO (DM, the optical setup, and the SHWS RTC), Durham University (SHS) and Arcetri (PWS including its dedicated RTC).

Realistic conditions are achieved simulating the VLT pupil (8m) with a F/50 beam and applying different pupil masks. The HOT bench incorporates a turbulence generator with phase screens to simulate real seeing conditions for three cases: low reduced turbulence (0.5 arcsecond, 0.85 arcsecond seeing) and full kolmogorov turbulence (0.65 arcsecond seeing). Two deformable mirrors for WFE correction are integrated in the system. A first deformable mirror (60 bimorph elements) is used to correct the static aberrations of the bench and will work in a second phase of the project as woofer. This mirror is placed on a TTM (tip-tilt mount), so the deformable mirrors do not need to use stroke to correct these modes. The second one is a micro deformable mirror (electrostatic MEMS device) to correct the high order modes of the generated turbulence. A cube beamsplitter divides the optical beam in two channels. Wavefront sensing is achieved either with a Shack-Hartmann or a Pyramid.

All the optical elements and subsystems are installed and aligned checking aspects such as: pupil size, conjugate planes, homogeneity illumination and F number. Both mirrors are characterized in terms of voltage-stroke behavior, coupling, defective actuators. The optical quality was checked on different points of the setup. The bimorph mirror was used to reduce the static aberrations under the specifications, thus a WFE of 50 nm RMS was achieved (measured on the WFS path).

The micro deformable mirror is an electrostatic MEMS device from Boston Micromachines. It is a 10.8 mm squared deformable mirror with 340μm actuator pitch for a total of 1024 actuators.

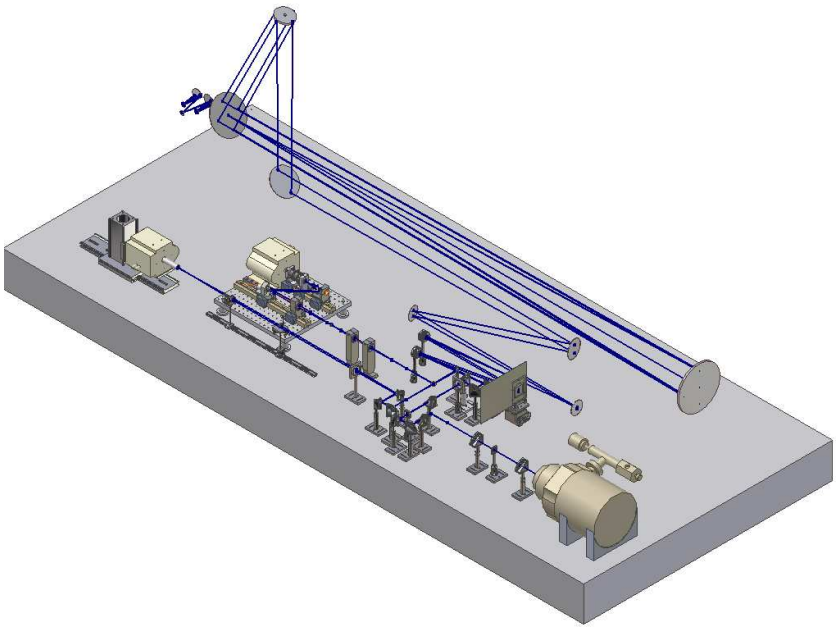

Figure 12.1: Shematic HOT setup on the MACAO testbench including IR coronagraphic path.

The HOT Shack-Hartmann wavefront sensor designed by the University of Durham, is modeled with an input beam from a 8 m class telescope with a 400 m focal length (F/50). The WFS provides a plate scale of 0.5 arcsec/pixel, with 31×31 subapertures, each detected on 4×4 pixels of a 24 μm pixel CCD.

The HOT Pyramid wavefront sensor designed by Arcetri has two pupil sampling configurations which are selected by changing the final camera lens. These are a low sampling mode with 31×31 subapertures and a high sampling mode with 48×48 subapertures.

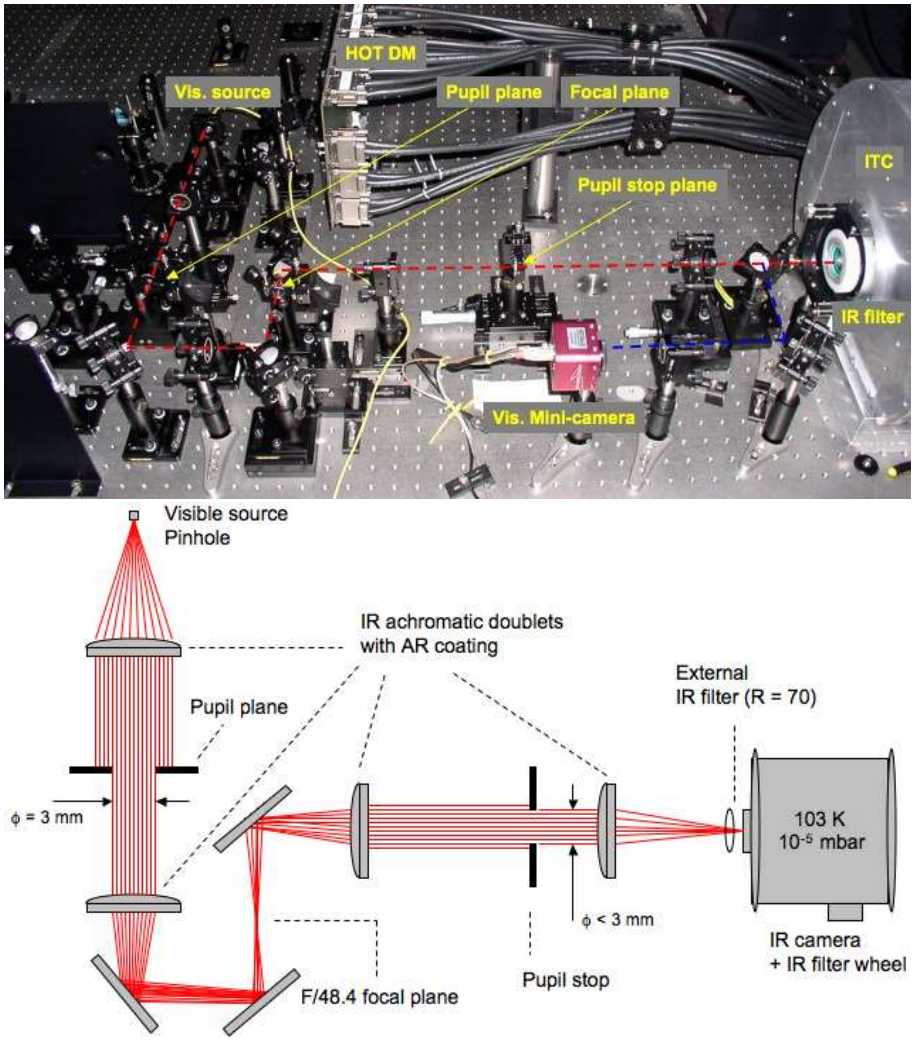

Figure 12.2: *Top*: Picture of the IR coronagraphic test-bench on HOT. The red dot line shows the IR coronagraphic path while the blue dot line shows the pupil imager system path when placing a mirror on a magnetic mount before the external IR filter. *Bottom*: shematic setup of the coronagraphic testbench.

More details on AO common path optics, optical quality, turbulence generator and phase screens, micro deformable mirror, SHWS, PWS and laboratory demonstration are presented in different papers (Vernet et al. 2006, Aller Carpentier et al. 2008 [101, 10]).

12.1.2 The IR coronagraphic path

The IR coronagraphic path configuration is shown is Fig. 12.2. The facility we used is a part of the High Order Testbench (HOT). All the optics are set on a table with air suspension in a dark room. HOT is fully covered with protection panels forming a nearly closed box. The infrared (IR) coronagraphic optical path of HOT can be used separately from the rest of the general optical path by replacing a mirror after the dichroic with a visible source on a magnetic mount (the optical IR coronagraphic path is described in Fig. 12.2 (top) using dot red line on the picture). In other words, an independent IR coronagraphic testbench is available on HOT.

The optical system was designed using the optics program ZEMAX. The optical setup is designed to simulate the 8 m VLT pupil. When used separately from HOT, it does so by scaling the 8 m VLT pupil to 3mm ± 0.002 mm using a laser-cut stainless steel sheet. The central obscuration is scaled to 0.47 mm ± 0.002 mm and the spider

vanes thickness is 15μm ± 4μm.

The test bench uses an F/48.4 at the coronagraphic focal plane. Our coronagraphic system consists of λ/10 IR achromatic doublets. The quality of the collimation in the pupil plane and re-imaged pupil plane (where the pupil stop is placed) was checked and adjusted using an HASO 64 Shack-Hartmann sensor. The coronagraphic focal plane was localized using a visible mini-camera with a HeNe laser light and tuned in the final IR image on the detector. A pupil imager system (see Fig. 12.2, a dot blue line describe its optical path) has been implemented for the alignment of the pupil stop mask with respect to the entrance pupil mask (alignment in x and y direction, orientation of the spider vanes and focalisation as well). This facility insure a good accuracy of the pupil stop mask positioning (conjugated to the entrance pupil mask). In practice, this was also useful for the apodizer alignment with respect to the entrance pupil mask.

We use a broadband white-light source combined either with an IR narrow filter ($\Delta\lambda/\lambda$ = 1.4%, central wavelength of 1.64μm, with a peak transmission of 64.4%, checked with an Fourier Transform Spectrometer) or multiple choice of IR filter, installed inside the IR camera and accessible through a filter wheel, in J, H (narrow or broadband), and K band (narrow or broadband). In practice, most of the time we use a broadband H filter (center at 1.6μm, $\Delta\lambda/\lambda$ = 20%) combined or not with the H narrow external one presented previously. The camera used is the ESO Infrared Test Camera (ITC), cooled at 103 K degree with a vacuum of 10^{-5} mbar and with internal optics designed to enable pixel-scaled of 5.3 mas / pixel. The Strehl ratio of the IR path was evaluated at 94%. It was determined by measuring the peak intensity of an experimental PSF (Fig. 12.3, left) to that of a theoretical PSF. The theoretical PSF is created by performing the foward fast Fourier transform of the autocorrelation of an oversampled and uniformly illuminated entrance pupil image from our telescope pupil mask (Fig. 12.3, right). Our pupil and focal planes masks are mounted on (x, y, z, θ) stages to minimize positioning error.

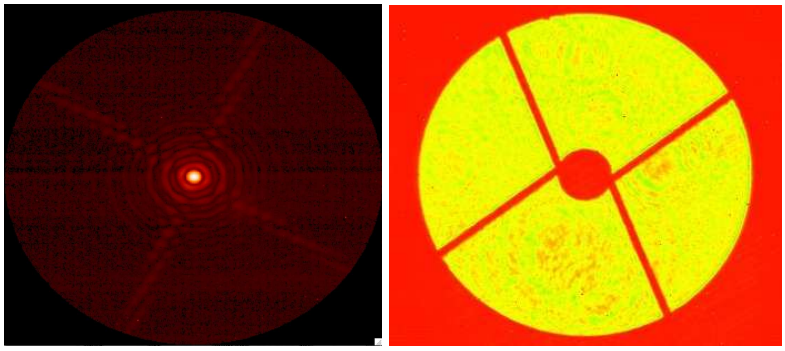

Figure 12.3: Left: PSF of the IR coronagraphic bench ($\Delta\lambda/\lambda$ = 1.4%). Right: VLT pupil image recorded with the ITC.

12.2 Four quadrant phase mask

As a baseline, the FQPMs chosen for HOT are monochromatic. Achromatic devices, either FQPMs using half-waves plates (Mawet et al. 2005a [67]), or AGPM (Mawet et al. 2005b [68]) will be implemented on HOT in the framework of EPICS phase A in the next future. FQPMs were manufactured by GEPI (Galaxies Etoiles Physique et Instrumentation) in collaboration with LESIA at the Paris Observatory. Several runs was necessary to reach specifications presented hereafter.

12.2.1 Derived requirements of the mask

The manufactured FQPM must be as close to the theoretically perfect FQPM as possible to reach the expected performance. One can expect not to be limited by the intrinsic manufacturing defects of the component. To do so, the manufactured FQPM as been specified to deliver performance that correspond to the case where the limitation only comes from the diffraction by the edges of the pupil (VLT-like pupil at the entrance pupil of HOT). In this ideal case, uncorrected aberrations that are leaking through the AO system are not considered but will decrease the

FQPM efficiency when implemented on HOT. Accuracy of critical parameters that GEPI has reached are detailed hereafter and presented in Table. 12.1 where we compare performance imposed by manufactured defects to ideal performance expected when the Strehl ratio is 100%. A microscope inspection of the quadrants is presented in Fig. 12.4 (left). The total nulling of the coronagraph refers to the total rejection rate (τ): ratio of the total integrated intensity with and without the FQPM.

Substrate specifications

- Glass: INFRASIL 301 (Heraeus)
- Size: diameter = 16 mm, thickness = 3 mm (± 0,1 mm)
- Edge: standard polished with light level
- Optical quality for the two faces: λ/20 PTV at 633 nm with good polish
- Parallelism: 15 arcsec

Quadrants specifications

- Accuracy on the quadrants orthogonality: ≤ 0.8 arcmin
- Width of the quadrants transition: ≤ 2 μm
- Operating wavelength of FQPM: λ = 1.65 μm
- Step thickness: e = 1.89 μm ± 3 %
- Anti reflection coating on the two faces (for λ_0 = 1.65 μm) R ≤ 0.5 % per face (from 1.2 to 1.8 μm).

12.2.2 Operating wavelength precision

The monochromatic FQPM is manufactured by engraving of two opposite quadrants on an optical substrate. The thickness of the FQPM step directly defines the optimal wavelength λ_0 (Eq. 12.1)for which the attenuation is the best. A difference between the optimized and the working wavelength λ reduces the attenuation of the FQPM (Riaud et al. 2001 [79]). A dedicated visible spectroscopic bench was used at LESIA (Laboratoire d'Etudes Spatiales et d'Instrumentation en Astrophysique, from Paris Observatory) to measure the thickness of the FQPM step (Riaud et al. 2001 [79]). A precision of less than 3% was required on the FQPM step thickness, GEPI has reached a depth accuracy of 0.2% after several runs (see Table. 12.1).

This facility enables to measure, in the visible, the wavelength that corresponds to the perfect nulling for a given FQPM (even IR FQPM). The principle is described hereafter: we recorded low resolution spectra between 450 and 900 nm with a source centered on the FQPM (coronagraphic spectrum) and with the source out of the FQPM (direct spectrum). Studying the ratio of these two spectra, we can observe different coronagraphic minima that correspond to a phase difference between the quadrant of $\Delta\Phi = k \times \pi$ (with k = 1, 3, 5, 7 and so).

The spectral calibration is obtained in two points with two separated lasers at 0.633 and 0.532 μm. From results of a given identified order (odd value of k), we can derive from these data and from the optical index of the deposit (well known) the operating wavelength of the FQPM (λ_0) at $k = 1$.

$$\Phi = \frac{2\pi(n-1)e}{\lambda_0} \tag{12.1}$$

12.2.3 FQPM transition precision

Ideally the transition between the four quadrants must be infinitely small. Departure from this ideal case decreases the capability of the real device (Riaud et al. 2001 [79]). Microscopic inspection of the manufactured FQPM (Fig. 12.4, left) shows that the transition quality is less then 1μm (2μm peak-to-peak transitions). The impact of this defects is estimated in Table 12.1. At this level, the efficiency of the FQPM will be set by external parameters (diffraction of the pupil).

12.2.4 Chromaticity

The chosen FQPM is monochromatic. The effect of chromaticity has been defined in a previous paper (Riaud et al. 2001 [79]). The selection of a filter resolution is then critical. In Table 12.1, attenuation reachable with IR filter resolution of 1.4% and 20% are presented. For the first one, having a monochromatic device is not a limiting factor, compared to telescope defects. For the filter resolution of 5 (i.e $\Delta\lambda/\lambda$ = 20%), only a detailed study including aberrations left by the AO system can determine whether or not chromaticity will be dominant.

Parameters	Achievable total rejection (τ)
Step thickness: 0.2 [%]	120668
Transition: 1[μm]	1890 (R = 1.4%, F/D= 48.4)
Chromaticity (R = 1.4%)	23830
Chromaticity (R = 20%)	121

Table 12.1: Summary of manufacturing defects and chromaticity impact on the FQPM efficiency. Theoretical rejection is 140 assuming diffraction of the VLT-like pupil (Strehl = 100%).

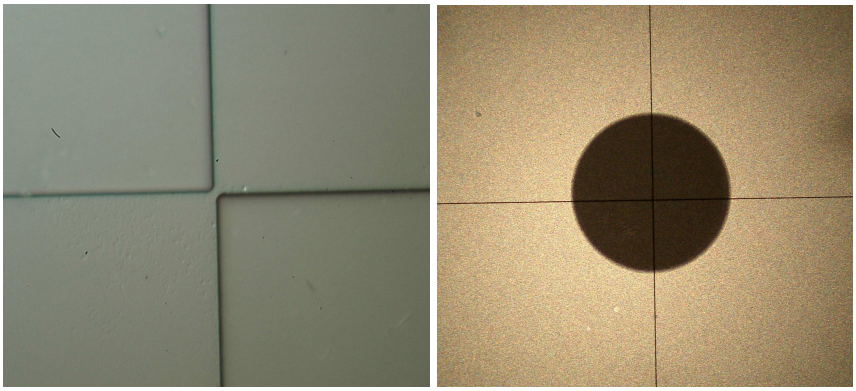

Figure 12.4: Left : microscopic inspection of the FQPM quadrants (x 50). Peak-to-peak transition is 2 μm and distance between two adjacent transitions is < 1 μm. Right : shadowgraph inspection of a 360 μm (diameter) Lyot coronagraph (x 50).

12.3 Lyot mask

A large range of Lyot mask diameters have been manufactured in 2005 using wet etch lithography process on BK7 glass by Precision Optical Imaging (Rochester, New-York). They are made by Cr deposit to reach an OD of 6.0 at 1.65 microns. Nine different Lyot masks have been made with diameters starting from 2.25 λ/D to 14.40 λ/D at 1.65μm. All these masks were deposited on the same glass substrate (λ/4) with AR coating on both faces (R<1%) and allows the selection of a different mask simply by translation along the x and y directions. The nine chromium dots are deposited on the top of a 6×6 mm^2 square grid, centered on a 50×50 mm^2 square glass substrate. They are arranged increasingly as described on the diagram (Fig. 12.5). Two sets have been manufactured. First run of test in October 2007 demonstrated that the OD (6.0 at 1.65μm) was not fitting specifications. To check the value of the OD (actually it is only an estimation since we do not use a densitometer) we performed simple coronagraphic test at F/33 (R = 1.4%) with a full pupil and a stop at ~73% in order to minimize alignment problems. For all the nine Lyot the peak rejection (τ_0) was limited to the same value of 250. Hence, we derive the value of the OD at 1.64μm to 2.5 instead of 6.0. This estimation is possible since we are limited by the OD. Same measurements

performed at 633nm converged to an OD of at least 4.0 since in that case we were not limited by the OD, hence only a pessimistic case can be derived. After discussion with the company, it was revealed that the OD of the prototypes have been only checked in the visible. New ones are expected to be provided in the next month and the OD will be certified at 1.65μm. We also asked to add Aluminium or Gold layer to the Cr deposit to improve to opacity.

Substrate specifications

- Glass: BK7
- Optical quality: λ/4 ptv at 1.65μm
- Anti-reflection coating on the back face at 1.65 μm
- Length and width: 50.5 ± 0.5 mm
- Thickness: 1.5 ± 0.05 mm
- Parallelism: < 1'

Mask specifications

- Dots: Chrome + Aluminium
- Optical density: 6.0 ± 0.5 at 1.65 μm
- Operating wavelength: 1.65 μm
- Diameter: ± 1.0 μm
- Center spacing: 12.0 ± 0.1 mm

In parallel GEPI has produced individuals Lyot masks (4.5, 4.9, 7.5 λ/D) using Cr deposition (+Au) with the same requirements for the OD. In both case accuracy on the mask is close to 1 micron on the diameter and each mask are perfectly circular and clean (see Fig. 12.4, right). The 4.5 λ/D correspond to nominal Lyot of the APLC (see next section), the 4.9 λ/D is also dedicated for the APLC but considering mask size re-optimization for broadband (R=20% in H band).

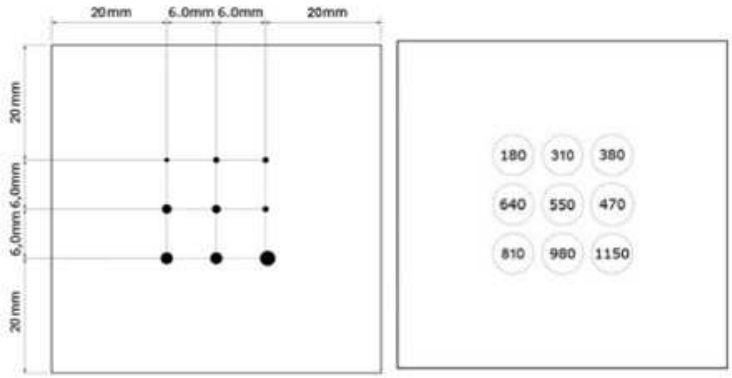

Figure 12.5: Diagram of the nine Lyot masks produced by POI.

12.4 Apodized Pupil Lyot Coronagraph

In this section, we will only discuss the apodizer prototyping. Lyot mask to combine with the APLC has been described in the previous section. Two prototype apodizers have been purchased with different techniques. The first one was manufactured using metal-layer deposition (same process as the SPHERE apodizer prototype). The second one use halftone dot process. Since the later is a new approach, developed in the context of R&D activities for EPICS, a specific Chapter will be addressed (Chap. 13). Hence, in this section only aspects pertaining to metal-layer deposition process will be discussed.

12.4.1 Apodizer description

Considering our application (VLT-pupil like), the apodizer considered is calculated for a 15% central obscuration pupil (bagel regime, Soummer et al. 2005 [88]). The selection of the apodizer function / Lyot mask size combination is based on a previous analysis (Martinez et al. 2007 [65]). In the following, we consider a $4.5\lambda/D$ APLC. The apodizer profile is illustrated in Fig. 12.6. Our manufactured apodizer has a 3mm diameter due to constraints on our optical bench.

Substrate specifications

- Glass : Infrasil
- Size : 0.5"
- Optical quality : λ/10 PTV at 633 nm
- Anti Reflection coating on back face (λ = 1.2 to 1.8 μm, R<1%)

Apodizer specifications

- Inconel deposit
- Diameter : 3.0 ± 0.04 mm
- IR wavelength : 1.65 μm
- Profile tolerance : 5 % (goal : 3%)

12.4.2 Apodizer manufacturing using metal-layer deposition

The technology used for this apodizer is a thin deposited film of Inconel 600 on a glass substrate. This kind of deposit is commonly used for neutral densities manufacturing. Inconel has two advantages: a low reflectivity coefficient and a flat spectral transmission in visible and near-IR. Prototypes have been manufactured to Reynard Corp. (USA) The first prototype has been ordered in May 2007 and received in September 2007. A that time the IR coronagraphic path of HOT was not yet implemented on the MACAO bench. In October 2007, a separate bench was built on the VLTI table (ESO/Garching) using the same optical path and components as the forthcoming HOT IR coronagraphic path to enables preliminary coronagraphic tests of prototypes such as the APLC and profile measurements of the apodizer. Results of these preliminary tests are described bellow. As seen in Fig. 12.6 and 12.7, the apodizer was out of the specifications. Discussion with the company leads to a new prototype delivered in March 2008 but with the same problems. No improvements have been revealed during a new run of tests. Therefore, considering these unsuccessful results, a new approach (i.e manufacturing technic) has been considered (microdots) which will be further developed in Chapter 13.

Apodizer general cosmetic

The Apodizer has been homogeneously illuminated by an entrance source using an IR fiber and an achromatic doublet and imaged with the ITC (R = 1.4%). One can see on Fig. 12.6 (right) an important mismatch between the center of the apodizer with respect to the real center position of the pattern. A mean error of 3.5 % of the pupil diameter has been revealed.

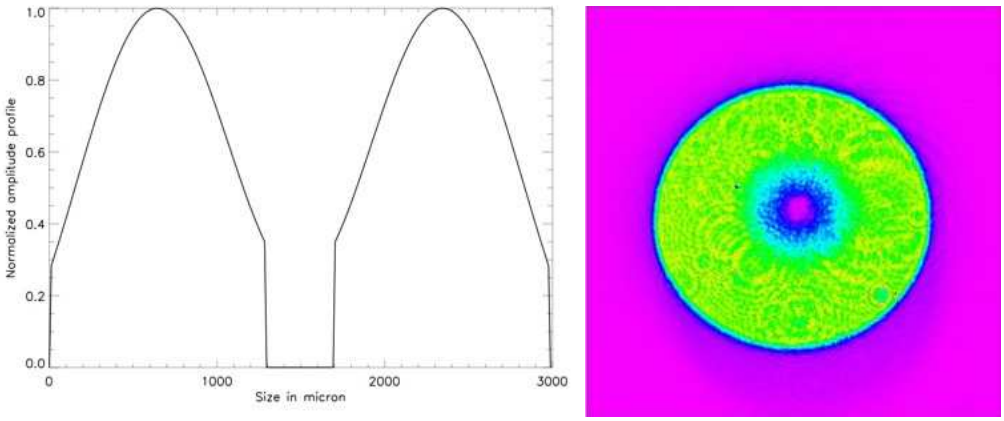

Figure 12.6: Left: Theoretical apodizer amplitude profile. Right: near-IR recorded image of the apodizer using metal-layer deposition.

Apodizer transmission profile measurements

Precise inspection of the apodizer profile has been done. The principle of this measurement is to acquire pupil images with the apodizer and without the apodizer, and to divide the first one by the second one. Sinde the component is an amplitude one, to obtain the amplitude profile of the component, a square root has been performed on the two later images. Then we plot a radial mean profile of this divided image (Fig. 12.7). An important mismatch has been also revealed (out of the tolerances). In particular a strong saturation on the maximum transmission has been revealed, and a huge discrepancy with specifications on the inner and outer part as well.

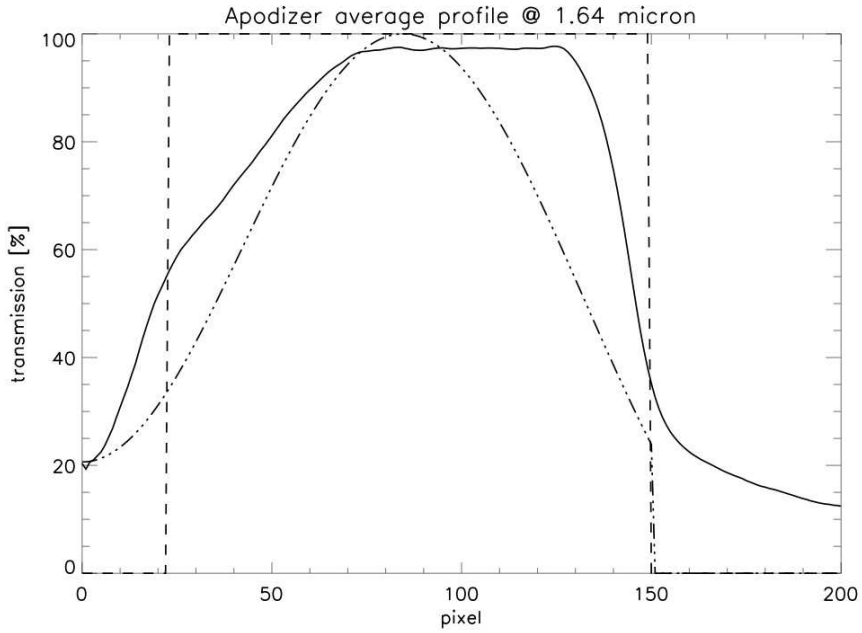

Figure 12.7: Transmission profile comparison between specification (full line) and measurements (dot line).

Effect on the PSF

The net effect on the PSF is pretty null. Tests demonstrated that the apodizer does not work.

Discussion are still on going with the company and the second specimen has been tested in laboratory in April 2008, with the same conclusions. No improvements have been revealed. Considering these bad results, we investigated a new manufacturing technique in parallel (microdots apodizer using halftone dot process). A full description of this technique, inspection of the prototype and coronagraphic results as well are presented in the next Chapter.

12.5 Pupil stop manufacturing

The optical setup of the IR coronagraphic bench is designed to simulate the 8 m VLT pupil. It does so by scaling the 8 m VLT pupil to 3mm ± 0.002 mm using a laser-cutting technic (Fig. 12.8, top left). The central obscuration is scaled to 0.47 mm ± 0.002 mm and the spider vanes thickness is 15μm ± 4μm.

The APLC pupil stop used in practice mimics the VLT pupil mask (Fig. 12.8, top middle) with spider vanes thickness increased by a factor 4 (60μm ± 4μm), and outer diameter reduced by 0.96×Φ (2.88 mm ± 0.002 mm) and the central obscuration is equal to 0.16×Φ (0.49 mm ± 0.002 mm). The pupil stop throughput is about 90% and has been optimized and designed for misalignment and chromaticism issues.

The FQPM pupil stop (Fig. 12.8, top right) mimics the VLT-pupil mask: spider vanes thickness are increased by a factor 5 (75μm ± 4μm), and outer diameter reduced by 0.90×Φ (2.70 mm ± 0.002 mm) and the central obscuration is equal to 0.30×Φ (0.90 mm ± 0.002 mm).

Although we have a wide number of Lyot mask size, we only have defined one as a baseline. The Lyot stop mimics the VLT-pupil mask (Fig. 12.8, bottom): spider vanes thickness are increased by a factor 4 (60μm ± 4μm), and outer diameter reduced by 0.78×Φ (2.36 mm ± 0.002 mm) and the central obscuration is equal to 0.166×Φ (0.50 mm ± 0.002 mm).

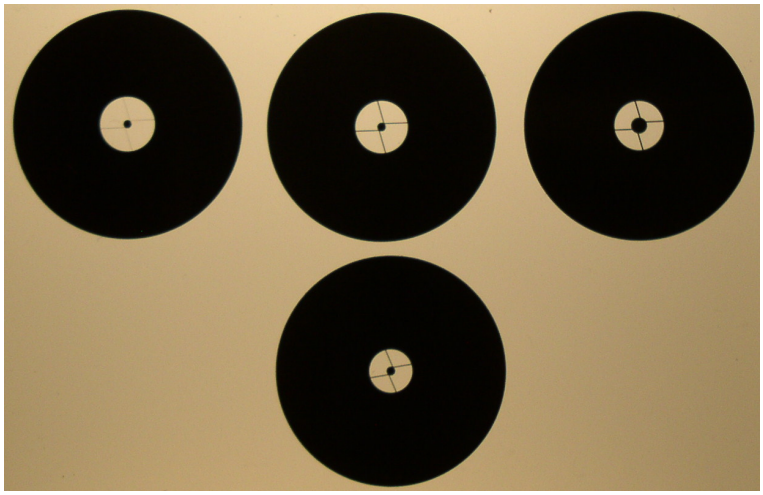

Figure 12.8: Pupil stops example: VLT-pupil (top left), APLC stop (top middle), FQPM stop (top right), Lyot stop (bottom) using laser-cuting.

13

Development of a Microdots apodizer for APLC

Contents

Abstract - *In this Chapter, we present results of microdot apodizer prototyping and laboratory experiment using near-infrared light in the context of future near-infrared instrument R&D activities for the European-Extremely Large Telescope (E-ELT). The intent of this work is to demonstrate the feasibility and performance of binary apodizers for the Apodized Pupil Lyot Coronagraph (APLC). Binary apodizers are believed to be an attractive solution for APLC (i.e alternative solution of metal-layer deposition technique). This study can be generalized to any coronagraphs using amplitude pupil apodization mask. A binary pixellated apodizer prototype has been designed using a halftone dot process, where the binary array of pixels with 0% or 100% transmission is calculated to approximate the required continuous transmission. An error diffusion algorithm was used to optimize the distribution of pixels that best approximates the required field transmission. However, pixellated apodizers introduce high frequencies noise that must be controlled through a fine adjustment of the pixel size.*

13.1 Halftoning techniques

13.1.1 Principle

Halftoning is the process of transforming an image with greater amplitude resolution to one with lesser amplitude resolution. This has been and remains an active area of research with a wide number of methods and purposes. Halftoning has been practiced for over a hundred years in the printing industry: a solution for displaying continuous images with only black or white dots. On its early story, halftoning was used for transmitting image over telephone or telegraph lines. The goal of all halftoning techniques is to generate an image with fewer amplitude levels that is perceptually similar to the original.

One can understood that criteria are mandatory to state whether or not the resulting pattern is similar with the original. Criteria are in first order linked to the characteristics of human vision. Cosmetic aspects are the concern of printing industry but not an issue for our problematic (i.e in the precise case of a coronagraph, we are not striving to produce the illusion of the original tonal quality of an apodizer image by judicious placement of the dots, but rather to produce a pattern that reach similar coronagraphic performance as the original).

Then, it is understood that a precise analysis is mandatory with a special care to the frequency rendering of such digital pattern that may compromise coronagraphic efficiency. Analysis are required on the way dots are distributed across the apodizer physical size to best approximate the field transmission (Sect. 13.1.2 and 13.2) and on the dot sizes (noise issue, purpose of the section 13.3).

13.1.2 Halftone characteristics in the frequency domain

The problem of how to distribute pixels and how to select pixel sizes is not trivial. Working in the frequency domain can often simplify complexity seen in the spatial domain. This is indeed the case with digital patterns. It allows us to predict the distribution of energy and its consequences on the quality of the patterns, i.e the noise they will introduce.

Even though noise is a random signal, it can have characteristic statistical properties. Spectral density (power distribution in the frequency spectrum) is such a property, which can be used to distinguish different types of noise. This classification by spectral density is given by "color" terminology which is commonly used to describe various type of noise. The most well know example is the so-called "white noise" because it produces flat power spectrum across all frequencies (in linear space). The pink noise, produces flat power spectrum in logarithmic space. Many others color of noise have been defined (brown, purple, grey...).

In the precise case of a coronagraph (i.e apodizer), it is obvious that noise in the low and middle frequency domains are the main enemies because potentially compromising the coronagraphic cancellation process in the area where faint objects are expected to be observed. In such a case, one can expect from a digital pattern to only introduce high frequencies noise (i.e blue noise, the high frequency compliment of the pink noise). The level of this high frequencies noise is an other issue (related to dots spatial characteristics). Hence, distribution of the dots must follow a specific distribution algorithm introducing hopefully only blue noise.

13.2 Principle of microdots apodizer

13.2.1 Principle

A binary pixellated apodizer is an array of pixels that are either opaque or transparent. It is fabricated by lithography of a light-blocking metal layer deposited on a transparent glass substrate. The so-called microdots apodizer is therefore a binary array of pixels with 0% or 100% transmission designed to approximate the required continuous transmission. The local transmission control is obtained by varying the relative density of the opaque and transparent pixels. An error diffusion algorithm was used to calculate a distribution of pixels that best approximates the required field transmission (Floyd et al. 1976, Ulichney 1987, Dorrer 2007 [38, 95, 37]). This deterministic algorithm treats the pixels in a lexicographic order (i.e. top to bottom and left to right). It chooses the transmission of a given pixel of the apodizer (either 0% or 100%) by comparing the transmission required at this location to a 50% threshold, i.e. the transmission is set to zero if the required transmission is smaller than 50 %, and to one otherwise (see Fig. 13.1). The induced transmission error is diffused to adjacent pixels that have not been processed yet by biasing the transmission required at the corresponding locations. This locally cancels the error of

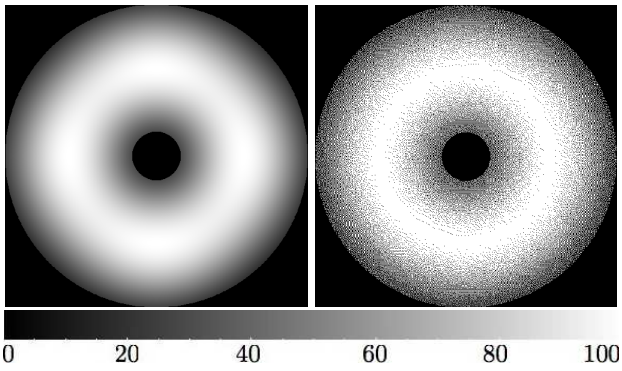

Figure 13.1: Left: Shaper target (continuous apodizer). Right: Resulting microdots pattern using algorithm discussed in Sec. 13.2.2. The scale of transmission is expressed in %.

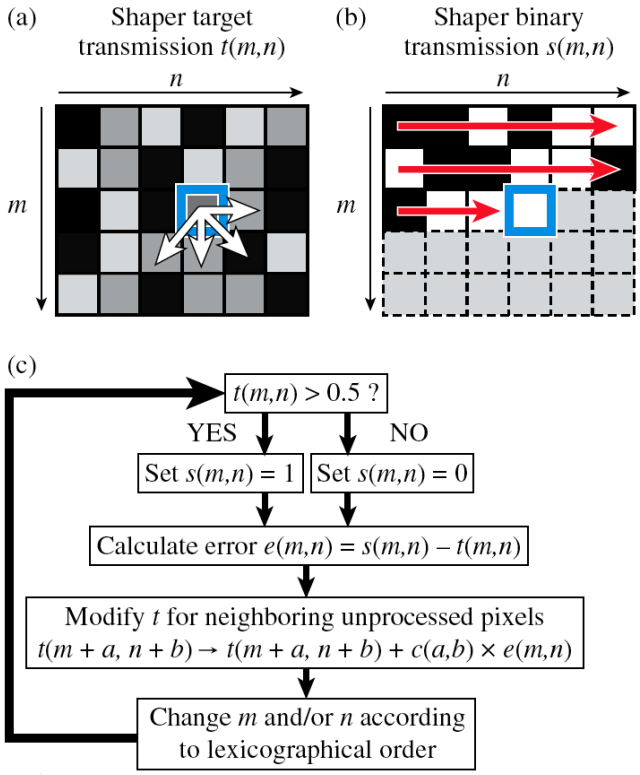

Figure 13.2: Principle of the error diffusion algorithm. (a) Representation of the target shaper transmission, (b) representation of the binary shaper transmission being designed, (c) schematic representation of the design process. The thick squares on (a) and (b) represent the pixel being processed. The horizontal arrows on (b) schematize the lexicographical process over the already processed pixels. The white arrows on (a) represent the error diffusion to adjacent non-processed pixels (From Dorrer 2007 [37]).

the binary optics relative to the required transmission. Such procedure has been used for gray-level reproduction with black-and-white printing techniques (Ulichney 1987 [95]). Shaping of coherent laser beams has also been demonstrated (Dorrer 2007 [37]). Pixellated apodizers, unlike those based on a metallic layer with spatially varying thickness, do not introduce a spatially varying phase. This is advantageous since any wavefront error might compromise cancellation at all radial distances.

In general, better shaping results are obtained as the pixel size decreases (Dorrer 2007 [37]), since this allows finer control of the local transmission and pushes the binarization noise to higher frequency. In theory, the radial distance under which a good match between the specified PSF and the binary shaper PSF is obtained can be increased by decreasing the pixel size. In practice, the shaping accuracy can be significantly impacted by the actual size and shape of the features of the binary apodizer.

13.2.2 Neighborhood process

In Fig. 13.2, a pixelated representation of the target transmission of the shaper, $t(m,n)$ and of the binary shaper being designed $s(m,n)$ are shown. On the latter, processed pixels have a transmission $s(m,n)$ equal to either 0 or 1 and are plotted in black or white, while non-processed pixels have been arbitrarily plotted in gray. Since the target transmission takes values in between 0 and 1, while the shaper transmission is either 0 or 1, the choice of the value of each pixel in the binary mask introduces a transmission error. Following the schematic representation of the process (Fig. 13.2), the choice of transmission $s(m,n)$ is made by comparing the target shaper transmission to 0.5. If the target transmission is smaller than 0.5, $s(m,n)$ is set to 0 and to 1 conversely. The resulting error is diffused to pixels that have not yet been processed, usually neighboring pixels, to bias the binary choice for these pixels and locally compensate the transmission error. This is done by adding a fraction of the error $e(m,n)$ to the target transmission for these pixels. The way that the error will be diffused (weight and number of neighbor pixels) is governed by a specific error filter (c, four-weights error filter, eight-weights error filter...). The algorithm then proceeds with the next pixel, following the lexicographical order.

The error diffusion algorithm is advantageous because the binarization noise is blue, i.e. the noise spectral density is only significant at high frequencies. This allows the accurate generation of gray levels and quickly spatially varying shaping functions. In the specific case of the design of a coronagraph, this allows to match the PSF of the binary apodizer to the required apodized PSF within some radial distance (in the control radius of the AO system, for instance). In other words, these high frequencies are pushed out of the AO correction domain (this issue will be address in Sec. 13.3.2).

13.3 Design optimization: the pixellation noise issue

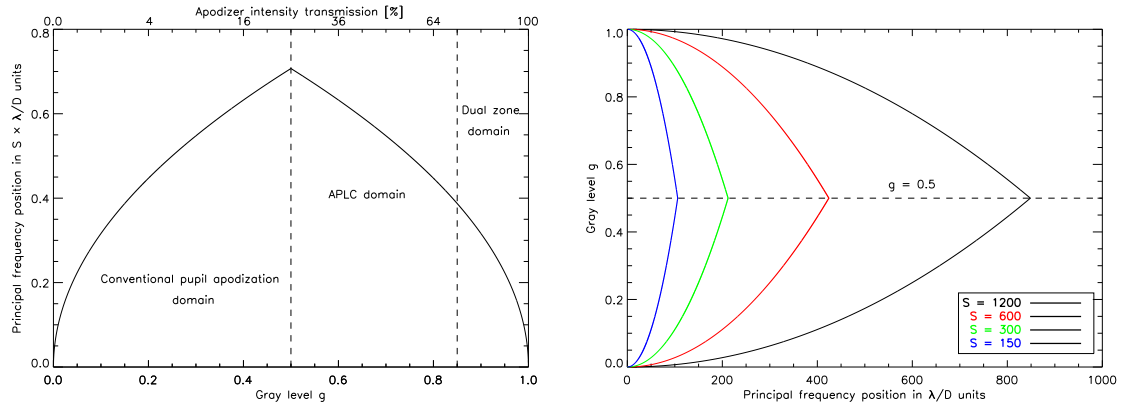

Figure 13.3: *Left* : Principal frequency f_g position in $S \times \lambda/D$ units as a function of gray level g. Typical domain of application of apodizer masks are reported on the plot. *Right* : Principal frequency f_g position in λ/D units as a function of gray level g and the scaling factor S.

13.3.1 Apodizer profile

Considering our application (VLT-pupil like), the apodizer considered is calculated for a 15% central obscuration pupil (bagel regime, Soummer et al. 2005 [88]). The selection of the apodizer function / Lyot mask size combi-

nation is based on a previous analysis (Martinez et al. 2007 [65]). In the following, we consider a $4.5\lambda/D$ APLC. The apodizer shape is illustrated in Fig. 13.1 (left image). Our manufactured apodizer has a 3mm diameter due to constraints on our optical bench. In such application, performance is related to the ratio of the smallest feature of the specification to the pixel size. Hence, for the sake of clarity, we denote by S the scaling factor, ratio between the apodizer useful diameter (i.e pupil diameter, denoted Φ hereafter) by the pixel size (p) :

$$S = \frac{\Phi}{p} \tag{13.1}$$

13.3.2 Pixel size selection

In Sec. 13.2.2, we discussed the optimization of the pixels distribution that best approximates the required field transmission. At this point, it is convenient to discuss the choice of the pixel size that will set the level of the binarization noise (high frequencies noise). Although a good agreement between the amplitude specification and the obtained amplitude with a binary pattern is reached, it does not insure a good result after coronagraphic process. Smaller pixels do not significantly increase the agreement between specified and obtained transmission in the low-frequency range, but since the pixellation noise is pushed toward higher frequencies as the pixel size gets smaller, the coronagraphic process becomes better in the medium frequency range. Note that in the precise case of APLC (or Dual zone, for instance), having a good agreement between theoretical apodized PSF and binary apodized PSF within a large angular separation, does not neither insure to reach a good result on the coronagraphic PSF. To avoid a mismatch for a given field of view between theoretical coronagraphic PSF and binary coronagraphic PSF due to high frequencies noise, pixels size optimization is mandatory and must be tackled at the coronagraphic PSF level. This issue is analyzed via simulation.

Microdots diffraction stray light

The microdots apodizer can be understood as an aperiodic under-filled two-dimensional grating that exhibit behaved blue noise properties owing to the error diffusion algorithm used. In such conditions and by considering the general problem of rendering a fixed average gray level g with binary pixels from a shaper target with intensity transmission T, g is therefore defined as:

$$g = \sqrt{T} \tag{13.2}$$

where it is ranging from $g = 0$ (black, i.e fully-covered by metal dots) to $g = 1.0$ (white, i.e fully covered by non-metal dots). The resulting pattern spectral energy will increase as the number of minority pixels increases, peaking at $g = 0.5$ (Ulichney 1987, 1988 [95, 96]). Assuming the distribution to be homogenous, pixels would be separated by an average distance, called the principal wavelength (λ_g). For the precise case of square pixels, it would have the value defined by Ulichney 1988 [95, 96]:

$$\lambda_g = \begin{cases} p/\sqrt{g} & g \leq 1/2 \\ p/\sqrt{(1-g)} & g > 1/2 \end{cases} \tag{13.3}$$

The principal wavelength would be manifested as a principal frequency in the power spectrum of the pattern, $f_g = 1/\lambda_g$, where most of the energy is concentrated:

$$f_g = \begin{cases} \sqrt{g}/p & g \leq 1/2 \\ \sqrt{(1-g)}/p & g > 1/2 \end{cases} \tag{13.4}$$

Expressing this principal frequency in λ/D units, one obtains:

$$f_g = \begin{cases} \sqrt{g} \times S & g \leq 1/2 \\ \sqrt{(1-g)} \times S & g > 1/2 \end{cases} \tag{13.5}$$

For a given g value, the pattern power spectrum has a peak at a principal frequency f_g. As the gray level, g, increases from 0 to 0.5, the principal frequency moves to further angular distance with an increase of energy. Above $g = 0.5$, situation is similar to (1-g), minority pixels has only changed from non-metal dots to metal dots. The PSF of such pattern can be therefore expressed as function of two effects:

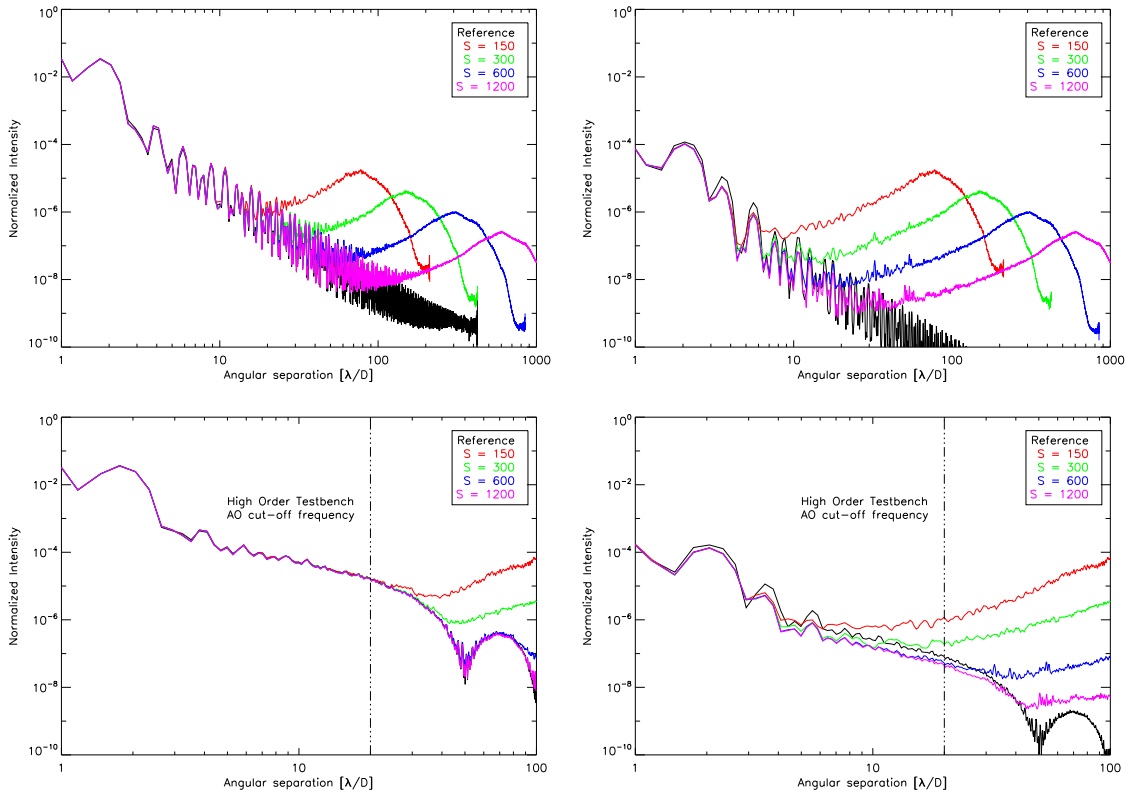

Figure 13.4: Top: Apodized PSFs (left) and APLC coronagraphic PSFs (right) using several dots size for the binary apodizer compared to that with continuous apodizer (i.e theory, in black). It assumes a pupil with 15% central obscuration. Bottom : Apodized PSFs (left) and APLC coronagraphic PSFs (right) using several dots size for the binary apodizer compared to that with continuous apodizer (i.e theory, in black). It assumes bench conditions (a VLT-like pupil). Profiles presented are azimuthal averages.

- A deterministic effect: principal peak diffraction localized at $\sqrt{g} \times S$ for $g \leq 1/2$ and $\sqrt{(1-g)} \times S$ for $g > 1/2$.
- A stochastic effect: speckles will appear since dots distribution is not regular.

At this point, it is convenient to discuss the intensity of this first order diffraction (i.e the principal frequency) effect in the final coronagraphic image. Stray effects of micro obscurations occurring in the entrance pupil can be well described by classical Fraunhofer diffraction theory. Following Babinet's theorem (Born & Wolf 1989 [28]), the far field pattern of an obscuration is equal to that of an aperture of identical dimensions. In the following we describe a simplified model for order-of-magnitude estimation of microdots effects (i.e pixellation noise) in coronagraphic systems. This model is based on a study performed by Dohlen 2008 [36], where effects of dusts and cosmetic errors are analytically described for the SPHERE instrument image quality. It assumes a perfect coronagraph and ignores any interaction with pupil diffraction residual. We note that a finer analysis including the error diffusion algorithm properties would be mandatory to accurately determine the microdots first order diffraction intensity as started in a forthcoming study.

Each opaque dot of the microdots apodizer is equivalent to a square pupil (diameter p). Each dot then scatters light by diffraction and creates a 2-D sinus cardinal function halo in the focal plane with $\frac{1}{p}$ extent (i.e $\frac{\Phi}{p}$ in λ/D units). The halo intensity (first order peak diffraction) for a single dot normalized to the stellar peak intensity is

S	p [μm]	High frequency noise angular position [λ/D]		Microdots halo intensity	
		Apodized PSF	Coronagraphic PSF	Theory (I)	simulation
150	20	20	5	1.0×10^{-5}	1.7×10^{-5}
300	10	30	10	2.6×10^{-6}	4.2×10^{-6}
600	5	40	20	6.5×10^{-7}	1.0×10^{-6}
1200	2.5	50	40	1.6×10^{-7}	2.6×10^{-7}

Table 13.1: Angular position where the high frequencies noise appears on the apodized PSF and coronagraphic PSF as function of the pixel size (column 3 and 4). Microdots halo intensity as function of the pixel size: comparison between simulation (measured on the halo peak) and analytical expression I (column 5 and 6). In our case, $T = 0.51$. Results presented refers to Fig. 14.1 (top).

$\left(\frac{p}{\Phi}\right)^4$ (Dohlen 2008 [36]). Assuming halos from all the dots add incoherently, the final halo intensity (I) would be:

$$I = N_{dots} \times \left(\frac{p}{\Phi}\right)^4 \tag{13.6}$$

where N_{dots} is the total number of the minority dots present in the pattern (e.g, for the APLC, $g \sim 0.7$, hence the minority dots in the apodizer is the opaque metal dots). N_{dots} can be easily calculated through the surface ratio of the pupil by a square dot, times the density of minority dots (η, hereafter). The minority dots density can be expressed as:

$$\eta = \begin{cases} g & g \leq 1/2 \\ 1-g & g > 1/2 \end{cases} \tag{13.7}$$

then N_{dots} is:

$$N_{dots} = \eta \times \frac{\pi}{4} \times \left(\frac{\Phi}{p}\right)^2 \tag{13.8}$$

The resulting relative halo intensity is then:

$$I = \eta \times \frac{\pi}{4} \times \left(\frac{p}{\Phi}\right)^2 \tag{13.9}$$

and using Eq. **??** one obtains:

$$I = \eta \times \frac{\pi}{4} \times \left(\frac{1}{S}\right)^2 \tag{13.10}$$

therefore, using Eq. 13.7 one finally obtains:

$$I = \begin{cases} g \times \frac{\pi}{4} \times \left(\frac{1}{S}\right)^2 & g \leq 1/2 \\ (1-g) \times \frac{\pi}{4} \times \left(\frac{1}{S}\right)^2 & g > 1/2 \end{cases} \tag{13.11}$$

Eq. 13.5 and 13.11 allow to precisely localize the first order diffraction halo and estimate its intensity. Considering our APLC apodizer ($T = 51\%$, $g = 0.71$), the principal frequency would be localized at $f_g \sim S/2$ in λ/D units with an intensity of $I \sim 1/(4\times S^2)$.

As written in Sect. 1, a binary apodizer can be in principle designed for a wide range of apodization mask types. In the following, we briefly discuss the case of the Dual Zone coronagraph and Conventional pupil apodizations:

- For the Dual Zone coronagraph, T is typically around 80%, hence $g \sim 0.9$. In such a case, the principal frequency moves closer to the central core of the PSF while its intensity decreases with respect to the APLC case: $f_g \sim S/3$ in λ/D with an intensity of $I \sim 1/(13\times S^2)$.
- For Conventional pupil apodization, $T \sim 25\%$, hence $g \sim 0.5$. In such a case, the principal frequency moves further away from the central core of the PSF while its intensity increases: $f_g \sim 1/\sqrt{2} \times S$ in λ/D (the highest frequency for this precise example, see Fig. 13.3) with an intensity of $I \sim 2/(5\times S^2)$.

Principal frequency position is presented in Fig. 13.3, where apodizer mask coronagraph types are indicated as function of the gray level value. Therefore, the choice of S (dot size) will be more critical for Dual Zone than for a conventional pupil apodization, while the APLC case is in between.

This optimization was done in two steps by looking at the impact of the pixel size on the apodized PSF and coronagraphic image. The first step strives to analyze the limit imposed by the pixel size only on the correspondence of apodized PSF and coronagraphic PSF between an ideal continuous apodizer and a binary shaper. From results resumed in Table 14.1 we can derive some conclusions:

S	p [μm]	High frequency noise angular position [λ/D]	
		Apodized PSF	Coronagraphic PSF
150	20	20	5
300	10	30	10
600	5	40	20
1200	2.5	50	40

Table 13.2: Angular position where the high frequencies noise appears on the apodized PSF and coronagraphic PSF as function of the pixel size.

- Reduction of the pixel size by a factor 2 increases by $10\lambda/D$ the frequency for which the mismatch between the specified PSF and the binary shaper PSF appears.
- Reduction of the pixel size by a factor of 2 increases the radial distance corresponding to an adequate agreement with the specification by a factor of 2 for the coronagraphic PSF.
- At a given frequency, in the coronagraphic images, the level of the noise increases as a fourth power law with S (for instance, at $80\lambda/D$ noise increase from 3.2×10^{-9} to 3.5×10^{-5} over the octave of scaling factor considered).
- First order diffraction halo position predicted by Eq. 13.5 fits simulation results ($f_g \sim S/2$).
- Analytical model (Eq. 13.11) is consistent with simulation predictions. This model is enough representative of the APLC situation.

We also found that the binarization noise reveals on the binary shaper PSF has an intensity level reduced by an order of magnitude at the angular separation where it starts to matter the coronagraphic propagation. However, at longer angular separation the noise level remains the same. This noise reduction is only du to a depth accessibility to low intensity level, i.e to reach a sufficient intensity reduction to revealed to pixellation noise presence that would otherwise be hidden.

The second step analyzes the impact of the pixel size taking into account the entrance pupil of our optical test bench (including secondary support) and the AO correction domain. A full design of the pupil is necessary since it can matter the achievable contrast (intensity level as function of the angular separation) and hence relax constraints on the pixel size with respect to the intensity level where the binarization noise appears. For instance, for conventional circular aperture telescope, the envelope of diffracted light falls off with the angular distance from the optical axis as θ^{-3} while for most complex pupils (including spider vanes, for instance), it falls as θ^{-2}. The AO correction domain (defines by the AO cut-off frequency) sets the angular separation in which we are looking at and hence where we are taking care of high frequencies noise. Here, we assume a VLT-like pupil and our AO system cut-off frequency is $20\lambda/D$. In Fig. 14.1, we plotted apodized PSF (left) using different value of S compared to theory (continuous apodizer in black) and coronagraphic PSF as well (right). As expected, the radial distance corresponding to an adequate agreement with the specification (ideal model) moved to further angular separation while the intensity level where the noise appears remains in the order of the previous case.

Considering our application, the field of view we are interested can not be met with a structure with $S = 150$. Even if $S = 300$ is in the order of what we are expecting, it appears to be potentially a risky choice. Hence two values of S are in agreement with our specifications (S = 600, 1200). The $S = 1200$ configuration leads to

really small pixel size close to the μm. In such a case, when the pixel size approaches the size of the operating wavelength (1.65μm for our application) a Rigorous Coupled-Wave Analysis (RCWA) is mandatory to know how the field reacts to small perturbations in the shaper. Gratings with small periods generally have some diffracted orders cut off for visible and IR radiations. Hence, we found that $S \sim 600$ would be a good compromise.

In our application, performance is related to the ratio of the smallest feature of the specification to the pixel size (S). Therefore, shaping performance (including cancellation of high-frequencies) will improve if the shaper can be designed to be in a space where its dimensions are large. The 3 mm pupil diameter (Φ) is a significant constraint, and constraints on the pixel size would be relaxed using a larger pupil plane.

We also note that the high-frequency noise might have different distributions at different wavelengths. This would be a situation similar to diffraction gratings, where only diffracted orders (i.e corresponding to large values of the transverse wavevector k) are frequency-dependent. For such finer analysis, Fresnel propagators and a thorough modeling of the binary shaper (including process errors on the shape and size of each pixel such as edge effect resulting from the isotropic wet etching process, see Sec. 13.4) would be mandatory. However, our simulation make use of simple Fraunhofer propagators between pupil and image planes, which is implemented as fast Fourier transform (FFTs) generated with an IDL code. In our simulation conditions, we do not find that changing bandpass filter matters the localization and intensity level of the high frequency noise.

13.4 Manufacturing process

The microdots apodizer was fabricated by Precision Optical Imaging in Rochester, New York. To minimize the effect of misalignment of the apodizer with the pupil telescope, the designed profile of the apodizer (3mm in diameter) was not obscured at the center by the central obscuration (no 0% transmission values) and was prolonged with a Gaussian function on the outer part (from 1.5 mm to 3 mm in radius) to slowly decrease the transmission to zero . Moreover, having a sharp edge on the apodizer might be detrimental to the characterization process (inspection of the profile), because of strong diffraction effects. The shaper was fabricated using wet-etch contact lithography of a Chrome layer (OD of 4.0) deposited on a BK7 glass substrate (λ/20 peak-to-valley). The back face of the apodizer has an antireflection coating for the H band (1.2 to 1.8 μm, $R < 1\%$).

In the case of wet-ech lithography, etching can lead to a reduction in the light-blocking metal pixel sizes (smaller than specified in the digital design), which potentially leads to an increased transmission. This effect is a result of an isotropic wet etching process (see Fig. 13.5)

Some etches undercut the masking layer and form cavities with sloping sidewalls. Modern processes greatly prefer anisotropic etches, because they produce sharp, well-controlled features. This reduction of the feature sizes can potentially leads to an increased transmission of the shaper. It is important to understand the scaling of this effect, quantify it and come up with pre-compensation solutions.

To get rid of this effect, the mask design was numerically precompensated by estimating the feature size which would be obtained after fabrication (Dorrer et al. 2007 [37]). Because of the undercut resulting from the isotropic etch, the metal features (dots) end up being smaller than the theory (see Fig. 13.6, 4.5 μm instead of 6 μm). Then, these changes are taken into account in the design so that getting the correct transmission is possible.

Considering the small size of the apodizer (3mm in diameter), it was chosen to use pixels on a 6 microns grid ($S = 500$) for the binary optics, as discussed in the previous section. In practice, some runs were necessary to finely calibrate the process and reach specifications. Reproducibility was confirmed with a last run following the optimal conditions.

The 4.5 λ/D hard-edge opaque Lyot mask has been fabricated by GEPI (Paris Observatory) with a good accuracy (360μm $\pm$ 1μm in diameter). With the Chrome deposit (20 nm), Au deposit has been added (200 nm) to reach an OD of 6.0 at 1.65 μm. No antireflection coating has been deposited yet. A temporary lack of BK7 substrates lead to the use of fused silica substrates with an optical quality of λ/4 peak-to-valley (ptv).

13.5 Validity of the component

13.5.1 General inspection of the prototype

Precise inspection of the quality of the apodizer has been realized in the laboratory (see Fig. 13.6 and 13.7) where we determined the size of the square chrome dots to be 4.5×4.5 μm using a microscope ($\times$ 100). The global shape

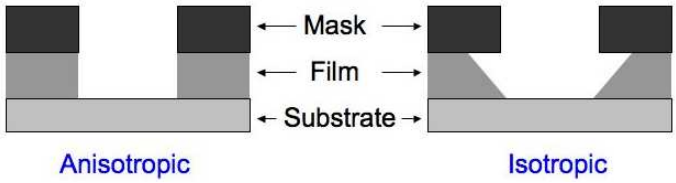

Figure 13.5: Wet etching process comparison: anisotropic etch produces vertical sidewalls (*left*), while isotropic etch produces round sidewalls (*right*). The latter introduces edge effects when used for manufacturing a microdots apodizer and can leads to an increased transmission if not pre-compensated.

(excellent circular symmetry, Fig. 13.6, left) of the binary apodizer and the dots spatial distribution across the pupil diameter has been also analyzed using a shadowgraph (×50, see Fig. 13.7) and can be compared to simulation map (5×5 μm dots). Fig. 13.8 shows that the accuracy on the profile is quite impressive, and the transmission error is about 3%. Achromaticity of the profile is also demonstrated : the profile error only increases by about 2% from narrow H filter to broadband J filter. The requested accuracy was 5% at 1.64 μm, and the binary device is within the specifications even in the J band. Having smaller pixel size than the digital design (6×6 μm) was expected (see Sec. 13.4) and demonstrates that precompensation of the transmission error due to the feature size was necessary and works well.

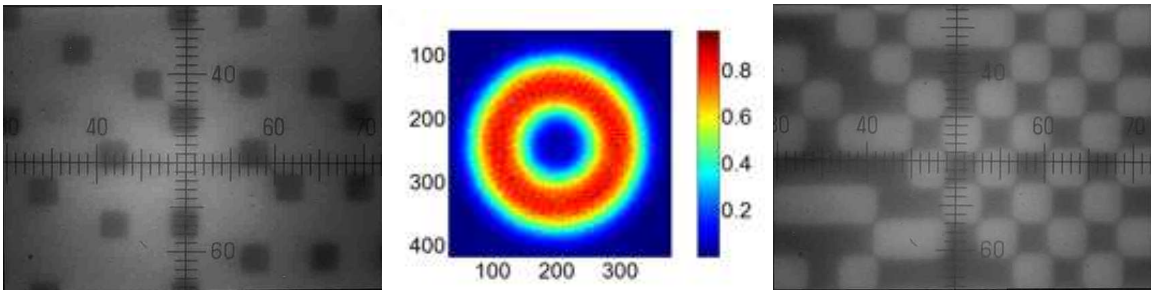

Figure 13.6: *Left*: microscope inspection of the dots (× 100, scale is equal to 1.5μm) where size of the dots were determined to 4.5×4.5μm. *Middle*: Infrared recorded image of the apodizer. *Right*: microscope inspection of the dots to illustrate edge effect resulting from the isotropic wet etching process (opaque dots are reduced in size compare to transparent dots).

13.5.2 Testbench conditions

Testing our microdots apodizer has been done through the infrared (IR) coronagraphic optical path of HOT which can be used separately from the rest of the general optical path by replacing a mirror after the dichroic by a visible source on a magnetic mount. In other words, an independent IR coronagraphic testbench is available on HOT. Although we plan to use the adaptive optics system in future experiments, it was not used in this work. Hence, only the IR coronagraphic path was used for the experiment part presented hereafter.

The test bench uses an F/48.4 at the coronagraphic focal plane. Our coronagraphic system consists of λ/10 IR achromatic doublets. The quality of the collimation in the pupil plane and re-imaged pupil plane (where the pupil stop is placed) was checked and adjusted using an HASO 64 Shack-Hartmann sensor. The coronagraphic focal plane was localized using a visible mini-camera with a HeNe laser light and tuned in the final IR image on the detector. A pupil imager system has been implemented for the alignment of the pupil stop mask with respect to the entrance pupil mask (alignment in x and y direction, orientation of the spider vanes and focalisation as well). This facility insure a good accuracy of the pupil stop mask positioning (conjugated to the entrance pupil mask). In practice, this was also useful for the apodizer alignment with respect to the entrance pupil mask.

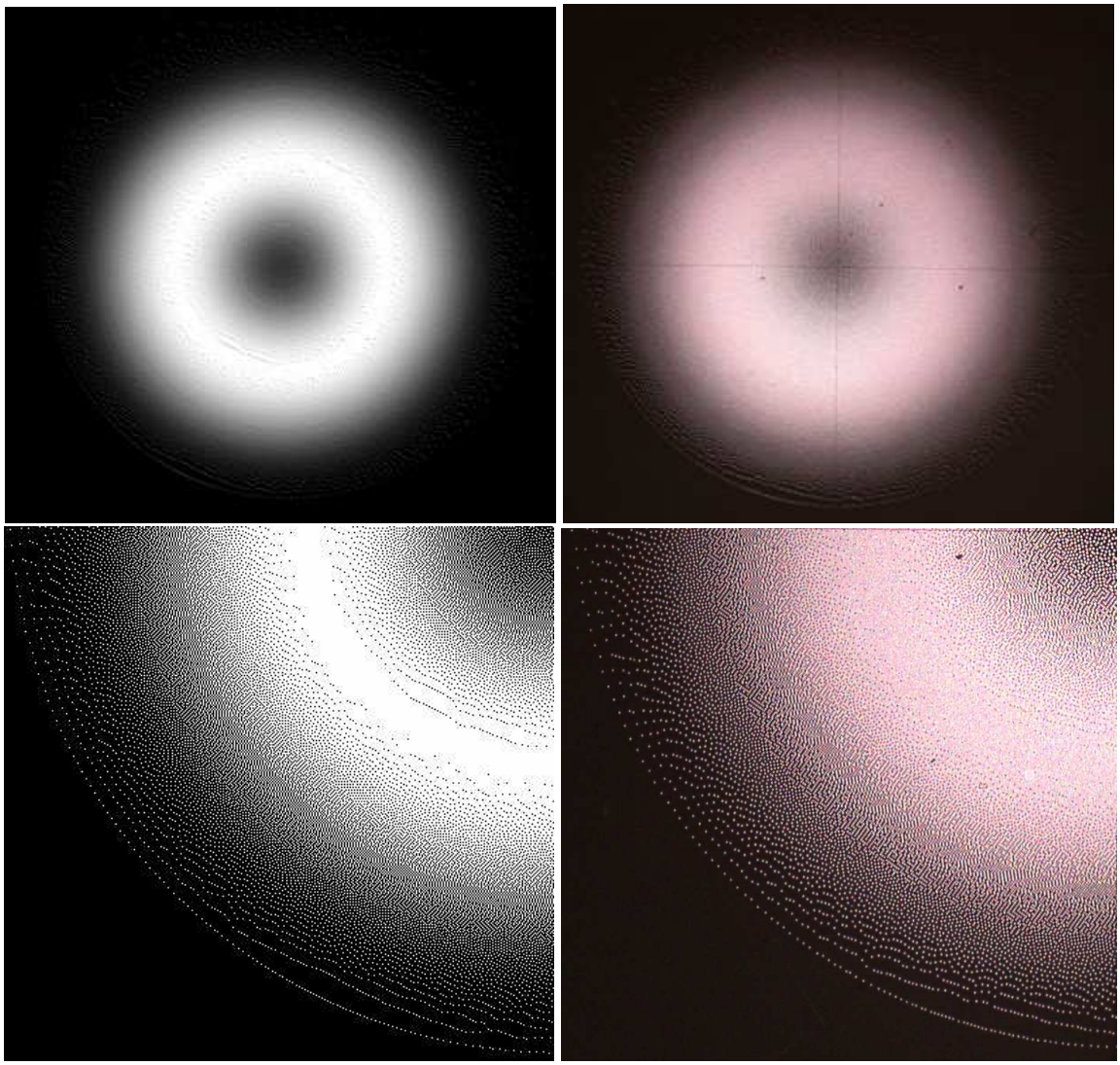

Figure 13.7: Top left: simulation map of the apodizer (5×5μm dots), Top right: shadowgraph inspection of the manufactured microdots apodizer (×50). Bottom left: simulation map of a quarter of the binary apodizer with 5×5μm dots. Bottom right: shadowgraph inspection of a quarter of the manufactured microdots apodizer (×50).

Considering the available place on HOT, in our IR coronagraphic testbench we installed the entrance pupil mask and the apodizer in the same collimated beam. Hence, it is not physically possible to insure that the apodizer is in the pupil plane considering the optomechanical mounts used for each components. To minimize the defocalisation of the apodizer with respect to the pupil mask, the apodizer was placed inside a rotating adjustable-length lens tube that allows a translation of ~3.5mm from the pupil mask.

The APLC pupil stop used in practice mimics the VLT pupil mask (Fig. 12.8) with spider vanes thickness increased by a factor 4 (60μm ± 4μm), and outer diameter reduced by 0.96×Φ (2.88 mm ± 0.002 mm) and the central obscuration is equal to 0.16×Φ (0.49 mm ± 0.002 mm). The pupil stop throughput is about 90% and has been optimized and designed for misalignment and chromaticism issues.

Although the pupil and APLC pupil stop masks were produce using laser cutting on inox substrate, to preserve their integrity (especially the spider vanes) none of them were black-coated because of the high temperature used during the process.

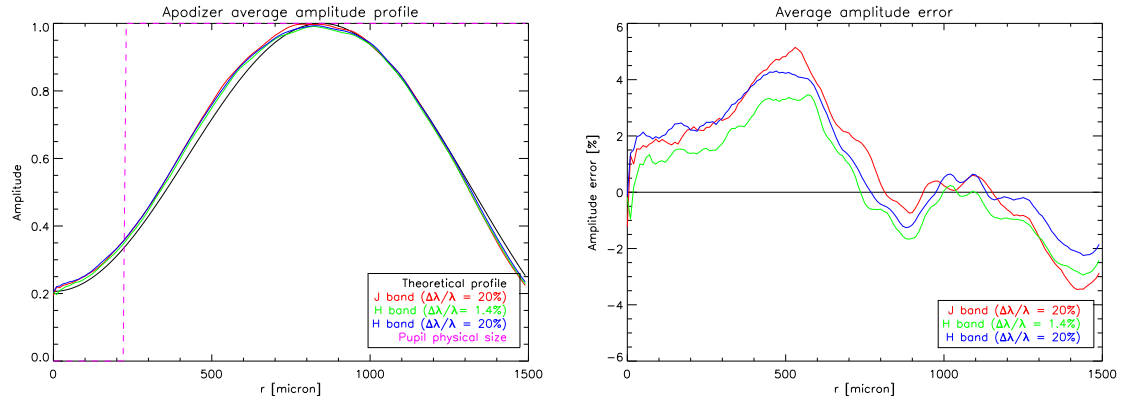

Figure 13.8: Left: Apodizer azimuthally average profile (from center to the edges) using different filters (J, H and narrow H band) compared to specification (black curve). Right: corresponding average amplitude error as function of the position using the same filters.

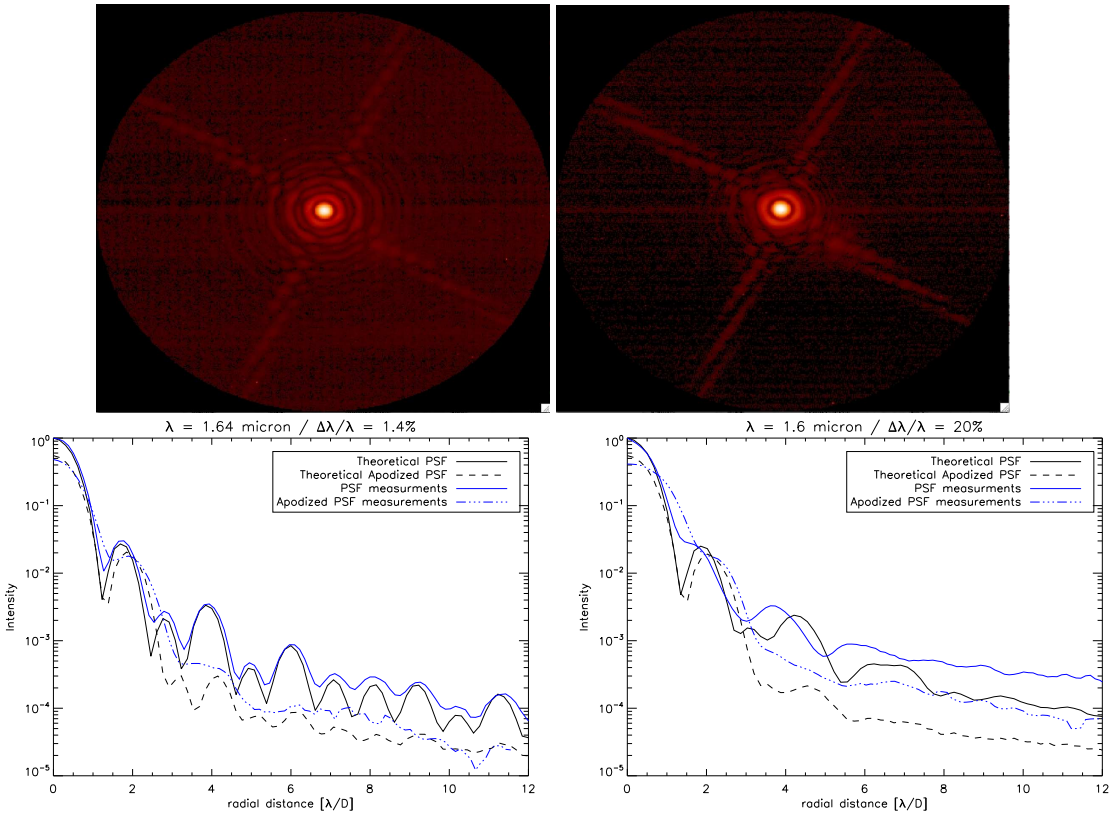

Figure 13.9: Top (left) : VLT-like pupil PSF recorded on the bench (λ= 1.64 μm, $\Delta\lambda/\lambda$ = 1.4%). Top (right) : VLT-like pupil apodized PSF in the same conditions. Bottom (left) : PSF and apodized PSF recorded on the bench (blue lines) compared to theoretical ones (black lines) with narrow H filter (λ= 1.64 μm, $\Delta\lambda/\lambda$ = 1.4%). Bottom (right) : Same measurements as previous ones but with broadband H filter ($\Delta\lambda/\lambda$ = 20%).

13.5.3 Effect on the PSF

This first series of tests intend to demonstrate the correct behavior of the binary apodizer on the PSF. In other words, in the IR path we do not place the Lyot coronagraph on the focal plane nor the APLC pupil stop. We

only compare the PSF without apodizer to that with the apodizer. Qualitatively (Fig. 13.9 top pictures) it is demonstrated that the apodizer works well : the PSF´s wings of the apodized PSF has been reduced in intensity and by energy concern one can see that there is more energy inside the core of the apodized PSF compared to the non-apodized one (exposure time are here identical). This behavior agrees well with the theoretical predictions. Although there is some discrepancy between theory and measurements (Fig. 13.9, bottom, for $\Delta\lambda/\lambda = 20\%$ in H band), the gain between measured PSF and measured apodized PSF is fully consistent with theory. This results has been demonstrated in the H-band with a narrow filter ($\Delta\lambda/\lambda = 1.4\%$) and with a broadband filter ($\Delta\lambda/\lambda = 20\%$). The discrepancy can be well understood since theoretical profile comes from simulation assuming perfect components (pupil mask, apodizer) and ideal propagation through the optical system. The net effect of the binary apodizer on the PSF is then demonstrated and consistent with theory. Its achromaticity in H band is also confirmed.

13.5.4 Effect on the coronagraphic image

This second series of tests intend to demonstrate the coronagraphic behavior of the APLC using the microdots apodizer.

Qualitatively the coronagraphic PSF (Fig. 13.10, H band with $\Delta\lambda/\lambda = 1.4\%$) has a profile agreeing with the theory: a PSF-like pattern homogeneously reduce in intensity with most of the energy inside the first rings. In this observed raw image, a best local contrast of 6.5×10^{-7} has been reached between the spider vane spike diffractions.

Metrics	Recorded on bench		Theory	
	$\Delta\lambda/\lambda$[%]			
	1.4	20	1.4	20
Contrast at $3\lambda/D$	$5.0\ 10^{-5}$	$1.5\ 10^{-4}$	$1.4\ 10^{-6}$	$1.2\ 10^{-5}$
Contrast at $12\lambda/D$	$2.3\ 10^{-6}$	$3.5\ 10^{-6}$	$2.1\ 10^{-7}$	$2.8\ 10^{-7}$
Contrast at $20\lambda/D$	$1.2\ 10^{-6}$	$1.8\ 10^{-6}$	$1.0\ 10^{-7}$	$1.3\ 10^{-7}$
Total rejection	489	355	1000	641
Peak rejection	627	674	1058	788

Table 13.3: Summary of coronagraphic results and comparison with theory

In Fig. 13.11 we present apodized PSFs and coronagraphic PSFs recorded on the bench using a narrow ($\Delta\lambda/\lambda = 1.4\%$) and broadband filter ($\Delta\lambda/\lambda = 20\%$) in H band. Most of the time, an order of magnitude discrepancy (mostly in the halo) is found between theory and recorded data (Table. 13.3) where we have compared contrast at 3, 12 and $20\lambda/D$. Theoretical results assume bench configuration and perfect conditions (components and propagations). The contrast is defined as the ratio of the maximum intensity of the apodized PSF image on the detector to the local (i.e at a given angular separation) intensity on the coronagraphic image on the detector. The total rejection rate (ratio between the total intensity of the PSF image on the detector and the total intensity of the coronagraphic PSF image on the detector, in practice limited in a $20\lambda/D$ radius area on the images) is only at a factor 2 and 1.8 from theory at 1.4% and 20% filter bandpass respectively. This discrepancy is reduced when considering the peak rejection (ratio between the maximum intensity of the PSF to the maximum intensity of the coronagraphic PSF) to a factor 1.7 and 1.2, respectively. Chromatism impact is only slightly revealed at small angular separation (before $4\lambda/D$), otherwise achromaticity is demonstrated in the halo for the H band. The discrepancy found between recorded data and theory can be understood since theoretical results assume ideal pupil mask, apodizer and optical propagation. In practice, the beam propagates through IR doublets, neutral density (for apodized PSF to not saturate the detector), IR filters and camera optics. Moreover, as discussed in Sec. 13.5.2, the microdots apodizer is localized at 3.5mm from the pupil mask. Such a defocalisation is believed to impact performance (non-blackcoated pupil masks as well).

Despite the discrepancy discussed above, these first results of APLC using microdots apodizer are already beyond the SPHERE requirements (Boccaletti et al. 2008 [22]).

During our laboratory test, no high frequencies noise due to the apodizer pixellation has been revealed. However, simulation analysis presented in Sec. 13.3.2 predicts pixellation noise at about $20\lambda/D$ on the coronagraphic

image at a contrast between 10^{-7} and 10^{-8} (S = 600). In our case, the contrast was not deep enough even between the diffraction spike of the spider vanes to reveal the predicted noise. Therefore, we can only conclude on the performance and suitability of our configuration for HOT (even for SPHERE) but not on the pixellation noise predicted by simulation.

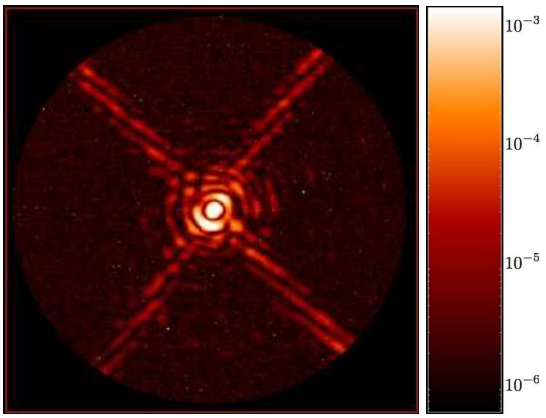

Figure 13.10: Observed raw coronagraphic image (log scale) recorded on the bench at λ= 1.64 μm ($\Delta\lambda/\lambda$ = 1.4%).

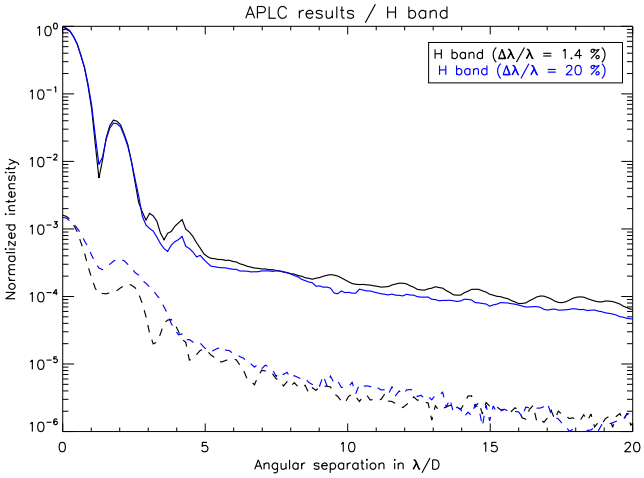

Figure 13.11: Azimuthally average coronagraphic PSF at λ= 1.64 μm, $\Delta\lambda/\lambda$ = 1.4% (black lines) and $\Delta\lambda/\lambda$ = 20% (blue lines)

13.6 Conclusion

In this Chapter, we reported the results from development and laboratory experiment of APLC using microdots apodizer in the near-IR. Halftone dot process is a promising alternative solution to continuous metal layer deposition. Using a diffusion error algorithm, and optimized pixel size and fabrication techniques, we demonstrate impressive agreement between the specified and measured transmission profiles, as well as the achromatic behavior of such apodizer. Coronagraphic properties are consistent with the expected properties, and have already reached the SPHERE requirements. Achromaticity in H band is also demonstrated.

An additional predicted advantage of pixellated apodizers is that they do not introduce a spatially-varying spatial phase which might compromise coronagraphic cancellation at all radial distances.

Therefore, we conclude that microdots apodizer mask is a very attractive solution for APLC. Although this study was carried out for the specific case of APLC in the context of R&D activities for the future near-infrared instrument of the E-ELT, it can be extend for other near-IR or visible instruments (SPHERE, for instance) and to other coronagraphs as well (Dual zone, for instance). We note that a RCWA analysis would be mandatory if the pixel size is comparable to the wavelength.

14

Microdots physical properties laboratory investigations

Contents

Abstract - *In this Chapter, we present near-IR laboratory results to characterize a new technology solution – presented in the previous chapter – for apodizers manufacturing. This technique aims at solving drawbacks of a continuous deposit of a metal layer with spatially varying thickness approach. Main advantages of a microdots apodizer are listed below: 1/ accuracy of the profile, 2/ achromaticity, 3/ no exhibition of a spatially-varying phase, 4/ reproducibility. In the last chapter, we reported that microdots apodizers exhibit blue noise properties (i.e high frequency noise), when designed for coronagraphy. Although, numerical simulations as well as theoretical predictions confirm pixellation noise in the coronagraphic image, its impact was found negligible during experiment since our first prototype (mask 1, hereafter) was designed to push this noise out of our field of view of interest at a deep contrast level. Here, our purpose is precisely to investigate the pixellation noise properties using 5 new masks with same profile as mask 1, but by successively degrading the pixel size. The interest is twofold: 1/ confirm theory predictions on the physical properties of such devices with laboratory proofs, 2/ derive relevant informations to design any amplitude microdots apodization mask whatever the coronagraph.*

14.1 Introduction

Pixellated apodizers introduce high frequencies that are function of the pixel size. The aim of this work is precisely to characterize the pixel size impact on the coronagraphic image. Estimation of both the noise intensity and its localization in the field of view is the objective of this study.

A set of 5 new masks has been designed with different pixel sizes, and tested in the near-IR.

For the reader's convenience, we briefly remind microdots apodizer theoretical properties using same notations as defined in Chapter 13. A microdots apodizer is modeled as an aperiodic under-filled two-dimensional grating. Such device exhibits blue noise properties owing to the error diffusion algorithm used to calculate a distribution of pixels (i.e dots) that best approximates the required field transmission [38, 95, 37]. The binary pattern produces an average gray level value ($g = \sqrt{T}$, i.e average amplitude transmission) from an apodizer profile with intensity transmission T. The resulting pattern spectral energy of such device is set by the minority pixels present on the device (i.e by g, non-metal pixels when $g < 0.5$ and by metal pixels conversely). The spectral energy therefore increases as the number of minority pixels increases, peaking at $g = 0.5$ [95]. In the precise case of square pixels [96], the power spectrum of the pattern exhibits energy concentration around a first order diffraction peak (f_g) localized in the field of view in λ/D units as

$$f_g = \begin{cases} \sqrt{g} \times S & g \leq 1/2 \\ \sqrt{(1-g)} \times S & g > 1/2 \end{cases} \tag{14.1}$$

where S is the scalling factor, ratio between the pupil diameter (Φ) and the pixel size, i.e dot size (p). Higher order diffraction peaks are less relevant since out of the field of view when dots are small enough. Each order diffraction peaks are separated by S in λ/D units with S extent, i.e dots scatters light by diffraction and creates a 2D-sinus cardinal function halo in the focal plane.

In Chapter 13 we present a simplified model for order-of-magnitude estimation of the pixellation noise intensity in coronagraphic systems [36]. The speckles halo in the coronagraphic image resulting from the non-regular dots distribution broaden the first order diffraction peak f_g with an intensity I_g defined as

$$I_g = \begin{cases} g \times \frac{\pi}{4} \times \left(\frac{1}{S}\right)^2 & g \leq 1/2 \\ (1-g) \times \frac{\pi}{4} \times \left(\frac{1}{S}\right)^2 & g > 1/2 \end{cases} \tag{14.2}$$

Fig. 14.1 gathers high frequencies noise localization in the field, and intensity (normalized by the stellar flux), as function the gray level for the set of scaling factors (S) we used for prototyping. Decreasing the scaling factor, i.e increasing the pixel size, therefore moves closer the principal frequency with an increase of energy.

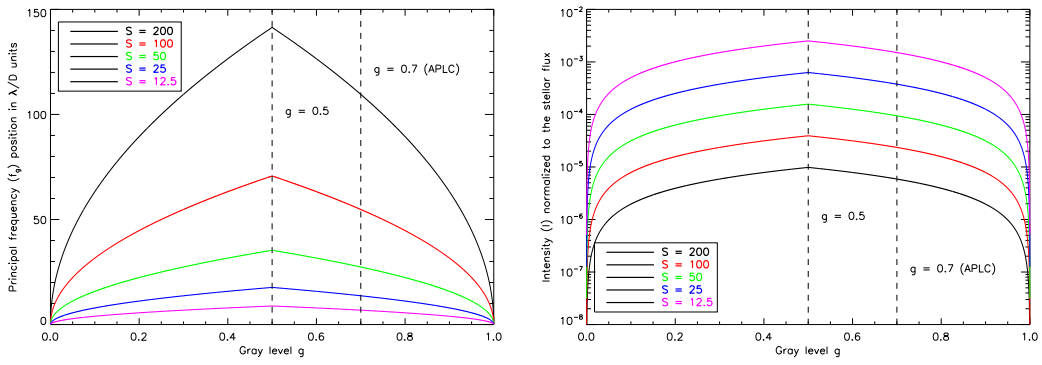

Figure 14.1: *Left*: First order diffraction peak position (f_g in λ/D units) as a function of gray level g. *Right*: Speckles halo intensity I normalized to the reference star intensity as function of gray level g. In both plots, the APLC case ($g = 0.7$) is localized with dashed line.

14.2 Experiment

14.2.1 Masks design and optical setup

The configuration of the apodizer profile is similar to that described in Chapter 13 (4.5 λ/D APLC, $\Phi = 3mm$ due to constraints on our optical bench). The 5 new apodizer masks were fabricated by Precision Optical Imaging in Rochester, New York. Masks were fabricated using wet etch contact lithography of a regular Chrome layer ($OD = 4$) deposited on a BK7 glass substrate ($\lambda/20$ peak-to-valley), with antireflection coating for the H band (1.2 to 1.8μm, $R < 1\%$) on their back faces. Mask 1 had a scaling factor of 500 corresponding to 6μm pixels grid, but finally appear smaller (4.5μm), as a predictable result of the manufacturing process. Hereafter mask 2, 3, 4, 5, and 6, have a scaling factor of 200, 100, 50, 25 and 12.5 corresponding to 15, 30, 60, 120 and 240μm pixel size, respectively. Therefore, pixels size, i.e dots size, increases by a factor 2 mask by mask. Table 14.1 gathers all the masks characteristics and noise properties predicts by theory (Eq. 14.1 and 14.2).

The experiment configuration is similar to that described in Chapter 13. The optical setup is designed to simulate the 8-m VLT pupil and to operate in the near-infrared (H-band). The Strehl ratio of the bench is $\sim$ 94%. The IR camera used (the Infrared Test Camera) is designed to reach a pixel scale of 5.3 mas. The APLC pupil-stop is also similar to that of paper I and remains the same during the experiment. The pupil-stop features outer VLT-pupil diameter reduction and oversized central obscuration while the spider vanes are increased by a factor 4. The 4.5 λ/D Lyot mask is installed at a F/48.4 beam.

14.2.2 Inspection of the apodizers

Metrology inspection of these 5 masks has been made using a infrared pupil images (Fig. 14.4) and a Shadowgraph ($\times$50, see left column of Fig. 14.4). Chrome dots size have been determined to 15 - 29 - 57 - 119 and 240 μm $\pm 1\mu$m for mask 2 to 6 respectively. Unlike mask 1, mask 2 to 6 designs were not numerically pre-compensated to avoid an increase of transmission – as a result of a reduction of the metal dots during the wet-ech lithography process – since dot size was less critical than for mask 1.

The spatially-resolved transmissions of each apodizers has been measured. An iris in the far field has been used to obtain the low-frequency component of each mask to verify the global shape (i.e the symmetry). Accuracy of the profile is about 3-5% in near-IR (achromaticity has been demonstrated with mask 1 along J and H-band). Images have been recorded without the iris as well. As the pixel size increases from mask 2 to mask 6, the high-frequency contents of the recorded images becomes predominant. The evaluation of the impact of the high-frequency contents at the coronagraphic image level is precisely the objective of this study.

14.3 Results and discussion

Coronagraphic images recorded on the bench using masks 2 to 6 are presented in Fig. 14.4 (central column: $\Delta\lambda/\lambda = 1.4\%$, right column: $\Delta\lambda/\lambda = 20\%$). Speckles are clearly visible as well as speckle elongation when a broadband filter is used (right column). Qualitatively, reducing the pixel size (from mask 6 to mask 2) moves further away the first order diffraction halo. When the first order diffraction halo is away enough from the central core of the PSF, a usable field of view cleaned of speckles appears and reveals the residual diffraction from the pupil (spider vane diffraction spikes).

Coronagraphic profiles obtained with each masks are presented on Fig. 14.2 (left), and can be compared to simulations (right). Simulations assumed perfect microdots apodizers and bench conditions (VLT-like pupil, same bandwidth and similar Strehl ratio). In Table 14.1 we compare the intensity and localization of the first order diffraction halo measured and predicted by Eq. 14.1 and Eq. 14.2. The intensity has been measured on the halo peak. In the following, we successively discuss results obtain with each masks:
Mask 6 – The pixel size is 240μm (S = 12.5). The black curve of Fig. 14.2 (left) revealed several order diffraction peaks broadened by speckles. The first order diffraction peak localization as well as its peak intensity are consistent with theory (Table 14.1). The first peak is localized at $S/2$ (i.e 7 λ/D) with 1.1×10^{-3} intensity (normalized to the stellar flux). The 4 diffraction peaks revealed are separated by $\sim$S factor (i.e 12.5 λ/D) and are localized at $S/2$, $3S/2$, $5S/2$ and $7S/2$ with extent in the order of S in λ/D.

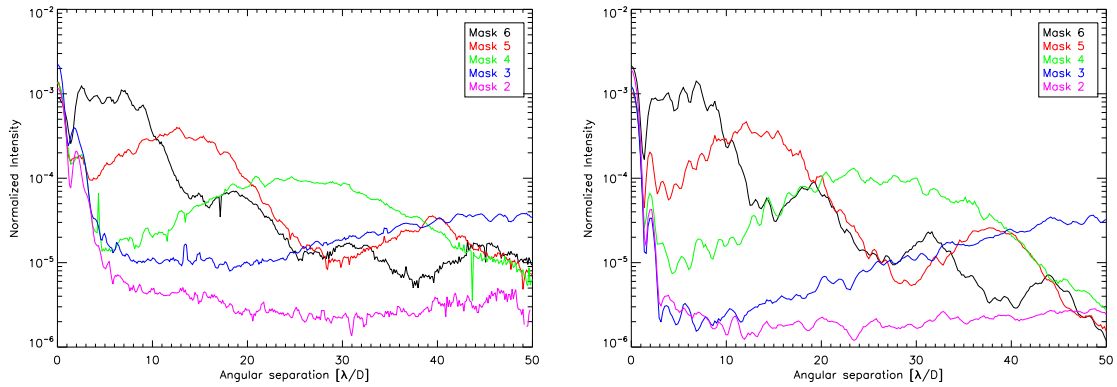

Figure 14.2: Summary of coronagraphic radial profiles ($\Delta\lambda/\lambda = 1.4\%$) for mask 2 to mask 6, profiles are azimuthally averaged. *Left*: recorded on the bench, *Right*: simulations assuming bench conditions.

Prototype	S	p [μm]	f_g [λ/D]		I_g	
			Theory	Experiment	Theory	Experiment
Mask 2	200	15	107	-	5.7×10^{-6}	-
Mask 3	100	30	54	53	2.3×10^{-5}	3.3×10^{-5}
Mask 4	50	60	27	25	9.1×10^{-5}	9.9×10^{-5}
Mask 5	25	120	13	13	3.6×10^{-4}	3.5×10^{-4}
Mask 6	12.5	240	7	7	1.4×10^{-3}	1.1×10^{-3}

Table 14.1: Summary of theory and laboratory measurements of the pixellation noise properties (localization in the field and intensity).

Mask 5 – The pixel size is 120μm (S = 25). Here, two order diffraction peaks are observable (Fig. 14.2 (left), red curve) at $S/2$ and $\sim 3S/2$ (i.e 13 and $39\lambda/D$ respectively). First order diffraction peak halo intensity is consistent with theory.

Mask 4 – The pixel size is 60μm (S = 50). In that case only the first order diffraction peak is revealed at $S/2$ (i.e 25 λ/D, Fig. 14.2, (left) green curve). Intensity is fitting theory.

Mask 3 – The pixel size is 30μm (S = 100). Only the rise to the first order diffraction peak is visible (peaking at $\sim S/2$, blue curve) with intensity consistent with theory.

Mask 2 – The pixel size is 15μm (S = 200). No diffraction peaks have been observed (pink curve, Fig. 14.2 (left)). The first one is theoretically localized at $107\lambda/D$ from the center core of the coronagraphic image, and therefore it is out of the accessible field of view. For that reason no evaluation of the intensity is possible. However, the halo seems to start its rise to the first order diffraction peak (i.e the halo level is increasing).

All the tests performed with these new masks but mask 2 confirmed Eq. 14.1 and Eq. 14.2. We carried out the same test with a broadband filter in H ($\Delta\lambda/\lambda = 20\%$), and we did not observed any modification of the behavior. Comparison with simulated coronagraphic profiles (Fig. 14.2,right) presents a slight discrepancy, mainly for mask 2 and 3, at small angular distance without impacting the halo intensity and position. This discrepancy can be explained as the result of profile errors or apodizer alignment (mostly on the focalization, as a results of available room on the bench, i.e pupil mask and apodizer are in the same collimated beam, therefore not rigorously in the same plane).

Theory predictions are therefore confirmed. The simplify model used for order-of-magnitude estimation of the pixellation noise intensity in coronagraphic image is impressively representative of the APLC situation.

14.4 Conclusion

Considering the validity of Eq. 14.1 and Eq. 14.2, resumed in Fig. 14.1, we can therefore properly designed microdots apodizer (i.e select pixel size) for any coronagraph concepts featuring amplitude pupil apodization. The selection of the pixel size must be defined by pushing out of the field of interest the first order diffraction halo (Eq. 14.1) and by reducing its intensity (Eq. 14.2) to avoid any limitations imposed even by the rise to the speckle halo. The apodizer amplitude transmission (g) as well as the sampling factor (S) drive this choice. Ideally, going to very small pixels size improves the accuracy of the profile transmission (sampling problem) but when the pixel size is comparable to the wavelength of light, the transmission is affected by plasmons [40, 50].

This last aspect is actually under investigations by R. Soummer for GPI where microdots apodizers have been developed with 2 microns configuration (H-band application). Modification of the profile transmission have been revealed as function of the wavelength. These investigations are important and lead to very interesting results that will certainly be published soon.

The microdots technique will be the baseline approach for the apodizer of the Apodized Pupil Lyot Coronagraph for EPICS [56] as well as for GPI [61]. Extending this technique for SPHERE would be as well a relevant choice.

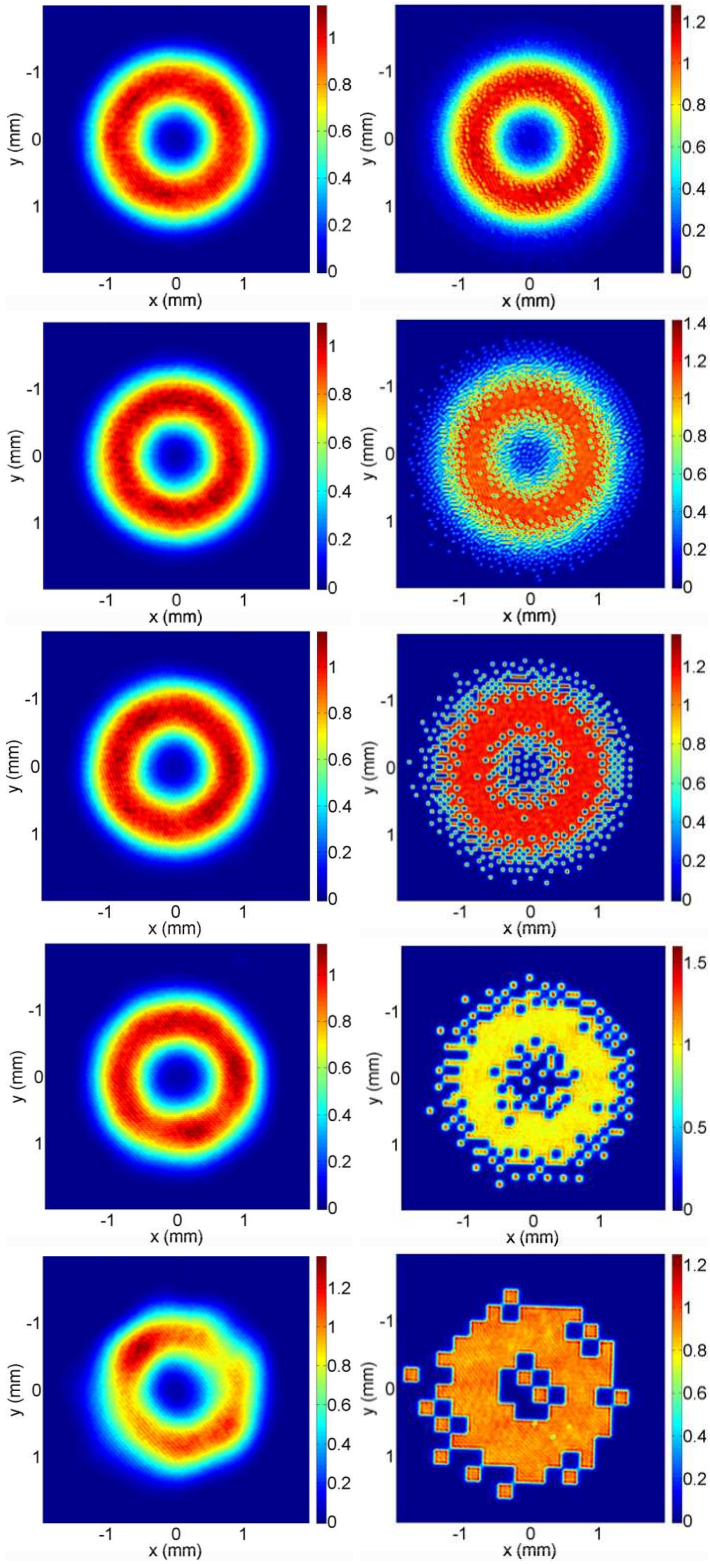

Figure 14.3: Infrared apodizer images of Mask 2 to 6. Left: low-frequency contents, Right: all frequencies included.

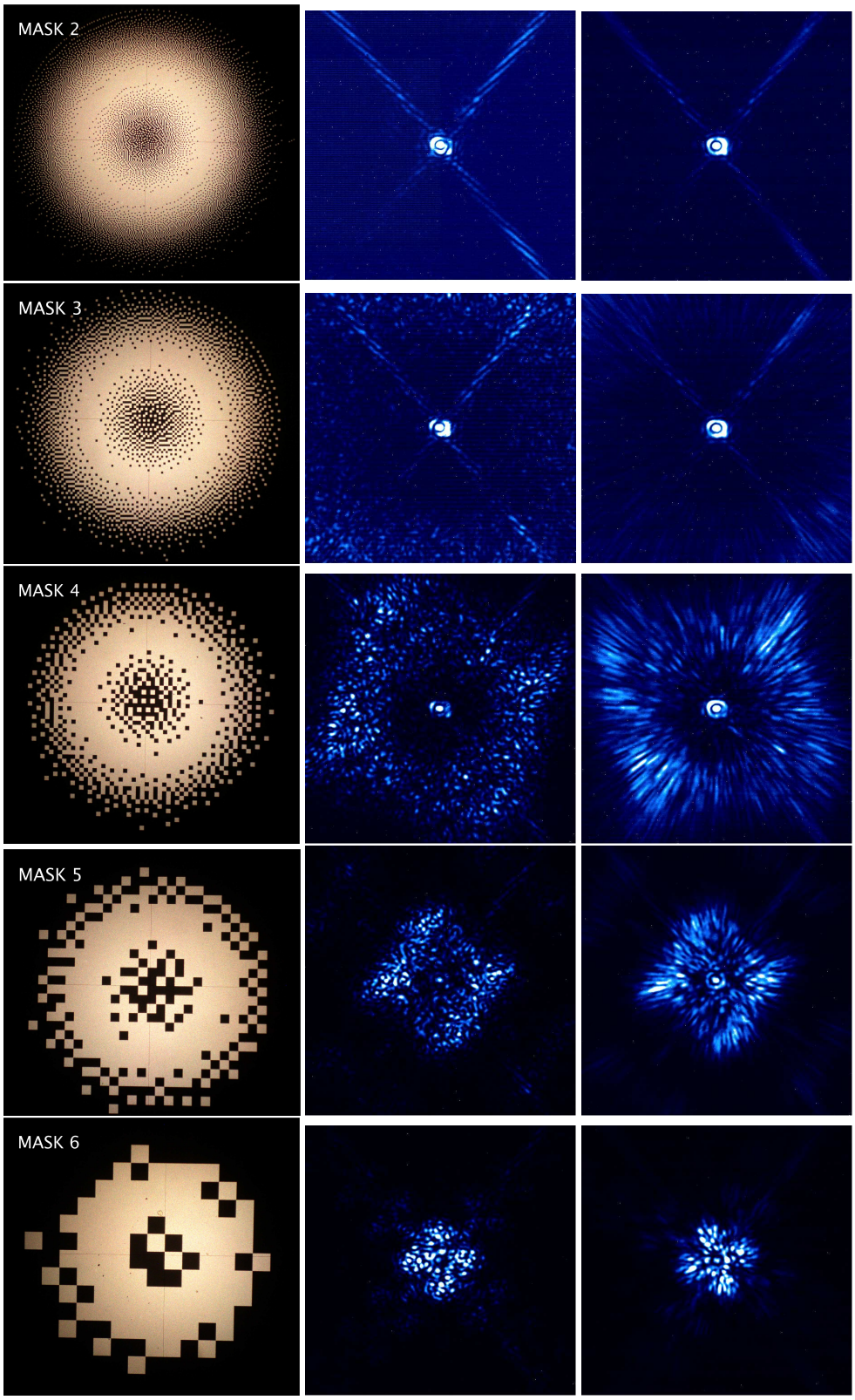

Figure 14.4: Left: Shadowgraph inspection (×50) of mask 2 to 6 (top row to bottom row), middle: infrared coronagraphic images ($\Delta\lambda/\lambda$ = 1.4%), and on the right: infrared coronagraphic images ($\Delta\lambda/\lambda$ = 20%).

Conclusion

Along this present thesis, we attempted to study a wide range of coronagraph designs in different conditions with the goal to propose promising concepts for ELTs. The comparison of their sensitivity/dependency to ELTs parameters is a critical issue. The ambition of this work was therefore to provide relevant informations to anyone thinking about how to select coronagraphs for ground-based large telescopes. For that, we managed to assemble an analysis of coronagraphic XAO systems, trying to consider a large number of variables.

As a fair comparison between coronagraphs, we started to investigate the possibility of optimizing coronagraph parameter space to ELTs characteristics. We demonstrated that optimal configurations of APLC exist, and are mainly driven by the central obscuration ratio of a telescope. In the same time, interest of Band-limited coronagraphs have been questioned from throughput point of view, severely restricted by ELTs parameters.

A first order system analysis underlined coronagraph dependencies to aberrations that occur in a coronagraphic telescope. Again, Band-limited interest has been discussed because of their similar response as the other concepts to low-order segment phase aberrations.

We evaluated the effect of several aberrations on the performance of a coronagraphic eXtreme Adaptive Optics (XAO) and Differential imaging systems. We derived same conclusions when limits on the halo are set either by the residual phase aberrations that are leaking through the XAO system, or the static aberration of a differential imaging system. We extracted from this analysis three kind of coronagraphs according to the angular separation accessibility to the parent star, and in each case we proposed promising designs. Among these conclusions, we selected the APLC as a baseline design for ELTs. By "baseline" design for ELTs, we mean that the APLC gathers enough advantages to be used with any forthcoming planet finder instrument. However, by "baseline" design, we do not mean that the APLC must be the only coronagraph design for ELTs. It is clear that several concepts (or families) must be used and selected as function of sciences objectives as already done for SPHERE. Having a choice of different techniques is definitely a key advantage to adapt to changing observing needs.

Since after simulations, the expected step is the laboratory experiment, we made an effort for developing several coronagraphs, among them the FQPM, Lyot, and APLC. Even if the FQPM is a well known manufactured concepts, reaching the accuracy on the quadrants step thickness was a difficult task and a reason of important delay on the delivery of a final prototype. Experience with metal layer deposition for producing the apodizer of the APLC was problematic as well. As a result we investigated new technology approach. Therefore, there was some regrettable delays on the comparison of these concepts with the AO of HOT. But this is a result of the nature of instrumental PhD.

However, the satisfactory results of the development of a microdots apodizer for the APLC is encouraging and was enthralling. We are currently extending this technique to produce new coronagraphs such as Band-limited masks. In the next two years, owing to EPICS phase A, Dual zone and AGPM coronagraphs could potentially extend our list of coronagraphic devices to be implemented on HOT.

In the following, – might be inappropriate for a PhD conclusion – forthcoming studies that will be investigated are listed:

- Development of Band-limited masks using microdots technique. This is actually on going: masks have been designed and are currently under manufacturing step. Laboratory tests are planned for the middle of November 2008. Conventional pupil apodization developments are considered as well.
- Investigate manufacturing solutions to make achromatic the Lyot mask of the APLC.
- Test all the coronagraphs coupled with the AO of HOT with both the VLT and E-ELT pupil configuration, which will be done along 2009.

- Improving the peak suppression (effect of the large residual amount of diffracted light by the pupil central obscuration) and pointing error in the precise case of phase mask (e.g AGPM) is mandatory since any other aberrations are pinned to the contrast level imposed by the central obscuration. A solution would be to use a small Lyot mask placed in the center of the phase mask. A trade-off analysis is therefore mandatory to select the diameter of this additional Lyot mask.
- Further analysis/comparison of coronagraphs involving: S/N ratio estimation with different types of astrophysical objects, a thorough telescope/instrument design, speckle suppression systems and data post-processing are mandatory and will be handle by the EPICS consortium.

Publication list

Journals

- Optimization of Apodized Pupil Lyot Coronagraph for ELTs, **Martinez, P.**, Boccaletti, A., Kasper, M., Baudoz, P., and Cavarroc, C., , A&A 2007 (474 p.671-678).
- Comparison of coronagraphs for high contrast imaging in the context of Extremely Large Telescope, **Martinez, P.**, Boccaletti, A., Kasper, M., Cavarroc, C., Yaitskova, N., Fusco, T. and Vérinaud, C., Accepted in A&A 2008.
- Design, analysis and test of a microdots apodizer for Apodized Pupil Lyot Coronagraph, **Martinez, P.**, Dorrer, C., Aller Carpentier, E., Kasper, M., Boccaletti, A., and Dohlen, K., Accepted in A&A 2008.
- Microdots pupil apodizers properties characterization – Research Note –, **Martinez, P.**, Dorrer, C., Kasper, M. et al., to be submitted in A&A 2008.

Conferences

- Optimization of Apodized Pupil Lyot Coronagraph for planet finder instrument, **Martinez, P.**, Boccaletti, A., Kasper, M., Baudoz, P., and Cavarroc, C., Proceedings of the conference In the Spirit of Bernard Lyot: The Direct Detection of Planets and Circumstellar Disks in the 21st Century. June 04 - 08, 2007. University of California, Berkeley, CA, USA. Edited by Paul Kalas.
- Phase and Lyot-type coronagraphs for the High Order Testbench: prototyping and first laboratory results, **Martinez, P.**, Vernet, E., Dorrer, C., Aller Carpentier, E., Boccaletti, A., Kasper, Baudrand, J. and Chaumont, C., Proceeding s of the SPIE 2008.
- Limitations on Earth-like planet detection with perfect and real coronagraphs on ELTs. Cavarroc, C., Boccaletti, A., Baudoz, P., Fusco, T., **Martinez, P.**, and Rouan, D., Proceeding of the SPIE 2006.
- High Order test bench for extreme adaptive optics system optimization, Aller Carpentier, E., Kasper, M., **Martinez, P.**, Vernet, E., Fedrigo, E., Soenke, C., Tordo, S., Hubin, N., Vérinaud, C., Pinna, E., Puglisi, A., Tozzi, A., Quiros, F., Basden, A. G., Goodsell, S. J., Love, G. D., and Myers, R. M., Proceeding of the SPIE 2008

Optimization of Apodized Pupil Lyot Coronagraph for ELTs

A&A 474, 671–678 (2007)
DOI: 10.1051/0004-6361:20077708

Astronomy & Astrophysics

Optimization of apodized pupil Lyot coronagraph for ELTs

P. Martinez[1], A. Boccaletti[1], M. Kasper[2], P. Baudoz[1], and C. Cavarroc[1]

[1] LESIA, Observatoire de Paris Meudon, 5 pl. J. Janssen, 92195 Meudon, France
e-mail: patrice.martinez@obspm.fr
[2] European Southern Observatory, Karl-Schwarzschild-Strasse 2, 85748 Garching, Germany

Reveived 24 April 2007 / Accepted 14 July 2007

ABSTRACT

Aims. We study the optimization of the Apodized Pupil Lyot Coronagraph (APLC) in the context of exoplanet imaging with ground-based telescopes. The APLC combines an apodization in the pupil plane with a small Lyot mask in the focal plane of the instrument. It has been intensively studied in the literature from a theoretical point of view, and prototypes are currently being manufactured for several projects. This analysis is focused on the case of Extremely Large Telescopes (ELTs), but is also relevant for other telescope designs.
Methods. We define a criterion to optimize the APLC with respect to telescope characteristics such as central obscuration, pupil shape, low-order segment aberrations and reflectivity as functions of the APLC apodizer function and mask diameter. Specifically, the method was applied to two possible designs of the future European-ELT (E-ELT).
Results. Optimum configurations of the APLC were derived for different telescope characteristics. We show that the optimum configuration is a stronger function of central obscuration size than of other telescope parameters. We also show that APLC performance is quite insensitive to the central obscuration ratio when the APLC is operated in its optimum configuration, and demonstrate that APLC optimization based on throughput alone is not appropriate.

Key words. techniques: high angular resolution – instrumentation: high angular resolution – telescopes

1. Introduction

Over the past ten years many diffraction suppression systems have been developed for direct detection of extrasolar planets. At the same time, promising ground-based projects were proposed and are currently under development like SPHERE at the VLT (Beuzit et al. 2006a) and GPI (Macintosh et al. 2006). Larger telescopes are desirable to improve performance of exoplanet searches towards lower masses and closer angular distances, ideally down to Earth-like planets. Several concepts of Extremely Large Telescopes (ELTs) are currently being studied worldwide: European-ELT (E-ELT, Dierickx et al. 2004), Thirty Meter Telescope (TMT, Nelson & Sanders 2006), Giant Magellan Telescope (GMT, Johns et al. 2004).

The characteristics of these telescope designs may have an impact on their high contrast imaging capabilities. Parameters such as central obscuration, primary mirror segmentation, and large spider arms, can impose strong limitations for many coronagraphs. It is therefore essential to indentify and evaluate a coronagraph concept which is well-suited to ELTs.

The Apodized Pupil Lyot Coronagraph (APLC) is one of the most promising concepts for ELTs. Its sensitivity to central obscuration is less critical than, e.g., for phase masks (Rouan et al. 2000; Mawet et al. 2005) but the APLC still allows for a small inner working angle (IWA) and high throughput if properly optimized. Other amplitude concepts (e.g. Kuchner & Traub 2002) are also usable with centrally obscured aperture but suffer from low throughput especially if the IWA is small. The potential of the APLC has been demonstrated for arbitrary apertures (Aime et al. 2002; Soummer et al. 2003) and specific solutions for obscured apertures have been proposed (Soummer 2005).

In this paper, we analyze the optimization of the APLC and evaluate its sensitivity with respect to the main parameters mentioned above. In Sect. 2 we briefly revise the APLC formalism and define a criterion for optimizing the coronagraph parameters. The impact of several telescope parameters on the optimal configuration is evaluated in Sect. 3. Section 4 shows an application of the APLC optimization to two potential ELT designs. We then derive conclusions.

2. Apodization for centrally obscured pupils

2.1. Formalism

In this section, we briefly revise the formalism of the APLC. The APLC is a combination of a classical Lyot coronagraph (hard-edged occulting focal plane mask, hereafter FPM) with an apodization in the entrance aperture.

In the following, for the sake of clarity, we omit the spatial coordinates r and ρ (for the pupil plane and focal plane respectively). The function that describes the mask is noted M (equal to 1 inside the coronagraphic mask and to 0 outside). With the mask absorption ε ($\varepsilon = 1$ for an opaque mask), the FPM is then equal to:

$$1 - \varepsilon M \tag{1}$$

P is the telescope aperture, and ϕ the profile of the apodizer. Π describes the pupil stop function, which is considered – in the initial approximation – to be equal to the telescope aperture ($\Pi = P$). The coronagraphic process, corresponding to propagation from the telescope entrance aperture to the detector plane, is expressed in Eqs. (2) to (6). Planes A, B, C and D correspond to the telescope aperture, the coronagraphic focal plane,

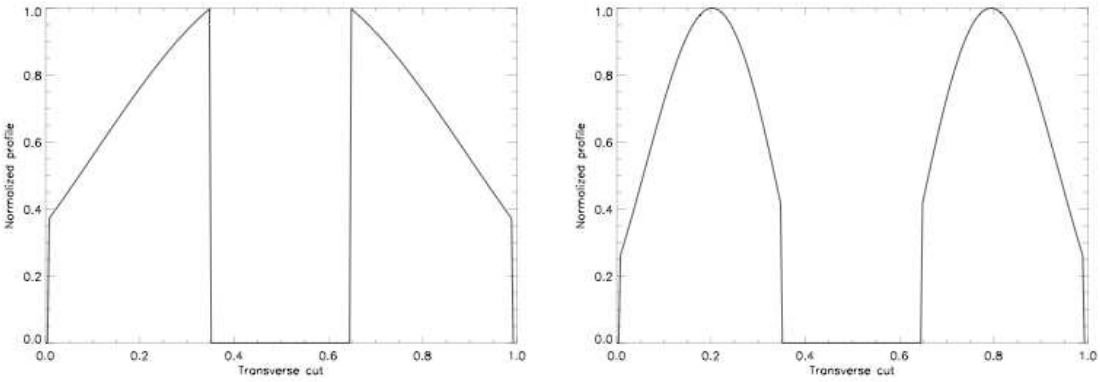

Fig. 1. Typical apodizer shape for the bell regime (*left*) and the bagel regime (*right*). Central obscuration is 30%.

the pupil stop plane and the detector plane respectively as defined in Fig. 2. The Fourier transform of a function f is noted $\hat{f}$. The symbol $\otimes$ denotes the convolution product. The entrance pupil is apodized in the pupil plane:

$$\psi_A = P\phi. \quad (2)$$

The complex amplitude of the star is spatially filtered (low frequencies) by the FPM:

$$\psi_B = \hat{\psi}_A \times [1 - \varepsilon M]. \quad (3)$$

The exit pupil image is spatially filtered (high frequencies) by the stop:

$$\psi_C = \hat{\psi}_B \times \Pi \quad (4)$$

$$\psi_C = [\psi_A - \varepsilon\psi_A \otimes \hat{M}] \times \Pi. \quad (5)$$

The coronagraphic amplitude on the detector plane becomes:

$$\psi_D = \hat{\psi}_C = [\hat{\psi}_A - \varepsilon\hat{\psi}_A M] \otimes \hat{\Pi}. \quad (6)$$

The coronagraphic process can be understood as a destructive interference between two waves (Eq. (5)): the entrance pupil wave $P\phi$, noted ψ_A and the diffracted wave by the mask (corresponding to $\varepsilon\psi_A \otimes \hat{M}$). In the non-apodized case ($\phi = 1$), the two wavefronts do not match each other, and the subtraction does not lead to an optimal starlight cancellation in the Lyot stop pupil plane. A perfect solution is obtained if the two wavefronts are identical (i.e., the diffracted wave by the mask (M) is equal to the pupil wave in amplitude). This latter case is obtained with the Apodized Pupil Phase Mask Coronagraph (Roddier & Roddier 1997; Aime et al. 2002; Soummer et al. 2003). For the APLC, the coronagraphic amplitude is minimized and proportional to the apodizer function.

Considering a pupil geometry, the apodization function is related to the size of the FPM. More precisely, the shape of the apodizer depends on the ratio between the extent of $\hat{M}$ and the central obscuration size (Soummer 2005; Soummer et al. 2007). If the extent of $\hat{M}$ is bigger than the central obscuration, the apodizer takes a "bell" shape (typically it maximizes the transmission near the central obscuration of the pupil (Fig. 1, left). On the contrary, if the extent of $\hat{M}$ is smaller than the central obscuration, the apodizer takes a "bagel" shape reducing transmission in the inner and outer part of the pupil (Fig. 1, right). Thus, the apodizer shape depends on both the FPM size and the central obscuration size.

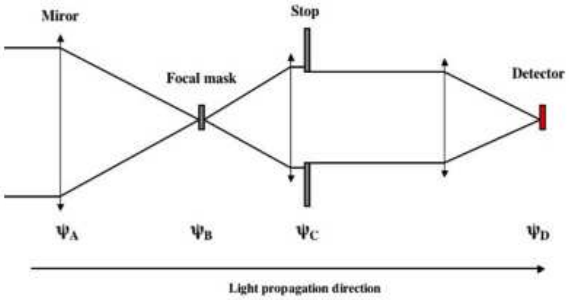

Fig. 2. Diagram of a coronagraph showing the pupil plane containing the apodizer (ψ_A), the focal plane with the FPM (ψ_B), the pupil image spatially filtered by the stop (ψ_C) and the detector plane (ψ_D).

Throughputs (apodizer transmission/pupil transmission) as a function of the FPM size is given in Fig. 3 for different obscuration sizes (15 to 35%). These curves show a second maximum corresponding to the transition between the two apodizer regimes which depends on the central obscuration size. Since apodizer throughput does not evolve linearly with FPM diameter, it is not trivial to determine the optimal FPM/apodizer combination. Moreover, throughput might not be the only relevant parameter when optimizing a coronagraph.

A thorough signal-to-noise ratio analysis is definitely the right way to define the optimal FPM/apodizer system, but this would be too instrument-specific for the scope of this study. Here, we investigate a general case for any telescope geometry and derive the corresponding optimal FPM size.

2.2. APLC optimization criteria

Usually, in Lyot coronagraphy, the larger the FPM diameter the larger the contrast. However, in the particular case of the apodized Lyot coronagraph the transmission of an off-axis point-like object is not linear (Fig. 3) and a trade-off has to be made between contrast and throughput. This problem has been studied by Boccaletti (2004) who evaluated optimal Lyot stops for any telescope pupil geometry and for any type of coronagraph. Based on this study, we propose a criterion adapted to the APLC to optimize the apodizer/FPM combination. This criterion maximizes the coronagraphic performance while minimizing the loss of flux of the off-axis object. While not replacing a thorough signal-to-noise ratio evaluation, our criterion takes into account

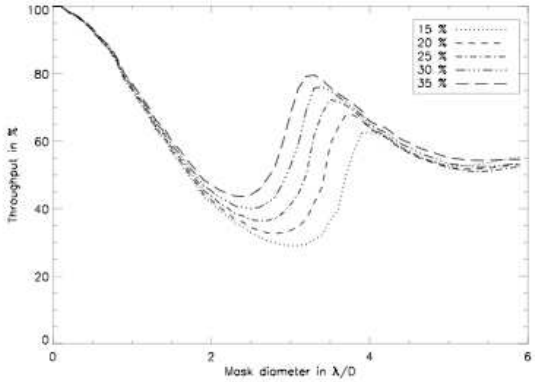

Fig. 3. Apodizer throughput (relative to full transmission of the telescope pupil) as a function of FPM diameter for different obscuration sizes.

the modification of the off-axis PSF (in intensity and in shape) when changing the coronagraph parameters.

Several metrics can be used to quantify the capability of a coronagraph (e.g. Boccaletti 2004). Here, we use the contrast ($\mathscr{C}$) averaged over a range of angular radii:

$$\mathscr{C} = \frac{\max\left(|\,\psi_{\mathrm{D}}(\rho,\alpha)_{\varepsilon=0}\,|^2\right)}{\left(\int_0^{2\pi}\int_{\rho_{\mathrm{i}}}^{\rho_{\mathrm{f}}} |\,\psi_{\mathrm{D}}(\rho,\alpha)\,|^2\,\rho\,\mathrm{d}\rho\,\mathrm{d}\alpha\right)/\pi({\rho_{\mathrm{f}}}^2-{\rho_{\mathrm{i}}}^2)} \tag{7}$$

where $\mathscr{C}$ is expressed in polar coordinates ρ and α. We denote by ρ_{i} and ρ_{f} the short radii and the large radii, respectively, defining the area of calculation for $\mathscr{C}$.

The attenuation of the off-axis object is given by the ratio of maximum image intensity with the apodizer only to that without the coronagraph, i.e., without the apodizer and the FPM. This quantity differs from the throughput, since it also takes into account the modification of the PSF structure when changing the apodizer profile:

$$\max\left(\frac{|\,\psi_{\mathrm{D}}(\rho,\alpha)_{\varepsilon=0}\,|^2}{|\,\hat{P}(\rho,\alpha)\,|^2}\right). \tag{8}$$

Now, let us define the criterion $C_{\mathscr{C}}$ as the product of $\mathscr{C}$ and Eq. (8).

$$C_{\mathscr{C}} = \mathscr{C} \times \max\left(\frac{|\,\psi_{\mathrm{D}}(\rho,\alpha)_{\varepsilon=0}\,|^2}{|\,\hat{P}(\rho,\alpha)\,|^2}\right). \tag{9}$$

The first term of $C_{\mathscr{C}}$ (Eq. (7), which characterizes the performances of the coronagraphic system) is then adapted to the region of interest in the coronagraphic image and can be well matched to the instrument parameters.

The second term (Eq. (8)) takes into account the modification of the PSF structure when changing the apodizer profile and guarantees a reasonably moderate attenuation of the off-axis PSF maximum intensity (i.e., guarantees that when the coronagraph rejects the star it does not reject the planet as well).

Although our criterion cannot replace a thorough signal-to-noise ratio analysis (no instrumental model, no noise terms), it presents a reasonable approach by assuming the residual light leaking through the coronagraph as noise. Our criterion allows us to investigate the trade-off between performance and throughput while keeping the study general and independent of a specific instrument setup.

Moreover, the validity of this criterion is supported by the pupil stop optimization study of Boccaletti (2004) who facied a problem similar to ours, and also by the results presented and discussed in this paper.

3. Sensitivity analysis

3.1. Assumptions

Based on the previously defined criterion, we now analyze the behavior of several telescope parameters as a function of the size of the FPM (and hence APLC characteristics) with the main objective of exploring possibilities of how to optimize the APLC configuration for a given ELT design. One advantage of $C_{\mathscr{C}}$ is that the area of optimization in the focal plane can be well matched to the instrumental parameters. For this reason, we have limited the search area and investigated $C_{\mathscr{C}}$ only between $\rho_{\mathrm{i}} = 3\lambda/D$ at small radii and $\rho_{\mathrm{f}} = 100\lambda/D$ at large radii. These limits correspond to the IWA (distance at which an off-axis object reaches a significant transmission) and to the high-order Adaptive Optics (AO) cut-off frequency, respectively. At radii larger than the AO cut-off frequency, the coronagraph will only have a minor effect since atmospheric turbulence is not corrected and atmospheric speckles dominate.

For the simulations presented in the next sections, we assume a circular pupil with 30% central obscuration. The central obscuration ratio is left as a free parameter only in Sect. 3.2.1 where we evaluate its impact. The pupil stop is assumed identical to the entrance pupil including spider arms (Sivaramakrishnan & Lloyd 2005). Section 3.2.2, where the impact of the spider arms' size is analyzed, assumes 42-m telescope. Elsewhere, simulation results do not depend on the telescope diameter. Apodizer profiles were calculated numerically with a Gerchberg-Saxton iterative algorithm (Gerchberg & Saxton 1972). The pixel sampling in the focal plane is 0.1 λ/D, and the pupil is sampled with 410 pixels in diameter. When phase aberrations are considered we adopt a wavelength of 1.6 μm corresponding to the H-band in the near infrared.

3.2. Critical parameter impacts

In the following sub-sections, we study the impact of two major categories of diffraction effects. The first category deals with amplitude variations: central obscuration, spider arms, primary mirror segmentation, segment-to-segment reflectivity variation, and pupil shear (misalignment of the coronagraph stop with respect to the instrument pupil). Inter-segment gaps and other mechanical secondary supports are not considered, since they would require finer pixel sampling in the pupil image, resulting in prohibitively large computation times with a non-parallel computer. In addition, some mechanical secondary supports can be much smaller than the main spider arms. At the first approximation, their effects can be considered to be similar to those produced by spider arms.

The second category is related to phase aberrations, which we assumed are located in the pupil plane (no instrumental scintillation). We only modeled low-order segment aberrations (piston, tip-tilt, defocus, astigmatism). Higher orders are less relevant for the optimization of the FPM size, but can have a significant impact on the coronagraphic performance.

The amplitude diffraction effect of gaps is partially accounted for (at least for infinitely small gaps) by the phase transition we are generating between primary mirror segments.

Table 1. Optimum FPM diameter (and hence APLC characteristics) for several obscuration sizes and criteria.

	$C_{\mathscr{C}}$		Max. throughput	
Obstruction size (%)	FPM (λ/D)	Throughput (%)	FPM (λ/D)	Throughput (%)
10	4.3	59.4	4.1	62.2
15	4.3	58.3	4.0	62.4
20	4.4	55.8	3.8	65.5
25	4.6	52.7	3.6	67.9
30	4.7	51.2	3.5	68.7
35	4.9	49.4	3.3	70.4

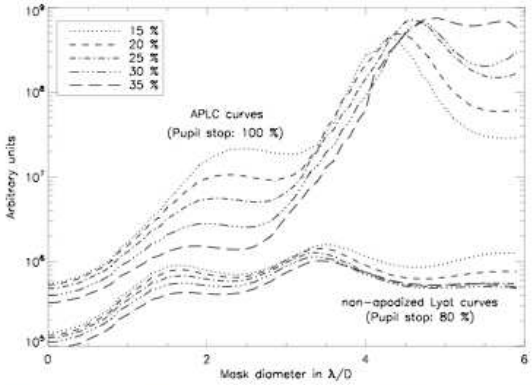

Fig. 4. $C_{\mathscr{C}}$ average between 3 and 100 λ/D as a function of the FPM diameter and obscuration sizes, in the case of the APLC and classical Lyot coronagraph.

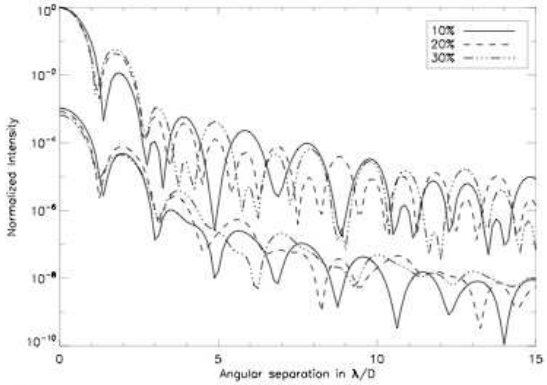

Fig. 5. Radial profiles of PSFs and coronagraphic images obtained with optimal APLC (using $C_{\mathscr{C}}$) for several obscuration sizes.

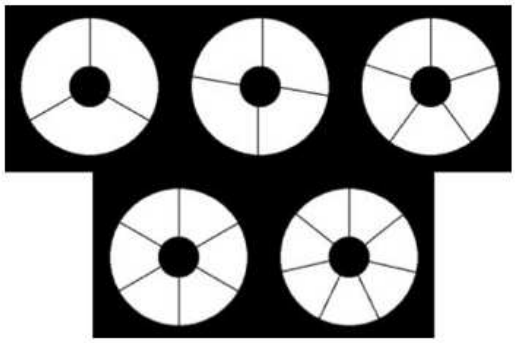

Fig. 6. Pupil configurations considered in this paper.

3.2.1. Central obscuration

The first parameter we evaluate is the central obscuration. High contrast instruments have to deal with central obscuration ratios which typically range from 10% to 35% (CFHT: 35%, HST: 33%, VLT: 14%). ELTs will likely have larger obscurations than current 8-m class telescopes to preserve a reasonable size for the telescope structure. In Fig. 4, the criterion $C_{\mathscr{C}}$ is shown for different obscuration sizes ranging from 10 to 35%. The curves show two maxima. The first is located near 2 λ/D and experiences a large contrast variation while the second (near 4λ/D) shows a smaller dispersion.

Table 1 summarizes these results and gives the position of the second maximum versus the obscuration size for the previously-mentioned criterion and for a criterion based solely on the maximum throughput (as in Fig. 3).

If we only consider the second maximum, which is more promising in terms of contrast and appears less sensitive, the optimal FPM diameter ranges from 4.3 to 4.9 λ/D for obscuration ratios between 10 to 35%. Here, our criterion $C_{\mathscr{C}}$ is more relevant than throughput, since it is better adapted to the region of interest in the coronagraphic image and to the modification of the PSF structure. We see a non-linear increase of optimum FPM size with the obscuration ratio because more starlight is redistributed in the Airy rings of the PSF. A solely throughput-based consideration shows the opposite behavior with a larger dispersion of the FPM size, which is not consistent with the effect on the PSF structure. However, at small obscuration sizes (10%−15%), maximum throughput yields a similar optimal FPM diameter as $C_{\mathscr{C}}$. We consider this result to be evidence for the relevance of our criterion $C_{\mathscr{C}}$ to optimize the FPM size (and hence the APLC characteristics) with respect to the size of the central obscuration. Moreover, the validity of our criterion is also supported by the comparison of coronagraphic PSFs using an optimized APLC in Fig. 5. The optimized APLC allows for a contrast performance which is rather insensitive to the central obscuration size.

3.2.2. Spider arms

On an ELT, the secondary mirror has to be supported by a complex system of spider arms (~50 cm) and cables (~30–60 mm) to improve stiffness. Evaluating the influence of these supports is important in the context of coronagraphy.

The pixel sampling of our simulations limited by available computer power does not allow us to model the thinnest mechanical supports. However, the impact of these supports on the PSF structure will be similar to that of spider arms but at a reduced intensity level. Several configurations were considered as shown in Fig. 6. As the number of spider arms increases from 3 to 7, the contrast worsens (but no more than by a factor of 2).

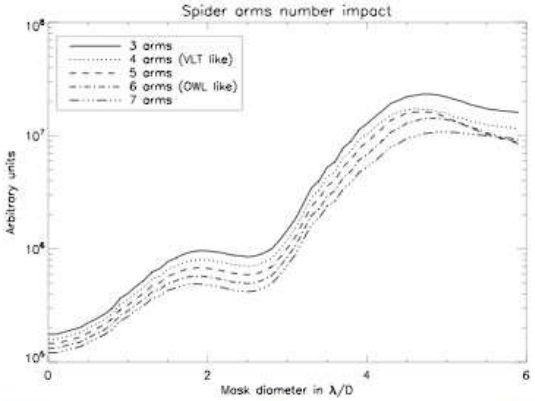

Fig. 7. $C_{\mathscr{C}}$ average between 3 and 100 λ/D as a function of the FPM diameter and number of spider arms. Spider thickness is set to 62 cm.

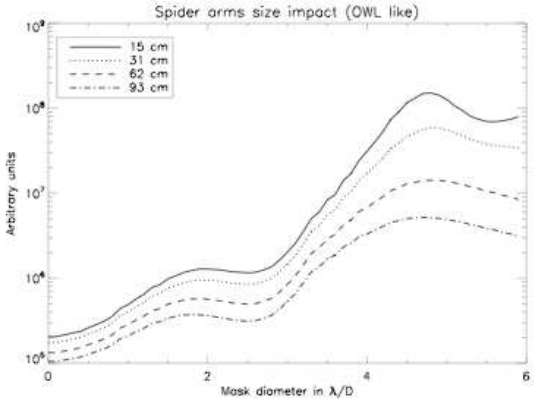

Fig. 9. $C_{\mathscr{C}}$ average between 3 and 100 λ/D as a function of the FPM diameter and spider arm thickness. Number of spider arms is set to 6.

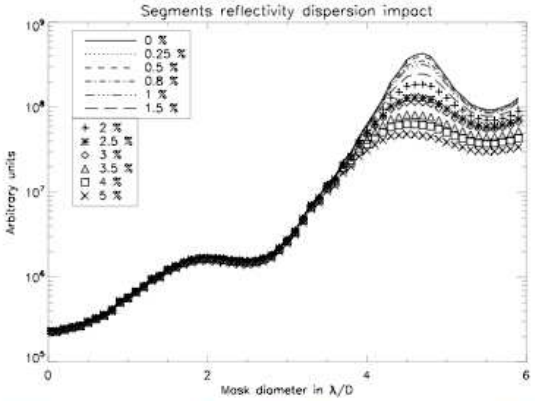

Fig. 8. $C_{\mathscr{C}}$ average between 3 and 100 λ/D as a function of the FPM diameter and reflectivity variations.

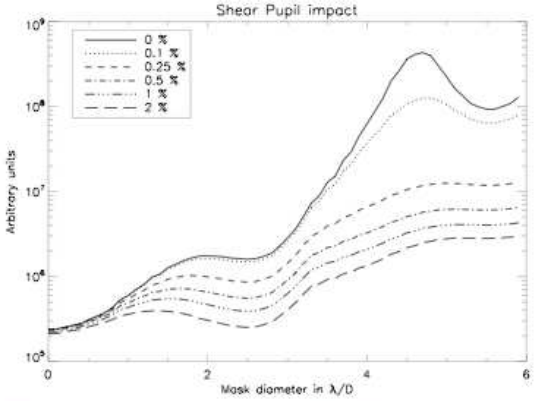

Fig. 10. $C_{\mathscr{C}}$ average between 3 and 100 λ/D as a function of the FPM diameter and pupil shear.

The curves in Fig. 7 are almost parallel, indicating that the number of spider arms has no significant influence on the optimal FPM size. The second maximum of $C_{\mathscr{C}}$ peaks at 4.7 λ/D with a small dispersion of 0.2 λ/D.

Assuming a 6-spider arms configuration (OWL-like), we also analyzed the sensitivity to spider arm thickness from 15 cm to 93 cm (Fig. 9). The increasing width of the spider arms tends to flatten the profile of $C_{\mathscr{C}}$, making the selection of an optimal FPM more difficult (or less relevant) for very large spider arms. However, for the actual size of spider arms likely being of the order of 50 cm, the optimal size of the FPM (and hence APLC) is still 4.7 λ/D.

3.2.3. Segments reflectivity variation

The primary mirror of an ELT will be segmented because of its size, and a potential resulting amplitude effect is segment-to-segment reflectivity variation. We show the APLC optimization sensitivity for segment reflectivity variation from 0 to 5% peak-to-valley in Fig. 8. For this simulation, the primary mirror was assumed to consist of ~750 hexagonal segments. The criterion $C_{\mathscr{C}}$ is robust for FPMs smaller than 4 λ/D. A loss of performance with reflectivity variation is observed for larger FPM. However, the optimal FPM size remains located at 4.7 λ/D with a small dispersion of 0.2 λ/D.

3.2.4. Pupil shear

As mentioned above, an APLC includes several optical components: apodizer, FPM and pupil stop. The performance of the APLC also depends on the alignment of these components. In particular, the pupil stop has to accurately match the telescope pupil image. This condition is not always satisfied, and the telescope pupil may undergo significant mismatch which could amount to more than 1% of its diameter. The pupil shear is the mis-alignment of the pupil stop with respect to the telescope pupil image. It is an issue especially for ELTs for which mechanical constraints are important for the design. For example, the James Webb Space Telescope is expected to deliver a pupil image for which the position is known at about 3–4%. Therefore, the performance of the mid-IR coronagraph (Boccaletti et al. 2004) will be strongly affected. On SPHERE, the planet-finder instrument for the VLT (2010), the pupil shear was identified as a major issue and a dedicated Tip-Tilt mirror was included in the design to preserve the alignment at a level of 0.2% (Beuzit et al. 2006b).

The behavior of $C_{\mathscr{C}}$ in Fig. 10 is somewhat different from that seen with the previous parameters. The loss of performance is significant even for small FPM. However, the criterion is still peaking at 4.7 λ/D with a variation of about 0.2 λ/D although above 4.5 λ/D the curves are rather flat indicating that a larger FPM would not improve performance.

Table 2. APLC optimization for an obscuration of 30%.

Parameters	Value range	Optimal APLC configuration (FPM range in λ/D)
Obscuration	30%	4.7
Spider (arm)	3–7	4.6–4.8
Spider (size)	15–90 cm	4.6–4.8
Shear pupil	0.5–2%	4.7–4.9
Segment reflectivity	0.25–5%	4.5–4.7
Low-order aberrations	1–100 nm rms	3.5–6.0
Chromatism ($\Delta\lambda/\lambda$)	1.4–5%	4.7–4.8
Chromatism ($\Delta\lambda/\lambda$)	5–20%	4.8–5.3

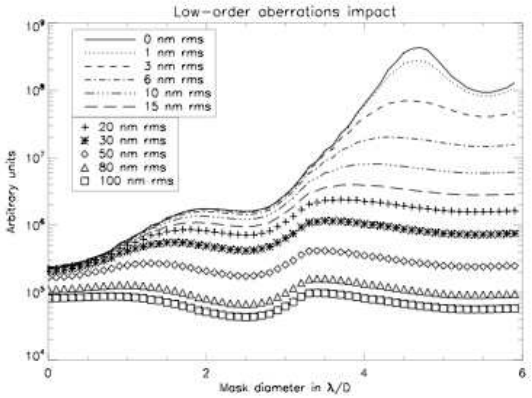

Fig. 11. $C_{\mathscr{C}}$ average between 3 and 100 λ/D as a function of the FPM diameter and low-order aberrations.

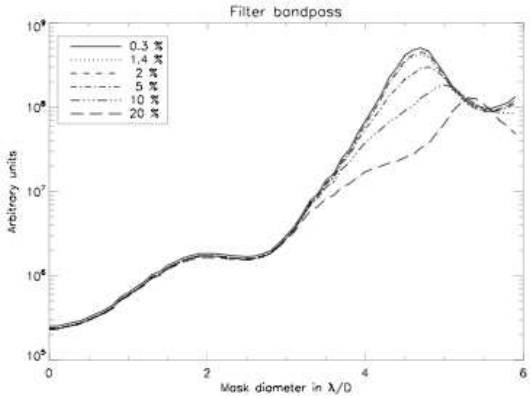

Fig. 12. $C_{\mathscr{C}}$ average between 3 and 100 λ/D as a function of FPM diameter and the filter bandpass.

3.2.5. Static aberrations

Here, static aberrations refer to low-order aberrations on the segments of the large primary mirror. We separately investigated the effect of piston, tip-tilt, defocus and astigmatism, and found the behavior to be similar for all these aberrations. In contrast to the other defects, both the performance and the optimal FPM diameter (optimal APLC) are very sensitive to low-order aberrations.

As the amplitude of aberrations increases, the dependency of $C_{\mathscr{C}}$ on FPM diameter becomes flatter and the optimal FPM size gets smaller (Fig. 11). A larger FPM would not decrease performance enormously. For values larger than 15 nm, there is no longer clear evidence of an optimal size beyond ~3.5 λ/D. The performance is rather insensitive to the actual FPM size.

Even though low-order aberrations strongly affect APLC performance, their presence has virtually no impact on the optimized configuration. The fairly constant performance in the presence of larger low-order aberrations indicates that low-order aberrations are not a relevant parameter for the optimization of the APLC.

3.2.6. Chromatism

All previous analysis was performed for monochromatic light of the wavelength λ_0. However, as with the classical Lyot coronagraph, the APLC performance should depend on the ratio between FPM size and PSF size and therefore on wavelength. Hence, the impact of chromatism on the APLC optimization must be evaluated. We note that the chromatism of the APLC can also be mitigated by a slight modification of the standard design (Aime 2005).

Table 3. Chromatism effects synthesis.

$\Delta\lambda/\lambda$ (%)	$FPM(\lambda/D)$	$FPM_{\lambda_{max}}$ (λ/D)	F_1	F_2
0.3	4.70	4.70	1.0	1.0
1.4	4.70	4.73	1.1	1.1
2	4.70	4.75	1.1	1.1
5	4.80	4.82	1.6	1.6
10	5.00	4.94	2.6	3.7
20	5.30	5.20	3.7	14.6
50	5.90	5.87	26.3	180.9

Figure 12 and Table 3 present the results of the simulations for several filter bandpass widths ($\Delta\lambda/\lambda$) when using the standard monochromatic APLC. As long as the filter bandpass is smaller than 5%, the optimal FPM size and performance are nearly the same as in the monochromatic case.

The values displayed in Cols. 4 and 5 of Table 3 quantify the loss of contrast due to chromaticity with respect to the monochromatic case for the APLC being optimized to the filter bandpass (F_1) and to the central wavelength of the band (F_2). These two factors begin to differ significantly from each other at a filter bandpass larger than 5%. Hence, optimization of the APLC for chromatism is needed for a filter bandpass exceeding this value.

An efficient way of optimizing an APLC for broad band application is to optimize it for the longest wavelength of the band, which leads to results that are within 0.1 λ/D of the true optimal FPM size. This behavior can be explained by the non-symmetrical evolution of the residual energy in the coronagraphic image around the optimal FPM size at λ_0 (Soummer et al. 2003). Another way to minimize chromaticity would be to calculate the apodizer profile for the central wavelength and only

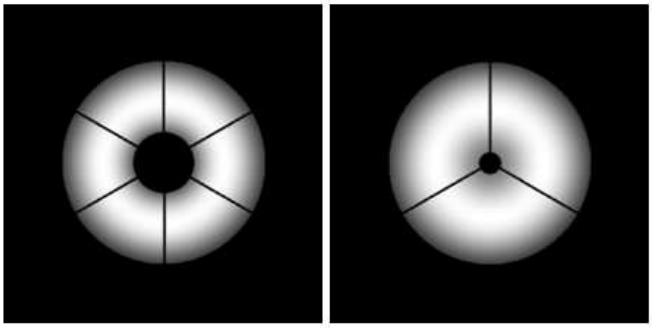

Fig. 13. Optimized apodized E-ELT apertures: telescope design 1 (*left*), telescope design 2 (*right*).

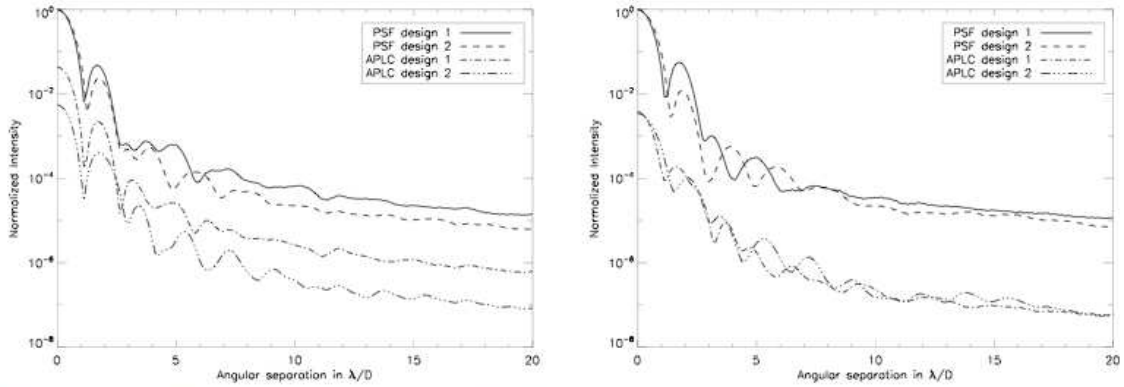

Fig. 14. Radial profiles of PSFs and coronagraphic images ($\Delta\lambda/\lambda = 20\%$) for the 2 designs considering throughput optimization (*up*) or $C_{\mathscr{C}}$ optimization (*bottom*).

optimize the FPM diameter considering the whole bandpass. We compared the behavior of both methods for $\Delta\lambda/\lambda = 20\%$: they are in fact very comparable in terms of performance.

4. Application to the E-ELT

In this section, we apply the tools and results from the APLC optimization study discussed in the previous section to the two telescope designs proposed for the E-ELT. The objective is to confirm our optimization method and to produce contrast idealized profiles which admittedly must not be confused with the final achievable contrast in the presence of a realistic set or instrumental error terms.

4.1. Starting with telescope designs

We assume a circular monolithic primary mirror of 42 m diameter. Segmentation errors are not taken into account, although we note that the E-ELT primary mirror consists of hexagonal segments with diameters ranging from 1.2 to 1.6 m in its current design.

Two competing telescope designs are considered: a 5-mirror arrangement (design 1) and a 2-mirror Gregorian (design 2). For our purpose, the two designs differ by their central obscuration ratios and the number of spider arms. Design 1 (Fig. 13 left) is a 30% obscured aperture with 6 spider arms of 50 cm and design 2 (Fig. 13 right) is a 11% obscured aperture with 3 spider arms of 50 cm. These numbers are likely to be subject to change as the telescope design study is progressing. Mechanical supports (non-radial cables of the secondary mirror support) and intersegment gaps are not considered for the reasons mentioned in Sect. 3.2.2.

In such conditions and taking into account the previous sensitivity analysis on central obscuration, spider arms, and chromatism ($\Delta\lambda/\lambda = 20\%$) we found an optimal APLC configuration with the apodizer designed for 4.8 and 4.3 λ/D and with a FPM size of 5 and 4.3 λ/D for design 1 and 2, respectively.

Sivaramakrishnan & Lloyd (2005) has demonstrated that optimization or under-sizing of the pupil stop is not necessary with the APLC. We independently verified and confirm this result using our criterion applied to the stop rather than to the mask.

4.2. Radial contrast

As shown in Sect. 3.2.1, the optimal APLC configuration with our criterion is different to the optimal configuration considering throughput as a metric. We can now demonstrate this difference using contrast profiles. Figure 14 compares the coronagraphic profiles based on throughput optimization (apodizer and FPM size are 3.5 and 4.1 λ/D for design 1 and 2, see Fig. 3) with that obtained from optimization with our criterion.

For design 2, the optimization with both methods leads to similar APLC configurations (4.3 and 4.1 λ/D). Hence, the contrast performance between them differs by only a factor of 3. On the other hand for design 1, the gain by using our criterion for the optimization is a staggering factor 10. In addition, the plot shows that APLC contrast performance only weakly depends on the telescope geometry with this optimization method. This is an important result, which means that the APLC can efficiently cope with a large variety of telescope designs.

5. Conclusion

The APLC is believed to be a well suited coronagraph for ELTs and for the search of extrasolar planets with direct imaging. The high angular resolution of such large telescopes relaxes the constraints on the IWA of a coronagraph which is an important issue for high contrast imaging instruments on 8-m class telescopes. Hence, coronagraphs with a relatively large IWA such as the APLC present an interesting alternative to the small IWA coronagraphs such as the phase mask coronagraphs.

The objective of this paper is to analyze the optimization of APLC in the context of ELTs. We defined a criterion ($C_{\mathscr{C}}$) similar to that used by Boccaletti (2004) for the general problem of Lyot stop optimization in coronagraphy. We then analyzed the behavior of this criterion as a function of the FPM diameter in the presence of different telescope parameters. The optimal FPM is determined by the maximum value of the criterion. A sensitivity analysis was carried out for the several telescope parameters such as central obscuration, spiders, segment reflectivity, pupil shear, low-order static aberrations and chromatism. Some of these parameters are not relevant for APLC optimization such as low-order aberrations which provide a pretty flat response of the criterion to FPM diameter when applied at reasonably large amplitudes. However, ELTs are not yet well enough defined to predict the level of static aberrations coronagraphs will have to deal with.

The parameter which had the largest impact on the optimum FPM diameter is the central obscuration. An obscuration ratio of 30% leads to an optimal APLC of 4.7 λ/D. In most cases, the optimal sizes derived for other telescope parameters are quite consistent with that imposed by the central obscuration. The dispersion of the FPM size is no larger than 0.2 λ/D given the range of parameters we have considered. We also demonstrated that APLC optimization based on throughput alone is not appropriate and leads to optimal FPM sizes which decrease with increasing obscuration ratios. This behavior is opposite to that derived using our criterion. The superior quality of our criterion is supported by the comparison of contrast profiles obtained with both optimization methods in Sects. 4.2 and 3.2.1.

Although the idealized simulations presented in this paper do not consider atmospheric turbulence and instrumental defects, they allow us to find the optimal APLC configuration and PSF contrast for each case. Cavarroc et al. (2006) show that the ultimate contrast achievable by differential imaging (speckle noise suppression system to enhance the contrast, Racine et al. 1999; Marois et al. 2000; Baba & Murakami 2003; Guyon 2004) with a perfect coronagraph is not sensitive to atmospheric seeing but depends critically on static phase and amplitude aberrations. Our results therefore present the possibility of extending this study to the more realistic case of a real coronagraph taking into account relevant effects releated to telescope properties.

In addition, we have also started development of APLC prototypes whose characteristics are defined with the present numerical analysis. Experiments with these prototypes will be carried out during the next year in the near IR on the High Order Test-bench (Vernet et al. 2006) developed at the European Southern Observatory. The practical study of the APLC will also benefit from prototyping activities led by the department of Astrophysics at the University of Nice (LUAN) and carried out for development of SPHERE for the VLT.

Acknowledgements. P.M. would thanks Pierre Riaud for helpful discussions. This activity is supported by the European Community under its Framework Programme 6, ELT Design Study, Contract No. 011863.

References

Aime, C. 2005, PASP, 117, 1012
Aime, C., Soummer, R., & Ferrari, A. 2002, A&A, 389, 334
Andersen, T., Ardeberg, A. L., Beckers, J., et al. 2003, in Future Giant Telescopes, Presented at the Society of Photo-Optical Instrumentation Engineers, ed. J. R. P. Angel, & R. Gilmozzi, Proc. SPIE Conf., 4840, 214
Baba, N., & Murakami, N. 2003, PASP, 115, 1363
Beuzit, J.-L., Feldt, M., Dohlen, K., et al. 2006a, The Messenger, 125, 29
Beuzit, J. L., Mouillet, D., Moutou, C., et al. 2006b, in Tenth Anniversary of 51 Peg-b: Status of and prospects for hot Jupiter studies, ed. L. Arnold, F. Bouchy, & C. Moutou, 353
Boccaletti, A. 2004, in EAS Publications Series, ed. C. Aime, & R. Soummer, 165
Boccaletti, A., Riaud, P., Baudoz, P., et al. 2004, in EAS Publications Series, ed. C. Aime, & R. Soummer, 195
Cavarroc, C., Boccaletti, A., Baudoz, P., Fusco, T., & Rouan, D. 2006, A&A, 447, 397
Dierickx, P., Brunetto, E. T., Comeron, F., et al. 2004, in Ground-based Telescopes, Presented at the Society of Photo-Optical Instrumentation Engineers, ed. J. M. Oschmann, Jr., Proc. SPIE Conf., 5489, 391
Gerchberg, R. W., & Saxton, W. O. 1972, in Optik 35, 237
Guyon, O. 2004, ApJ, 615, 562
Johns, M., Angel, J. R. P., Shectman, S., et al. 2004, in Ground-based Telescopes, Presented at the Society of Photo-Optical Instrumentation Engineers, ed. J. M. Oschmann, Jr., Proc. SPIE Conf., 5489, 441
Kuchner, M. J., & Traub, W. A. 2002, ApJ, 570, 900
Macintosh, B., Graham, J., Palmer, D., et al. 2006, in Advances in Adaptive Optics II, Presented at the Society of Photo-Optical Instrumentation Engineers, ed. B. L. Ellerbroek, & D. Bonaccini Calia, Proc. SPIE Conf., 6272, 62720L
Marois, C., Doyon, R., Racine, R., & Nadeau, D. 2000, PASP, 112, 91
Mawet, D., Riaud, P., Absil, O., & Surdej, J. 2005, ApJ, 633, 1191
Nelson, J., & Sanders, G. H. 2006, in Ground-based and Airborne Telescopes, Presented at the Society of Photo-Optical Instrumentation Engineers, ed. L. M. Stepp, Proc. SPIE Conf., 6267, 626728
Racine, R., Walker, G. A. H., Nadeau, D., Doyon, R., & Marois, C. 1999, PASP, 111, 587
Roddier, F., & Roddier, C. 1997, PASP, 109, 815
Rouan, D., Riaud, P., Boccaletti, A., Clénet, Y., & Labeyrie, A. 2000, PASP, 112, 1479
Sivaramakrishnan, A., & Lloyd, J. P. 2005, ApJ, 633, 528
Soummer, R. 2005, ApJ, 618, L161
Soummer, R., Aime, C., & Falloon, P. E. 2003, A&A, 397, 1161
Soummer, R., Pueyo, L., Ferrari, A., et al. 2007, ApJ, submitted
Vernet, E., Kasper, M., Vérinaud, C., et al. 2006, in Advances in Adaptive Optics II, ed. B. L. Ellerbroek, & D. Bonaccini Calia, Proc. SPIE, 6272, 62722K

Comparison of coronagraphs for high contrast imaging in the context of ELTs

Astronomy & Astrophysics manuscript no. article˙ELT˙corono˙Printer
October 17, 2008

Comparison of coronagraphs for high-contrast imaging in the context of Extremely Large Telescopes

P. Martinez[1,2,6], A. Boccaletti[2,6], M. Kasper[1], C. Cavarroc[3], N. Yaitskova[1], T. Fusco[4,6], and C. Vérinaud[5]

[1] European Southern Observatory, Karl-Schwarzschild-Strasse 2, D-85748, Garching, Germany
[2] LESIA, Observatoire de Paris Meudon, 5 pl. J. Janssen, 92195 Meudon, France
[3] CEA, Saclay, 91191 Gif-sur-Yvette cedex, France
[4] ONERA, BP 52, 29 avenue de la division Leclerc, 92320 Chatillon cedex, France
[5] LAOG, Observatoire de Grenoble, 38041 Grenoble, France
[6] Groupement d´intérêt scientifique PHASE (Partenariat Haute résolution Angulaire Sol Espace)

Preprint online version: October 17, 2008

ABSTRACT

Aims. We compare coronagraph concepts and investigate their behavior and suitability for planet-finder projects with Extremely Large Telescopes (ELTs, 30-42 meter class telescopes).
Methods. For this task, we analyzed the impact of major error sources that occur in a coronagraphic telescope (central obscuration, secondary support, low-order segment aberrations, segment reflectivity variations, pointing errors) for phase, amplitude, and interferometric type coronagraphs. This analysis was performed at two different levels of the detection process: under residual phase left uncorrected by an eXtreme Adaptive Optics system (XAO) for a wide range of Strehl ratios and after a general and simple model of speckle calibration, assuming common phase aberrations between the XAO and the coronagraph (static phase aberrations of the instrument) and non-common phase aberrations downstream of the coronagraph (differential aberrations provided by the calibration unit).
Results. We derive critical parameters cope by each concept in order of importance. We show three coronagraph categories as function of the accessible angular separation and proposed optimal one in each case. Most of the time amplitude concepts appear more favorable, and the Apodized Pupil Lyot Coronagraph specifically gathers the adequate characteristics to be a baseline design for ELTs.

Key words. Techniques: high angular resolution, adaptive optics –Instrumentation: high angular resolution –Telescopes

1. Introduction

Recent years have seen intensive research and the development of new high-contrast imaging techniques that are essential for detecting faint structures or companions around bright parent stars.

A variety of astrophysical topics (low-mass companions, circumstellar disks, etc.) have driven the next generation of high-contrast instruments like SPHERE and GPI (Beuzit et al. 2006a; Macintosh et al. 2006) expected in 2011, or EPICS (Kasper et al. 2008) for the longer term (~ 2018). Coronagraphy is a mandatory technique for these instruments so is a critical subsystem.

A large review of the different families of coronagraph was carried out by Guyon et al. (2006), and optimal concepts were proposed in the context of space-based observations. Results of this study cannot be generalized for ground-based observations because the problematic is different. Contrast level and inner working-angle requirements are relaxed, while telescopes parameters may have a different impact.

We have previously studied the contrast performance of Extremely Large Telescopes (ELTs) and limitations for an ideal coronagraph (Cavarroc et al. 2006) and in Martinez et al. (2007), we have shown how the Apodized Pupil Lyot Coronagraph (APLC) can be optimized with respect to the ELT parameters. Here, the objective is to investigate the trade-off for coronagraphy in the general context of ELTs. Telescope characteristics such as central obscuration ratio, primary mirror segmentation, and secondary mirror supports can have an impact on high-contrast imaging capabilities and impose strong limitations for many coronagraphs. Coronagraphs already selected for 8-10 m class telescopes are not necessary suited to future planet finder projects with 30-42 m ELTs for which the achievable angular resolution becomes extremely high (~ 10 mas).

On ground-based telescopes equipped with extreme adaptive optics systems (XAO), coronagraphs are expected to attenuate the on-axis star significantly; however, even at a high level of correction (Strehl ratio > 90%), a significant fraction of the star flux remains in the focal plane (<10%). The residual light sets the photon-noise contribution for high-contrast imaging, even if a dedicated calibration procedure like differential imaging is used (Racine et al. 1999; Marois et al. 2000; Baba & Murakami 2003; Guyon 2004). The estimation of this level is thus one byproduct of our study (as shown in Cavarroc et al. 2006)

The intent of this paper is twofold: 1/ determine limiting parameters and ideally derive specifications at the system level, 2/ initiate a general comparison of coronagraphs to identify valuable concepts and fields of application. All the simulation hypothesis are described in Sect. 2: coronagraph concepts, AO and calibration unit assumptions, metrics used and error sources considered. The impact of these error sources with respect to the AO correction level and their effects on the detectability using a differential imaging system are presented in Sect. 3 and discussed

Send offprint requests to: P. Martinez, martinez@eso.org

in Sect. 4. Other comparisons between two promising concepts are done in Sect. 5. Finally, in Sect. 6 we draw conclusions.

2. Methodology

2.1. Coronagraphs

For the past ten years, a large number of coronagraph concepts have been proposed. Nevertheless, at this ti, none of them can simultaneously meet all of the main high contrast requirements: sensitivity to telescope parameters (like the secondary support obscuration, residual aberrations, spider vanes), accessibility to small inner working-angle (IWA), lack of sensitivity to pointing errors, deliverability of high throughput, good imaging capabilities (large searchable area), compatibility with large bandwidth, and finally, manufacturing feasibility. The effect of the segmentation of the primary mirror (inter-segment gaps, segment reflectivity variations, segment aberrations) must be added to this long list because we are dealing with ELTs.

2.1.1. Concepts analyzed in this study

We consider the following coronagraph concepts: Lyot coronagraph (Lyot 1939), apodized pupil Lyot coronagraph (APLC, Aime et al. 2002; Soummer et al. 2003a), apodized Roddier & Roddier coronagraph (i.e Dual zone) (APRC, Soummer et al. 2003a,b), four-quadrant phase mask (FQPM, Rouan et al. 2000; Riaud et al. 2001), annular groove phase mask (AGPM, Mawet et al. 2005b), band-limited (BL, Kuchner & Traub 2002; Kuchner et al. 2005), achromatic interferometric coronagraph (AIC, Gay et al. 1997; Baudoz et al. 2000a,b, 2005).

In most figures presented in this paper, we will be make use of an ideal coronagraph model that removes the flat, non-tilted coherent wavefront from the pupil (Cavarroc et al. 2006). In such a way, the ideal coronagraph enables derivation of the maximum detection level imposed either by the residual phase aberrations left from the XAO system or the static aberrations from the differential imaging system (as defined in next sections). An ideal coronagraph is only designed for no wavefront aberrations, so comparison to other coronagraphs is useless.

2.1.2. Inner working-angle constraint

The IWA describes quantitatively how close a coronagraph design allows detection of a faint companion. In this paper we define the IWA as the angular separation for which the diffraction peak of a planet is reduced by a factor of 2. It assumes that the planet's throughput is radially averaged (i.e not favorably placed), while the star is point-like.
The AIC, FQPM/AGPM, APRC have a very small IWA owing to their intrinsic properties. In contrast, amplitude concepts (Lyot, APLC, and BLs) have a larger IWA depending on coronagraph parameters (d, diameter of the focal mask, or ϵ, bandwidth of the mask function, that actually depends on the application).

Since we are dealing with ELTs, the angular resolution of such large telescopes is relaxing the constraint on the IWA and hence the problematic is different than for planet-finder instruments on 8-m class telescopes. As a baseline, we fixed the limit of the IWA to the reasonable value of $4\lambda/D$. For instance, at 1.6 μm (H-band), $4\lambda/D$ correspond to 30 mas and 165 mas for a 42 and a 8 meter telescope, respectively.

In the next simulations, the Lyot coronagraph has a mask size of $7.5\lambda/D$ (i.e a corresponding IWA of 3.9 λ/D). The APLC has a $4.7\lambda/D$ mask diameter (i.e IWA = 2.4 λ/D). This size is the result of the optimization performed in Martinez et al. (2007). We also consider two band-limited masks with different orders: a 4^{th} order (BL4, Kuchner & Traub 2002, sin^4 intensity mask with $\epsilon = 0.21$) and an 8^{th} order (BL8, Kuchner et al. 2005, m=1, l=3 and $\epsilon = 0.6$). The BLs parameter ϵ controls both the IWA and Lyot-stop throughput.

2.1.3. Pupil stop optimization

The total amount of the rejected light by a coronagraph strongly depends on the pupil-stop size and shape. In this paper, pupil stops are optimized to match the diffraction in the relayed pupil as defined in Boccaletti (2004), hence are adapted to the way that each coronagraph deals with the diffracted light. However, in Sect. 3 we generate a wide different range of wavefront errors, so that an optimization of the pupil-stop with respect to the level of the residual phase could relax constraints on the pupil-stop shape and throughput, as discussed for instance in (Crepp et al. 2007), for the band-limited case. This optimization depends on the dominant source of noise (diffracted light or uncorrected atmospheric speckles).

In practice, we optimized pupil stops in the ideal case (no wavefront error), because the final comparison is made after differential imaging when the uncorrected atmospheric speckles have been removed. Pupil stops are assumed to be perfectly aligned except when we evaluate the impact of its misalignment. Pupil stop throughput and coronagraph parameters are summarized in Table 1.

2.2. Principle of numerical simulations

As a baseline we consider a 42-meter ELT with 30% (linear) central obscuration ratio as expected for the European ELT (E-ELT, Gilmozzi (2008)), except when we evaluate its impact. As for the wavelength, we adopt a baseline of $\lambda = 1.6\mu m$ (center of the H-band), a good compromise between angular resolution and AO correction. Our simulations make use of simple Fraunhofer propagators between pupil and image planes, which is implemented as fast Fourier transforms (FFTs) generated with an IDL code. The image plane is sampled with $0.125\lambda/D$ per pixel.

2.2.1. Extreme AO simulations

Since we are concerned with ELTs, we consider an eXtreme Adaptive Optics system (XAO) with a large number of actuators. Table 2 shows the characteristics for the simulations of the XAO phase residuals. As we want to analyze the behavior of the coronagraph under realistic conditions, we generate many phase screens with different Strehl ratios (from 84% to 96%). For that, we modify the atmospheric seeing (from 1.0″to 0.4″), while leaving the XAO system unchanged. As a fair comparison, all coronagraphs have been affected by the same set of phase screens. We use 100 phase realizations, and check that it was sufficient to produce long exposures at the contrast level we are dealing with.

2.2.2. Differential imaging simulations

The presence of a residual atmospheric wavefront perturbation, even if corrected with a XAO system, limits the contrast behind a coronagraph to about 10^4 - 10^6. The first series of simulations

Table 1. Parameters of coronagraphs optimized for a central obscuration of 30%. $^{\alpha}$Overall transmission. $^{\beta}$AGPM topological charge.

Coronagraph type	Specifications			State of art	
	IWA ($\lambda/D, \pm 0.1$)	$\mathscr{T}^{\alpha}$ (%)	Parameters	Laboratory tests	Sky observations
FQPM	0.9	82.4	-	vis. / near IR / mid IR	near IR
AGPM	0.9	82.7	$lp^{\beta} = 2$	-	-
AIC	0.4	50.0	-	vis. / near IR	near IR
Lyot	3.9	62.7	$d = 7.5\lambda/D$	vis. / IR	vis. / IR
APLC	2.4	54.5	$d = 4.7\lambda/D$	vis. / near IR	near IR
APRC	0.7	74.5	$d = 1.06\lambda/D$	-	-
BL4	4.0	22.4	$\epsilon = 0.21$	vis.	-
BL8	4.0	13.8	$\epsilon = 0.6$, m=1, l=3	vis.	-

to assess the impact of telescope parameters on coronagraph performance was carried out at this level (Sect. 3.1.1). However, it is important to perform the same analysis at the level of contrast that is adequate for planet detection (10^8 - 10^{10}) to evaluate how the sensitivity of coronagraph propagates. To enhance the contrast, a second step is required to suppress the speckle noise (composed of dynamical and static aberrations). On SPHERE and GPI, speckle calibration is implemented in the form of spectral and polarimetric differential imaging (Racine et al. 1999; Marois et al. 2000; Baba & Murakami 2003). A deeper contrast is then achievable through appropriate data reduction. Here, for sake of generality we assume a general and simple scheme of differential imaging (DI). A detailed analysis of contrast performance for ELTs with DI has been performed by Cavarroc et al. (2006).

For the reader's convenience we repeat the main assumptions and results used in this present study. We considered two images taken simultaneously using two channels downstream of the coronagraph (same spectral band, same polarization state). In such a case, the contribution to the wavefront error is made up of two terms: the static common aberrations (δ_c) in the instrument upstream of the coronagraph and non-common aberrations (δ_{nc}) downstream of the coronagraph. The latter corresponds to differential aberrations since the light goes through two different optical paths. Here, the residual phase left uncorrected by the XAO system is omitted since it will be averaged to an azimuthally constant pattern over time and suppressed by subtraction in the two channels (if the photon noise is neglected). Therefore, the detectability for an infinitely long exposure only depends on δ_c and δ_{nc}. The static aberrations δ_c and δ_{nc} are described by PSDs with f^{-2} variation (f is the spatial frequency). Since aberrations are critical at close angular separations, we assume that the PSDs at low frequencies were shaped (flat in the range $0 < f < f_c/4$, with f_c the cut-off frequency of the XAO.

Many combinations of δ_c, δ_{nc} are possible to reach the desired contrast level. But, as we are interested in the DI performance rather than the technique itself, we adopt in Sect. 3.2 an arbitrary amplitude of 10 nm rms and 0.3 nm rms for δ_c and δ_{nc}, respectively. A contrast level of 10^9 is thus achievable that is consistent with EPICS science contrast requirements (Kasper et al. 2008).

2.3. Metrics

In the following, we describe metrics used to evaluate the efficiency of coronagraphs. Caution: none of these metrics are weighted by the overall coronagraphic system transmission ($\mathscr{T}$). This throughput is set by the pupil-stop transmission (times the mask transmission for BLs). The system transmission (presented in Table. 1) basically remains a physical limitation that must influence the decision of which coronagraph to implement in practice (integration-time issue), but here we are more interested in the upper limit of coronagraphs for comparison clarity as regards external limitations. This point will be discussed further in Sect. 4. We also inform the reader that some coronagraph designs may attenuate the planet signal (e.g the four phase transitions between adjacent quadrants of the FQPM create four λ/D-blind zones or the repetitive throughput-less zones of some particular BLs functions) which is not quantified through our metrics.

2.3.1. Coronagraphic halo

Several metrics can be used to quantify the capability of a coronagraph (Boccaletti 2004, for instance). We have identified two metrics at the level of the coronagraphic image. The first one, $C_{CORO}(\rho)$, is the contrast profile averaged azimuthally, and the second, $\overline{C_{CORO}}$, gives the contrast between the star peak and an average intensity in an annular region of the focal plane where an off-axis companion is expected. These metrics read as

$$C_{CORO}(\rho) = \frac{\int_0^{2\pi} \psi_{CORO}(\rho, \alpha)\, d\alpha}{2\pi\, \psi_{PSF}(0)} \tag{1}$$

$$\overline{C_{CORO}} = \frac{\left(\int_{\rho_i}^{\rho_f} \int_0^{2\pi} \psi_{CORO}(\rho, \alpha) \rho\, d\rho\, d\alpha\right) / \pi({\rho_f}^2 - {\rho_i}^2)}{\psi_{PSF}(0)} \tag{2}$$

where ρ_i and ρ_f are the inner and outer radii of the annular region; $\psi_{PSF}(0)$ the maximum intensity of the star image on the detector (without the coronagraph, except for the APLC and APRC for which this term includes the apodizer transmission); and $\psi_{CORO}(\rho, \alpha)$ is related to the intensity of the coronagraphic image on the detector. We use these metrics to study the variation in performance with respect to telescope parameters and as a function of the Strehl ratio.

The area of calculation in the focal plane for $\overline{C_{CORO}}$ can be matched to the instrumental parameters. The width of the ring can be modified to match science requirements. For most results presented hereafter, the search area is bounded at $\rho_i = 4\lambda/D$ for short radii (IWA requirement) and at $\rho_f = 80\lambda/D$ for large radii (XAO cut-off frequency). These limits translate to 30mas and 0.63" respectively at $1.6\mu m$, and allow coronagraph comparison over a large region of interest, while keeping the study general and independent of a specific science requirement. The impact of ρ_i and ρ_f values will be further discussed in Sect. 3.1.1.

Table 2. Values and amplitudes of parameters used in the simulation.

	XAO simulation	DI simulation
Input parameters		
telescope diameter	42 m	42 m
seeing at 0.5 μm	$1.0'' - 0.4''$	-
wind speed	15 m/s	-
outerscale of turbulence L_0	20 m	-
number of actuators	2.10^4	-
inter-actuator distance	26 cm	-
AO frequency	2.5 KHz	-
wavelength	1.6 μm	1.6 μm
average Strehl ratio	83% – 96%	-
delay	0.04 s	-
focal sampling	0.125 λ/D / pixel	0.125 λ/D / pixel
static aberrations upstream of the coronagraph	-	10 nm rms
static aberrations downstream of the coronagraph	-	0.3 nm rms
central obscuration default value	30%	30%
Studied parameters		
central obscuration	10 - 30 [%]	10 - 30 [%]
spider vanes thickness	30 - 75 [cm]	30 - 75 [cm]
segments reflectivity (~750 of 1.5m diameter)	1 - 5 [% ptv]	1 - 5 [% ptv]
segments static aberrations (~750 of 1.5m diameter)	6 - 30 [nm rms]	6 - 30 [nm rms]
pointing errors	0.1 - 0.5 [mas rms]	0.1 - 0.5 [mas rms]
pupil shear	0.1 - 0.5 [%]	0.1 - 0.5 [%]

2.3.2. Differential Imaging residuals

When using a DI system, implying some image subtraction, the average contrast is no longer suitable. Results will be presented as radial contrast plots (5σ normalized contrast vs. angular separation) to compare coronagraphs:

$$C_{DI}(\rho) = \frac{5 \times \sigma[\psi_{CORO_1}(\rho) - \psi_{CORO_2}(\rho)]}{\psi_{PSF}(0)} \quad (3)$$

Here, $\sigma[]$ is an operator that denotes the azimuthal standard deviation measured in a ring of width λ/D on the subtracted image $\psi_{CORO_1} - \psi_{CORO_2}$, and C_{DI} quantifies the ability to pick out an off-axis companion at a given angular distance.

Here, we adopt that simple metric for the sake of clarity, but we note that more appropriate criteria adapted to the case of high-contrast images have been developed by Marois et al. (2008).

2.4. Studied parameters

2.4.1. Central obscuration

It is very likely that future high-contrast instruments will have to deal with high central obscuration ratios, possibly higher than the current 8-m class telescopes (e.g 30% for the future E-ELT). We evaluated its impact on coronagraphic performance for obscuration ranging between 10% to 30%. For each central obscuration ratio, APLC operates at its optimum configuration as defined in Martinez et al. (2007). For the range of obscuration we are considering, the Lyot mask of the APLC varies between 4.3 to $4.9\lambda/D$. The apodizer of the APRC is also re-optimized for each case. When it is not specified, the default value of the central obscuration ratio is 30%.

2.4.2. Spiders thickness

The analysis for the spider thickness is made for one configuration where six symmetrical cables are used to maintain the secondary support (Dierickx et al. 2004, Fig. 1, left). The thickness varies from 30 to 90 cm; and for each case and each coronagraph, the pupil stop is re-optimized to match the entrance aperture. In the particular case of BL8, the high order of the mask yields to unusable pupil stops (near to 0% throughput) to correctly match diffraction when spider vanes are included. Hence, we relax constraints on performance (no longer perfect at $S = 100\%$) to increase throughput. As a result, the performances presented in Sects. 3.1.2 and 3.2 are affected.

2.4.3. Segment reflectivity variations

The ELT primary mirrors will necessarily be segmented, and amplitude variations are expected due to a difference in reflectivity between the segments (optical coating). The variation in reflectivity through an optical system induces wavefront amplitude variation that leads to potentially bright static speckles in the focal plane of the instrument. It is important to know how robust a coronagraph is to these defects.

We assume ~ 750 hexagonal segments of 1.5 meters diameter (Fig. 1, right) and assess the impact of a uniform segment-to-segment reflectivity variation from 1% to 5% (peak-to-valley, hereafter ptv). For comparison, 5% (ptv) is the typical variation measured on the Keck telescope (Troy & Chanan 2003).

2.4.4. Static segment aberrations

Segment aberrations refer to low-order static aberrations (piston, tip-tilt, defocus, and astigmatism) producing speckles that fall relatively near the central core of the image. Higher order aberrations are not considered at this stage but will be implemented in the DI simulations. The limited number of actuators in the AO system imposes a control radius in the image plane that scales as $N/2$ if N is the linear number of actuators across the pupil. We assume that the static aberrations are already corrected inside this radius. To estimate the actual segment aberrations corrected by the XAO system, we set the PSD of the phase to a null contribution at frequencies lower than the cut-off frequency. This method gives the best possible correction that can be obtained,

but is only limited by the fitting error, and it does not include any wavefront sensor errors, influence function nor actuators space positioning. An analytic study of the AO correction of segment errors was performed in Yaitskova & Verinaud (2006) where the quantity γ_{AO}, the amount of wavefront correction achieved by an AO system on a particular segment aberration, was defined by the ratio of the corrected rms wavefront error to the initial uncorrected rms wavefront error:

$$\gamma_{AO} = \frac{\sigma_{corrected}}{\sigma_{initial}} \quad (4)$$

With the XAO system we have considered, the analytical method yields a theoretical value of ~ 0.32 for piston-like phasing error. With our simple PSD shaping, we obtained the following values for γ_{AO}: 0.22, 0.34, 0.27, 0.41 for piston, tip-tilt, defocus, and astigmatism, respectively, which is not very different from the analytical value. As a result, the XAO system significantly reduces the wavefront error of each segment as show in Fig. 2 (piston-phasing error example).

Predicting the level of low-order aberrations that ELT segments will feature is quite difficult. Nevertheless, measurements with the Keck telescope (Chanan et al. 2000) show that 10 nm rms is reachable. In our simulations, we consider a range of intial wavefront error from 6 to 30 nm rms, which is corrected by the XAO system and hence reduced to values ranging from 0.7 to 12 nm rms. In practice, we study each static aberration independently from each other, and find an undistinguishable impact on coronagraphic halo, so that only the case of piston will be presented.

2.4.5. Pointing errors and finite size of the star

The offset pointing error refers to the misalignment of the optical axis of the coronagraph with the star. Here, we assumed that the star is a point source. For instance, with SPHERE the goal is 0.5 mas rms, hence a direct translation of this requirement to a 42 meters telescope, would be a pointing error residual of less than 0.1 mas rms. In practice, we evaluate the effect of the pointing error between 0.1 and 0.5 mas rms.

If the star is not point-like but its disk is slightly resolved, it can be modeled as a sum of incoherent off-axis point sources. As for the offset pointing error, coronagraphs that allow a very small IWA will be more affected. Actually, the impact of the finite size of the star is quite similar to the one of the offset pointing.

2.4.6. Pupil shear

Most of coronagraphs include several optical components: apodizer, focal plane mask, and pupil stop. As a result their performance also depends on the alignment of these components. In particular, the pupil stop has to accurately match the telescope pupil image. This condition is not always satisfied, and the telescope pupil may undergo significant mismatch that could amount to more than a few % of its diameter. The pupil shear is the misalignment of the pupil stop with respect to the telescope pupil image. It is especially an issue for ELTs, for which mechanical constraints are important for the design. For example, the James Webb Space Telescope is expected to deliver a pupil image for whose position is known at about 3-4%. Therefore, the performance of the mid-IR coronagraph (Boccaletti et al. 2004) will be strongly affected. On SPHERE, the planet-finder instrument for the VLT (2010), the pupil shear was identified as a major issue, and a dedicated Tip-Tilt mirror was included in the design to preserve the alignment at a level of 0.2% (Beuzit et al. 2006b). In this study we consider a range of misalignments between 0.1 and 0.5% of the pupil diameter.

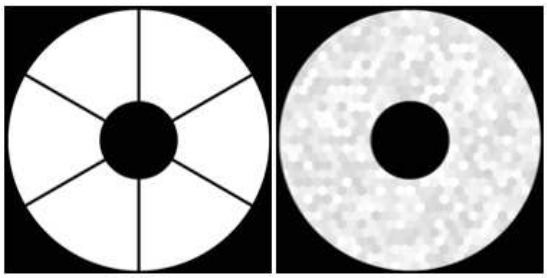

Fig. 1. Spider vanes configuration (left) considered in Sect. 2.4.2, pupil with reflectivity variations (right) considered in Sect. 2.4.3 (levels are exaggerated for the sake of clarity).

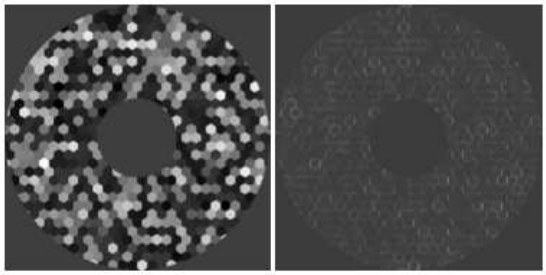

Fig. 2. left: Initial piston WFE of 30 nm rms, right: Residual piston of 6.7 nm rms after XAO correction. Levels are exaggerated for the sake of clarity.

3. Results

3.1. XAO simulation

3.1.1. Influence of the wavefront correction quality

We first started to compare the coronagraphic performance as a function of the Strehl ratio (S) with the $\overline{C_{CORO}}$ metric. The objective of this first analysis is to assess the raw contrast delivered for each coronagraph considering only the diffraction by the edges of the pupil and the residual atmospheric phase aberrations, which are leaking through the XAO system. Therefore, these defects will produce a perfectly averaged halo of speckles that sets the level of the photon noise in the coronagraphic image plane. Obviously the contrast level must be much better than this coronagraphic halo, but this noise contribution estimate will be necessary for investigating the signal-to-noise ratio achievable for detecting exoplanets with ELTs in later studies.

Figure 3 shows $\overline{C_{CORO}}$ as a function of the Strehl ratio for two locations in the coronagraphic image. On the left, for an angular separation of $4\lambda/D$=IWA and to the right, averaged in between the IWA and the AO cut off frequency ($\mathscr{F}_{AO} = 80\lambda/D$). In each case, $\overline{C_{CORO}}$ for a perfect coronagraph is plotted in dashed line. This ideal model is helpful since it reveals the limitations from the residual aberrations that are leaking through the XAO system alone, i.e on principle there is no pupil-edge diffraction contribution since all the coherent part of the light has been removed. The actual contribution of the limitation sets by the diffraction of the edges of the pupil is actually revealed by the discrepancy of

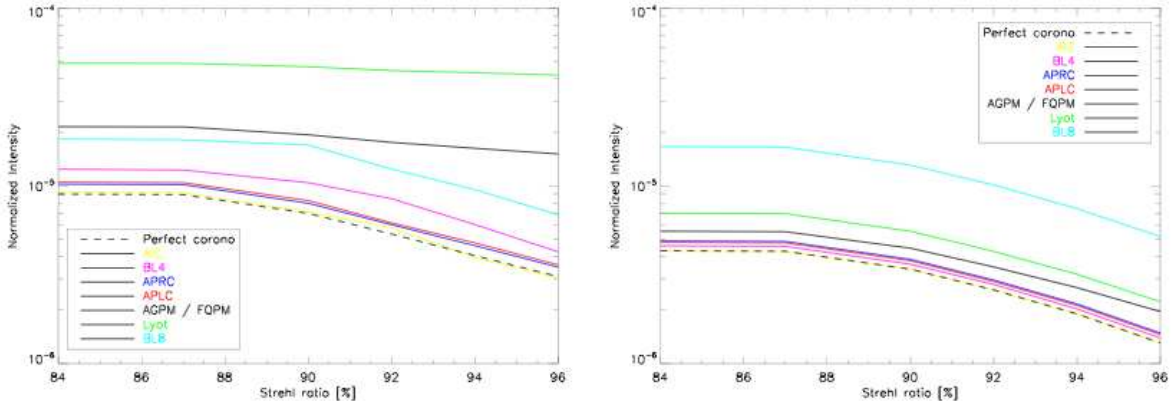

Fig. 3. Variation of $\overline{C_{CORO}}$ as a function of the Strehl ratio for all coronagraph concepts. Left: at $4\lambda/D$ (IWA), Right: averaged from $4\lambda/D$ (IWA) to $80\lambda/D$ (AO cut-off frequency).

real coronagraph $\overline{C_{CORO}}$ curves to that of the ideal model. Two regimes can be identified:

1/ where $\overline{C_{CORO}}$ of a coronagraph follows $\overline{C_{CORO}}$ of the ideal model, which corresponds to the speckle-dominated regime where coronagraphs perform much better than the XAO, so the performance is set by the XAO itself. In other words, improving the XAO correction is needed to improve final performance. In such a case, contrast increases with S and a substantial gain in starlight suppression requires reaching a high level of wavefront correction (S ~94%). For the considered range of S values (84 - 96%), all the coronagraphs considered are in this regime (Fig. 3, right), except for the AGPM/FQPM and the Lyot, but only when $\overline{C_{CORO}}$ is evaluated at the IWA (Fig. 3, left).

2/ the diffraction-dominated regime appears when $\overline{C_{CORO}}$ of a coronagraph no longer follows $\overline{C_{CORO}}$ of the ideal model and is about flat; i.e phase aberrations are small enough to reveal the actual limitation of the coronagraphs, so the limitation is mostly set by the diffraction by the edges of the pupil. In other words, improving the XAO correction is useless since the limitation comes from the coronagraph (AGPM/FQPM and Lyot cases previously underlined at IWA).

The particular case where $\overline{C_{CORO}}$ is nearly flat while still following the ideal model (below S = 88%) corresponds to a case where the limitation comes from the residual phase aberrations that are present in large amounts so improving the XAO correction (from 84 to 88%) does not yield any improvement in the performance.

The AGPM/ FQPM and Lyot coronagraphs have a strong dependency with the area where $\overline{C_{CORO}}$ is evaluated, which indicates that most of the residual energy is actually localized near the image center in contrast to other coronagraphs. This is a consequence of the diffraction by the central obscuration that is not favorable to such designs. At angular distances greater than $4\lambda/D$, the AGPM/FQPM and the Lyot perform as well as other designs. Thus, the choice performed in Sect. 2.3.1 for the value of ρ_i and ρ_f allows more homogeneous comparisons of coronagraphs.

The contrast achieved with the BL8 is significantly lower than with other coronagraphs. To operate with a 30% central obscuration and a somewhat small IWA of $4\lambda/D$, the BL8 requires a very aggressive pupil stop ($\mathcal{T}$ = 13.8). Although this optimization provides a very deep contrast in a perfect situation when phase aberrations are negligible (S = 100%), it is no longer the case realistic condition even at high Strehl ratios. This is obviously true for any concepts, but the decrease in contrast between the perfect and realistic situations is even more abrupt with the BL8.

3.1.2. Parameter dependencies

Figure 4 analyzes in detail the impact of each of the parameters defined in Sect. 2.4 for the particular case of S=90% using $C_{CORO}(\rho)$ the coronagraphic contrast as a function of the angular separation. The variation of each parameter is represented with error bars indicating the dispersion of contrast. Therefore, the sensitivity of $C_{CORO}(\rho)$ to each parameter within a given range of amplitude is shown as an error bar. The range is given in the legend and is identical for each coronagraph. For each case, the limit of detection achievable with a perfect coronagraph is plotted as a dashed line.

The specific case of $\overline{C_{CORO}}$, which shows the same quantity as in Fig. 3 but for the several parameters of Sect. 2.4 independently, is not plotted to simplify the paper. The variation in contrast as a function of the Strehl ratio is actually identical for all parameters and all coronagraphs. In other words, the curves are parallel and parallel to that of Fig. 3. This simply means that the contrast is usually dominated by the XAO halo and the diffraction by the edges of the pupil. For all coronagraphs but AIC, APRC, and APLC, the parameters affects the contrast at various levels.

In the following, we describe the impact for each coronagraph in the case of S=90% (Fig. 4):

AGPM / FQPM – At distances shorter than $3\lambda/D$, the image is dominated by the diffraction of the central obscuration, while beyond that angular distance the contrast limit is set by the spider diffraction spikes. For worst values of dominating parameter the contrast reaches 2.10^{-4} at $4\lambda/D$ and only improves by a factor of 2 at $10\lambda/D$. The achievable contrast is quite far from the ideal model.

AIC – In this case, pupil diffraction is negligible as far as it is centro-symmetrical, but pointing errors clearly dominate the contrast up to $20\lambda/D$. The impact is as large as that of the central obscuration for the AGPM/FQPM. At larger distances, the performance of the AIC is identical to that of a perfect coron-

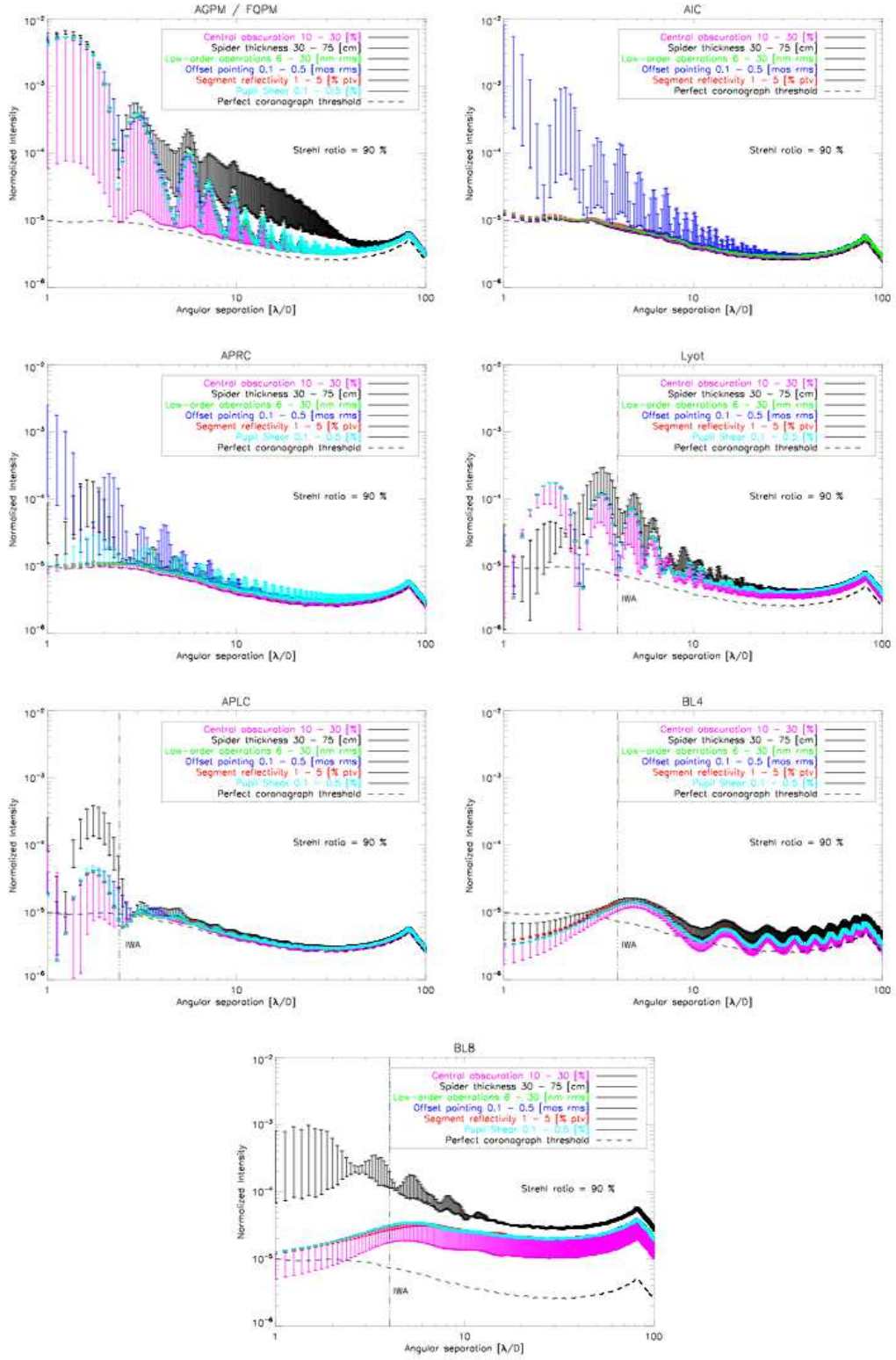

Fig. 4. Contrast profile $C_{CORO}(\rho)$ (right) for the different parameters and for the following coronagraphs: AGPM/FQPM, AIC, APRC, Lyot, APLC, BL4, and BL8. The Strehl ratio is 90 %. Error bars indicate the amplitude of the contrast variation. The dashed line stands for the ideal case.

agraph. At $4\lambda/D$ the contrast is 7.10^{-5}, while it is improved to 2.10^{-5} at $10\lambda/D$.

APRC – $10\lambda/D$ sets the limit between pointing-error dominated regime and pupil-shear dominated regime. At $4\lambda/D$ the contrast reaches 4.10^{-5} and 9.10^{-6} at $10\lambda/D$.

Lyot – Spider diffraction limits the contrast at any angular radius. However, the impact is not that important. The central obscuration also has a significant signature. At $4\lambda/D$ (near the mask edges), the contrast is only 1.10^{-4} but it improves by a factor of 10 at $10\lambda/D$.

APLC – The dispersion of contrast is negligible in that case for any parameter. The APLC achieves the same performance as the perfect coronagraph beyond the IWA and does not feature a dominant parameter. At $4\lambda/D$ the contrast reaches $\sim 1.10^{-5}$ and 5.10^{-6} at $10\lambda/D$.

BL4 – As for the APLC, the contrast is very close to the perfect case and the dispersion of contrast is small, however with a dominance of the spider diffraction spikes. At $4\lambda/D$ the contrast is 2.10^{-5}, while at $10\lambda/D$ is improved to 6.10^{-6}.

BL8 –The spider diffraction dominates significantly at any angular separation. The contrast is much worse than for the BL4 and reaches 2.10^{-4} at $4\lambda/D$ and 5.10^{-5} at $10\lambda/D$. The BL8 suffers from a severe reduction of the pupil stop, therefore distorting the off-axis PSFs while reducing the throughput. High-order BLs are actually not suited to ELTs.

The impact of spider diffraction must be mitigated since contrast profile are azimuthally averaged, therefore some image areas feature stronger contrasts. Planets could be observed within the clear areas between the spider spike diffractions. This choice depends on the observing strategy.

For all coronagraphs, amplitude and phase aberrations on segments in the considered range have much less impact than the diffraction by the pupil edges (central obscuration and spiders). For the small IWA coronagraphs, the pointing error is the most dominant factor.

3.2. DI simulation

As explained in Sect. 2.2.2, we adopted an arbitrary amount of static and differential aberrations to carry out the same analysis as in Sect. 3.1.1 but at a much higher level compatible with exoplanet detection. Instead of an azimuthally averaged contrast, Fig. 5 plots the 5σ detection level (Eq. 3).

First of all the parameters that limit the contrast of a given coronagraph are the same except that, at large angular distances the AO halo is no longer dominant and then the dispersion of parameters is much larger.

AGPM / FQPM – As in the previous section, a clear limit is seen at $3\lambda/D$ between a central obscuration-limited regime and a spider diffraction-limited regime. Also, the impact of the pupil shear predominates beyond $20\lambda/D$. The level of detectability is rather flat between 4 and $10\lambda/D$, achieving 2.10^{-7}.

AIC – Again, all symmetrical defects are quite small compared to the pointing errors. At $4\lambda/D$ the performance is similar to that of the AGPM/FQPM and improves to 7.10^{-8} at $10\lambda/D$, despite being far from the ideal model.

APRC – The separation between pointing errors and the pupil shear-limited regime has moved from 10 to $20\lambda/D$ with respect to Fig. 4. At $4\lambda/D$ the detectability reaches 3.10^{-8}, while at $10\lambda/D$ it improves to 7.10^{-9}. A gain of 1 order of magnitude is reached compared to AGPM/FQPM and AIC concepts.

Lyot – The spider diffraction still dominates the contrast, which reaches 1.10^{-7} at $4\lambda/D$ and improves by a factor of 10 at $10\lambda/D$. Considering its simplicity, the Lyot coronagraph is suitable for ELTs.

APLC – It features one of the best detectability levels with the BL4. In contrast to Fig. 4, it is dominated by the spider diffraction (and pupil shear at a very large angular separation, i.e after $50\lambda/D$) but achieves a level of 1.10^{-8} at $4\lambda/D$ and 8.10^{-9} at $10\lambda/D$.

BL4 – Very high contrast can be achieved close to the limit imposed by static aberrations. The sensitivities to the parameters are rather low. The level of detection is identical at 4 and $10\lambda/D$: 2.10^{-9}.

BL8 – For the same reasons as expressed in Sect. 3.1.1, BL8 is not as efficient as BL4. Up to $50\lambda/D$, the dominating parameter is the spider diffraction, and the pupil shear at larger angular separations. Compared to BL4, the performance degrades by about 2 orders of magnitude in the middle range of frequencies and about 1 order of magnitude at very large angular separations. At $4\lambda/D$ the detectability reaches 1.10^{-7}, while at $10\lambda/D$ it improves to 7.10^{-8}.

4. Interpretations of results

When considering the XAO halo, most coronagraphs (except BL8) provide roughly the same performance at mid angular radii (Fig. 3). Throughput consideration and sensitivity to parameters are then mandatory to make a difference. In this section we summarize the most important results of our study.

For each coronagraph, the sensitivity to parameters propagates similarly between the raw coronagrahic images (XAO) and differential images. The limiting factors are the same at these two contrast levels. As for band-limited, increasing the order of the mask (beyond the fourth order) is not advantageous since the Lyot stop throughput is severely restricted by the central obscuration and spiders. The Lyot-stop throughput places a limit on the order of the mask that can be implemented on an ELT. Fourth orders are preferable to eighth (or higher) orders. This result confirms the one obtained by Crepp et al. (2007), where they compare Lyot-type coronagraphs combined with AO system using a filled circular pupil. As already mentioned, the BL8 is very efficient for perfect optics, but its interest is questionable in the context of ELTs.

Coronagraphs with small IWA (AGPM/FQPM, AIC) are not able to reach the ultimate level sets by static aberrations. This is either a result of a high sensitivity to pointing errors (AIC) or an effect of the large residual amount of diffracted light by the pupil central obscuration, which is not sufficiently suppressed (AGPM/FQPM). We note that a solution exists to improve the peak suppression and pointing error sensitivity in the precise case of phase mask, such as the combination of a small Lyot mask placed in the center of the phase mask. A trade-off analysis would be mandatory to select the diameter of this additional Lyot mask.

For all coronagraphs, the signature of the central obscuration appears at the lowest contrast level but can still be a limitation. For instance, with the AGPM/FQPM, the other aberrations are pinned to the contrast level imposed by the central obscuration at small angular distances. Also, pointing errors and spider diffraction are critical for most coronagraph concepts (AGPM/FQPM, AIC, APRC, Lyot, BL8)

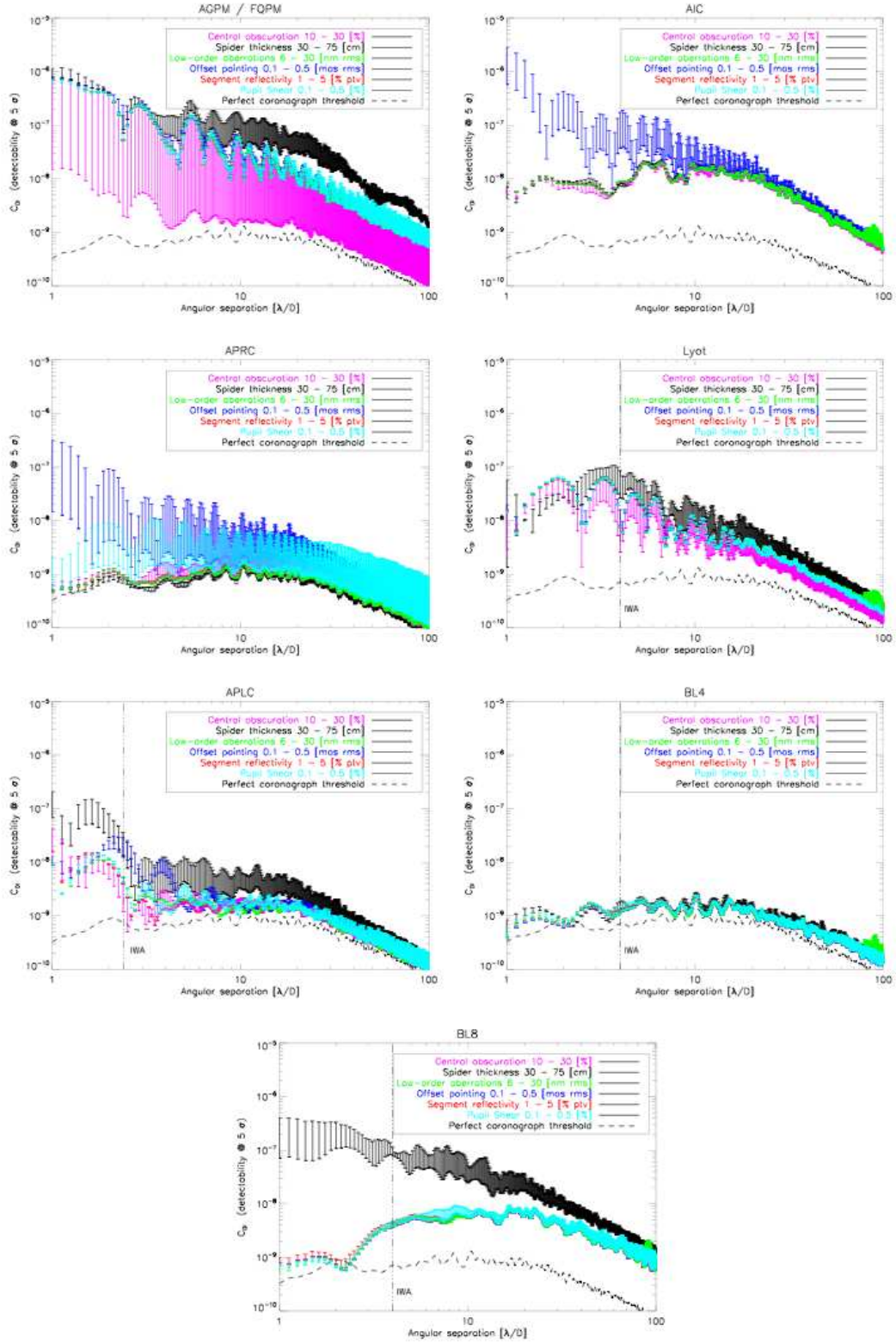

Fig. 5. Contrast profile at 5σ, $C_{DI}(\rho)$, for the different parameters and for each coronagraph. Error bars indicate the amplitude of the contrast variation. The dashed line stands for the ideal case and was obtained for static aberrations $\delta_c = 10$ nm rms, $\delta_{nc} = 0.3$ nm rms.

Table 3. Preliminary parameters specification to reach best performance (set by 30% central obscuration) for each coronagraph within the simulated space parameters.

Coronagraph type	Acceptable parameter error values				
	Spider [cm]	Segment error		Offset pointing [mas rms]	Pupil shear [%]
		Phase [nm rms]	Reflectivity [% ptv]		
AGPM/FQPM	30	30	5	0.5	0.5
AIC	75	30	5	0.2	-
APRC	75	30	5	0.2	0.3
Lyot	45	30	5	0.5	0.5
APLC	45	30	5	0.5	0.5
BL4	60	30	5	0.5	0.5
BL8	30	30	5	0.5	0.2

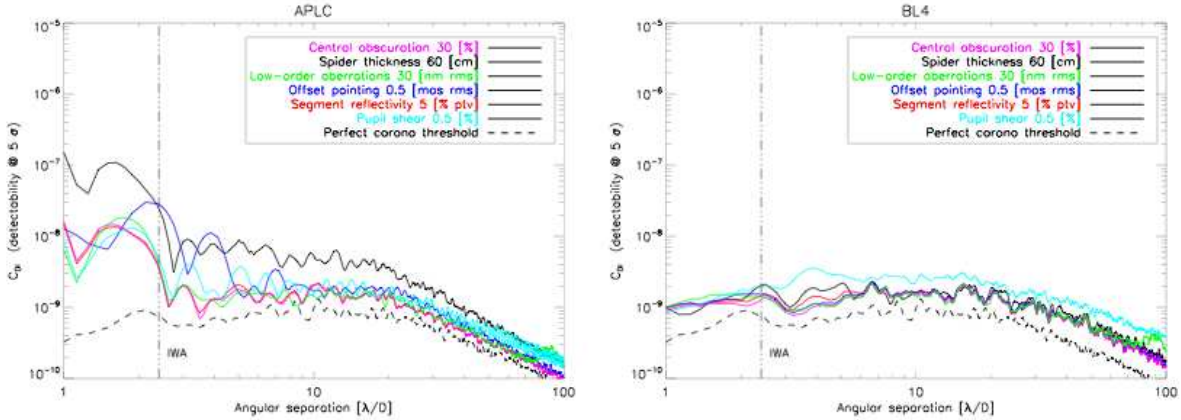

Fig. 6. C_{DI} (5σ detectability (δ_c = 10 nm rms, δ_{nc} = 0.3 nm rms)) vs. error sources for APLC (left) and BL4 (right) optimized for IWA = $2.4\lambda/D$

Among the concepts we studied here, some are able to provide good and homogenous performances, namely the APRC, the APLC, the Lyot and the BL4. To improve the contrast level further, the main effort will have to be made on the pointing errors (telescope vibrations and stability of the XAO environment) and on the pupil shear (alignment issue). The impact of the spider diffraction shows either the importance of a coronagraph that is not sensitive to this effect (APRC, BL4, AIC) or the necessity of a specific system that can remove their impacts (Abe et al. 2006).

Achieving a deep contrast imposes a concept of coronagraph that can accommodate some telescope characteristics, while preserving a reasonable throughput. Amplitude concepts like the APLC and the BL4 appear the best suited in that case. The APLC is foreseen as the baseline design for EPICS, and independent studies have shown that it is more suited to focal-plane wavefront correction, a mandatory technique for EPICS. In the next Section, impact of the design (IWA) on these concepts and throughput considerations will be addressed.

Finally, the simulation in Fig. 5 allows us to put a specification to each parameter of the simulation (within the range of values we considered) corresponding to the best contrast achievable with a given coronagraph (presented in Table. 3). This ultimate contrast level is driven in most cases by the central obscuration that we took equal to 30% in this analysis. It is assumed that within specifications coronagraphs do not delivered the same detectability. A coronagraph that potentially reaches high contrasts close to the level imposed by static aberrations also requires a more severe constraints on the parameters, while conversely, specifications can be relaxed for a less efficient coronagraph.

5. Further comparisons of APLC and BL4

In previous sections, the APLC focal-mask diameter ($4.7\lambda/D$, IWA=$2.4\lambda/D$) results from an optimization based on the size of the central obscuration while the mask of the BL4 is optimized for an IWA of $4\lambda/D$. This sections compares these two designs in more details for a similar IWA.

Figure 6 presents a DI simulation when both the APLC and the BL4 are optimized for IWA=$2.4\lambda/D$ For that, the BL4 was re-optimized ($\epsilon = 0.33$, $\mathscr{T} = 12.5\%$) while APLC has remained the same ($\mathscr{T} = 54.5\%$). Here, we only present the worst case corresponding to the highest values of parameters (except for the spider thickness, sets to 60cm, E-ELT as baseline). The net effect of a smaller IWA for the BL4 is a less transmissive pupil stop, and as a result pupil shear becomes the dominant effect. From 2.4 to $20\lambda/D$, the BL4 has a lower sensitivity to parameters, and both are quite comparable beyond $20\lambda/D$.

However, if we assume a similar system transmission for these coronagraphs, the APLC will then deliver a better performance. This can be done either with a more aggressive APLC pupil stop, and hence the achievable contrast is increased, or conversely with a more transmissive BL4 stop. Even if the performance of the BL4 with a small IWA is close to that of a perfect coronagraph, its interest is questionable since the transmission is a factor of 4 lower than that of the APLC.

The same analysis was performed for an IWA of $4\lambda/D$. In that case the APLC has been re-optimized to $7.5\lambda/D$ ($\mathscr{T}$ =

50.0%), while the BL4 is identical to previous sections (ϵ = 0.21, $\mathscr{T}$ = 22.4%). In such a case, the transmission is still favorable for APLC by a factor 2. Conclusions on contrast performance are identical to the previous case. The interest of the BL4 for ELTs would be relegated either to very bright objects or to large IWA to relax system transmission, but in that case further analysis would be needed to compare its performance to that of the Lyot mask.

6. Conclusion

The objective of this paper was to assess the impact of system parameters on several coronagraph concepts and to start a first-order comparison in the context of ELTs. We selected a few coronagraphs (or families) and evaluated the behavior of the delivered contrast with respect to the main sources of degradations that occur in a coronagraphic telescope at two levels of contrast when:

- considering the residuals of an XAO system,
- calibrating this halo with a differential imaging system. In that case, the residuals are set by the static aberrations.

The contrast plots that are presented in this paper are preliminary in the sense that we have considered a simple model of image formation with a limited number of parameters most of which are not yet fully defined. It is understood that a detailed study would involve a signal-to-noise ratio estimation considering different types of astrophysical objects as for SPHERE/VLT (Boccaletti & Mouillet 2005; Boccaletti et al. 2006). A parallel analysis has already been initiated for the EPICS project (Verinaud et al. 2007). We also note that some coronagraph concepts analyzed along this study can deliver a better performance when implemented in cascade (Aime & Soummer 2004; Baudoz et al. 2007). Performance resulting from these configurations in the precise case of ELTs must be investigated further, as already started for EPICS. Involving a wide number of existing coronagraph designs is mandatory as wel, e.g phase induced amplitude apodization coronagraph (PIAAC Guyon et al. 2004), checkerboard-mask coronagraphs (Vanderbei et al. 2004).

The study presented in this paper (preliminary results of system level specification are shown in Table. 3) is then one step toward this ultimate goal. Under these assumptions, we can derive three categories of coronagraphs:

- those adapted to short angular separations, but conversely sensitive to pointing errors: AGPM/FQPM, AIC, APRC. In that case, the APRC delivers the more robust performance since it is less sensitive to system parameters.
- those adapted to intermediate angular separations: APLC and Lyots where the APLC has the advantage of providing better performance with smaller IWA and low sensitivities to system parameters.
- those adapted to large angular separations: BL4 and APLC.

More specifically, the APLC gathers the adequate characteristics for baseline design in the case of ELTs. In addition, more sophisticated implementations are possible (Aime & Soummer 2004) with the goal of providing deeper contrast and/or relaxed IWA constraint. Potentially, it can be upgraded (although with a particular optical system) to feature a 100% throughput (using a two-mirror apodization system based on the phase induced amplitude apodization principle (PIAA, Guyon 2003; Guyon et al. 2004) to generate the apodizer through beam redistribution).

Chromatic effects can seriously drive the choice of which coronagraph to implement. Actually, amplitude concepts are more favorable for producing low chromatic dependencies. For instance, mask size of the APLC focal plane can be easily re-optimized to mitigate bandwidth effects. At the same time, many programs are striving to make other concepts achromatic, such as the AGPM or the multi-FQPM (Mawet et al. 2005a,b; Baudoz et al. 2007), achromatic and improved versions of the FQPM.

However, to take advantage fully of a coronagraph the most demanding parameter is clearly the level of the XAO residuals, and then a lot of effort has to be made to provide very high Strehl ratios on ELTs.

Finally, the manufacturing feasibility of coronagraphs is also a critical issue in developing a high contrast instrument for ELTs. We started to prototype several designs (APLC, FQPM, Lyot, and BL, (Martinez et al. 2008)) to be tested on the High-Order Test-bench developed at the European Southern Observatory (Vernet et al. 2006; Aller Carpentier et al. 2008). Results of these technical aspects will be presented in forthcoming papers.

Acknowledgements. P.M would like to thank Lyu Abe for helpful discussions of the two-mirror apodization for APLC. This activity is supported by the European Community under its Framework Programme 6, ELT Design Study, Contract No. 011863.

References

Abe, L., Murakami, N., Nishikawa, J., & Tamura, M. 2006, A&A, 451, 363
Aime, C. & Soummer, R. 2004, in Presented at the Society of Photo-Optical Instrumentation Engineers (SPIE) Conference, Vol. 5490, Advancements in Adaptive Optics. Edited by Domenico B. Calia, Brent L. Ellerbroek, and Roberto Ragazzoni. Proceedings of the SPIE, Volume 5490, pp. 456-461 (2004)., ed. D. Bonaccini Calia, B. L. Ellerbroek, & R. Ragazzoni, 456–461
Aime, C., Soummer, R., & Ferrari, A. 2002, A&A, 389, 334
Aller Carpentier, E., Kasper, M., Martinez, P., et al. 2008, in Proceedings of the SPIE, (2008).
Andersen, T., Ardeberg, A. L., Beckers, J., et al. 2003, in Presented at the Society of Photo-Optical Instrumentation Engineers (SPIE) Conference, Vol. 4840, Future Giant Telescopes. Edited by Angel, J. Roger P.; Gilmozzi, Roberto. Proceedings of the SPIE, Volume 4840, pp. 214-225 (2003)., ed. J. R. P. Angel & R. Gilmozzi, 214–225
Baba, N. & Murakami, N. 2003, PASP, 115, 1363
Baudoz, P., Boccaletti, A., Rabbia, Y., & Gay, J. 2005, PASP, 117, 1004
Baudoz, P., Boccaletti, A., & Rouan, D. 2007, in In the Spirit of Bernard Lyot: The Direct Detection of Planets and Circumstellar Disks in the 21st Century, ed. P. Kalas
Baudoz, P., Rabbia, Y., & Gay, J. 2000a, A&AS, 141, 319
Baudoz, P., Rabbia, Y., Gay, J., et al. 2000b, A&AS, 145, 341
Beuzit, J.-L., Feldt, M., Dohlen, K., et al. 2006a, The Messenger, 125, 29
Beuzit, J.-L., Feldt, M., Dohlen, K., et al. 2007, in Proceedings of the conference In the Spirit of Bernard Lyot: The Direct Detection of Planets and Circumstellar Disks in the 21st Century. June 04 - 08, 2007. University of California, Berkeley, CA, USA. Edited by Paul Kalas., ed. P. Kalas
Beuzit, J. L., Mouillet, D., Moutou, C., et al. 2006b, in Tenth Anniversary of 51 Peg-b: Status of and prospects for hot Jupiter studies, ed. L. Arnold, F. Bouchy, & C. Moutou, 353–355
Boccaletti, A. 2004, in EAS Publications Series, ed. C. Aime & R. Soummer, 165–176
Boccaletti, A. & Mouillet, D. 2005, in SF2A-2005: Semaine de l'Astrophysique Francaise, ed. F. Casoli, T. Contini, J. M. Hameury, & L. Pagani, 223–+
Boccaletti, A., Mouillet, D., Fusco, T., et al. 2006, in IAU Colloq. 200: Direct Imaging of Exoplanets: Science & Techniques, ed. C. Aime & F. Vakili, 519–524
Boccaletti, A., Riaud, P., Baudoz, P., et al. 2004, in EAS Publications Series, ed. C. Aime & R. Soummer, 195–204
Cavarroc, C., Boccaletti, A., Baudoz, P., Fusco, T., & Rouan, D. 2006, A&A, 447, 397
Chanan, G. A., Troy, M., & Ohara, C. M. 2000, in Presented at the Society of Photo-Optical Instrumentation Engineers (SPIE) Conference, Vol. 4003, Proc. SPIE Vol. 4003, p. 188-202, Optical Design, Materials, Fabrication, and Maintenance, Philippe Dierickx; Ed., ed. P. Dierickx, 188–202
Crepp, J. R., Vanden Heuvel, A. D., & Ge, J. 2007, ApJ, 661, 1323

Dierickx, P., Brunetto, E. T., Comeron, F., et al. 2004, in Presented at the Society of Photo-Optical Instrumentation Engineers (SPIE) Conference, Vol. 5489, Ground-based Telescopes. Edited by Oschmann, Jacobus M., Jr. Proceedings of the SPIE, Volume 5489, pp. 391-406 (2004)., ed. J. M. Oschmann, Jr., 391–406
Gay, J., Rabbia, Y., & Manghini, C. 1997, in Astrophysics and Space Science Library, Vol. 215, Astrophysics and Space Science Library, ed. C. Eiroa, 187–+
Gilmozzi, R. 2008, in Proceedings of the SPIE, (2008).
Guyon, O. 2003, A&A, 404, 379
Guyon, O. 2004, ApJ, 615, 562
Guyon, O., Pluzhnik, E., Martinache, F., Ridgway, S., & Galicher, R. 2004, in Bulletin of the American Astronomical Society, Vol. 36, Bulletin of the American Astronomical Society, 1564–+
Guyon, O., Pluzhnik, E. A., Kuchner, M. J., Collins, B., & Ridgway, S. T. 2006, ApJS, 167, 81
Johns, M., Angel, J. R. P., Shectman, S., et al. 2004, in Presented at the Society of Photo-Optical Instrumentation Engineers (SPIE) Conference, Vol. 5489, Ground-based Telescopes. Edited by Oschmann, Jacobus M., Jr. Proceedings of the SPIE, Volume 5489, pp. 441-453 (2004)., ed. J. M. Oschmann, Jr., 441–453
Kasper, M., Beuzit, J.-L., Verinaud, C., et al. 2008, in Proceedings of the SPIE, (2008).
Kuchner, M. J., Crepp, J., & Ge, J. 2005, ApJ, 628, 466
Kuchner, M. J. & Traub, W. A. 2002, ApJ, 570, 900
Lyot, B. 1939, MNRAS, 99, 580
Macintosh, B., Graham, J., Palmer, D., et al. 2006, in Presented at the Society of Photo-Optical Instrumentation Engineers (SPIE) Conference, Vol. 6272, Advances in Adaptive Optics II. Edited by Ellerbroek, Brent L.; Bonaccini Calia, Domenico. Proceedings of the SPIE, Volume 6272, pp. 62720L (2006).
Marois, C., Doyon, R., Racine, R., & Nadeau, D. 2000, PASP, 112, 91
Marois, C., Lafrenière, D., Macintosh, B., & Doyon, R. 2008, ApJ, 673, 647
Martinez, P., Boccaletti, A., Kasper, M., Baudoz, P., & Cavarroc, C. 2007, A&A, 474, 671
Martinez, P., Vernet, E., Dorrer, C., et al. 2008, in Proceedings of the SPIE, (2008).
Mawet, D., Riaud, P., Absil, O., Baudrand, J., & Surdej, J. 2005a, in Presented at the Society of Photo-Optical Instrumentation Engineers (SPIE) Conference, Vol. 5905, Wavefront amplitude variation of TPF's high-contrast imaging testbed: modeling and experiment. Edited by Shi, Fang; Lowman, Andrew E.; Moody, Dwight; Niessner, Albert F.; Trauger, John T. Proceedings of the SPIE, Volume 5905, pp. 486-495 (2005)., ed. D. R. Coulter, 486–495
Mawet, D., Riaud, P., Absil, O., & Surdej, J. 2005b, ApJ, 633, 1191
Nelson, J. & Sanders, G. H. 2006, in Presented at the Society of Photo-Optical Instrumentation Engineers (SPIE) Conference, Vol. 6267, Ground-based and Airborne Telescopes. Edited by Stepp, Larry M.. Proceedings of the SPIE, Volume 6267, pp. 626728 (2006).
Racine, R., Walker, G. A. H., Nadeau, D., Doyon, R., & Marois, C. 1999, PASP, 111, 587
Riaud, P., Boccaletti, A., Rouan, D., Lemarquis, F., & Labeyrie, A. 2001, PASP, 113, 1145
Rouan, D., Riaud, P., Boccaletti, A., Clénet, Y., & Labeyrie, A. 2000, PASP, 112, 1479
Sivaramakrishnan, A. & Lloyd, J. P. 2005, ApJ, 633, 528
Soummer, R. 2005, ApJ, 618, L161
Soummer, R., Aime, C., & Falloon, P. E. 2003a, A&A, 397, 1161
Soummer, R., Dohlen, K., & Aime, C. 2003b, A&A, 403, 369
Troy, M. & Chanan, G. A. 2003, in Presented at the Society of Photo-Optical Instrumentation Engineers (SPIE) Conference, Vol. 4840, Future Giant Telescopes. Edited by Angel, J. Roger P.; Gilmozzi, Roberto. Proceedings of the SPIE, Volume 4840, pp. 81-92 (2003)., ed. J. R. P. Angel & R. Gilmozzi, 81–92
Vanderbei, R. J., Kasdin, N. J., & Spergel, D. N. 2004, ApJ, 615, 555
Verinaud, C., Kasper, M., Beuzit, J.-L., et al. 2007, in In the Spirit of Bernard Lyot: The Direct Detection of Planets and Circumstellar Disks in the 21st Century, ed. P. Kalas
Vernet, E., Kasper, M., Vérinaud, C., et al. 2006, in Advances in Adaptive Optics II. Edited by Ellerbroek, Brent L.; Bonaccini Calia, Domenico. Proceedings of the SPIE, Volume 6272, pp. 62722K (2006).
Yaitskova, N. & Verinaud, C. 2006, in Presented at the Society of Photo-Optical Instrumentation Engineers (SPIE) Conference, Vol. 6267, Ground-based and Airborne Telescopes. Edited by Stepp, Larry M.. Proceedings of the SPIE, Volume 6267, pp. 62672N (2006).

Design, analysis and test of a microdots apodizer for Apodized Pupil Lyot Coronagraph

Astronomy & Astrophysics manuscript no. microdots˙printer
October 7, 2008

Design, analysis and test of a microdots apodizer for the Apodized Pupil Lyot Coronagraph

P. Martinez[1,2,5], C. Dorrer[3], E. Aller Carpentier[1], M. Kasper[1], A. Boccaletti[2,5], and K. Dohlen[4]

[1] European Southern Observatory, Karl-Schwarzschild-Strasse 2, D-85748, Garching, Germany
[2] LESIA, Observatoire de Paris Meudon, 5 pl. J. Janssen, 92195 Meudon, France
[3] Laboratory for Laser Energetics-University of Rochester, 250 East River Rd, Rochester, NY, 14623-USA
[4] LAM, Laboratoire d´Astrophysique de Marseille, 38 rue Frédéric Joliot Curie, 13388 Marseille cedex 13, France
[5] Groupement d´intérêt scientifique PHASE (Partenariat Haute résolution Angulaire Sol Espace)

Preprint online version: October 7, 2008

ABSTRACT

Context. Coronagraphic techniques are required to detect exoplanets with future Extremely Large Telescopes. One concept, the Apodized Pupil Lyot Coronagraph (APLC), is combining an apodizer in the entrance aperture and a Lyot opaque mask in the focal plane. This paper presents the manufacturing and tests of a microdots apodizer optimized for the near IR.
Aims. The intent of this work is to demonstrate the feasibility and performance of binary apodizers for the APLC. This study is also relevant for any coronagraph using amplitude pupil apodization.
Methods. A binary apodizer has been designed using a halftone dot process, where the binary array of pixels with either 0% or 100% transmission is calculated to fit the required continuous transmission, i.e. local transmission control is obtained by varying the relative density of the opaque and transparent pixels. An error diffusion algorithm was used to optimize the distribution of pixels that best approximates the required field transmission. The prototype was tested with a coronagraphic setup in the near IR.
Results. The transmission profile of the prototype agrees with the theoretical shape within 3% and is achromatic. The observed apodized and coronagraphic images are consistent with theory. However, binary apodizers introduce high frequency noise that is a function of the pixel size. Numerical simulations were used to specify pixel size in order to minimize this effect, and validated by experiment.
Conclusions. This paper demonstrates that binary apodizers are well suited for being used in high contrast imaging coronagraphs. The correct choice of pixel size is important and must be adressed considering the scientific field of view.

Key words. Techniques: high angular resolution –Instrumentation: high angular resolution –Telescopes – Adaptive Optics

1. Introduction

Direct detection and characterization of faint objects around bright astrophysical sources is challenging due to the large flux ratio and small angular separation. For instance, self-luminous giant planets are typically 10^6 times fainter than the parent star in the near-infrared. Even higher contrasts of up to 10^{-10} are needed to reach the realm of mature giant or telluric planets. In order to achieve these contrast levels, dedicated instruments for large ground-based telescopes such as SPHERE or GPI (Beuzit et al. 2006a; Macintosh et al. 2006), or EPICS (Kasper et al. 2008) for the future European-Extremely Large Telescope (E-ELT) will use powerful Adaptive Optics (extreme AO or XAO) systems coupled with coronagraphs.

While the XAO system corrects for atmospheric turbulence and instrument aberrations, the coronagraph attenuates the starlight diffracted by the telescope in the image plane. Since the invention of the stellar Lyot coronagraph (Lyot 1939), there has recently been impressive progress in the field leading to a wealth of different coronagraphs that can be divided into different families. In particular, the Apodized Pupil Lyot Coronagraph (APLC) (Aime et al. 2002; Soummer et al. 2003a) appears to be well suited for ELTs and has been studied theoretically (Soummer 2005; Martinez et al. 2007). The APLC features amplitude apodization in the entrance aperture to reduce diffraction and a small Lyot mask in the focal plane. It is the baseline coronagraph for e.g. SPHERE, GPI, and the Lyot Project (Oppenheimer et al. 2004). Martinez et al. (2008a) further show that the APLC is also well suited to be used with ELTs considering their particular pupil shapes and segmented mirrors.

A major issue with the APLC (and other coronagraphs using apodization such as is the dual zone coronagraph, Soummer et al. (2003b)) is the manufacturing of the apodizer itself. So far, two concepts have been explored to manufacture apodizers: 1/ a metal layer of spatially variable thickness, and 2/ an array of opaque pixels with spatially variable density. The second concept has several advantages over the first one. It is intrinsically achromatic and avoids wavefront phase errors introduced by a metal layer of variable thickness.

In this paper, we report on the development (design and laboratory tests) of a binary apodizer for the APLC using a halftone dot process. First we describe the binary mask principle and the algorithm used to distribute pixels across the pupil to best fit the required field transmission (Sect.2). Optimization of the design through pixels size is discussed in Sect. 3 while in Sect. 4 we report on laboratory results obtained with a prototype using a near-IR bench which reproduces the Very Large Telescope (VLT) pupil. Finally, we conclude on the suitability of this technique for planet finder instruments in Sect. 5.

Send offprint requests to: P. Martinez, martinez@eso.org

2. Principle of microdots apodizer

A binary apodizer is made of an array of opaque pixels (i.e dots) on a transparent substrate. It is fabricated by lithography of a light-blocking metal layer deposited on a transparent glass substrate. Spatially variable transmission is obtained by varying pixel density. An error diffusion algorithm was used to calculate the density distribution that best fits the required field transmission (Floyd & Steinberg 1976; Ulichney 1987; Dorrer & Zuegel 2007). This algorithm chooses the transmission of a given pixel of the apodizer (either 0% or 100%) by comparing the transmission required at this location to a 50% threshold, i.e. the transmission is set to zero if the required transmission is smaller than 50 %, and to one otherwise (see Fig. 1). The induced transmission error is diffused to adjacent pixels that have not been processed yet by biasing the transmission required at the corresponding locations. This locally cancels the error of the binary optics relative to the required transmission. Such procedure is used for gray-level reproduction with black-and-white printing techniques (Ulichney 1987).

Shaping of coherent laser beams has also been demonstrated (Dorrer & Zuegel 2007) using this technique. The error diffusion algorithm has the advantage that the introduced noise is blue, i.e., the noise spectral density is only significant at high spatial frequencies. This allows the accurate generation of gray levels and rapidly varying shaping functions. In the specific case of the design of a coronagraph, the algorithm allows us to well match the PSF of the binary apodizer to the required apodized PSF up to a certain radial distance which could be chosen as the control radius of the AO system. In theory, better shaping results are obtained with smaller pixels (i.e sampling problem, Dorrer & Zuegel 2007), since this allows finer control of the local transmission and pushes the binarization noise to higher frequency. This will be further discussed in Sect. 3.

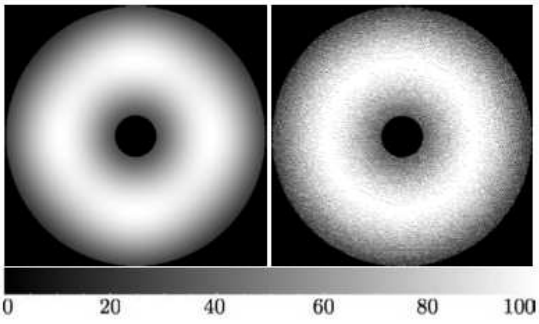

Fig. 1. Left: Shaper target (continuous apodizer). Right: Resulting microdots pattern using algorithm discussed in Sec. 2. The spatial scale of these maps is 600×600 pixels. The scale of transmission is given in %.

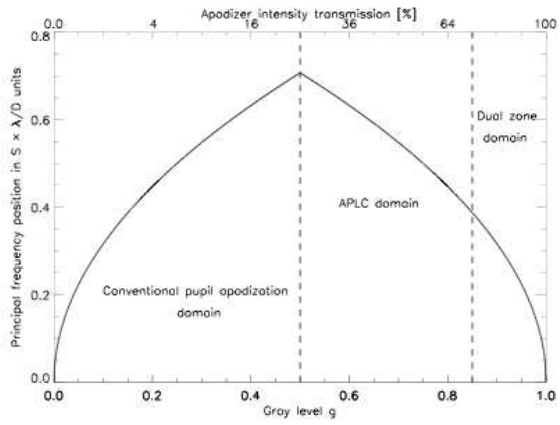

Fig. 2. First order peak diffraction f_g position in $S \times \lambda/D$ units as a function of gray level g. Typical domain of application of apodizer masks are reported on the plot.

3. Design optimization

Assuming a VLT-like pupil, the apodizer is defined for a 15% central obscuration pupil (bagel regime, Soummer 2005). We consider a $4.5\lambda/D$ APLC (Martinez et al. 2007). The apodizer shape is illustrated in Fig. 1 (left image).

The manufactured apodizer has a diameter of 3mm due to constraints on our optical bench (Sect. 3.3 and 4). For microdots, the performance is related to the ratio of the smallest feature to the pixel size. Hence, for the sake of clarity, we denote by S the scaling factor, the ratio between the apodizer useful diameter (i.e pupil diameter, denoted Φ hereafter) and the pixel spacing, i.e pixel size (dot size), denoted p hereafter:

$$S = \frac{\Phi}{p} \tag{1}$$

The individual pixels of a binary apodizer scatter light towards spatial frequencies depending on the pixel size. The smaller the pixels are, the higher are the spatial frequencies at which the light is scattered, and the better the achieved transmission profiel matches the desired one.

We also note that the high-frequency noise might have different distributions at different wavelengths. This would be a situation similar to diffraction gratings, where only diffracted orders (i.e corresponding to large values of the transverse wavevector k) are frequency-dependent. For such finer analysis, Fresnel propagators and a thorough modeling of the binary shaper (including process errors on the shape and size of each dot such as edge effects resulting from the isotropic wet etching process, Sect. 3.3) would be mandatory.

3.1. Microdots diffraction stray light

The microdots apodizer is modeled as an aperiodic under-filled two-dimensional grating which exhibits blue noise properties because of the error diffusion algorithm used (Ulichney 1987; Dorrer & Zuegel 2007). The binary pattern produces an averaged gray level ($g = \sqrt{T}$, i.e averaged amplitude transmission) from an apodizer profile with intensity transmission T. The resulting pattern spectral energy is set by g (i.e by the minority pixels present on the device: non-metal pixels when $g < 0.5$ and by metal pixels conversely). The spectral energy will increase as the number of minority pixels increases, peaking at $g = 0.5$ (Ulichney 1987, 1988). Most of the energy in the power spectrum of the pattern will be concentrated around the first order diffraction which would appear in the field of view at the spatial frequency f_g (in λ/D units):

$$f_g = \begin{cases} \sqrt{g} \times S & g \leq 1/2 \\ \sqrt{(1-g)} \times S & g > 1/2 \end{cases} \tag{2}$$

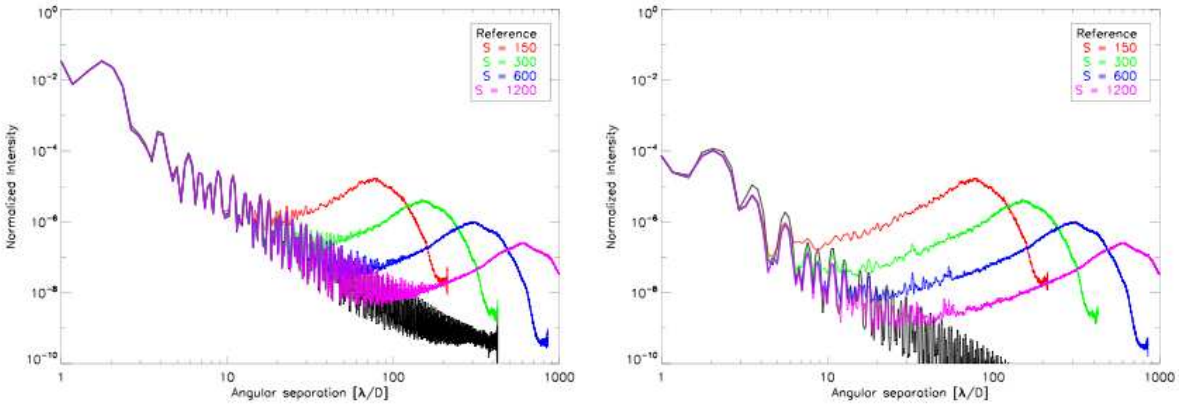

Fig. 3. Apodized PSFs (left) and APLC coronagraphic PSFs (right) using several dots size for the binary apodizer compared to that with continuous apodizer (i.e theory, in black). It assumes a pupil with 15% central obscuration. Profiles presented are azimuthal averages.

Therefore, for a given g, the pattern power spectrum has a peak diffraction at f_g (Ulichney 1987, 1988). As the gray level, g, increases from 0 to 0.5, the peak diffraction moves to further angular distance (Fig. 2) with an increase of energy. Above $g = 0.5$, situation is similar to (1-g), minority pixels has only changed from non-metal dots to metal dots. The PSF of a microdots device can be therefore expressed as function of a deterministic effect (the first order diffraction peak) bordered by speckles by stochastic effect (i.e dots distribution is not regular). Higher order diffraction peaks are not relevant since out of the sciences field of view. The intensity of the first order diffraction peak in the final coronagraphic image is function of g as well. The model presented hereafter is based on a study performed by Dohlen (2008), where effects of micro-obscurations such as dusts or cosmetic errors are analytically described for the SPHERE instrument image quality. The coronagraphic halo intensity (I) of the first order peak diffraction for N dots normalized to the stellar peak intensity is $N_{dots} \times \left(\frac{p}{\Phi}\right)^4$ (Dohlen 2008, assuming halos from all the dots add incoherently). N_{dots} is the total number of the minority dots present in the pattern and can be easily calculated through the surface ratio of the pupil by a square dot, times the density of minority dots (η, hereafter). The minority dots density can be expressed as:

$$\eta = \begin{cases} g & g \leq 1/2 \\ 1-g & g > 1/2 \end{cases} \quad (3)$$

then N_{dots} is:

$$N_{dots} = \eta \times \frac{\pi}{4} \times \left(\frac{\Phi}{p}\right)^2 \quad (4)$$

The resulting relative halo intensity is then:

$$I = \eta \times \frac{\pi}{4} \times \left(\frac{1}{S}\right)^2 \quad (5)$$

therefore, using Eq. 3 one finally obtains:

$$I = \begin{cases} g \times \frac{\pi}{4} \times \left(\frac{1}{S}\right)^2 & g \leq 1/2 \\ (1-g) \times \frac{\pi}{4} \times \left(\frac{1}{S}\right)^2 & g > 1/2 \end{cases} \quad (6)$$

Considering our APLC apodizer ($T = 51\%$, $g = 0.71$), the first order diffraction peak would be therefore localized at $f_g \sim S/2$ in λ/D units with an intensity of $I \sim 1/(4 \times S^2)$. For the Dual Zone coronagraph ($T \sim 80\%$, therefore $g \sim 0.9$), the first order diffraction peak moves closer to the central core of the PSF while its intensity decreases with respect to the APLC case: $f_g \sim S/3$ in λ/D with an intensity of $I \sim 1/(13 \times S^2)$. For Conventional pupil apodization ($T \sim 25\%$, hence $g \sim 0.5$), the first order diffraction peak moves further away from the central core of the PSF while its intensity increases: $f_g \sim 1/\sqrt{2} \times S$ in λ/D with an intensity of $I \sim 2/(5 \times S^2)$.

3.2. Numerical simulations

Our simulations make use of Fraunhofer propagators between pupil and image planes, which is implemented as fast Fourier transforms (FFTs) generated with an IDL code. In the following, pixels describe the resolution element of the simulation, while dots describe the physical units forming the apodizer. We use 0.3 λ/D per pixel, while dots are sampled by 4 pixels to allow enough field of view to image the 1st order diffraction peak for each S. Validity of the numerical dot sampling has been verified by comparing simulations with different dot sampling (1, 4 and 16 pixels per dot for $S = 150$).

We first analyze how the dot size affects the apodized PSF (Fig. 3, left) and the coronagraphic PSF (Fig. 3, right) with respect to an ideal continuous apodizer. From the results summarized in Table 1 we derive the following conclusions:

- Reduction of the dot size by a factor of 2 increases the radial distance corresponding to an adequate agreement with the specification by a factor of 2 for the coronagraphic image. Eq. 2 is confirmed by simulation.
- Analytical model (Eq. 6) is consistent with simulation predictions. This model is representative for the APLC situation.
- At a given frequency, in the coronagraphic images, the level of the noise decreases proportional to S^4 (for instance, at $80\lambda/D$ noise increases from 3.2×10^{-9} to 3.5×10^{-5} when increasing S by a factor 8)

In practice, for the selection of S (dots size), we modeled in simulation our specific pupil (VLT-like including the secondary

S	p [μm]	High frequency noise angular position [λ/D]		Microdots halo intensity	
		Apodized PSF	Coronagraphic PSF	Theory (I)	simulation
150	20	20	5	1.0×10^{-5}	1.7×10^{-5}
300	10	30	10	2.6×10^{-6}	4.2×10^{-6}
600	5	40	20	6.5×10^{-7}	1.0×10^{-6}
1200	2.5	50	40	1.6×10^{-7}	2.6×10^{-7}

Table 1. Angular position where the high frequencies noise appears on the apodized PSF and coronagraphic image as function of the pixel size (column 3 and 4). Microdots halo intensity as function of the pixel size: comparison between simulation (measured on the halo peak) and analytical expression I (column 5 and 6). Results presented refers to Fig. 3.

support, i.e contrast accessibility issue) and taking into account the field of view of interest (sets by the AO correction domain: $20\lambda/D$ like in SPHERE). We found that as expected, the radial distance corresponding to an adequate agreement with the specification (ideal model) moved to larger angular separations while the intensity level where the noise appears remains in the order of the previous case.In our context, $S = 600$ ($5\mu m$ dots) meets our specifications. The $S = 1200$ configuration leads to really small dot size (2.5μm). In such a case, when the dot size is of the order or lower than the operating wavelength (1.65μm for our application) a Rigorous Coupled-Wave Analysis (RCWA) is mandatory to know how the field reacts to small perturbations in the shaper (**??**). Gratings with small periods generally have some diffracted orders cut off for visible and IR light.

3.3. Other specifications

The microdots apodizer was fabricated by Precision Optical Imaging in Rochester, New York. To reduce the effect of misalignment of the apodizer with the telescope pupil, the designed profile of the apodizer ($\Phi = 3mm$) was not obscured at the center by the central obscuration (no 0% transmission values) and was extrapolated by a Gaussian function on the outer part (from 1.5 mm to 3 mm in radius, i.e above the apodizer function radius) to slowly decrease the transmission to zero. Moreover, having a sharp edge on the apodizer might be detrimental to the characterization process (inspection of the profile), because of strong diffraction effects. The shaper was fabricated using wet-etch contact lithography of a Chrome layer (Optical Density of 4.0) deposited on a BK7 glass substrate ($\lambda/20$ peak-to-valley). The back face of the apodizer has an antireflection coating for the H band (1.2 to 1.8 μm, $R < 1\%$).

In the case of wet-ech lithography, etching can lead to a reduction in the light-blocking metal dot sizes (smaller than specified in the digital design), which potentially leads to an increased transmission. Dot spacing remains the same, while opaque dot size are reduced in size due to an undercut of the masking layer which form cavities with sloping sidewalls. To minimize the impact of this effect on the obtained transmission, the mask design was numerically precompensated by estimating the feature size which would be obtained after fabrication (Dorrer & Zuegel 2007). In practice, we adopted a pixel grid of $6\mu m$ (i.e dot size, $S = 500$), and several runs were necessary to finely calibrate the process and reach the specification. Reproducibility was confirmed with a last run after optimal conditions were set.

The 4.5 λ/D hard-edge opaque Lyot mask has been fabricated by GEPI, Paris Observatory (360μm $\pm$ 1μm in diameter, OD = 6.0 at 1.65 μm using two metallic layers of Chrome (20 nm) and Gold (200 nm)).

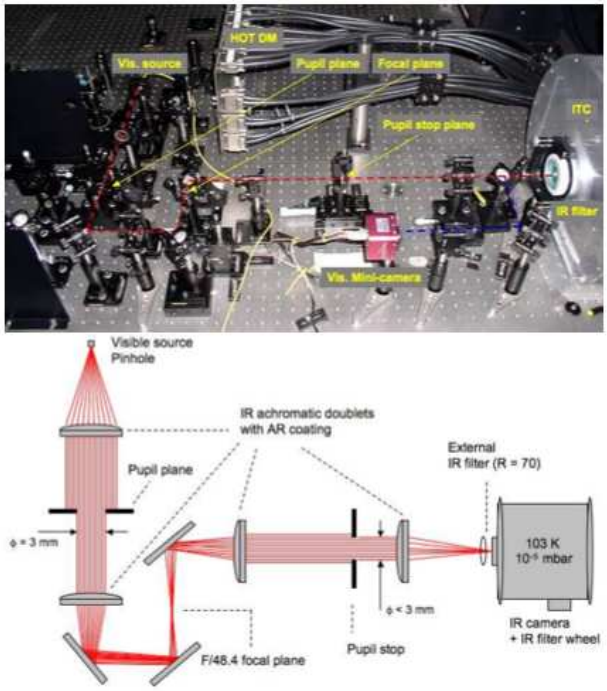

Fig. 4. *Top*: Picture of the IR coronagraphic test-bench on HOT. The red dot line shows the IR coronagraphic path while the blue dot line shows the pupil imager system path when placing a mirror on a magnetic mount before the external IR filter. *Bottom*: shematic setup of the coronagraphic testbench.

4. Experiment

4.1. Optical setup

The experiment configuration is shown is Fig. 4. where the optical IR coronagraphic path is described (top) using dot red line on the picture. The optical setup is designed to simulate the 8 m VLT pupil. The 3mm entrance aperture diameter is made in a laser-cut stainless steel sheet with an accuracy of 0.002 mm. The central obscuration is scaled to 0.47 mm $\pm$ 0.002 mm and the spider vanes thickness is 15μm $\pm$ 4μm. The coronagraphic mask is installed at an F/48.4 beam. Re-imaging optics are made with $\lambda/10$ achromatic IR doublets. The quality of the collimation in the pupil plane and re-imaged pupil plane (where the pupil stop is placed) was checked and adjusted using an HASO 64 Shack-Hartmann sensor. A pupil imager system (see Fig. 4, a dot blue line describe its optical path) has been implemented for the alignment of the pupil stop mask with respect to the entrance

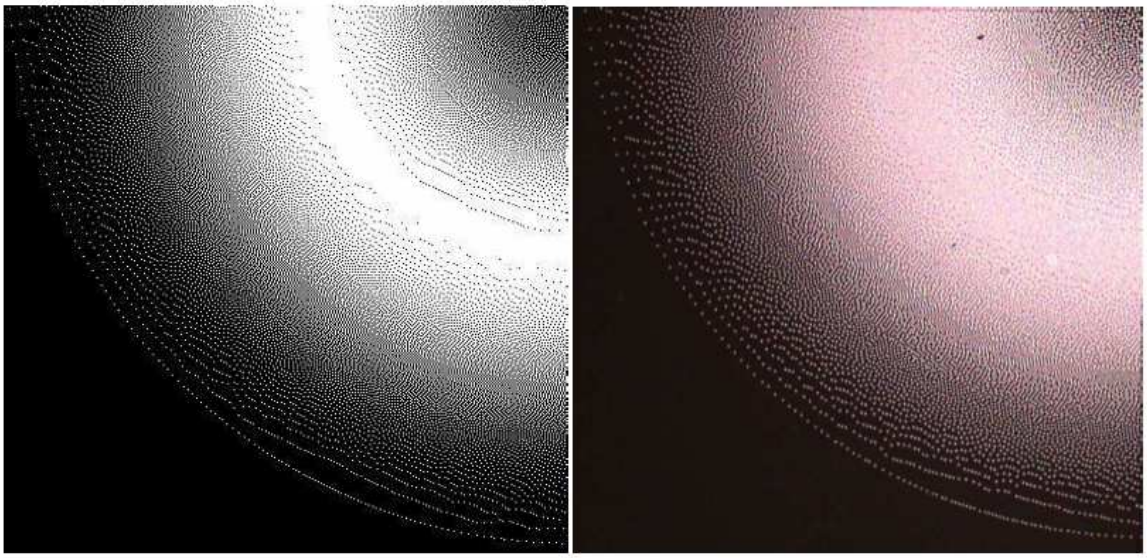

Fig. 5. Left: simulation map of the binary apodizer with 5×5μm dots. Right: Shadowgraph inspection of the manufactured microdots apodizer (×50). For the sake of clarity, only a quarter of the apodizer is shown.

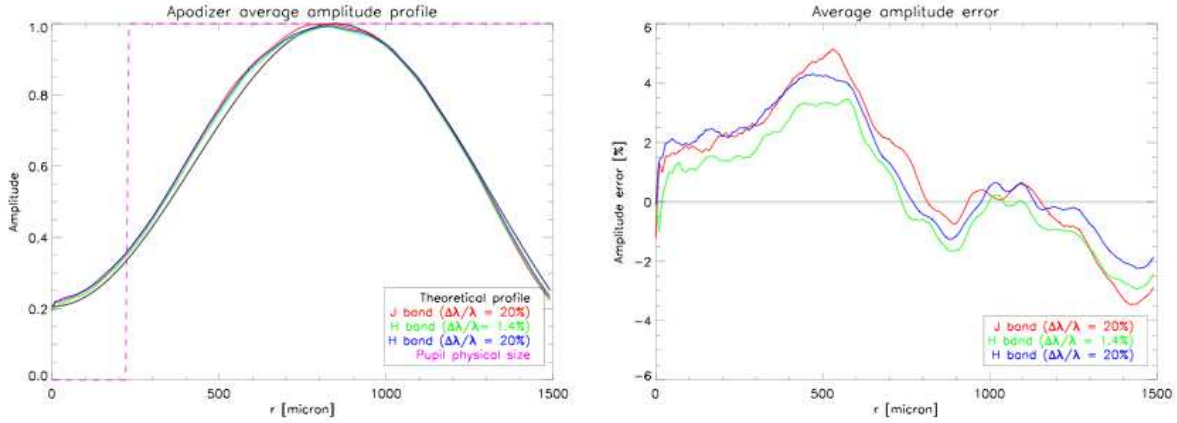

Fig. 6. Left: Apodizer azimuthally average profile (from center to the edges) using different filters (J, H and narrow H band) compared to specification (black curve). Right: corresponding average amplitude error as function of the position using the same filters.

pupil mask (alignment in x and y direction, orientation of the spider vanes and focalisation as well).

We installed the entrance pupil mask and the apodizer in the same collimated beam. Hence, the apodizer is not perfectly in the pupil plane.The apodizer was placed inside a rotating adjustable-length lens tube that allows a translation of ~3.5mm from the pupil mask.

We used a white-light source combined either with an IR narrow band filter ($\Delta\lambda/\lambda$ = 1.4%, central wavelength of 1.64μm, with a peak transmission of 64.4% or IR filters (J, H, K), installed inside the filter wheel of the IR camera where the H filter is centered at 1.6μm, $\Delta\lambda/\lambda$ = 20%. The camera used is the ESO Infrared Test Camera (ITC), cooled at 103 K degree with a vacuum of 10^{-5} mbar. Internal optics are designed to reach a pixel scale of 5.3 mas. The Strehl ratio was evaluated at 94%.

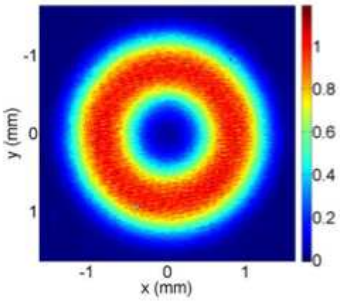

Fig. 7. Top: Infrared recorded image of the apodizer.

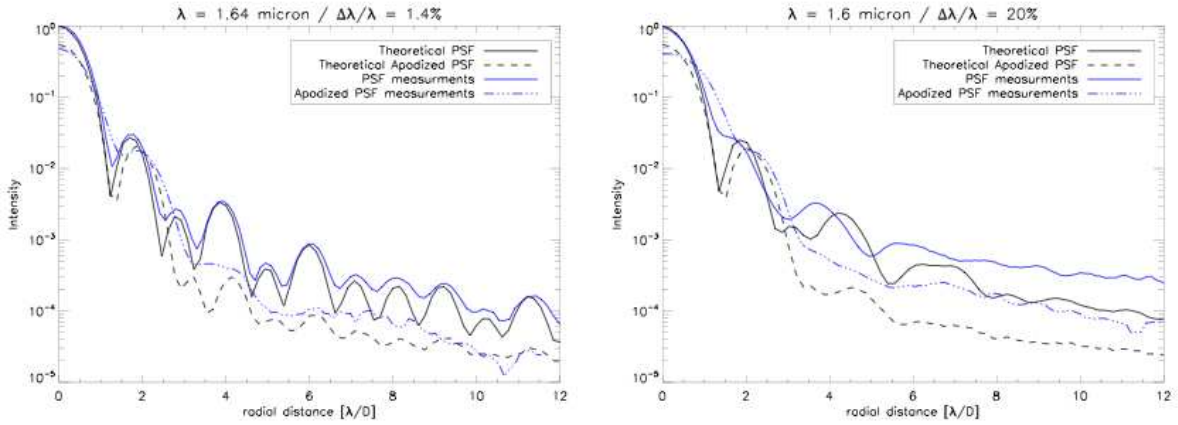

Fig. 8. Left : PSF and apodized PSF recorded on the bench (blue lines) compared to theoretical ones (black lines) with narrow H filter (λ= 1.64 μm, $\Delta\lambda/\lambda$ = 1.4%). Right : Same measurements as previous ones but with broadband H filter ($\Delta\lambda/\lambda$ = 20%).

The APLC pupil stop mimics the VLT pupil mask with spider vanes thickness increased by a factor 4 (60μm ± 4μm), and outer diameter reduced by 0.96×Φ (2.88 mm ± 0.002 mm) and the central obscuration is equal to 0.16×Φ (0.49 mm ± 0.002 mm). The pupil stop throughput is about 90%.

4.2. Quality of the binary apodizer

The size of the square chrome dots has been determined to 4.5 × 4.5 μm using a microscopic inspection. The global shape of the binary apodizer is presented in Fig. 7. The dots spatial distribution across the pupil diameter has been also analyzed using a shadowgraph (×50, Fig. 5) and compared to simulation map (5 × 5 μm dots). Figure 6 shows that the accuracy on the profile well matches the expected profile, and the transmission error is about 3%. Achromaticity of the profile is also demonstrated : the profile error only increases by about 2% from the narrow H filter to the broadband J filter. Having smaller pixel size than the digital design (6×6 μm) was expected (Sect. 3.3) and demonstrates that precompensation of the transmission error due to the feature size was necessary and works well.

4.3. Coronagraphic results and discussion

4.3.1. Effect on the PSF

This first series of tests intend to demonstrate the correct behavior of the binary apodizer on the PSF. We only compare the PSF without apodizer to that with the apodizer. Qualitatively (Fig. 9) it is demonstrated that the apodizer works well : the PSF's wings of the apodized PSF are reduced in intensity while the core of the apodized PSF gets larger (exposure time are here identical, no neutral density is applied). This behavior agrees well with the theoretical predictions. Although there are some discrepancies between theory and measurements (Fig. 8, bottom, for $\Delta\lambda/\lambda$ = 20% in H band), the gain between PSF and apodized PSF is consistent with theory. This results has been demonstrated in the H-band with a narrow band filter ($\Delta\lambda/\lambda$ = 1.4%) and with a broadband filter ($\Delta\lambda/\lambda$ = 20%). Its achromaticity in H band is therefore confirmed. The fact that we are using a real optical system and the 3.5mm defocus between the apodizer and the entrance pupil may explain the discrepancies.

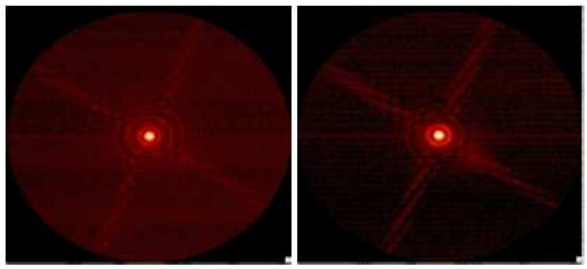

Fig. 9. Images recorded on the bench (λ= 1.64 μm, $\Delta\lambda/\lambda$ = 1.4%), left: VLT-like pupil PSF, right: VLT-like pupil apodized PSF.

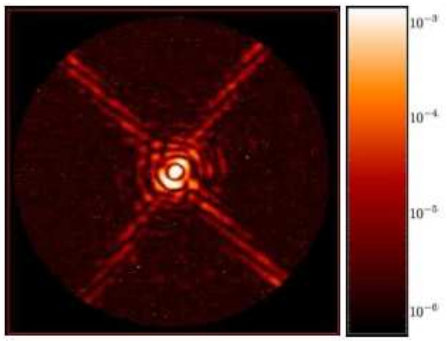

Fig. 10. Observed raw coronagraphic image (log scale) with its scale of contrast (λ= 1.64 μm, $\Delta\lambda/\lambda$ = 1.4%).

4.3.2. Effect on the coronagraphic PSF

This second series of tests intend to demonstrate the coronagraphic behavior of the APLC using the microdots apodizer.

Qualitatively, the profile of the coronagraphic image (Fig. 10, H band with $\Delta\lambda/\lambda$ = 1.4%) agrees well with theory: a PSF-like pattern homogeneously reduced in intensity with most of the energy inside the first rings. In this observed raw image, a local contrast as large as 6.5×10^{-7} has been reached between the diffraction spikes. In Fig. 11 we present apodized PSFs and

coronagraphic images recorded on the bench using a narrow ($\Delta\lambda/\lambda$ = 1.4%) and broadband filter ($\Delta\lambda/\lambda$ = 20%) in the H band. Most of the time, an order of magnitude discrepancy (mostly in the halo) is found between theory and measured data (Table. 2) where we have compared contrast at 3, 12 and 20λ/D. The contrast is defined as the ratio of the local intensity (i.e at a given angular separation) on the coronagraphic image to the maximum intensity of the apodized PSF image. The total rejection rate (ratio between the total intensity of the PSF image and the total intensity of the coronagraphic image, in practice limited to 20λ/D) is only at a factor of 2 and 1.8 from theory for the narrow and broad band filters respectively. This discrepancy is reduced when considering the peak rejection (ratio between the maximum intensity of the PSF to the maximum intensity of the coronagraphic image) to a factor of 1.7 and 1.2, respectively. The impact of chromatism is only slightly revealed at small angular separation (before 4λ/D), otherwise achromaticity is demonstrated in the halo in H band.

The discrepancy may find its origin in different error sources (we only discuss here the main ones): 1/ apodizer profile error (~ 3%), 2/ quality of the bench ($Strehl$ = 94%) and 3/ defocus between the apodizer and the pupil plane (~ 3.5mm). Simulations were carried out to analyze independently the impact of the two first ones. For the impact of the defocus we refer to a sensitivity analysis performed for SPHERE (Boccaletti et al. 2008) where the apodizer mask positioning requirement in defocus is set to ±0.1mm. Such error in the positioning impacts mainly the halo. Including in simulation the measured profile of the apodizer (Fig. 6) reduces the discrepancy from 1.7 to 1.2 on the peak rejection and from ~10 to ~3 in the halo. When the Strehl ratio is set to 94% (λ/25 nm rms) while the apodizer is perfect, the discrepancy is reduced to 1.08 on the peak rejection and to ~4 in the halo. It is therefore difficult to conclude on the dominant source of error. The discrepancy with theory is certainly a result of a combination of all theses error sources.

During our laboratory tests, no high frequencies noise due to the apodizer pixellation was revealed. However, simulation analysis presented in Sect. 3 predicts pixellation noise at about 20λ/D on the coronagraphic image at a contrast between 10^{-7} and 10^{-8} (S = 600). In our case, the contrast level is not deep enough even between the diffraction spikes to reveal the predicted noise. Therefore, we can only conclude on the performance and suitability of our configuration for HOT (the High Order Testbench developed at ESO, and even for SPHERE) but not on the pixellation noise simultaneously predicted by analytical development (Eq. 2 and 6) and by simulation. We note that smaller pixels size (< 5μm) would certainly help at reducing the 3% error on the profile which could potentially improve performance. Despite the discrepancy discussed above, these first results of APLC using microdots apodizer are already beyond the SPHERE requirements (Boccaletti et al. 2008).

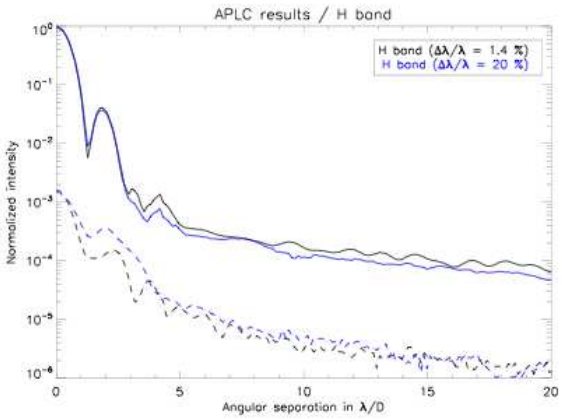

Fig. 11. Azimuthally averaged coronagraphic profiles at λ= 1.64 μm, $\Delta\lambda/\lambda$ = 1.4% (black lines) and $\Delta\lambda/\lambda$ = 20% (blue lines).

Metrics	Measured on bench		Theory	
	$\Delta\lambda/\lambda$[%]			
	1.4	20	1.4	20
Contrast at 3λ/D	5.0 10^{-5}	1.5 10^{-4}	1.4 10^{-6}	1.2 10^{-5}
Contrast at 12λ/D	2.3 10^{-6}	3.5 10^{-6}	2.1 10^{-7}	2.8 10^{-7}
Contrast at 20λ/D	1.2 10^{-6}	1.8 10^{-6}	1.0 10^{-7}	1.3 10^{-7}
Total rejection	489	355	1000	641
Peak rejection	627	674	1058	788

Table 2. Summary of coronagraphic results and comparison with theory

5. Conclusion

We report on the development and laboratory experiments of an Apodized Pupil Lyot Coronagraph using microdots apodizer in the near-IR. Halftone dot process is a promising alternative solution to continuous metal layer deposition. Using a diffusion error algorithm, and optimized pixel size and fabrication techniques, we demonstrate impressive agreement between the specified and measured transmission profiles, as well as the achromatic behavior of this apodizer. Coronagraphic properties are consistent with the expected properties, and have already reached the SPHERE requirements. Achromaticity in H band is also demonstrated.

Additionally, pixellated apodizers do not produce a spatially-varying phase aberration which might compromise the coronagraphic effect at all radial distances.

We therefore conclude that microdots apodizers represent a very attractive solution for the APLC.

Although this study was carried out in a context of Research & Development for future near IR instruments on E-ELT it is already applicable to other instruments like SPHERE and other coronagraphs like the Dual Zone. Finally, we note that a RCWA analysis would be mandatory for a finer analysis of the pixel size with respect to the wavelength.

Acknowledgements. P.M would like to thank Sebastien Tordo and Christophe Dupuy from ESO for their helpful support with the ITC and metrology inspection. This activity is supported by the European Community under its Framework Programme 6, ELT Design Study, Contract No. 011863.

References

Aime, C. 2005, A&A, 434, 785
Aime, C., Soummer, R., & Ferrari, A. 2002, A&A, 389, 334
Aller Carpentier, E., Kasper, M., Martinez, P., et al. 2008, in Proceedings of the SPIE, (2008).
Beuzit, J.-L., Feldt, M., Dohlen, K., et al. 2006a, The Messenger, 125, 29
Beuzit, J.-L., Feldt, M., Dohlen, K., et al. 2007, in Proceedings of the conference In the Spirit of Bernard Lyot: The Direct Detection of Planets and Circumstellar Disks in the 21st Century. June 04 - 08, 2007. University of California, Berkeley, CA, USA. Edited by Paul Kalas., ed. P. Kalas
Beuzit, J. L., Mouillet, D., Moutou, C., et al. 2006b, in Tenth Anniversary of 51 Peg-b: Status of and prospects for hot Jupiter studies, ed. L. Arnold, F. Bouchy, & C. Moutou, 353–355

Boccaletti, A., Abe, L., Baudrand, J., et al. 2008, in Proceedings of the SPIE, (2008).
Born, M. & Wolf, E. 1989, Pergamon Press, Oxford
Dohlen, K. 2008, in Proceedings of the SPIE, (2008).
Dorrer, C. & Zuegel, J. D. 2007, Journal of the Optical Society of America B, 24, 1268
Enya, K., Abe, L., Tanaka, S., et al. 2008, A&A, 480, 899
Enya, K., Tanaka, S., Abe, L., & Nakagawa, T. 2007, A&A, 461, 783
Floyd, R. W. & Steinberg, L. 1976, J. Soc. Inf. Disp. 17, 7577 (1976)
Jacquinot, P. & Roisin-Dossier, B. 1964, Prog. Opt., 3, 29
Kasdin, N. J., Vanderbei, R. J., Spergel, D. N., & Littman, M. G. 2003, ApJ, 582, 1147
Kasper, M., Beuzit, J.-L., Verinaud, C., et al. 2008, in Proceedings of the SPIE, (2008).
Kuchner, M. J. & Traub, W. A. 2002, ApJ, 570, 900
Lyot, B. 1939, MNRAS, 99, 580
Macintosh, B., Graham, J., Palmer, D., et al. 2006, in Presented at the Society of Photo-Optical Instrumentation Engineers (SPIE) Conference, Vol. 6272, Advances in Adaptive Optics II. Edited by Ellerbroek, Brent L.; Bonaccini Calia, Domenico. Proceedings of the SPIE, Volume 6272, pp. 62720L (2006).
Martinez, P., Boccaletti, A., Kasper, M., Baudoz, P., & Cavarroc, C. 2007, A&A, 474, 671
Martinez, P., Boccaletti, A., Kasper, M., et al. 2008a, in Submitted in A&A (2008)
Martinez, P., Vernet, E., Dorrer, C., et al. 2008b, in Proceedings of the SPIE, (2008).
Nisenson, P. & Papaliolios, C. 2001, ApJ, 548, L201
Oppenheimer, B. R., Digby, A. P., Newburgh, L., et al. 2004, in Presented at the Society of Photo-Optical Instrumentation Engineers (SPIE) Conference, Vol. 5490, Advancements in Adaptive Optics. Edited by Domenico B. Calia, Brent L. Ellerbroek, and Roberto Ragazzoni. Proceedings of the SPIE, Volume 5490, pp. 433-442 (2004)., ed. D. Bonaccini Calia, B. L. Ellerbroek, & R. Ragazzoni, 433–442
Soummer, R. 2005, ApJ, 618, L161
Soummer, R., Aime, C., & Falloon, P. E. 2003a, A&A, 397, 1161
Soummer, R., Dohlen, K., & Aime, C. 2003b, A&A, 403, 369
Ulichney, R. 1987, The MIT Press.
Ulichney, R. 1988, Proc. IEEE, vol. 76, 1, 56-79 (1988)
Vanderbei, R. J., Kasdin, N. J., & Spergel, D. N. 2004, ApJ, 615, 555
Vanderbei, R. J., Spergel, D. N., & Kasdin, N. J. 2003, ApJ, 590, 593
Vernet, E., Kasper, M., Vérinaud, C., et al. 2006, in Advances in Adaptive Optics II. Edited by Ellerbroek, Brent L.; Bonaccini Calia, Domenico. Proceedings of the SPIE, Volume 6272, pp. 62722K (2006).

Microdots pupil apodizers properties characterization – Research Note –

Astronomy & Astrophysics manuscript no. microdots2
October 20, 2008

Microdots pupil apodizer properties characterisation *(Research Note)*

P. Martinez[1], C. Dorrer[2], and M. Kasper[1]

[1] European Southern Observatory, Karl-Schwarzschild-Strasse 2, D-85748, Garching, Germany
[2] Laboratory for Laser Energetics-University of Rochester, 250 East River Rd, Rochester, NY, 14623-USA

Preprint online version: October 20, 2008

ABSTRACT

Context. The Apodized Pupil Lyot Coronagraph (APLC) is the baseline coronagraphic device for future near-IR instruments on the European-Extremely Large Telescope for exoplanets direct detection. This concept features amplitude apodization in the entrance aperture and a small Lyot opaque mask in the focal plane. We present new near-IR laboratory results using binary apodizers – the so-called microdots apodizer – which represent a very attractive and advantageous solution for the APLC.
Aims. Pixellated apodizers introduce high frequencies that are function of the pixel size. The aim of this work is precisely to characterize the pixel size impact on the coronagraphic image. Estimation of both the noise intensity and its localization in the field of view is the objective of this study.
Methods. Microdots masks, consisting of array of pixels that are either opaque or transparent, were manufactured by lithography of a light-blocking metal layer deposited on a transparent substrate. A set of 5 new masks has been designed with different pixel sizes, and tested in the near-IR.
Results. Pixellation noise has been revealed during the experiment. Localization of the noise in the coronagraphic image as well as intensity confirm theory predictions.
Conclusions. The physical properties of these microdots apodizer have been demonstrated in laboratory. Microdots apodizer is a suitable solution for any coronagraphs using pupil amplitude apodization if properly designed.

Key words. Techniques: high angular resolution –Instrumentation: high angular resolution –Telescopes

1. Introduction

Overcoming the contrast issue between bright astrophysical sources and sub-stellar companions is mandatory for direct detection and spectroscopy of extra-solar planets. To improve performance of exoplanet searches towards lower masses, ideally down to Earth-like planets, challenging contrast are required. In this context, a coronagraph used in conjonction with an XAO system can be a powerful tool to improve the sensitivity of an imaging system to faint structure surrounding a bright source. Efficient XAO systems are required to correct wavefront errors due to the atmospheric turbulence, while coronagraphs are designed to suppress or at least attenuate the starlight diffracted by the telescope.

So far, the Apodized Pupil Lyot Coronagraph (Aime et al. 2002; Soummer et al. 2003a, APLC) appears to be a major concept for any forthcoming planet-finder instruments for large ground-based telescopes (Martinez et al. 2007, 2008a).

The realization of high-contrast coronagraphic concepts requires the development of new technologies. APLC prototypes are currently being developed using different approaches and tested to validate the concept in laboratory conditions (Boccaletti et al. 2008; Martinez et al. 2008b; Thomas et al. 2008).

In this paper, we present near-IR laboratory results to characterize a new technology solution for apodizers manufacturing. In a former study (Martinez et al. 2008b, hereafter Paper I), we explored halftone dot process to generate an array of binary pixels, either transparent or opaque, where the density of opaque pixels is spatially varying. This technique aims at solving drawbacks of a continuous deposit of a metal layer with spatially varying thickness approach. Main advantages of a microdots apodizer are listed below: 1/ high accuracy of the profile, 2/ achromaticity, 3/ no exhibition of a spatially-varying phase, 4/ reproducibility. In Paper I, we reported that microdots apodizers exhibit blue noise properties (i.e high frequency noise), when designed for coronagraphy. Although, numerical simulations as well as theoretical predictions confirm pixellation noise in the coronagraphic image, its impact was found negligible during experiment since our first prototype (mask 1, hereafter) was designed to push this noise out of our field of view of interest at a deep contrast level. This was a result of a fine adjustment of the pixel size ($\sim 4.5\mu$m). Here, our purpose is precisely to investigate the pixellation noise properties using 5 new masks with same profile as mask 1, but by successively degrading the pixel size. The interest is twofold: 1/ confirm theory predictions on the physical properties of such devices with laboratory proofs, 2/ derive relevant informations to design any amplitude microdots apodization mask whatever the coronagraph. Sect. 2 briefly reminds microdots apodizer theoretical properties, while Sect. 3 describes the experiment as well as the manufacturing details of the new masks. In Sect. 4 we present and discuss results obtained in the experiment, and finally in Sect. 5 we draw conclusions.

Send offprint requests to: P. Martinez, martinez@eso.org

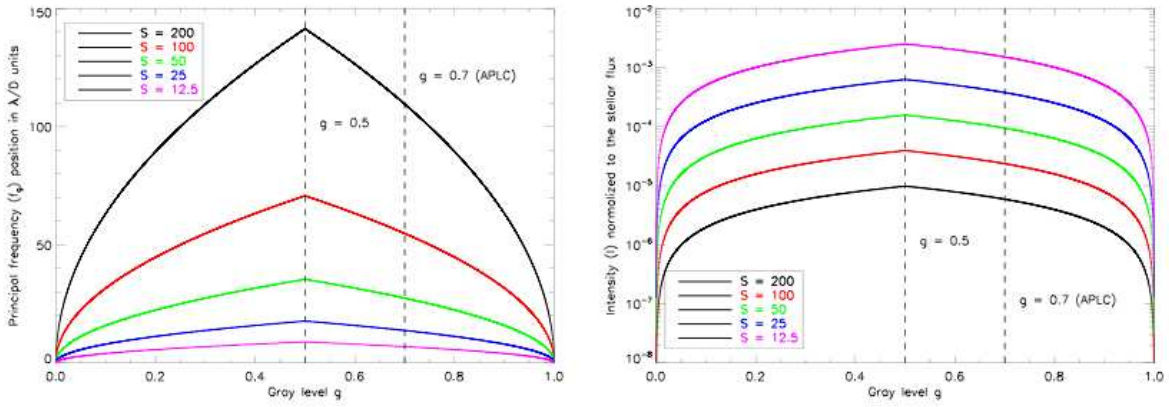

Fig. 1. *Left*: First order diffraction peak position (f_g in λ/D units) as a function of gray level g. *Right*: Speckles halo intensity I normalized to the reference star intensity as function of gray level g. In both plots, the APLC case ($g = 0.7$) is localized with dashed line.

2. Microdots apodizer theoretical properties

For the reader's convenience, we briefly remind microdots apodizer theoretical properties using same notations as defined in Paper I. A microdots apodizer is modeled as an aperiodic under-filled two-dimensional grating. Such device exhibits blue noise properties owing to the error diffusion algorithm used to calculate a distribution of pixels (i.e dots) that best approximates the required field transmission (Floyd & Steinberg 1976; Ulichney 1987; Dorrer & Zuegel 2007). The binary pattern produces an average gray level value ($g = \sqrt{T}$, i.e average amplitude transmission) from an apodizer profile with intensity transmission T. The resulting pattern spectral energy of such device is set by the minority pixels present on the device (i.e by g, non-metal pixels when $g < 0.5$ and by metal pixels conversely). The spectral energy therefore increases as the number of minority pixels increases, peaking at $g = 0.5$ (Ulichney 1987). In the precise case of square pixels (Ulichney 1988), the power spectrum of the pattern exhibits energy concentration around a first order diffraction peak (f_g) localized in the field of view in λ/D units as

$$f_g = \begin{cases} \sqrt{g} \times S & g \leq 1/2 \\ \sqrt{(1-g)} \times S & g > 1/2 \end{cases} \quad (1)$$

where S is the scalling factor, ratio between the pupil diameter (Φ) and the pixel size, i.e dot size (p). Higher order diffraction peaks are less relevant since out of the field of view when dots are small enough. Each order diffraction peaks are separated by S in λ/D units with S extent, i.e dots scatters light by diffraction and creates a 2D-sinus cardinal function halo in the focal plane.

In Paper I we present a simplified model for order-of-magnitude estimation of the pixellation noise intensity in coronagraphic systems (Dohlen 2008). The speckles halo in the coronagraphic image resulting from the non-regular dots distribution broaden the first order diffraction peak f_g with an intensity I_g defined as

$$I_g = \begin{cases} g \times \frac{\pi}{4} \times \left(\frac{1}{S}\right)^2 & g \leq 1/2 \\ (1-g) \times \frac{\pi}{4} \times \left(\frac{1}{S}\right)^2 & g > 1/2 \end{cases} \quad (2)$$

Fig. 1 gathers high frequencies noise localization in the field, and intensity (normalized by the stellar flux), as function the gray level for the set of scaling factors (S) we used for prototyping. Decreasing the scaling factor, i.e increasing the pixel size, therefore moves closer the principal frequency with an increase of energy.

3. Experiment

3.1. Masks design and optical setup

The configuration of the apodizer profile is similar to that described in Paper I (4.5 λ/D APLC, $\Phi = 3mm$ due to constraints on our optical bench). The 5 new apodizer masks were fabricated by Precision Optical Imaging in Rochester, New York. Masks were fabricated using wet etch contact lithography of a regular Chrome layer ($OD = 4$) deposited on a BK7 glass substrate ($\lambda/20$ peak-to-valley), with antireflection coating for the H band (1.2 to 1.8μm, $R < 1\%$) on their back faces. Mask 1 had a scaling factor of 500 corresponding to 6μm pixels grid, but finally appear smaller (4.5μm), as a predictable result of the manufacturing process. Hereafter mask 2, 3, 4, 5, and 6, have a scaling factor of 200, 100, 50, 25 and 12.5 corresponding to 15, 30, 60, 120 and 240μm pixel size, respectively. Therefore, pixels size, i.e dots size, increases by a factor 2 mask by mask. Table 1 gathers all the masks characteristics and noise properties predicts by theory (Eq. 1 and 2).

The experiment configuration is similar to that described in Paper I. The optical setup is designed to simulate the 8-m VLT pupil and to operate in the near-infrared (H-band). The Strehl ratio of the bench is $\sim$ 94%. The IR camera used (the Infrared Test Camera) is designed to reach a pixel scale of 5.3 mas. The APLC pupil-stop is also similar to that of paper I and remains the same during the experiment. The pupil-stop features outer VLT-pupil diameter reduction and oversized central obscuration while the spider vanes are increased by a factor 4. The 4.5 λ/D Lyot mask is installed at a F/48.4 beam.

3.2. Inspection of the apodizers

Metrology inspection of these 5 masks has been made using a Shadowgraph (×50, see left column of Fig. 2). Chrome dots size have been determined to 15 - 29 - 57 - 119 and 240 μm $\pm 1\mu$m

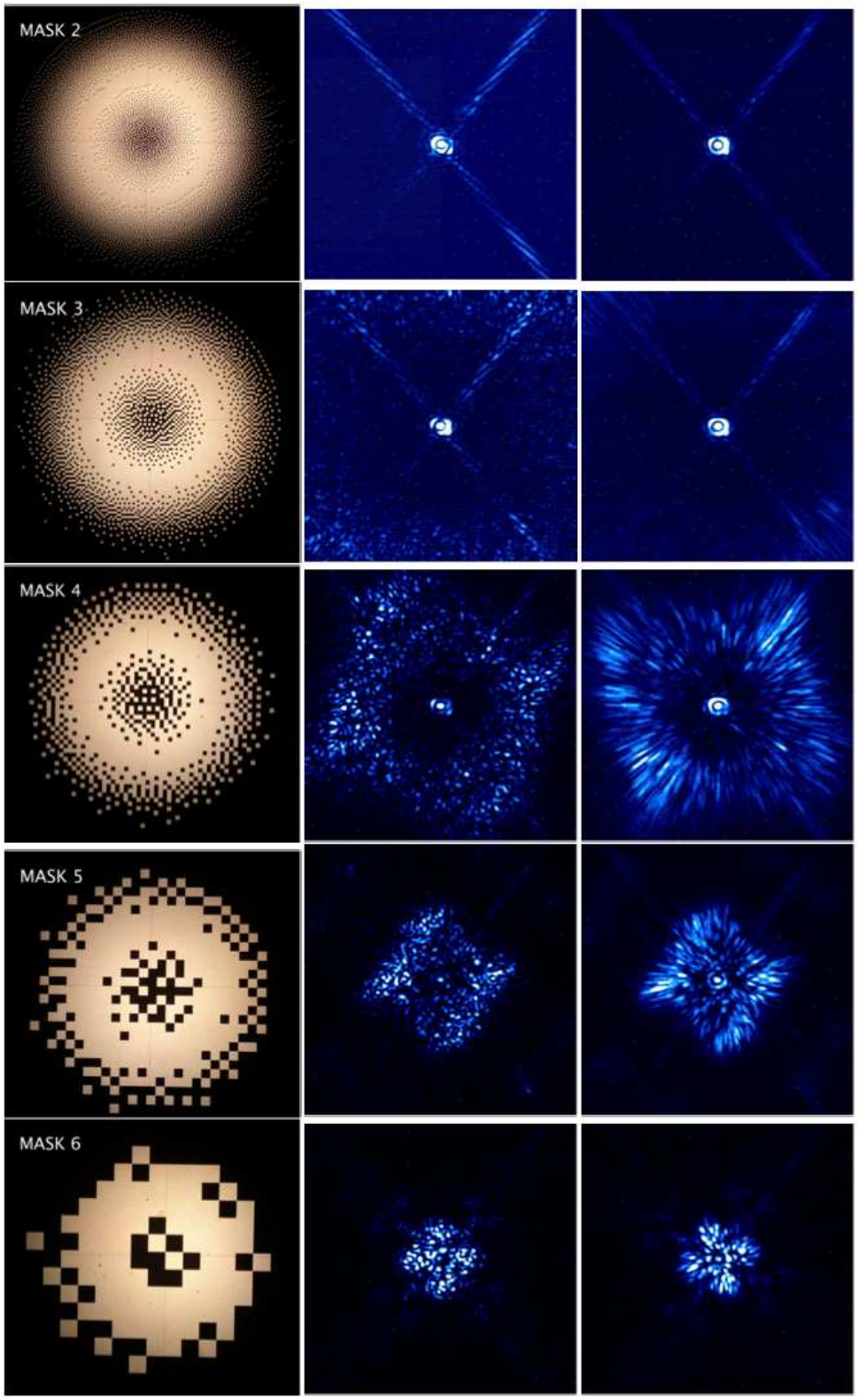

Fig. 2. Left: Shadowgraph inspection (×50) of mask 2 to 6 (top row to bottom row), middle: infrared coronagraphic images ($\Delta\lambda/\lambda$ = 1.4%), and on the right: infrared coronagraphic images ($\Delta\lambda/\lambda$ = 20%).

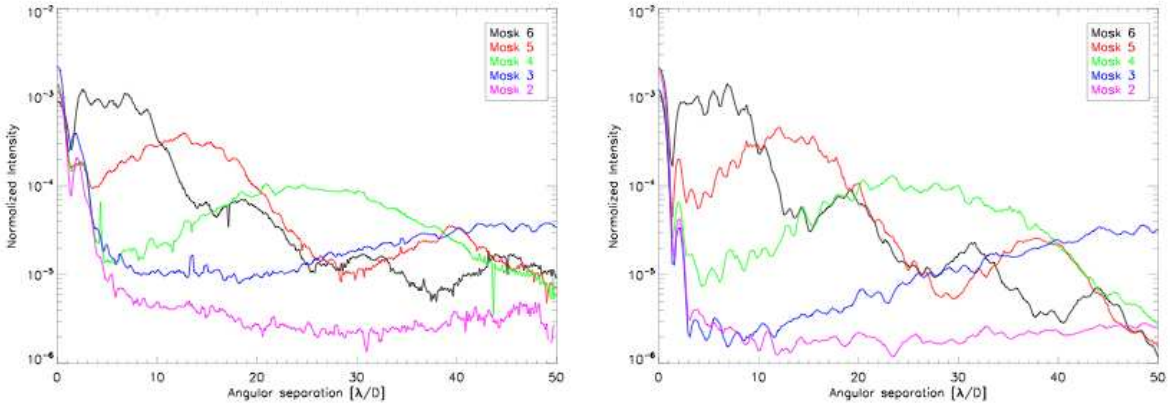

Fig. 3. Summary of coronagraphic radial profiles ($\Delta\lambda/\lambda = 1.4\%$) for mask 2 to mask 6, profiles are azimuthally averaged. *Left*: recorded on the bench, *Right*: simulations assuming bench conditions.

Prototype	S	p [μm]	High frequency noise angular position (f_g [λ/D])		High frequency noise intensity (I_g)	
			Theory	Experiment	Theory	Experiment
Mask 2	200	15	107	-	5.7×10^{-6}	-
Mask 3	100	30	54	53	2.3×10^{-5}	3.3×10^{-5}
Mask 4	50	60	27	25	9.1×10^{-5}	9.9×10^{-5}
Mask 5	25	120	13	13	3.6×10^{-4}	3.5×10^{-4}
Mask 6	12.5	240	7	7	1.4×10^{-3}	1.1×10^{-3}

Table 1. Summary of theory and laboratory measurements of the pixellation noise properties (localization in the field and intensity).

for mask 2 to 6 respectively. Unlike mask 1, mask 2 to 6 designs were not numerically pre-compensated to avoid an increase of transmission – as a result of a reduction of the metal dots during the wet-ech lithography process – since dot size was less critical than for mask 1.

The spatially-resolved transmissions of each apodizers has been measured. An iris in the far field has been used to obtain the low-frequency component of each mask to verify the global shape (i.e the symmetry). Accuracy of the profile is about 3-5% in near-IR (achromaticity has been demonstrated with mask 1 in Paper I along J and H-band). Images have been recorded without the iris as well. As the pixel size increases from mask 2 to mask 6, the high-frequency contents of the recorded images becomes predominant. The evaluation of the impact of the high-frequency contents at the coronagraphic image level is precisely the objective of this paper.

4. Results and discussion

Coronagraphic images recorded on the bench using masks 2 to 6 are presented in Fig. 2 (central column: $\Delta\lambda/\lambda = 1.4\%$, right column: $\Delta\lambda/\lambda = 20\%$). Speckles are clearly visible as well as speckle elongation when a broadband filter is used (right column). Qualitatively, reducing the pixel size (from mask 6 to mask 2) moves further away the first order diffraction halo. When the first order diffraction halo is away enough from the central core of the PSF, a usable field of view cleaned of speckles appears and reveals the residual diffraction from the pupil (spider vane diffraction spikes).

Coronagraphic profiles obtained with each masks are presented on Fig. 3 (left), and can be compared to simulations (right). Simulations assumed perfect microdots apodizers and bench conditions (VLT-like pupil, same bandwidth and similar Strehl ratio). In Table 1 we compare the intensity and localization of the first order diffraction halo measured and predicted by Eq. 1 and Eq.2. The intensity has been measured on the halo peak. In the following, we successively discuss results obtain with each masks:

Mask 6 – The pixel size is 240μm (S = 12.5). The black curve of Fig. 3 (left) revealed several order diffraction peaks broadened by speckles. The first order diffraction peak localization as well as its peak intensity are consistent with theory (Table 1). The first peak is localized at $S/2$ (i.e 7 λ/D) with 1.1×10^{-3} intensity (normalized to the stellar flux). The 4 diffraction peaks revealed are separated by ~S factor (i.e 12.5 λ/D) and are localized at $S/2, 3S/2, 5S/2$ and $7S/2$ with extent in the order of S in λ/D.

Mask 5 – The pixel size is 120μm (S = 25). Here, two order diffraction peaks are observable (Fig. 3 (left), red curve) at $S/2$ and ~ $3S/2$ (i.e 13 and 39λ/D respectively). First order diffraction peak halo intensity is consistent with theory.

Mask 4 – The pixel size is 60μm (S = 50). In that case only the first order diffraction peak is revealed at $S/2$ (i.e 25 λ/D, Fig. 3, (left) green curve). Intensity is fitting theory.

Mask 3 – The pixel size is 30μm (S = 100). Only the rise to the first order diffraction peak is visible (peaking at ~ $S/2$, blue curve) with intensity consistent with theory.

Mask 2 – The pixel size is 15μm (S = 200). No diffraction peaks have been observed (pink curve, Fig. 3 (left)). The first one is theoretically localized at 107λ/D from the center core of the coronagraphic image, and therefore it is out of the accessible field of view. For that reason no evaluation of the intensity is possible. However, the halo seems to start its rise to the first order diffraction peak (i.e the halo level is increasing).

All the tests performed with these new masks but mask 2 confirmed Eq. 1 and Eq. 2. We carried out the same test with a broadband filter in H ($\Delta\lambda/\lambda$ = 20%), and we did not observed any modification of the behavior. Comparison with simulated coronagraphic profiles (Fig. 3,right) presents a slight discrepancy, mainly for mask 2 and 3, at small angular distance without impacting the halo intensity and position. This discrepancy can be explained as the result of profile errors or apodizer alignment as discussed in Paper I.

Theory predictions are therefore confirmed. The simplify model used for order-of-magnitude estimation of the pixellation noise intensity in coronagraphic image is representative of the APLC situation.

Considering the validity of Eq. 1 and Eq. 2, resumed in Fig. 1, we can therefore properly designed microdots apodizer (i.e select pixel size) for any coronagraph concepts featuring amplitude pupil apodization. The selection of the pixel size must be defined by pushing out of the field of interest the first order diffraction halo (Eq. 1) and by reducing its intensity (Eq. 2) to avoid any limitations imposed even by the rise to the speckle halo. The apodizer amplitude transmission (g) as well as the sampling factor (S) drive this choice. Ideally, going to very small pixels size improves the accuracy of the profile transmission (sampling problem) but when the pixel size is comparable to the wavelength of light, the transmission is affected by plasmons (Genet & Ebbesen 2007; Huang & Zhu 2007).

5. Conclusion

We report additional development and laboratory experiments of microdots apodizers for the Apodized Pupil Lyot Coronagraph. Testing different pixel size configurations allows to confirm theoretical predictions of paper I. We demonstrate agreement between laboratory measurements and theoretical models.

Therefore, coronagraphic properties of microdots apodizer are confirmed, and any coronagraphs that require amplitude pupil apodization can be properly designed. Furthermore, the microdots technique will be the baseline approach for the apodizer of the Apodized Pupil Lyot Coronagraph for EPICS (Kasper et al. 2008) as well as for GPI (Macintosh et al. 2006).

In addition, we are currently extending the technique to the manufacture of Band-Limited masks (Kuchner & Traub 2002). Results of this development will be present in a forthcoming paper.

Acknowledgements. This activity is supported by the European Community under its Framework Programme 6, ELT Design Study, Contract No. 011863.

References

Aime, C., Soummer, R., & Ferrari, A. 2002, A&A, 389, 334
Boccaletti, A., Abe, L., Baudrand, J., et al. 2008, in Proceedings of the SPIE, (2008).
Dohlen, K. 2008, in Proceedings of the SPIE, (2008).
Dorrer, C. & Zuegel, J. D. 2007, Journal of the Optical Society of America B, 24, 1268
Floyd, R. W. & Steinberg, L. 1976, J. Soc. Inf. Disp. 17, 7577 (1976)
Genet, C. & Ebbesen, T. W. 2007, Nature, 445, 39
Huang, C.-P. & Zhu, Y.-Y. 2007, 2007
Kasper, M., Beuzit, J.-L., Verinaud, C., et al. 2008, in Proceedings of the SPIE, (2008).
Kuchner, M. J. & Traub, W. A. 2002, ApJ, 570, 900
Macintosh, B., Graham, J., Palmer, D., et al. 2006, in Presented at the Society of Photo-Optical Instrumentation Engineers (SPIE) Conference, Vol. 6272, Advances in Adaptive Optics II. Edited by Ellerbroek, Brent L.; Bonaccini Calia, Domenico. Proceedings of the SPIE, Volume 6272, pp. 62720L (2006).
Martinez, P., Boccaletti, A., Kasper, M., Baudoz, P., & Cavarroc, C. 2007, A&A, 474, 671
Martinez, P., Boccaletti, A., Kasper, M., et al. 2008a, in A&A (2008)
Martinez, P., Dorrer, C., Aller Carpentier, E., et al. 2008b, in A&A (2008)
Martinez, P., Vernet, E., Dorrer, C., et al. 2008c, in Proceedings of the SPIE, (2008).
Soummer, R. 2005, ApJ, 618, L161
Soummer, R., Aime, C., & Falloon, P. E. 2003a, A&A, 397, 1161
Soummer, R., Dohlen, K., & Aime, C. 2003b, A&A, 403, 369
Thomas, J. S., Soummer, R., Dillon, D., et al. 2008, in Proceedings of the SPIE, (2008).
Ulichney, R. 1987, The MIT Press.
Ulichney, R. 1988, Proc. IEEE, vol. 76, 1, 56-79 (1988)

Phase and Lyot-type coronagraphs for HOT: prototyping and first laboratory results

Phase and Lyot-type coronagraphs for the High Order Testbench: prototyping and first laboratory results

Patrice Martinez[*a, b, e], Elise Vernet[a], Christophe Dorrer[c], Emmanuel Aller Carpentier[a], Anthony Boccaletti[b, e], Markus Kasper[a], Jacques Baudrand[b, e], Christine Chaumont[d, e]

[a] European Southern Observatory, Adaptive optics Department – Telescope System Division - Karl Schwarzschild Str. 2 - D-85748 Garching Bei München - Germany

[b] Observatoire de Paris Meudon (LESIA), 5 place Jules Janssen, 92190 Meudon, France

[c] Laboratory for Laser Energetics-University of Rochester, 250 East River Rd, Rochester, NY, 14623-USA

[d] Observatoire de Paris Meudon (GEPI), 5 place Jules Janssen, 92190 Meudon, France

[e] Groupement d'intérêt scientifique PHASE (Partenariat Haute résolution Angulaire Sol Espace)

ABSTRACT

We report laboratory development of coronagraphic devices to be implemented on the High Order Testbench (HOT) to assess intensity reduction between them at a high Strehl ratio regime. The high order test bench implements extreme adaptive optics with realistic telescope conditions reproduced by star and turbulence generators. A 32×32 actuator micro deformable mirror, one pyramid wave front sensor, one Shack-Hartmann wave front sensor and the ESO SPARTA real-time computer. This will enable characterization and comparative study of different types of coronagraphs in realistic conditions. We have developed several prototypes of promising coronagraphs concepts: Four Quadrants Phase Mask[1] (FQPM), Lyot[2] coronagraphs and Apodized Pupil Lyot Coronagraph[3] (APLC). We will describe the design of the IR coronagraphic path on HOT, prototyping processes used for each coronagraph and discuss quality control and first results obtained on a IR coronagraphic testbench (Strehl ratio ~ 94%). Finally, we will present our experiment plan and future coronagraph developments.

Keywords : high angular resolution, Extreme adaptive optics, coronagraphy

INTRODUCTION

A coronagraph used in conjonction with AO system can improve the sensitivity of an imaging system to faint structure surrounding a bright source. These devices block the core of the image of an on-axis source and suppress the bright diffraction rings and halo, removing light that would otherwise reduce the dynamic range of the imaging. This enables faint off-axis objects to be observed. The state-of-the-art of coronagraphy has impressively envolved during the last ten years. Coronagraphs are now able to provide a very large on-axis exctinction as demonstrated in laboratory conditions. But their capabilities during sky observations are damped by the large amount of residual phase aberrations that are left uncorrected by the AO system. Coronagraphy is a mandatory technique to suppress on-axis starlight, but a coronagraph can only reduce the contribution of the coherent part of the light. Hence, their capabilities on sky are in strong relation with AO efficiencies.

Any high contrast instrument concepts for large ground-based telescopes such as SPHERE[4], GPI[5] or EPICS[6] for the future E-ELT use a combination of XAO and a coronagraph.

Therefore, implementation of coronagraphs on HOT provide an ideal environment to assess the contrast delivered by each device considering the diffraction by the edges of the pupil and the residual phase aberrations that are leaking through the AO system. We have produced several coronagraphs to compare them in this advantageous environment. Hopefully, outputs of this comparison will present the possibility to extend this study to the case of Extremely Large Telescopes.

* martinez@eso.org, phone: +498932006398

1. OPTICAL SETUP OVERVIEW

The High Order Testbench (HOT, see Fig. 1) implements an XAO system on the MACAO (Multi Application Curvature Adaptive Optics) test bench which includes star and turbulence generators to mimic realistic conditions at a telescope. The bench is installed at ESO/Garching. Responsibilities are split between ESO (DM, the optical setup, and the SHWS RTC), Durham University (SHS) and Arcetri (PWS including its dedicated RTC).
In this section we will further discuss the IR coronagraphic optical path of HOT, more details on AO common path optics, optical quality, turbulence generator and phase screens, micro deformable mirror, SHWS, PWS and laboratory demonstration are presented in separate papers[7,8].

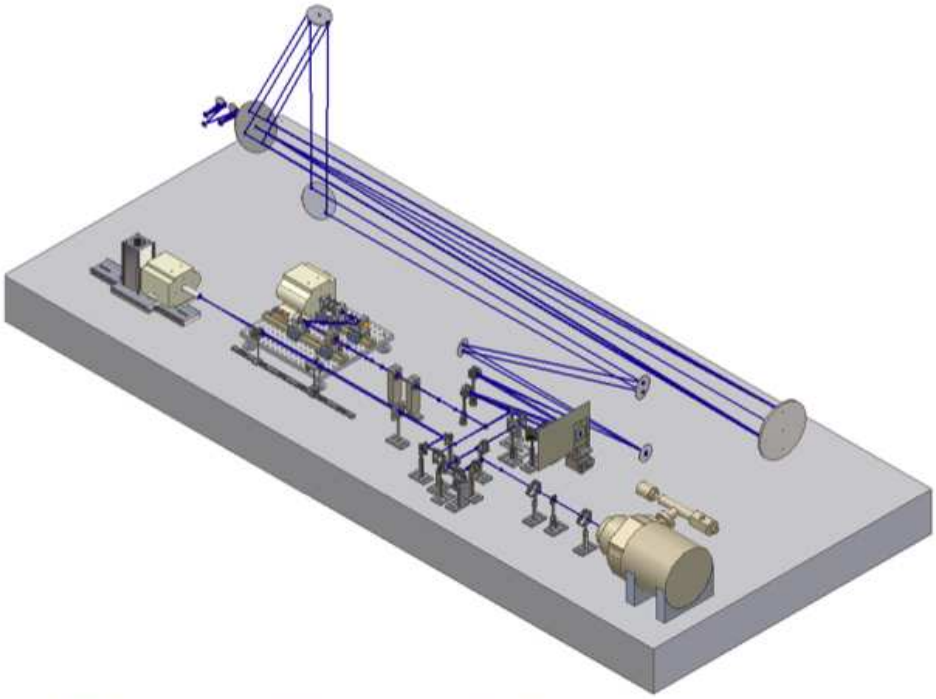

Figure 1 : Shematic HOT setup on the MACAO testbench including IR coronagraphic path

To avoid any delay in the AO implementation/work on HOT, the IR coronagraphic path has been mounted and installed on a separate bench. So, this separate IR coronagraphic test bench mimics the IR coronagraphic optical path of HOT. The optical system was designed using the optics program ZEMAX. The optical setup is designed to simulate the 8 m VLT pupil. It does so by scaling the 8 m VLT pupil to 3mm ± 0.002 mm using a laser-cut stainless steel sheet. The central obscuration is scaled to 0.47 mm ± 0.002 mm. The spider vanes thickness has an incorrect value (60 μm instead of 15 μm) in our first pupil mask. This will somehow impact coronagraphic tests since most of the time pupil stops have oversized spider vanes to get rid of misalignement problems (APLC) or to block light diffracted by the spider vanes of the pupil that is leaking through the coronagraph and reappears in the relayed pupil (FQPM, Lyot). Update of the pupil mask with 15-micron vanes has been ordered and is currently tested.
The test bench uses an F/48.4 at the coronagraphic focal plane. Our coronagraphic system consists of λ/10 IR achromatic doublets. We use a broadband white-light source combined either with an IR narrow filter (R = 70, central wavelength of 1.64 μm, BW = 0.024nm with a peak transmission of 64.4%, checked with an FTS) or multiple choice of IR filter, installed inside the IR camera and accessible through a filter wheel, in J, H, and K band. In practice, most of the time we use a broadband H filter (center at 1.6 μm, R = 5) combined or not with the H narrow external one presented previously.
The camera used is the ITC (Infrared Test Camera), cooled at 103 K degree with a vacuum of 10^{-5} mbar. The Strehl ratio was evaluated at 94%. It was determined by measuring the peak level of an experimental PSF divided by its total flux, divided by the peak level of a theoretical PSF divided by its total flux. The theoretical PSF is created by performing the

forward fast Fourier transform of the autocorrelation of an oversampled and uniformly illuminated entrance pupil image from our telescope pupil mask (Fig. 2, left). Our pupil and focal planes masks are mounted on (x, y, z, θ) stages to minimize positioning error.

2. CORONAGRAPH PROTOTYPING

Several coronagraph concepts have been developed in the frame of WP 04500 of ELT design study such as the Four Quadrant Phase Mask, non-apodized Lyot coronagraphs and the Apodized Pupil Lyot Coronagraph. In the following, we describe the main characteristics of these devices and manufacturing considerations as well.

2.1 Four Quadrants Phase Mask

As a baseline, the FQPM chosen for HOT are monochromatic. Achromatic devices (either FQPMs using half-waves plates[10] or AGPM[11]) will be implemented on HOT in the framework of EPICS phase A in the next future. FQPM was developed by GEPI (Galaxies Etoiles Physique et Instrumentation) from Paris Observatory.

Derived requirements of the mask – The manufactured FQPM must be as close to the theoretically perfect FQPM as possible to reach the expected performance. One can expect not to be limited by the intrinsic manufactured defects of the component. To do so, the manufactured FQPM as been specified to deliver performance that correspond to the case where the limitation only comes from the diffraction by the edges of the pupil (VLT-like pupil at the entrance pupil of HOT). In this ideal case, uncorrected aberrations that are leaking through the AO system are not considered but will decrease the FQPM efficiency when implemented on HOT. Accuracy of critical parameters that GEPI has reached are detailed hereafter and presented in Table 1 where we compare performance imposed by manufactured defects to ideal performance expected when the Strehl ratio is 100%. A microscope inspection of the quadrants is presented in Fig. 3. The total nulling of the coronagraph refers to the total rejection rate (τ): ratio of the total integrated intensity with and without the FQPM.

Operating wavelength precision – The monochromatic FQPM is manufactured by engraving of two opposite quadrants on an optical medium. The thickness of the FQPM step directly defines the optimal wavelength λ_0 for which the attenuation is the best. A difference between the optimized and the working wavelength λ reduces the attenuation of the FQPM[12]. A dedicated visible spectroscopic bench was used at LESIA (Laboratoire d'Etudes Spatiales et d'Instrumentation en Astrophysique, from Paris Observatory) to measure the thickness of the FQPM step[12]. A precision of less than 3% was required on the FQPM step thickness, GEPI has reached a depth accuracy of 0.2% (see Table 1).

FQPM transition precision – Ideally the transition between the four quadrants must be infinitely small. Departure from this ideal case decreases the capability of the real device[12]. Microscopic inspection of the manufactured FQPM (Fig. 3, right) shows that the transition quality is less then 1 μm (2 μm peak-to-peak transitions). The impact of this defects is estimated in Table 1. At this level, the efficiency of the FQPM will be set by external parameters (diffraction of the pupil).

Chromaticity – The chosen FQPM is monochromatic. The effect of chromaticity has been defined in previous paper[12]. The selection of a filter resolution is then critical. In Table 1, attenuation reachable with IR filter resolution of 70 and 5 are presented. For the first one, having a monochromatic device is not a limiting factor, compared to telescope defects. For the filter resolution of 5, only a detailed study including aberrations left by the AO system can determine whether or not chromaticity will be dominant.

Parameters	**Achievable total nulling (τ)**	**Theoretical total nulling Strehl = 100% / VLT-like pupil**
Step thickness : 0.2 [%]	120668	140 (1300 peak attenuation)
Transition : 1 [μm]	1890 (R = 70, F/D = 48.4)	
Chromaticity (R = 70)	23830	
Chromaticity (R = 5)	121	

Table 1 Manufacturing defects and chromaticity impact on the FQPM efficiency

2.2 Lyot Coronagraphs

A large range of Lyot mask diameters have been manufactured using wet etch lithography process on BK7 glass by Precision Optical Imaging (Rochester, NY, http://www.precisionopticalimaging.com). They are made by Cr deposit (+Al) to reach an OD of 6.0 at 1.65 microns. Nine different Lyot masks have been developed with diameter starting from 2.25 λ/D to 14.40 λ/D.
All these masks were deposited on the same glass substrate (λ/4) with AR coating on both faces (R<1%) and allows the selection of a different mask simply by translation along the x and y directions.
In parallel GEPI has produced individuals Lyot masks (4.5, 4.9, 7.5 λ/D) using Cr deposition (+Au) with the same requirements for the OD. In both case accuracy on the mask is close to 1 micron on the diameter and each mask are perfectly circular and clean (see Fig. 3, left). AR coating still needs to be done.

2.3 Apodized Pupil Lyot Coronagraph

General description – We adopt a 4.5 λ/D APLC configuration based on a previous sensitivity analysis[13]. For this coronagraph, manufacturing of the apodizer is an issue. So far, we explored two techniques : either using a continuous deposit (inconel , for instance) or binary pattern. For the latter, the apodizer is an array of binary pixels, as described hereafter. Since the continuous deposit process has not been succesful yet for our application, we will not go into deeper details on that process. However, details related to some devices produced and tested in the context of SPHERE are described in separate papers[14].

Lyot masks – The 4.5 λ/D hard-edge opaque Lyot mask has been fabricated by GEPI using precise mask pattern of about 1 μm accuracy (from Optimask). With the Chrome deposit (20 nm), Au deposit has been added (200 nm) to reach an OD of 6.0 at 1.65 μm. Antireflection coating still need to be done. A temporary lack of BK7 substrates lead to the use of fused silica substrates with an optical quality of λ/4 peak-to-valley (ptv).

Microdots apodizer – A binary pixellated apodizer has been designed and fabricated by Precision Optical Imaging using lithography techniques. Such apodizer is an array of pixels that are either blocking or letting through the incident light. It is fabricated by lithography of a light-blocking metal layer deposited on a transparent glass substrate. An error diffusion algorithm was used to optimize the distribution of pixels that best approximates the required field transmission[15,16,17]. This deterministic algorithm treats the pixels in a lexicographic order (i.e. top to bottom and left to right). It chooses the transmission of a given pixel of the apodizer (either 0 % or 100 %) by comparing the transmission required at this location to a 50 % threshold, i.e. the transmission is set to zero if the required transmission is smaller than 50 %, and to one otherwise. The induced transmission error is "diffused" to adjacent pixels that have not been processed yet by biasing the transmission required at the corresponding locations. This locally cancels the error of the binary optics relative to the required transmission. Such procedure has been used for gray-level reproduction with black-and-white printing techniques[16]. Shaping of coherent laser beams has also been demonstrated[17]. The error diffusion algorithm is advantageous because the binarization noise is "blue", i.e. the noise spectral density is only significant at high frequencies. This allows the accurate generation of gray levels and quickly spatially varying shaping functions. In the specific case of the design of a coronagraph, this allows to match the PSF of the binary apodizer to the required apodized PSF within some radial distance (in the control radius of the AO system). In other words, these high frequencies are pushed out of the AO corrrection domain.
An advantage of a pixellated apodizers versus continuous ones is that the apodizer does not have a spatial phase, while a continuous metal layer with spatially-varying thickness introduces a wavefront error that might compromise cancellation at all radial distances.
In general, better shaping results are obtained as the pixel size decreases[17], since this allows finer control of the local transmission and pushes the binarization noise to higher frequency. In theory, the radial distance under which a good match between the specified PSF and the binary shaper PSF is obtained can be increased by decreasing the pixel size. In practice, the shaping accuracy can be significantly impacted by the actual size and shape of the features of the binary apodizer. Considering the small size of the apodizer (3mm in diameter), it was chosen to use pixels on a 6 microns grid for the binary optics. The mask design was numerically precompensated by estimating the feature size which would be obtained after fabrication[17].

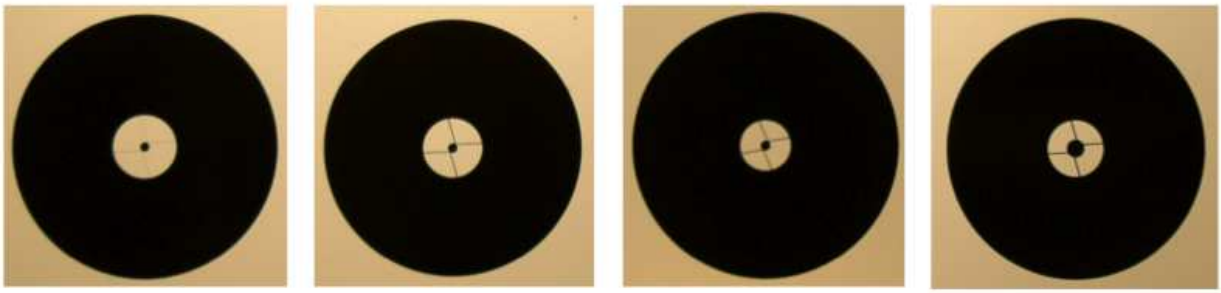

Figure 2 Several high frequencies filters (pupil stop) manufactured with laser-cuting (substrate diameter is 12.7 mm). From left to right : VLT pupil mask (updated), APLC pupil stop, Lyot pupil stop and FQPM pupil stop.

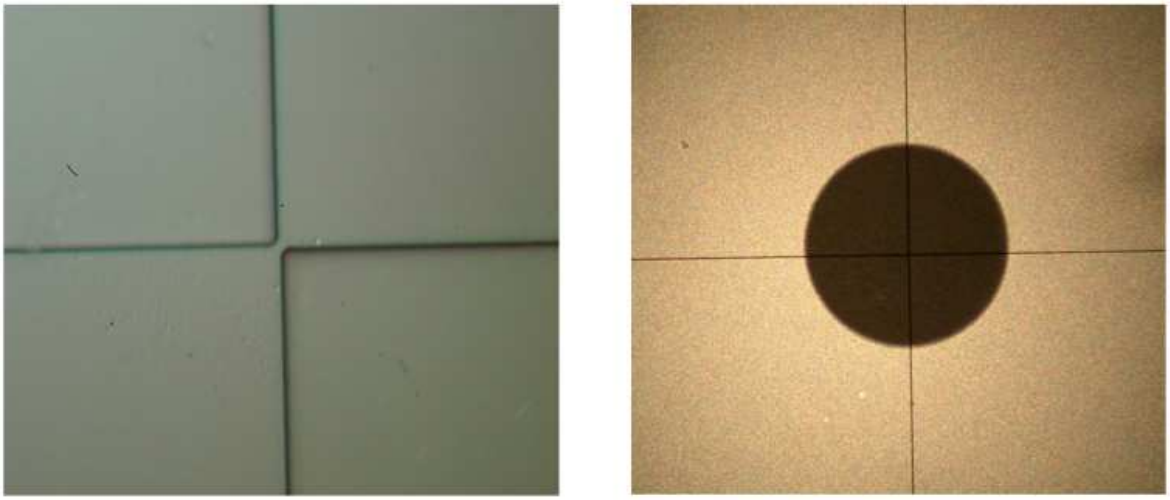

Figure 3 Left : microscopic inspection of the FQPM quadrants (x 50). Peak-to-peak transition is 2 μm and distance between two adjacent transitions is < 1 μm. Right : shadowgraph inspection of a 360 μm (diameter) Lyot coronagraph (x 50).

The shaper was fabricated using wet-etch contact lithography of a Cr layer (OD of 4.0) deposited on a glass substrate (BK7, λ/20). The measured transmission of the apodizer is plotted in Fig. 4, image of the apodizer using a shadowgraph is compared to simulation map as well. The fabricated part matches the field transmission specification within 2.5% (local profile, Fig. 4 bottom left) and 3% (azimutally average profile, Fig. 4 middle left), and has excellent circular symmetry (Fig. 4, bottom right).

3. LABORATORY RESULTS

Testing our laboratory coronagraphs is relatively recent and still on going. Hence, a comparison of these three devices considered as a baseline for HOT is premature. The intent of these tests on a separate bench was for quality inspection and validation before implementation on HOT. In this section, we will discuss the APLC quality/first results only.

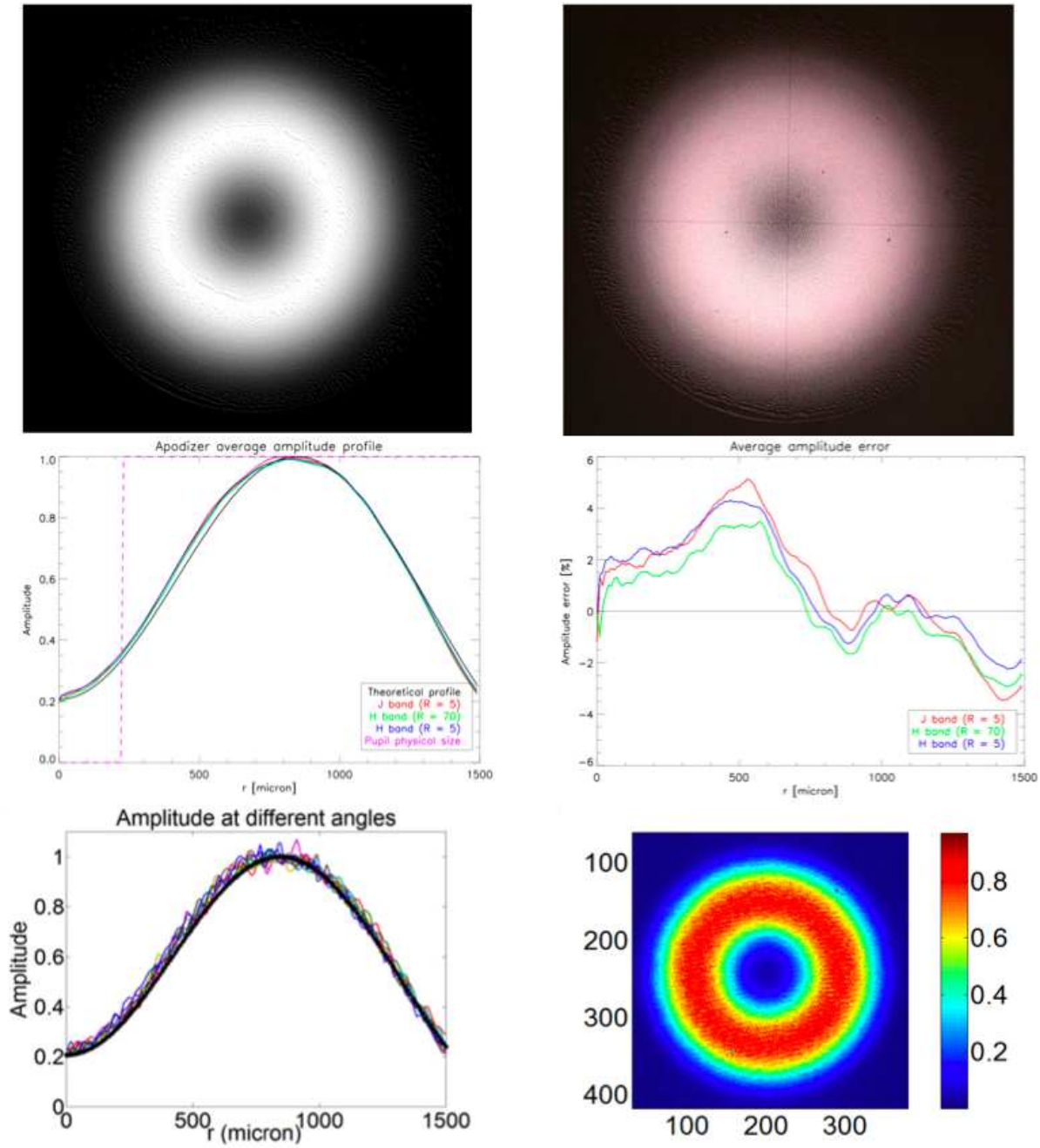

Figure 4 Upper row (left) : Simulation map with 5x5 microns dots, plotted as an example. Upper row (right) : shadowgraph inspection (x20) of the device (real dots are 4.5 x 4.5 microns determined using microscope inspection x100). Middle row (left) : Apodizer azimutally average profile (from center to the edges) using different filters (J, H and narrow H band) compared to specification. Middle row (right) : corresponding average amplitude error as function of the position using the same filters. Bottom row (left) : profile cut at 8 different angles (0, π/4, π/2…-π/4), Bottom row (right) : image of the apodizer with IR camera.

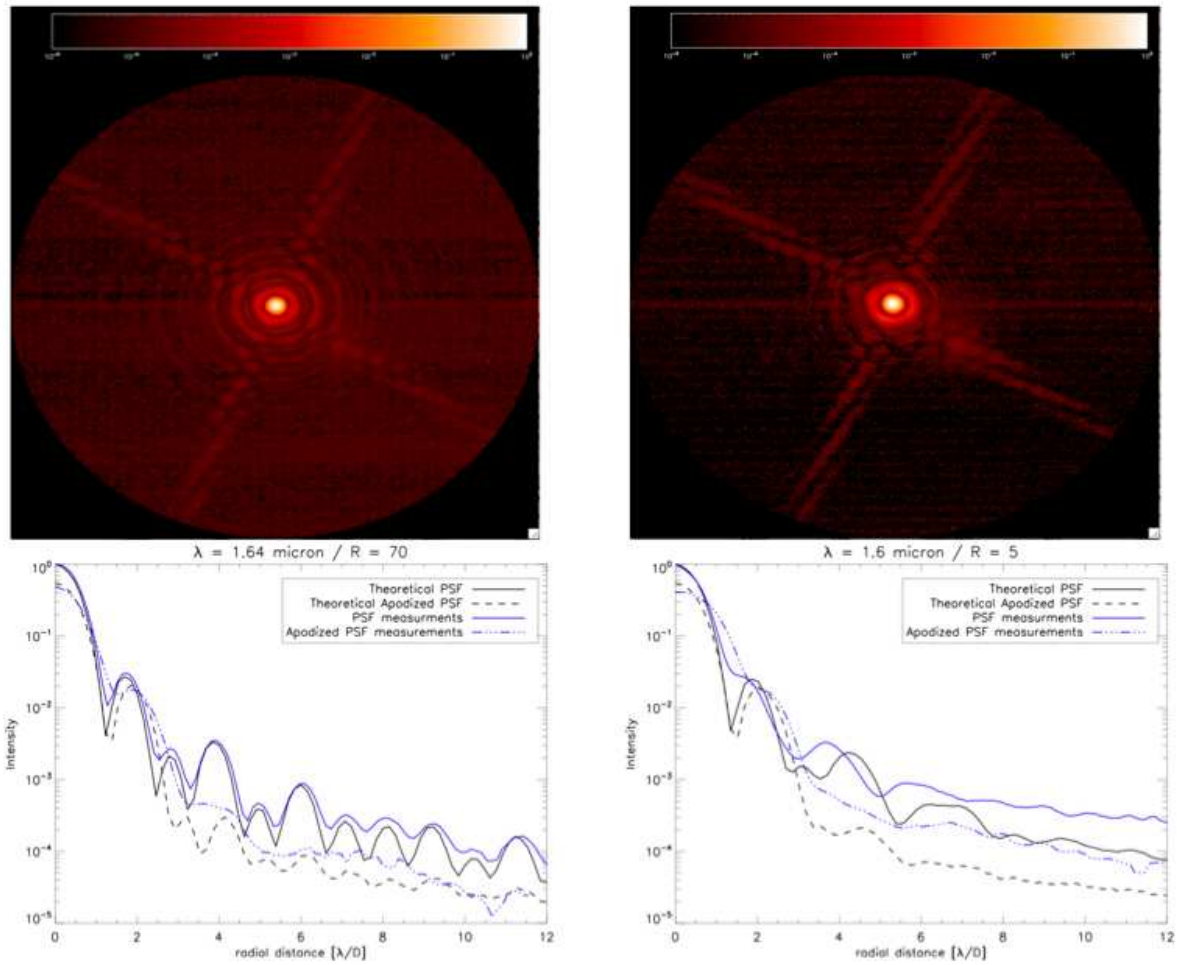

Figure 5 Top row (left) : VLT-like pupil PSF recorded on the bench (λ= 1.64 µm, R = 70). Top row (right) : VLT-like pupil apodized PSF in the same conditions. Bottom (left) : PSF and apodized PSF recorded on the bench (blue lines) compared to theoretical ones (black lines) with narrow H filter (λ= 1.64 µm, R = 70). Bottom (right) : Same measurements as previous ones but with broadband H filter (R=5).

Precise inspection of the quality of the apodizer has been realized in the laboratory (see Fig. 1) where we determined the size of the square chrome dots to 4.5 x 4.5 µm using a microscope. The accuracy on the profile is quite impressive, and is at about 3% of the specifications. Achromaticity of the profile is also demonstrated : error on the profile only increase about 2% from narrow H filter to broadband J filter. The requested accuracy was 5% at 1.64 µm indeed. So, even in J band the binary device is in the specifications.

In Fig. 5 we present data recorded on the bench. This first series of tests intends to demonstrate the correct behavior of the binary apodizer on the PSF. In other words, we do not place the Lyot coronagraph on the focal plane but only compare the PSF without apodizer to that with the apodizer. Qualitatively (Fig. 5 top pictures) it is demonstrated that the apodizer works well : the PSF's wings of the apodized PSF has been reduced in intensity and by energy concern one can see that there is more energy inside the core of the apodized PSF compare to the non-apodized one (exposure time are here identical). This behavior agrees well with the theoretical predictions.
Apart from some discrepancies between theory and measurements (Fig. 5, bottom, for R = 5 in H band), the gain between measured PSF and measured apodized PSF is fully consistent with theory. This results has been demonstrated in H with a narrow filter (R = 70) and with a broadband filter as well (R = 5).

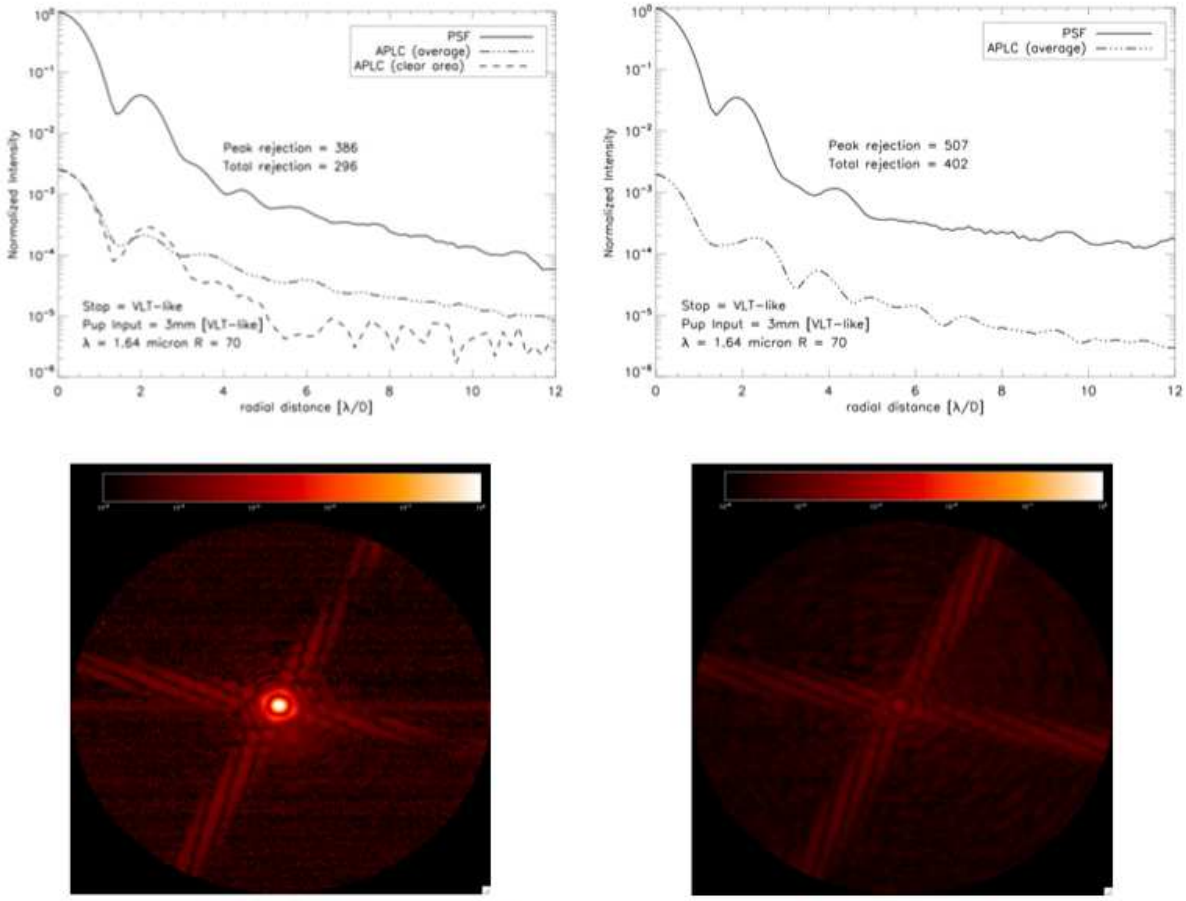

Figure 6 Top left: Results obtained at 1.64 μm (R = 70), full line is the apodized PSF, dot line is an azimutally average of the coronagraphic PSF and dash line is a cut in the clear area between the peak diffraction ot the spider vanes on the coronagraphic PSF. Pupil spider vanes are egal on the pupil mask and pupil stop (60 μm). Total rejection is 296 while peak rejection is 386. Top right : first run of test using the updated pupil mask (15 μm spider vanes) : total rejection is 402 and peak rejection is 507. Bottom : images recorded on bench using neutral density for the apodized PSF (left) and without on the coronagraphic PSF (right).

The discrepancy can be well understood since theoretical profile comes from simulation assuming perfect components (pupil mask, apodizer) and ideal propagation through the optical system.
The net effect of the binary apodizer on the PSF is then demonstrated and consistent with theory. Its achromaticity in H band is confirmed as well.

The second series of test strives to demonstrate the correct coronagraphic behavior of the whole system (binary apodizer + Lyot focal plane mask). In Fig. 6, results recorded on the bench are presented. As discussed in Sec. 1 our pupil mask has wrong value for the spider vanes thickness (60 μm instead of 15 μm). In the precise case of APLC, the pupil stop has also 60 μm spider vanes thickness. Hence, for this first run of test, alignment of the pupil stop with respect to the pupil mask is an issue and will matters the APLC performance. Alignment is made using a 633 nm laser and tuned at the end on the basis of the final IR image on the detector. Total nulling obtained is 296 and peak attenuation is 386. The discrepancy with theory (total nulling about 1100 and peak attenuation of 1200) can be well understood as misalignment errors in the system. In Fig. 7 (left) we assume in simulation (same condition as on the bench) a pupil shear of 0.4% and 1.2° of mismatch in rotation between the pupil mask and stop (spider orientation issue). The pupil shear refers to the misalignment of the pupil stop with the telescope pupil image (in x- and y-directions) and is express in % of the pupil

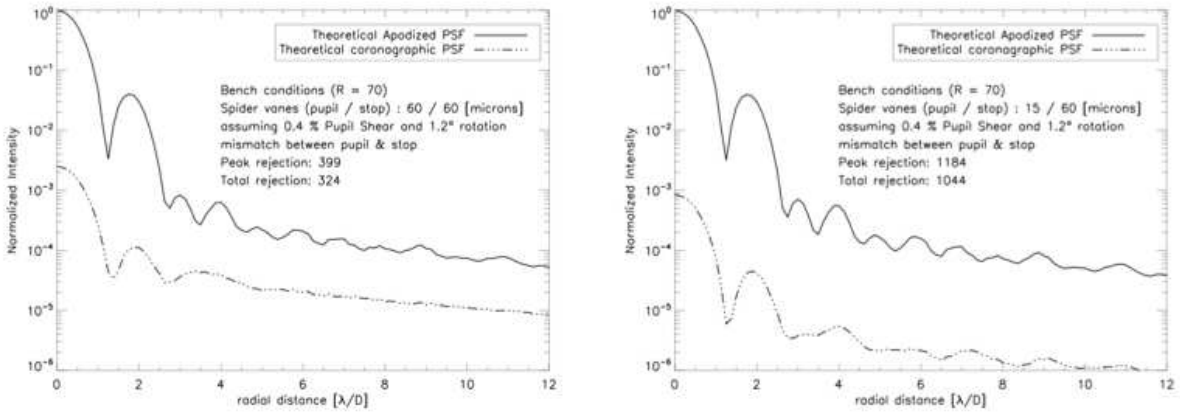

Figure 7 Results from simulation in the bench condition (R = 70 H band) assuming 0.4% pupil shear and 1.2° mistmatch between pupil and pupil stop. Left : pupil mask and pupil stop with same spider vanes thickness (as used in laboratory, i.e 60 µm). Right : pupil mask updated (spider vanes thickness : 15 µm) in same conditions.

diameter. So, 0.4% pupil shear is equivalent to 12 µm mismatch between the pupil and the stop, hence it is realistic with our experiment conditions. Results derived from simulation are equivalent to that on laboratory.
In Fig. 7 (right) same error conditions are assumed while the entrance pupil spider vanes thickness are updated to the correct value. As a result, performance is consistent with theory since in this case the spider vanes in the pupil stop appear oversized (x4) as expected to avoid any misalignment problem.

First run of test with the updated 15-micron spider vanes pupil mask leads to better performance (Fig. 6, top right) as expected. We are currently implementing a pupil imager system to get rid of misalignment limitations (pupil shear and spider vanes orientation mismatch). Performance will hopefully be improved in the next weeks.
These first tests already confirmed the good behavior of the coronagraphic effect of the APLC using a microdot apodizer.

4. TEST PLAN & FUTUR DEVELOPMENTS

The IR coronagraphic optical path has been installed recently on the High Order Testbench and hence we are currently implementing and testing most of the coronagraph components we developed. Coronagaph devices alignment is an issue and specific solutions for their optimization are currently investigated as pupil imager system for instance. These conditions will enable a realistic comparison between several coronagraphs combined with high order AO correction already started from a theoretical point of view[18]. Further investigations on other coronagraph prototyping will be adress (such as Band-limited coronagraph[19], for instance).
In the framework of EPICS Phase A, AGPM and Dual Zone prototypes[20] will be installed on HOT in 2009/2010. AGPM is currently developed in collaboration between LESIA, IAGL (Institut d'Astrophysique et de Géologie de Liège) and CSL (Centre Spatial de Liège), and is considered for EPICS and SPHERE also (as a possible update of achromatic FQPM devices). Dual Zone coronagraph is currently developed by LAM (Laboratoire d'Astrophysique de Marseille) and tested at LESIA in IR for SPHERE.
The High Order Testbench developed at ESO will be an ideal experiment bench for coronagraphy combined with AO. It will take advantage of using two different wavefront sensors such as SHWS and PWS, and make possible comparison between at least 6 different kinds of coronagraph (phase and amplitude-type concepts) in the next years.

5. ACKNOWLEDGEMENTS

The author would thanks Sebastian Tordo and Christophe Dupuis from ESO for helpful support with the ITC and metrology inspection. This activity is supported by the European Community under its Framework Programme 6, ELT Design Study, Contract No. 011863.

REFERENCES

[1] D. Rouan, P. Riaud, A. Boccaletti, Y. Clénet, and A. Labeyrie. The Four-Quadrant Phase-Mask Coronagraph. I. Principle. *PASP*, 112:1479–1486, November 2000.
[2] B. Lyot. The study of the solar corona and prominences without eclipses (George Darwin Lecture, 1939). *MNRAS*, 99:580–+, June 1939.
[3] R. Soummer. Apodized Pupil Lyot Coronagraphs for Arbitrary Telescope Apertures. *ApJ*, 618:L161–L164, January 2005.
[4] Beuzit, J.-L., Feldt, M., Dohlen, K., et al. 2006a, The Messenger, 125, 29
[5] Macintosh, B., Graham, J., Palmer, D., et al. 2006, in Presented at the Society of Photo-Optical InstrumentationEngineers (SPIE) Conference, Vol. 6272, Advances in Adaptive Optics II. Edited by Ellerbroek, Brent L.; Bonaccini Calia, Domenico. Proceedings of the SPIE, Volume 6272, pp. 62720L (2006).
[6] Kasper, M., Verinaud, C., Beuzit, J.-L., et al. 2007, in In the Spirit of Bernard Lyot: The Direct Detection of Planets and Circumstellar Disks in the 21st Century, ed. P. Kalas
[7] E. Vernet, M. Kasper, C. Vérinaud, E. Fedrigo, S. Tordo, N. Hubin, S. Esposito, E. Pinna, A. Puglisi, A. Tozzi, A. G. Basden, S. J. Goodsell, G. D. Love, and R. M. Myers. Extreme adaptive optics system optimization with the high order test bench. In *Advances in Adaptive Optics II. Edited by Ellerbroek, Brent L.; Bonaccini Calia, Domenico. Proceedings of the SPIE, Volume 6272, pp. 62722K (2006).*, July 2006.
[8] E. Aller Carpentier, M. Kasper, P. Martinez, E. Vernet, C. Vérinaud, E. Fedrigo, C. Soenke, S. Tordo, N. Hubin, S. Esposito, E. Pinna, A. Puglisi, A. Tozzi, F. Quiros, A. G. Basden, S. J. Goodsell, G. D. Love, R. M. Myers and M. Harrison, High order test bench for extreme adaptive optics system optimization, SPIE 2008
[9] D. Rouan, A. Boccaletti, P. Baudoz, C. Cavarroc, J. Baudrand, J.M Reess, The Coronagraphic Mode of MIRI/JWST, In the Spirit of Bernard Lyot: The Direct Detection of Planets and Circumstellar Disks in the 21st Century, 2007, ed. P. Kalas
[10] D. Mawet, P. Riaud, J. Baudrand, P. Baudoz, A. Boccaletti, O. Dupuis, and D. Rouan. The four-quadrant phase-mask coronagraph: white light laboratory results with an achromatic device. *A&A*, 448:801–808, March 2006.
[11] D. Mawet, P. Riaud, O. Absil, and J. Surdej. Annular Groove Phase Mask Coronagraph. *ApJ*, 633:1191–1200, November 2005.
[12] P. Riaud, A. Boccaletti, D. Rouan, F. Lemarquis, and A. Labeyrie. The Four-Quadrant Phase-Mask Coronagraph. II. Simulations. *PASP*, 113:1145–1154, September 2001.
[13] P. Martinez, A. Boccaletti, M. Kasper, P. Baudoz, and C. Cavarroc. Optimization of apodized pupil Lyot coronagraph for ELTs. *A&A*, 474:671–678, November 2007.
[14] A. Boccaletti, Prototyping achromatic coronagraphs for exoplanet characterization with SPHERE, SPIE 2008
[15] R. W. Floyd and L. Steinberg, An adaptive algorithm for spatial greyscale, J. Soc. Inf. Disp. 17, 7577 (1976).
[16] R. Ulichney, Digital Halftoning, The MIT Press.
[17] C. Dorrer and J. D. Zuegel, Design and analysis of binary beam shapers using error diffusion, J. Opt. Soc. Am. B 24, 1268-1275 (2007)
[18] P. Martinez et al. Comparison of coronagraphs for high contrast imaging in the context of Extremely Large Telescopes, *A&A* to be submitted 2008.
[19] M. J. Kuchner and W. A. Traub. A Coronagraph with a Band-limited Mask for Finding Terrestrial Planets. *ApJ*, 570:900–908, May 2002.
[20]] R. Soummer, K. Dohlen, and C. Aime. Achromatic dual-zone phase mask stellar coronagraph. *A&A*, 403:369–381, May 2003.

List of Figures

List of Tables

Bibliography

Bibliography

[1] L. Abe. Numerical Simulations in Coronagraphy. Part I. In C. Aime and R. Soummer, editors, *EAS Publications Series*, volume 12 of *EAS Publications Series*, pages 157–164, 2004.

[2] L. Abe, A. Domiciano de Souza, Jr., F. Vakili, and J. Gay. Phase Knife Coronagraph. II - Laboratory results. *A&A*, 400:385–392, March 2003.

[3] L. Abe, N. Murakami, J. Nishikawa, and M. Tamura. Removal of central obscuration and spider arm effects with beam-shaping coronagraphy. *A&A*, 451:363–373, May 2006.

[4] L. Abe, F. Vakili, and A. Boccaletti. The achromatic phase knife coronagraph. *A&A*, 374:1161–1168, August 2001.

[5] C. Aime. Principle of an Achromatic Prolate Apodized Lyot Coronagraph. *PASP*, 117:1012, September 2005.

[6] C. Aime. Radon approach to shaped and apodized apertures for imaging exoplanets. *A&A*, 434:785–794, May 2005.

[7] C. Aime and R. Soummer. Multiple-stage apodized pupil Lyot coronagraph for high-contrast imaging. In D. Bonaccini Calia, B. L. Ellerbroek, and R. Ragazzoni, editors, *Advancements in Adaptive Optics. Edited by Domenico B. Calia, Brent L. Ellerbroek, and Roberto Ragazzoni. Proceedings of the SPIE, Volume 5490, pp. 456-461 (2004).*, volume 5490 of *Presented at the Society of Photo-Optical Instrumentation Engineers (SPIE) Conference*, pages 456–461, October 2004.

[8] C. Aime, R. Soummer, and A. Ferrari. Interferometric apodization of rectangular apertures. Application to stellar coronagraphy. *A&A*, 379:697–707, November 2001.

[9] C. Aime, R. Soummer, and A. Ferrari. Total coronagraphic extinction of rectangular apertures using linear prolate apodizations. *A&A*, 389:334–344, July 2002.

[10] E. Aller Carpentier, M. Kasper, P. Martinez, E. Vernet, C. Verinaud, E. Fedrigo, C. Soenke, S. Tordo, N. Hubin, S. Esposito, E. Pinna, A. Puglisi, A. Tozzi, F. Quiros, A. G. Basden, S. J. Goodsell, G. D. Love, R. M. Myers, and M. Harrison. High order test bench for extreme adaptive optics system optimization. In *Proceedings of the SPIE, (2008).*, June 2008.

[11] T. Andersen, A. L. Ardeberg, J. Beckers, A. Goncharov, M. Owner-Petersen, H. Riewaldt, R. Snel, and D. Walker. The Euro50 Extremely Large Telescope. In J. R. P. Angel and R. Gilmozzi, editors, *Future Giant Telescopes. Edited by Angel, J. Roger P.; Gilmozzi, Roberto. Proceedings of the SPIE, Volume 4840, pp. 214-225 (2003).*, volume 4840 of *Presented at the Society of Photo-Optical Instrumentation Engineers (SPIE) Conference*, pages 214–225, January 2003.

[12] J. C. Augereau, A. M. Lagrange, D. Mouillet, and F. Ménard. HST/NICMOS2 observations of the HD 141569 A circumstellar disk. *A&A*, 350:L51–L54, October 1999.

[13] N. Baba and N. Murakami. A Method to Image Extrasolar Planets with Polarized Light. *PASP*, 115:1363–1366, December 2003.

[14] P. Baudoz, A. Boccaletti, Y. Rabbia, and J. Gay. Stellar Coronagraphy: Study and Test of a Hybrid Interfero-Coronagraph. *PASP*, 117:1004–1011, September 2005.

[15] P. Baudoz, A. Boccaletti, and D. Rouan. Multiple-Stage Four Quadrant Phase Mask Coronagraph. In P. Kalas, editor, *In the Spirit of Bernard Lyot: The Direct Detection of Planets and Circumstellar Disks in the 21st Century*, June 2007.

[16] P. Baudoz, Y. Rabbia, and J. Gay. Achromatic interfero coronagraphy I. Theoretical capabilities for ground-based observations. *A&A S.*, 141:319–329, January 2000.

[17] P. Baudoz, Y. Rabbia, J. Gay, R. Burg, L. Petro, P. Bely, B. Fleury, P.-Y. Madec, and F. Charbonnier. Achromatic interfero coronagraphy. II. Effective performance on the sky. *A&A S.*, 145:341–350, August 2000.

[18] J.-L. Beuzit, M. Feldt, K. Dohlen, D. Mouillet, P. Puget, J. Antici, A. Baruffolo, P. Baudoz, A. Berton, A. Boccaletti, M. Carbillet, J. Charton, R. Claudi, M. Downing, P. Feautrier, E. Fedrigo, T. Fusco, R. Gratton, N. Hubin, M. Kasper, M. Langlois, C. Moutou, L. Mugnier, J. Pragt, P. Rabou, M. Saisse, H. M. Schmid, E. Stadler, M. Turrato, S. Udry, R. Waters, and F. Wildi. SPHERE: A 'Planet Finder' Instrument for the VLT. *The Messenger*, 125:29–+, September 2006.

[19] J.-L. Beuzit, M. Feldt, K. Dohlen, D. Mouillet, P. Puget, J. Antici, P. Baudoz, A. Boccaletti, M. Carbillet, J. Charton, R. Claudi, T. Fusco, R. Gratton, T. Henning, N. Hubin, F. Joos, M. Kasper, M. Langlois, C. Moutou, J. Pragt, P. Rabou, M. Saisse, H. M. Schmid, M. Turatto, S. Udry, F. Vakili, R. Waters, and F. Wildi. SPHERE: A Planet Finder Instrument for the VLT. In P. Kalas, editor, *Proceedings of the conference In the Spirit of Bernard Lyot: The Direct Detection of Planets and Circumstellar Disks in the 21st Century. June 04 - 08, 2007. University of California, Berkeley, CA, USA. Edited by Paul Kalas.*, June 2007.

[20] J. L. Beuzit, D. Mouillet, C. Moutou, K. Dohlen, T. Fusco, P. Puget, S. Udry, R. Gratton, H. M. Schmid, M. Feldt, M. Kasper, and The Vlt-Pf Consortium. A "Planet Finder" instrument for the VLT. In L. Arnold, F. Bouchy, and C. Moutou, editors, *Tenth Anniversary of 51 Peg-b: Status of and prospects for hot Jupiter studies*, pages 353–355, February 2006.

[21] A. Boccaletti. Numerical Simulations for Coronagraphy. part II. In C. Aime and R. Soummer, editors, *EAS Publications Series*, pages 165–176, 2004.

[22] A. Boccaletti, L. Abe, J. Baudrand, J. B. Daban, R. Douet, G. Guerri, S. Robbe-Dubois, P. Bendjoya, K. Dohlen, and D. Mawet. Prototyping achromatic coronagraphs for exoplanet characterization with SPHERE. In *Proceedings of the SPIE, (2008).*, June 2008.

[23] A. Boccaletti, G. Chauvin, P. Baudoz, and J.-L. Beuzit. Coronagraphic near-IR photometry of AB Doradus C. *A&A*, 482:939–943, May 2008.

[24] A. Boccaletti and D. Mouillet. VLT Planet Finder III.: expected performance. In F. Casoli, T. Contini, J. M. Hameury, and L. Pagani, editors, *SF2A-2005: Semaine de l'Astrophysique Francaise*, pages 223–+, December 2005.

[25] A. Boccaletti, D. Mouillet, T. Fusco, P. Baudoz, C. Cavarroc, J.-L. Beuzit, C. Moutou, and K. Dohlen. Analysis of ground-based differential imager performance. In C. Aime and F. Vakili, editors, *IAU Colloq. 200: Direct Imaging of Exoplanets: Science & Techniques*, pages 519–524, 2006.

[26] A. Boccaletti, P. Riaud, P. Baudoz, J. Baudrand, J.-M. Reess, and D. Rouan. Coronagraphy with JWST in the thermal IR. In C. Aime and R. Soummer, editors, *EAS Publications Series*, pages 195–204, 2004.

[27] A. Boccaletti, P. Riaud, P. Baudoz, J. Baudrand, D. Rouan, D. Gratadour, F. Lacombe, and A.-M. Lagrange. The Four-Quadrant Phase Mask Coronagraph. IV. First Light at the Very Large Telescope. *PASP*, 116:1061–1071, November 2004.

[28] M. Born and E. Wolf. Principles of Optics 6th edition. *Pergamon Press, Oxford*, 1989.

[29] A. Carlotti, G. Ricort, C. Aime, Y. El Azhari, and R. Soummer. Interferometric apodization of telescope apertures. I. First laboratory results obtained using a Mach-Zehnder interferometer. *A&A*, 477:329–335, January 2008.

[30] C. Cavarroc, A. Boccaletti, P. Baudoz, T. Fusco, and D. Rouan. Fundamental limitations on Earth-like planet detection with extremely large telescopes. *A&A*, 447:397–403, February 2006.

[31] G. A. Chanan, M. Troy, and C. M. Ohara. Phasing the primary mirror segments of the Keck telescopes: a comparison of different techniques. In P. Dierickx, editor, *Proc. SPIE Vol. 4003, p. 188-202, Optical Design, Materials, Fabrication, and Maintenance, Philippe Dierickx; Ed.*, volume 4003 of *Presented at the Society of Photo-Optical Instrumentation Engineers (SPIE) Conference*, pages 188–202, July 2000.

[32] G. Chauvin, A.-M. Lagrange, C. Dumas, B. Zuckerman, D. Mouillet, I. Song, J.-L. Beuzit, and P. Lowrance. Giant planet companion to 2MASSW J1207334-393254. *A&A*, 438:L25–L28, August 2005.

[33] J. R. Crepp, J. Ge, A. D. Vanden Heuvel, S. P. Miller, and M. J. Kuchner. Laboratory Testing of a Lyot Coronagraph Equipped with an Eighth-Order Notch Filter Image Mask. *Ap.J*, 646:1252–1259, August 2006.

[34] J. R. Crepp, A. D. Vanden Heuvel, and J. Ge. Comparative Lyot Coronagraphy with Extreme Adaptive Optics Systems. *Ap.J*, 661:1323–1331, June 2007.

[35] P. Dierickx, E. T. Brunetto, F. Comeron, R. Gilmozzi, F. Y. J. Gonté, F. Koch, M. le Louarn, G. J. Monnet, J. Spyromilio, I. Surdej, C. Verinaud, and N. Yaitskova. OWL phase A status report. In J. M. Oschmann, Jr., editor, *Ground-based Telescopes. Edited by Oschmann, Jacobus M., Jr. Proceedings of the SPIE, Volume 5489, pp. 391-406 (2004).*, volume 5489 of *Presented at the Society of Photo-Optical Instrumentation Engineers (SPIE) Conference*, pages 391–406, October 2004.

[36] K. Dohlen. Aspects of error budgeting for coronagraphic differential imaging: Effects of dust and cosmetic errors. In *Proceedings of the SPIE, (2008).*, June 2008.

[37] C. Dorrer and J. D. Zuegel. Design and analysis of binary beam shapers using error diffusion. *Journal of the Optical Society of America B Optical Physics*, 24:1268–1275, June 2007.

[38] R. W. Floyd and L. Steinberg. An adaptive algorithm for spatial greyscale. *J. Soc. Inf. Disp. 17, 7577 (1976)*, 1976.

[39] J. Gay, Y. Rabbia, and C. Manghini. Interfero-Coronagraphy Using Pupil π-ROTATION. In C. Eiroa, editor, *Astrophysics and Space Science Library*, volume 215 of *Astrophysics and Space Science Library*, pages 187–+, 1997.

[40] C. Genet and T. W. Ebbesen. Light in tiny holes. *Nature*, 445:39–46, January 2007.

[41] R. W. Gerchberg and W. O. Saxton. A practical algorithm for the determination of phase from image and diffraction plane pictures. In *Optik 35, 237-246*, 1972.

[42] R. Gilmozzi. The European ELT: status, science, size. In *Proceedings of the SPIE, (2008).*, June 2008.

[43] R. Gonsalves and P. Nisenson. Calculation of Optimized Apodizers for a Terrestrial Planet Finder Coronagraphic Telescope. *PASP*, 115:706–711, June 2003.

[44] D. Gratadour, D. Rouan, A. Boccaletti, P. Riaud, and Y. Clénet. Four quadrant phase mask K-band coronagraphy of NGC 1068 with NAOS-CONICA at VLT. *A&A*, 429:433–437, January 2005.

[45] O. Guyon. Phase-induced amplitude apodization of telescope pupils for extrasolar terrestrial planet imaging. *A&A*, 404:379–387, June 2003.

[46] O. Guyon. Imaging Faint Sources within a Speckle Halo with Synchronous Interferometric Speckle Subtraction. *Ap.J*, 615:562–572, November 2004.

[47] O. Guyon, E. Pluzhnik, F. Martinache, S. Ridgway, and R. Galicher. The Phase-Induced Amplitude Apodization Coronagraph (PIAAC): A High Performance Coronagraph for Exoplanet Imaging. In *Bulletin of the American Astronomical Society*, volume 36 of *Bulletin of the American Astronomical Society*, pages 1564–+, December 2004.

[48] O. Guyon, E. A. Pluzhnik, M. J. Kuchner, B. Collins, and S. T. Ridgway. Theoretical Limits on Extrasolar Terrestrial Planet Detection with Coronagraphs. *Ap.J supl.*, 167:81–99, November 2006.

[49] O. Guyon and M. Shao. The Pupil-swapping Coronagraph. *PASP*, 118:860–865, June 2006.

[50] C-P. Huang and Y-Y. Zhu. Plasmonics: manipulating light at the subwavelength scale. 2007, October 2007.

[51] P. Jacquinot and B. Roisin-Dossier. . *Prog. Opt.*, 3:29, 1964.

[52] R. Jayawardhana, S. Fisher, L. Hartmann, C. Telesco, R. Pina, and G. Fazio. A Dust Disk Surrounding the Young A Star HR 4796A. *Ap.J Lett.*, 503:L79+, August 1998.

[53] M. Johns, J. R. P. Angel, S. Shectman, R. Bernstein, D. G. Fabricant, P. McCarthy, and M. Phillips. Status of the Giant Magellan Telescope (GMT) project. In J. M. Oschmann, Jr., editor, *Ground-based Telescopes. Edited by Oschmann, Jacobus M., Jr. Proceedings of the SPIE, Volume 5489, pp. 441-453 (2004).*, volume 5489 of *Presented at the Society of Photo-Optical Instrumentation Engineers (SPIE) Conference*, pages 441–453, October 2004.

[54] L. Jolissaint and J.-P. Veran. Fast computation and morphologic interpretation of the Adaptive optics point spread function. In E. Vernet, R. Ragazzoni, S. Esposito, and N. Hubin, editors, *European Southern Observatory Astrophysics Symposia*, volume 58 of *European Southern Observatory Astrophysics Symposia*, pages 201–+, 2002.

[55] N. J. Kasdin, R. J. Vanderbei, M. G. Littman, and D. N. Spergel. Optimal Shaped Pupils for Planet Finding Coronagraphy. In *Bulletin of the American Astronomical Society*, volume 35 of *Bulletin of the American Astronomical Society*, pages 1205–+, December 2003.

[56] M. Kasper, J.-L. Beuzit, C. Verinaud, N. Yaitskova, P. Baudoz, A. Boccaletti, R. Gratton, N. Hubin, F. Kerber, R. Roeljsema, H. M. Schmid, N. Thatte, K. Dohlen, M. Feldt, and S. Wolf. EPICS, the exoplanet imager for the E-ELT. In *Proceedings of the SPIE, (2008).*, June 2008.

[57] M. J. Kuchner. A Unified View of Coronagraph Image Masks. *ArXiv Astrophysics e-prints*, January 2004.

[58] M. J. Kuchner, J. Crepp, and J. Ge. Eighth-Order Image Masks for Terrestrial Planet Finding. *Ap.J*, 628:466–473, July 2005.

[59] M. J. Kuchner and W. A. Traub. A Coronagraph with a Band-limited Mask for Finding Terrestrial Planets. *Ap.J*, 570:900–908, May 2002.

[60] B. Lyot. The study of the solar corona and prominences without eclipses (George Darwin Lecture, 1939). *MNRAS*, 99:580–+, June 1939.

[61] B. Macintosh, J. Graham, D. Palmer, R. Doyon, D. Gavel, J. Larkin, B. Oppenheimer, L. Saddlemyer, J. K. Wallace, B. Bauman, J. Evans, D. Erikson, K. Morzinski, D. Phillion, L. Poyneer, A. Sivaramakrishnan, R. Soummer, S. Thibault, and J.-P. Veran. The Gemini Planet Imager. In *Advances in Adaptive Optics II. Edited by Ellerbroek, Brent L.; Bonaccini Calia, Domenico. Proceedings of the SPIE, Volume 6272, pp. 62720L (2006).*, volume 6272 of *Presented at the Society of Photo-Optical Instrumentation Engineers (SPIE) Conference*, July 2006.

[62] C. Marois, R. Doyon, R. Racine, and D. Nadeau. Efficient Speckle Noise Attenuation in Faint Companion Imaging. *PASP*, 112:91–96, January 2000.

[63] C. Marois, D. Lafrenière, B. Macintosh, and R. Doyon. Confidence Level and Sensitivity Limits in High-Contrast Imaging. *Ap.J*, 673:647–656, January 2008.

[64] F. Martinache. Phase Contrast Apodisation. In C. Aime and R. Soummer, editors, *EAS Publications Series*, volume 12 of *EAS Publications Series*, pages 311–316, 2004.

[65] P. Martinez, A. Boccaletti, M. Kasper, P. Baudoz, and C. Cavarroc. Optimization of apodized pupil Lyot coronagraph for ELTs. *A&A*, 474:671–678, November 2007.

[66] P. Martinez, E. Vernet, C. Dorrer, A. Boccaletti, M. Kasper, E. Aller Carpentier, J. Baudrand, and Chaumont. Phase and Lyot-type coronagraphs for the High Order TestBench: prototyping and laboratory results. In *Proceedings of the SPIE, (2008).*, June 2008.

[67] D. Mawet, P. Riaud, O. Absil, J. Baudrand, and J. Surdej. The four quadrant-ZOG and annular groove phase mask coronagraphs. In D. R. Coulter, editor, *Wavefront amplitude variation of TPF's high-contrast imaging testbed: modeling and experiment. Edited by Shi, Fang; Lowman, Andrew E.; Moody, Dwight; Niessner, Albert F.; Trauger, John T. Proceedings of the SPIE, Volume 5905, pp. 486-495 (2005).*, volume 5905 of *Presented at the Society of Photo-Optical Instrumentation Engineers (SPIE) Conference*, pages 486–495, January 2005.

[68] D. Mawet, P. Riaud, O. Absil, and J. Surdej. Annular Groove Phase Mask Coronagraph. *Ap.J*, 633:1191–1200, November 2005.

[69] D. Mawet, P. Riaud, J. Baudrand, P. Baudoz, A. Boccaletti, O. Dupuis, and D. Rouan. The four-quadrant phase-mask coronagraph: white light laboratory results with an achromatic device. *A&A*, 448:801–808, March 2006.

[70] M. Mayor and D. Queloz. A Jupiter-Mass Companion to a Solar-Type Star. *Nature*, 378:355–+, November 1995.

[71] B. P. Mennesson, M. Shao, B. M. Levine, J. K. Wallace, D. T. Liu, E. Serabyn, S. C. Unwin, and C. A. Beichman. Optical Planet Discoverer: how to turn a 1.5-m class space telescope into a powerful exo-planetary systems imager. In A. B. Schultz, editor, *High-Contrast Imaging for Exo-Planet Detection. Edited by Alfred B. Schultz. Proceedings of the SPIE, Volume 4860, pp. 32-44 (2003).*, volume 4860 of *Presented at the Society of Photo-Optical Instrumentation Engineers (SPIE) Conference*, pages 32–44, February 2003.

[72] J. Nelson and G. H. Sanders. TMT status report. In *Ground-based and Airborne Telescopes. Edited by Stepp, Larry M.. Proceedings of the SPIE, Volume 6267, pp. 626728 (2006).*, volume 6267 of *Presented at the Society of Photo-Optical Instrumentation Engineers (SPIE) Conference*, July 2006.

[73] P. Nisenson and C. Papaliolios. Detection of Earth-like Planets Using Apodized Telescopes. *Ap.J Lett.*, 548:L201–L205, February 2001.

[74] B. R. Oppenheimer, A. P. Digby, L. Newburgh, D. Brenner, M. Shara, J. Mey, C. Mandeville, R. B. Makidon, A. Sivaramakrishnan, R. Soummer, J. R. Graham, P. Kalas, M. D. Perrin, L. C. Roberts, Jr., J. R. Kuhn, K. Whitman, and J. P. Lloyd. The Lyot project: toward exoplanet imaging and spectroscopy. In D. Bonaccini Calia, B. L. Ellerbroek, and R. Ragazzoni, editors, *Advancements in Adaptive Optics. Edited by Domenico B. Calia, Brent L. Ellerbroek, and Roberto Ragazzoni. Proceedings of the SPIE, Volume 5490, pp. 433-442 (2004).*, volume 5490 of *Presented at the Society of Photo-Optical Instrumentation Engineers (SPIE) Conference*, pages 433–442, October 2004.

[75] J. E. Oti, V. F. Canales, and M. P. Cagigal. The Optical Differentiation Coronagraph. *Ap.J*, 630:631–636, September 2005.

[76] D. M. Palacios. An optical vortex coronagraph. In D. R. Coulter, editor, *Techniques and Instrumentation for Detection of Exoplanets II. Edited by Coulter, Daniel R. Proceedings of the SPIE, Volume 5905, pp. 196-205 (2005).*, volume 5905 of *Presented at the Society of Photo-Optical Instrumentation Engineers (SPIE) Conference*, pages 196–205, August 2005.

[77] M. A. C. Perryman. Extra-solar planets. *Reports of Progress in Physics*, 63:1209–1272, 2000.

[78] R. Racine, G. A. H. Walker, D. Nadeau, R. Doyon, and C. Marois. Speckle Noise and the Detection of Faint Companions. *PASP*, 111:587–594, May 1999.

[79] P. Riaud, A. Boccaletti, D. Rouan, F. Lemarquis, and A. Labeyrie. The Four-Quadrant Phase-Mask Coronagraph. II. Simulations. *PASP*, 113:1145–1154, September 2001.

[80] P. Riaud, D. Mawet, O. Absil, A. Boccaletti, P. Baudoz, E. Herwats, and J. Surdej. Coronagraphic imaging of three weak-line T Tauri stars: evidence of planetary formation around PDS 70. *A&A*, 458:317–325, October 2006.

[81] F. J. Rigaut, J.-P. Veran, and O. Lai. Analytical model for Shack-Hartmann-based adaptive optics systems. In D. Bonaccini and R. K. Tyson, editors, *Society of Photo-Optical Instrumentation Engineers (SPIE) Conference Series*, volume 3353 of *Presented at the Society of Photo-Optical Instrumentation Engineers (SPIE) Conference*, pages 1038–1048, September 1998.

[82] F. Roddier and C. Roddier. Stellar Coronograph with Phase Mask. *PASP*, 109:815–820, July 1997.

[83] D. Rouan, P. Riaud, A. Boccaletti, Y. Clénet, and A. Labeyrie. The Four-Quadrant Phase-Mask Coronagraph. I. Principle. *PASP*, 112:1479–1486, November 2000.

[84] G. Rousset, F. Lacombe, P. Puget, N. N. Hubin, E. Gendron, T. Fusco, R. Arsenault, J. Charton, P. Feautrier, P. Gigan, P. Y. Kern, A.-M. Lagrange, P.-Y. Madec, D. Mouillet, D. Rabaud, P. Rabou, E. Stadler, and G. Zins. NAOS, the first AO system of the VLT: on-sky performance. In P. L. Wizinowich and D. Bonaccini, editors, *Adaptive Optical System Technologies II. Edited by Wizinowich, Peter L.; Bonaccini, Domenico. Proceedings of the SPIE, Volume 4839, pp. 140-149 (2003).*, volume 4839 of *Presented at the Society of Photo-Optical Instrumentation Engineers (SPIE) Conference*, pages 140–149, February 2003.

[85] S. B. Shaklan and J. J. Green. Low-Order Aberration Sensitivity of Eighth-Order Coronagraph Masks. *Ap.J*, 628:474–477, July 2005.

[86] A. Sivaramakrishnan and J. P. Lloyd. Spiders in Lyot Coronagraphs. *Ap.J*, 633:528–533, November 2005.

[87] B. A. Smith and R. J. Terrile. A circumstellar disk around Beta Pictoris. *Science*, 226:1421–1424, December 1984.

[88] R. Soummer. Apodized Pupil Lyot Coronagraphs for Arbitrary Telescope Apertures. *Ap.J*, 618:L161–L164, January 2005.

[89] R. Soummer, C. Aime, and P. E. Falloon. Stellar coronagraphy with prolate apodized circular apertures. *A&A*, 397:1161–1172, January 2003.

[90] R. Soummer, K. Dohlen, and C. Aime. Achromatic dual-zone phase mask stellar coronagraph. *A&A*, 403:369–381, May 2003.

[91] R. Soummer, L. Pueyo, A. Ferrari, C. Aime, A. Sivaramakrishnan, and N. Yaitskova. Apodized Pupil Lyot Coronagraphs for arbitrary apertures. II. Theoretical properties and Application to Extremely Large Telescopes. In *submitted to ApJ*, 2007.

[92] W. A. Traub, M. Levine, S. Shaklan, J. Kasting, J. R. Angel, M. E. Brown, R. A. Brown, C. Burrows, M. Clampin, A. Dressler, H. C. Ferguson, H. B. Hammel, S. R. Heap, S. D. Horner, G. D. Illingworth, N. J. Kasdin, M. J. Kuchner, D. Lin, M. S. Marley, V. Meadows, C. Noecker, B. R. Oppenheimer, S. Seager, M. Shao, K. R. Stapelfeldt, and J. T. Trauger. TPF-C: status and recent progress. In *Advances in Stellar Interferometry. Edited by Monnier, John D.; Schöller, Markus; Danchi, William C.. Proceedings of the SPIE, Volume 6268, pp. 62680T (2006).*, volume 6268 of *Presented at the Society of Photo-Optical Instrumentation Engineers (SPIE) Conference*, July 2006.

[93] M. Troy and G. A. Chanan. Diffraction effects from giant segmented mirror telescopes. In J. R. P. Angel and R. Gilmozzi, editors, *Future Giant Telescopes. Edited by Angel, J. Roger P.; Gilmozzi, Roberto. Proceedings of the SPIE, Volume 4840, pp. 81-92 (2003).*, volume 4840 of *Presented at the Society of Photo-Optical Instrumentation Engineers (SPIE) Conference*, pages 81–92, January 2003.

[94] S. Udry and M. Mayor. Extra-solar planets around solar-type strs. In P. Ehrenfreund, O. Angerer, and B. Battrick, editors, *Exo-/Astro-Biology*, volume 496 of *ESA Special Publication*, pages 65–72, August 2001.

[95] R. Ulichney. Digital Halftoning. *The MIT Press.*, 1987.

[96] R. Ulichney. Dithering with blue noise. *Proc. IEEE, vol. 76, 1, 56-79 (1988)*, 1988.

[97] R. J. Vanderbei, N. J. Kasdin, and D. N. Spergel. Checkerboard-Mask Coronagraphs for High-Contrast Imaging. *Ap.J*, 615:555–561, November 2004.

[98] R. J. Vanderbei, D. N. Spergel, and N. J. Kasdin. Circularly Symmetric Apodization via Star-shaped Masks. *Ap.J*, 599:686–694, December 2003.

[99] R. J. Vanderbei, D. N. Spergel, and N. J. Kasdin. Spiderweb Masks for High-Contrast Imaging. *Ap.J*, 590:593–603, June 2003.

[100] C. Verinaud, M. Kasper, J.-L. Beuzit, N. Yaitskova, V. Korkiakoski, K. Dohlen, P. Baudoz, T. Fusco, L. Mugnier, and N. Thatte. EPICS Performance Evaluation through Analytical and Numerical Modeling. In P. Kalas, editor, *In the Spirit of Bernard Lyot: The Direct Detection of Planets and Circumstellar Disks in the 21st Century*, June 2007.

[101] E. Vernet, M. Kasper, C. Vérinaud, E. Fedrigo, S. Tordo, N. Hubin, S. Esposito, E. Pinna, A. Puglisi, A. Tozzi, A. G. Basden, S. J. Goodsell, G. D. Love, and R. M. Myers. Extreme adaptive optics system optimization with the high order test bench. In *Advances in Adaptive Optics II. Edited by Ellerbroek, Brent L.; Bonaccini Calia, Domenico. Proceedings of the SPIE, Volume 6272, pp. 62722K (2006).*, July 2006.

[102] A. Wolszczan and D. A. Frail. A planetary system around the millisecond pulsar PSR1257 + 12. *Nature*, 355:145–147, January 1992.